Green Energy and Technology

Vyacheslav Romanov *Editor*

Greenhouse Gases and Clay Minerals

Enlightening Down-to-Earth Road Map to Basic Science of Clay-Greenhouse Gas Interfaces

Springer

Green Energy and Technology

More information about this series at http://www.springer.com/series/8059

Vyacheslav Romanov
Editor

Greenhouse Gases and Clay Minerals

Enlightening Down-to-Earth Road Map to Basic Science of Clay-Greenhouse Gas Interfaces

Springer

Editor
Vyacheslav Romanov
National Energy Technology Laboratory
Pittsburgh, PA
USA

ISSN 1865-3529 ISSN 1865-3537 (electronic)
Green Energy and Technology
ISBN 978-3-319-12660-9 ISBN 978-3-319-12661-6 (eBook)
https://doi.org/10.1007/978-3-319-12661-6

Library of Congress Control Number: 2017952932

© Springer International Publishing AG 2018
This work is subject to copyright. All rights are reserved by the Publisher, whether the whole or part of the material is concerned, specifically the rights of translation, reprinting, reuse of illustrations, recitation, broadcasting, reproduction on microfilms or in any other physical way, and transmission or information storage and retrieval, electronic adaptation, computer software, or by similar or dissimilar methodology now known or hereafter developed.
The use of general descriptive names, registered names, trademarks, service marks, etc. in this publication does not imply, even in the absence of a specific statement, that such names are exempt from the relevant protective laws and regulations and therefore free for general use.
The publisher, the authors and the editors are safe to assume that the advice and information in this book are believed to be true and accurate at the date of publication. Neither the publisher nor the authors or the editors give a warranty, express or implied, with respect to the material contained herein or for any errors or omissions that may have been made. The publisher remains neutral with regard to jurisdictional claims in published maps and institutional affiliations.

Printed on acid-free paper

This Springer imprint is published by Springer Nature
The registered company is Springer International Publishing AG
The registered company address is: Gewerbestrasse 11, 6330 Cham, Switzerland

Acknowledgements

A significant portion of this book is a reflection on the clay/shale work that the editor had initiated in 2006, to complement the carbon sequestration research at the U.S. Department of Energy (DOE) National Energy Technology Laboratory (NETL) with support and encouragement from Dr. Yee Soong (NETL). A couple of years later, Dr. George D. Guthrie (currently at LANL) had really set a boat in motion by promoting our collaboration with the external colleagues. Many other NETL persons who are not named here had supported this effort and lended us a hand whenever we needed it. We have significantly benefited from the expert knowledge and ingenuity of the University of Illinois professors, Stephen J. Guggenheim and August F. Koster van Groos; as well as from the discussions with fellow DOE scientists at the Pacific Northwest National Laboratory (PNNL) Drs. John S. Loring, Vassiliki-Alexandra (Vanda) Glezakou, and Herbert T. Schaef. Communication with the Shell Corporation's geoscience experts, Drs. Andreas Busch and Tim J. Tambach, was also appreciated. Dr. Tae-Bong Hur (former NETL ORISE Fellow) is acknowledged for the carbonation data. This research was supported in part by appointments to the National Energy Technology Laboratory Research Participation Program, sponsored by the U.S. Department of Energy and administered by the Oak Ridge Institute for Science and Education (ORISE).

Disclaimer

This project was funded by the Department of Energy, National Energy Technology Laboratory, an agency of the United States Government, through a support contract with AECOM. Neither the United States Government nor any agency thereof, nor any of their employees, nor AECOM, nor any of their employees, makes any warranty, expressed or implied, or assumes any legal liability or responsibility for the accuracy, completeness, or usefulness of any information, apparatus, product, or process disclosed, or represents that its use would not infringe privately owned rights. Reference herein to any specific commercial product, process, or service by trade name, trademark, manufacturer, or otherwise, does not necessarily constitute or imply its endorsement, recommendation, or favoring by the United States Government or any agency thereof. The views and opinions of authors expressed herein do not necessarily state or reflect those of the United States Government or any agency thereof.

Contents

1 Motivation 1
Vyacheslav Romanov and Robert Dilmore

2 Greenhouse Gases and Their Role in Climate Change 15
Robert Dilmore and Liwei Zhang

3 Clay: Geologic Formations, Carbon Management, and Industry . . . 33
Daniel J. Soeder

4 Clay Mineralogy 55
Bret H. Howard and Jonathan W. Lekse

5 Advanced Experimental Techniques in Geochemistry 77
Vyacheslav Romanov

6 Experimental Studies: Molecular Interactions at Clay Interfaces . . . 95
Lei Hong and Vyacheslav Romanov

7 Experimental Studies: Clay Swelling 125
Vyacheslav Romanov and Evgeniy M. Myshakin

8 Monte Carlo and Molecular Dynamics Simulations of Clay Mineral Systems 147
Evgeniy M. Myshakin and Randall T. Cygan

9 Advances in Molecular Simulation Studies of Clay Minerals 175
Randall T. Cygan and Evgeniy M. Myshakin

Index 185

Contributors

Randall T. Cygan U.S. Department of Energy, Sandia National Laboratories (SNL), Albuquerque, USA

Robert Dilmore U.S. Department of Energy, National Energy Technology Laboratory (NETL), Pittsburgh, USA

Lei Hong U.S. Department of Energy, NETL–AECOM, Pittsburgh, USA

Bret H. Howard U.S. Department of Energy, National Energy Technology Laboratory (NETL), Pittsburgh, USA

Jonathan W. Lekse U.S. Department of Energy, National Energy Technology Laboratory (NETL), Pittsburgh, USA

Evgeniy M. Myshakin U.S. Department of Energy, NETL–AECOM, Pittsburgh, USA

Vyacheslav Romanov U.S. Department of Energy, National Energy Technology Laboratory (NETL), Pittsburgh, USA

Daniel J. Soeder U.S. Department of Energy, National Energy Technology Laboratory (NETL), Pittsburgh, USA

Liwei Zhang NETL, Oak Ridge Institute for Science and Education, Oak Ridge, TN, USA

Chapter 1
Motivation

Vyacheslav Romanov and Robert Dilmore

Some say the world will end in fire, Some say in ice.
—Robert Frost "Fire and Ice" in the selection "A Group of Poems"

Don't let me catch anyone talking about the Universe in my department.
—Quotations by Sir Ernest Rutherford

Abstract Environmental interactions are instrumental to sustainability of life on our planet. Evolution of life adapts to the environment and encompasses a wide range of phenomena, from the emergence of major lineages to mass extinctions. This book invites you to learn the science of carbon management, with particular focus on carbon capture and storage in geological formations. Rather than jumping to any conclusions, we will review the current state of knowledge and discuss the risks, available options, and likely scenarios. In the early chapters, students and avid readers who are passionate about the global challenges, can learn the basics about greenhouse gases and their role in the Earth's radiative balance, about natural carbon cycles and the challenges of controlled carbon management (capture, storage a.k.a. sequestration, and utilization) including the role of fossil fuels and common geological materials. More advanced chapters are reserved for recent research developments in understanding the nature of interactions between greenhouse gases and ubiquitous geomaterials, such as clay. Motivation for this exciting effort is to elucidate the state of understanding in the science of clay—CO_2 interactions, to bridge between traditional and modern geoscience perspectives, and to introduce consistent terminology that will facilitate communication between different generations and areas of scientific and technological inquiry.

V. Romanov (✉) · R. Dilmore
U.S. Department of Energy, National Energy Technology Laboratory (NETL), Pittsburgh, USA
e-mail: romanov@netl.doe.gov

© Springer International Publishing AG 2018

V. Romanov (ed.), *Greenhouse Gases and Clay Minerals*, Green Energy and Technology, https://doi.org/10.1007/978-3-319-12661-6_1

1.1 Is it Possible at All?!

Environmental interactions are instrumental to sustainability of life on our planet. Evolution of life adapts to the environment and encompasses a wide range of phenomena, from the emergence of major lineages to mass extinctions. One of the greatest mysteries facing humans is how on Earth life originated, in the first place. Most scientists today agree that the building blocks of life—such as amino acids and nucleotides (building blocks of DNA, deoxyribonucleic acid)—arose from nonliving matter. Evidence suggests that life on our planet first evolved around 3.8–3.5 billion years ago (Emiliani 1992). In early stages of the proto-Earth's formation, after a presumed collision (Fig. 1.1) with Theia (a roughly Mars-sized celestial body) about 4.5 billion years ago, it was a cauldron of erupting volcanoes, bombarding meteorites, and hot toxic gases. One billion years later, shortly after a violent period (4.1–3.8 billion years ago) of near-constant collisions with large asteroids and comets, it was teeming with anaerobic microbial life, in the absence of oxygen, relying on sulfates for the energy needs; the mantle temperature was still much higher than it is today, possibly as high as 1600 °C.

When Earth formed, the Solar System was undergoing the accretion process, and there was exchange of material between the planets; however, Earth's atmosphere acted as a barrier to genetic material that could have emerged from the outer space. In the 1950s, experiments on mixtures of reducing gases, thought to be present on primordial Earth, produced amino acids—but no nucleoside ribonucleic acid (RNA) bases—when subjected to electrical discharges. DNA (current biological replicator) requires an extensive array of protein components in order to replicate;

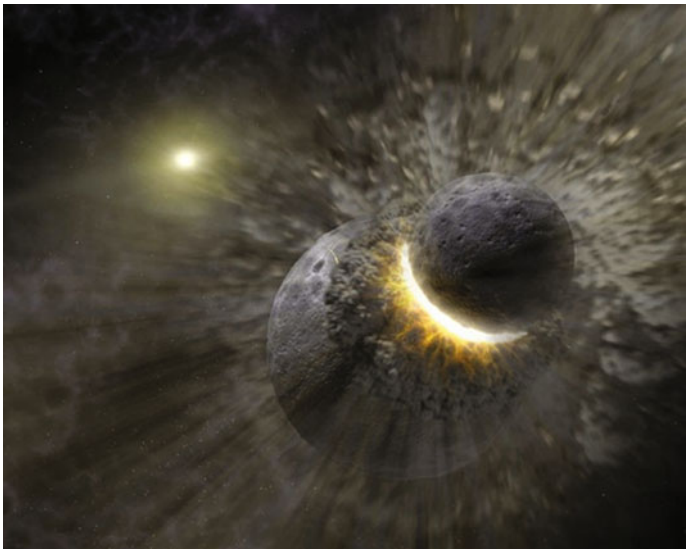

Fig. 1.1 Collision of the planet-sized objects. (artist's impression)—courtesy NASA/JPL-Caltech

and none of the proposed pre-RNA compounds have ever been shown to catalyze their own synthesis. Using DNA sequences of modern organisms, biologists have tentatively traced the most recent common ancestor of all known life to an aquatic microorganism that lived at extremely high temperatures. At that time, the acidic ocean was filled with positively charged protons, while deep-sea hydrothermal vents spewed out heated (at some 300 °C due to tectonic activity) hydrogen and methane-rich, mineral-laden highly alkaline fluids. The iron- and sulfur-rich, porous igneous-rock mineral interface formed between the two and created a natural charge gradient that powered the reduction of carbon dioxide with hydrogen into simple carbon-based molecules such as amino acids or proteins and then, hypothetically, drove the creation of some leaky cellular membranes, complex proteins and RNA. It is possible that a precursor to a cellular pump—a sodium pump that could power cellular reactions, enabling more complex life to form—had evolved in the membranes of the proto-cells. However, recent research findings by geochemists proved that a hydrothermal proto-metabolism pathway may not have been as easy in pre-biotic environments as previously assumed. Organic molecules are unstable at high temperatures, and are destroyed as quickly as they are produced, without being replicated—It has been estimated that life could not have arisen in the ocean unless the water temperature was less than 25 °C. Three billion years ago, the Sun was 30% less luminous than it is today. Still, DNA and RNA chains are affected by direct exposure to ultraviolet (UV) light. Without ozone layer, UV radiation would have been 100 times today's levels. With sufficient supply of organic molecules provided by the hydrothermal vents and several hundred meters of ice shielding the ocean-water ecosystem from UV and bolide impact frustration, many believe that this was the environment allowing extra-terrestrial life (frozen lipids, created in interstellar space and delivered by comets and meteorites) to get a foothold on hostile Earth (Fig. 1.2).

Fig. 1.2 What do we know or believe in? (adapted from www)

Terrestrial or extra-terrestrial, it remains unknown what exactly are the possible pathways to self-replication. There are several essential differences between living cells and inanimate formations of atoms: the former tend to be much better at capturing energy from their environment and dissipating it as heat while tending towards lower internal entropy; the living cells are resilient to decay while multiplying exponentially. According to recent studies, when a group of atoms is driven by an external source of energy and surrounded by a heat bath, it will gradually restructure or replicate itself in order to dissipate increasingly more energy. It was shown that the minimum value for the allowed rate of heat generation during irreversible self-replication is determined by the growth rate, internal entropy, and resilience (copying-fidelity and propensity to recover from reproductive errors) of the replicator (England 2013). The driving force of irreversibility phenomenon is, ostensibly, the arrow of time or else the generalized second law of thermodynamics, known as the law of increasing entropy. The hypothesis that microscopically detailed, quantitative relationship so far derived between irreversibility and entropy production is directly applicable to a class of phenomena that includes life remains unproven, yet. Conspicuously, the adaptability (via mutation and/or behavioral patterns) part of the resilience was left out of the studies mentioned here, as pertaining to more complex systems than the building blocks investigated by using a simple thermodynamic approach. Live (open and mobile) systems operate far from equilibrium, whereas the original second law states that isolated systems evolve toward thermodynamic equilibrium. Ilya Prigogine (1977 Nobel Prize in chemistry) made progress on predicting the behavior of open systems weakly driven by external energy sources; but the behavior of systems that are far from equilibrium, which are connected to the outside environment and strongly driven by external sources of energy, could not have been predicted until a generalized version of the fluctuation theorem for stochastic, microscopically reversible dynamics was deduced.

1.2 Here Comes Nothing!

The observed macroscopic irreversibility, however, is not a universal law and is attributed to a particular configuration of the universe as a consequence of the unusual low-entropy "initial" conditions 13.8 billion years ago, at the end of the Planck era of quantum gravity (10^{-43} s past the Big Bang (Hawking 1988), cosmological time zero singularity) marked by the separation of gravity and electronuclear forces. Soon (10^{-36} s later to be exact) after that period of quantum fluctuations—for which modern science does not provide any model or explanation other than a controversial string theory which describes elementary threads of energy—a phase transition tilted the balance between matter and antimatter and the universe's fabric had exponentially expanded for about 10^{-33} s (by a factor of 10^{30}–10^{40}, from subatomic- to golf-ball-sized; in a manner suggestive of self-replication of the space cells, driven by borrowed gravitational energy, in order to preserve a meta-stable false-vacuum equilibrium of the early universe that was possibly

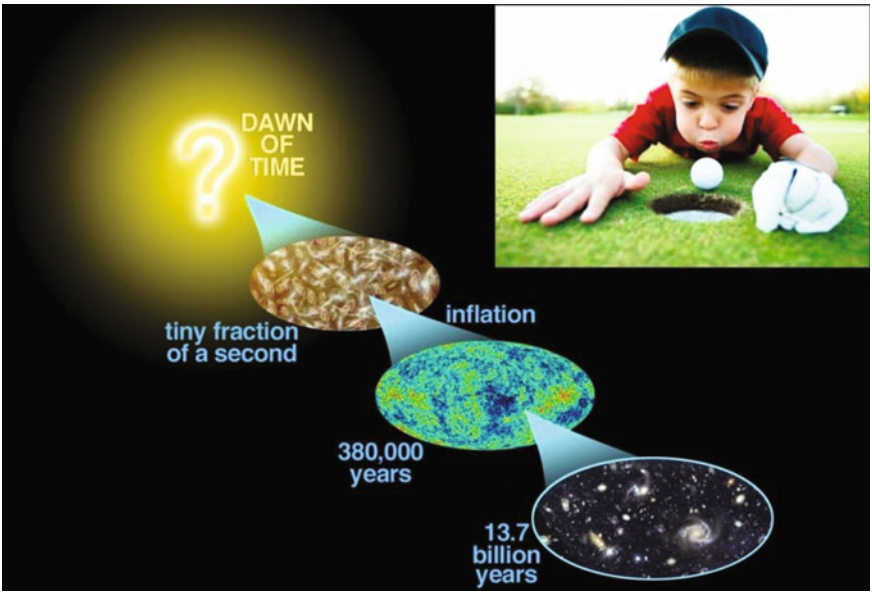

Fig. 1.3 Milestones in how the scientists view the universe. (adapted from https://science.nasa.gov/science-news/science-at-nasa/2003/11feb_map)

supercooled during the above-mentioned earlier phase transition from the Grand Unification to Electroweak era) after which the expansion of "cosmic egg" began to slow down due to gravitational forces (Fig. 1.3).

That is until about 5 billion years ago, when the dark energy of vacuum—allowed for by the Einstein's theory of general relativity—increased along with the metric expansion of space to the point that the generated negative pressure (vacuum energy density that causes space to repel itself) became sufficient to overcome the diminishing gravitational attraction forces. At that time, the expansion rate began to accelerate as discovered by Saul Perlmutter and colleagues (2011 Nobel Prize in physics). Coincidently, at about the same time (4.6 billion years ago) an external event at a passing-by giant star or supernova presumably caused the nascent Solar System's dust cloud to coalesce, which led to formation of the Sun and the planets orbiting it. However, little the scientists know about the properties of the dark energy ("antigravity" of sorts)—for decades, it had been known as Einstein's greatest mistake, until a few years ago—whose portion is already 72% in the current universe and is growing at an accelerating pace, and the dark matter (another 23%). So, it is quite possible that more surprises are coming our way (Fig. 1.4).

The biggest surprise so far is that our universe appears to have Goldilocks properties: an almost perfect balance of matter and energy among others, as if it were designed with engineering precision to support the development of life, at least for now. The Planck era quantum fluctuations, mapped by NASA (Bennett et al. 2013), are believed to be the original factories and cradles of life; but without gravity, it

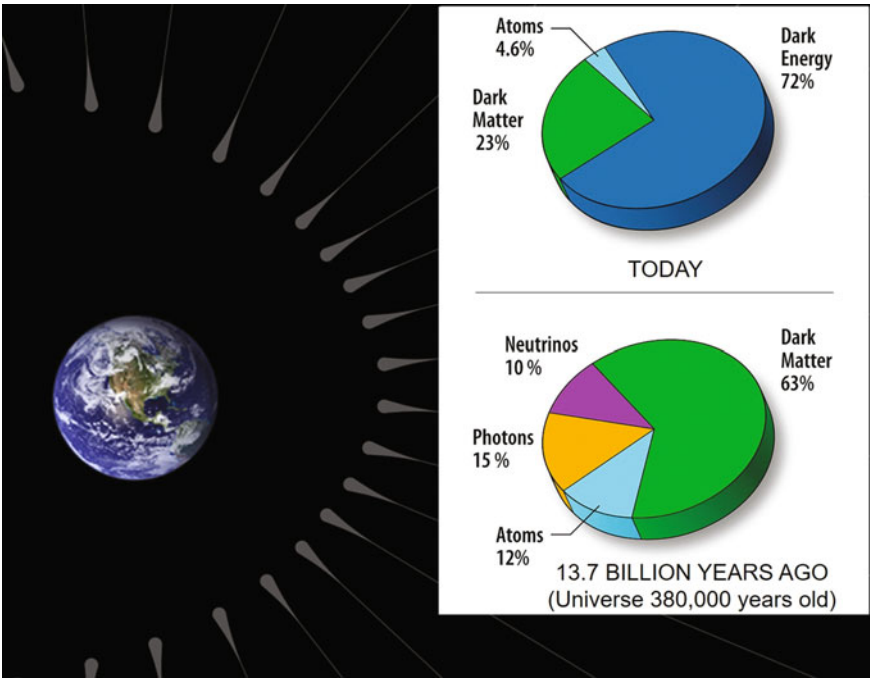

Fig. 1.4 (https://en.wikipedia.org/wiki/Chemical_element accessed 15 May 2017)

would not be possible. The pull of gravity gradually transformed the originally tiny fluctuations (in amazingly uniform and astonishingly flat early universe) into galaxies, stars, and planets; the ideal spatial dimension of the fluctuations is a mystery of its own: large enough for rapid formation of giant stars but not too large, to avoid widespread formation of black holes instead. The short-lived primordial stars (supergiants; past 400 million years from time zero) were quintessential to the evolution of the Universe and to life itself as they forged the heavy elements out of the clumps of hydrogen, helium, and some lithium (available after the separation of matter and radiation; past 380,000 years from time zero) and then exploded as supernovae, expelling these elements to be incorporated into the next generation of stars such as our Sun, and the time arrow presumably did the rest.

1.3 Evolution of Life (as We Know It)

Even so, the life on this planet had to go through a very long evolution before—according to the theory popularized by Charles Darwin (1809–1882)—the gradual process of natural selection (by means of the differential reproductive success of organisms interacting with their environment, as caused by inheritable random

mutations arising in genome of an individual organism) produced complex multicellular organisms via symbiotic relationship between cells of the same or different species (2.1 billion years ago) and much later the first sexually reproducing organisms (about 1.1 billion years ago). The latter events coincided with waves of free oxygen build-up in atmosphere-ocean system (Fig. 1.5), as the oxidizable-rock reservoirs near the surface of the Earth's crust eventually became saturated (first, near the ocean surface and much later, in deep ocean).

Most scientists believe the amount of atmospheric oxygen was insignificant up until about 2.4 billion years ago when the Great Oxidation Event (GOE) occurred. The seemingly sudden jumps in oxygen levels were almost certainly due to the origin and evolution of the photosynthetic organisms; although, Pennsylvania State University atmospheric scientists proposed (about two decades ago) that Earth gained an oxygen-rich atmosphere largely because molecular hydrogen belched out by volcanoes diffused into space. As the supply of free oxygen increased, most of the anaerobic organisms that had formerly occupied the Earth's surface were probably poisoned by oxygen. Cyanobacteria or blue-green algae became the first microbes to produce oxygen by photosynthesis, perhaps as long ago as 3.5 billion years ago and certainly by 2.7 billion years ago. It consumed water and carbon dioxide during photosynthesis, making organic matter and releasing oxygen. Other bacteria consumed the organic matter, yielding molecular hydrogen and acetate. These, in turn, were consumed by microbes that produced methane.

The ultimate and puzzling explosion of diversity and number of complex animal forms occurred during the Cambrian period of Paleozoic era, possibly due to the ultimate rise of atmospheric oxygen and formation of UV-protective ozone layer that allowed for land-colonization, the end of Cryogenian (or Sturtian-Varangian) ice age marked by the greatest ever glaciations (two Snowball Earths) or other, unidentified yet environmental changes; within 10–20 million years (about 530 million years ago) most of the major animal phyla appeared and marine animals evolved most of the basic body forms observed in modern groups. Still, the nature took its time developing the mammalian brain. Only very recently (2.4 million years ago) genus Homo first demonstrated the ability to utilize tools; *Homo sapiens*, the extant humans (the species that is most likely to read this book) evolved from Homo erectus about 200,000 years ago. But of course, the only species that are not afraid of playing with fire had to be developed, naturally, at the very onset of a new ice age. Admittedly, meeting that deadline was not a trivial matter at all. Due to its complexity, the human brain is very challenging to emulate: with a total power consumption of around 20 W, it is capable of performing tasks that would require the most efficient modern computers to consume megawatts of electricity; in fact, the engineered computing systems may not be able to fully emulate a human brain for decades yet.

Despite the many hurdles to overcome for intelligent life to evolve, it would seem unreasonable to believe that there have been no other forms of intelligent life present in the universe, outside of the planet Earth. In fact, the observed microwave background (a relic from the earliest universe when particles were first able to emit photons that were not simultaneously reabsorbed; past 380,000 years from time

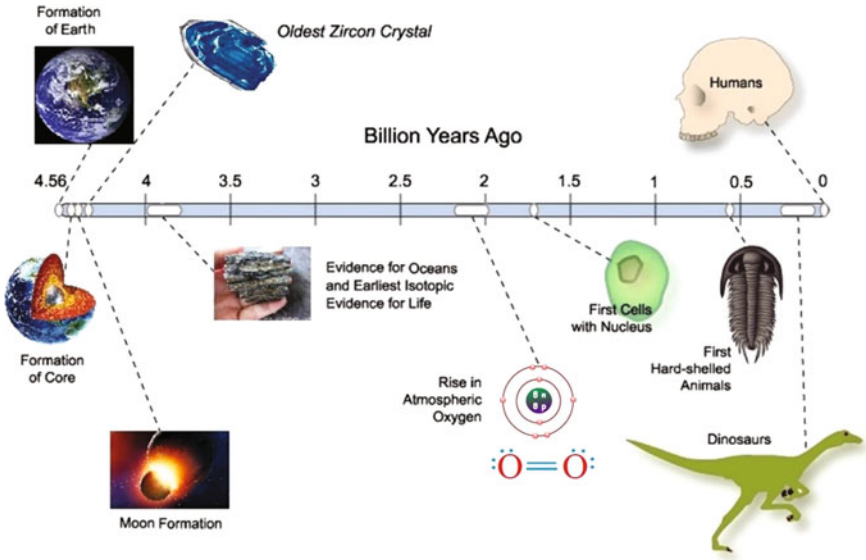

Fig. 1.5 Milestones in the history of Earth. (adapted from www)

zero) shows remarkable (within 0.001%) uniformity at a scale of 10^{24} m (> 100 million light-years) despite the primordial universe being partitioned into about 10^{80} regions which, presumably, were causally separated during the remarkably (and mysteriously) synchronized inflation at a pace far exceeding (by orders of magnitude) the speed of light, during the first second of its creation. So, it is reasonable to expect that, most likely, a multitude of extra-terrestrial life forms have been developing elsewhere at about the same pace, in comoving framework. There are about $7 \cdot 10^{22}$ stars in the visible part of the universe; since the knowledge acquired and technological progress achieved by the humans have advanced and expanded our capabilities at a rapidly accelerating, revolutionary pace for just a few past centuries, it might suggest that many extra-terrestrial civilizations that have had a step of a few hundred million years on us should have achieved the power to make their presence known. So far, no signals have been detected as coming from life elsewhere in the universe. We can only speculate what might be a possible answer to this Tsiolkovsky-Fermi-Viewing-Hart paradox, "Where Is Everybody?" Aside from the most speculative hypotheses like Earth was destined to be the cradle for the one and only or the most advanced civilization; or a possibility that every time a supercivilization advances to the critical level allowing them to possess a technological capability to perform stellar engineering or even significant stellar manipulation of any kind, they inevitably find out by then that an obvious collateral would be extremely detrimental and hence either deliberately refrain from such actions or simply do not bother to communicate using the signal transmission forms detectable by the low-life or immature civilizations; what on Earth would be considered more prudent explanations (Frank & Sullivan 2016)?

1.4 So, What Happens Next?

Well, half of the supply of hydrogen in the Sun has been used up; whence has the hydrogen in its core all been used, the fusion of hydrogen in a shell around the core will make the Sun swell and its luminosity increase. In about 600 million years, the growing luminosity will significantly increase the weathering of the Earth's surface rocks, thus trapping CO_2 in the ground. To make it harder, following a reunification of the continents (about 250 million years from now) plate tectonics will slow down, volcanoes will stop recycling carbon into the air and CO_2 levels will begin to fall. This will impede photosynthesis and, eventually, kill most of the plant life. In about 1 billion years, the Sun will be 10% more luminous than it is today. This will cause the average Earth's surface temperature to rise, up to about 47 °C (over 30 °C above the current levels) resulting in a runaway spiraling cycle of evaporation of the oceans and an extreme greenhouse gas effect—Water vapor is short-lived but is the most important greenhouse gas (GHG) because of this very powerful positive feedback loop. However, this is already beyond our concern as 200 million years prior to that the multicellular life will cease to exist, which will bring the Earth's biosphere back to square one or to a single-cell, most resilient microbial life. Mars may become a temporary habitable shelter for humans, but not for long. So, the window of opportunity does not look very wide then, does it—Our planet is near the end of a habitable cycle. Now, a large asteroid (6–12 miles in diameter) hits Earth approximately every 100 million years. The last time it happened 65 million years ago, allegedly resulting in extinction of the dinosaurs. Who is next in about 30 million years from now? Long-range forecasting is a fool's errand, especially when you have a limited knowledge about, optimistically, only 4% of the matter-energy involved, but you've got the idea. Now let's put our pessimistic hats on and hammer it home. By the end of this century, Earth is expected to heat up by 5°C or more above today's average temperature. The next century, climate change may kill millions of people, collapse many ecosystems and drive many wildlife species to extinction—and the current CO_2 emissions will still linger in the atmosphere, despite technological advances that will offset some climate-related problems. While more than half of the CO_2 emitted is naturally removed from the atmosphere within a century, about 20% of it remains there for thousands of years. Other greenhouse gases also have a variable atmospheric lifetime that cannot be specified precisely, for many it is longer than for CO_2. Human-produced greenhouse-gas emissions do tilt the balance in the wrong way (IPCC 2001). Which brings us back to the Tsiolkovsky paradox: one plausible reason why we do not hear from the would-be super civilizations is self-destruction at a certain level of their development due to explosive technological advances spinning out of control.

Despite resilience of the life's most primitive building blocks, there are many threats to continued existence of complex life forms once they even had a chance to develop. Living species constantly face the prospects of extinction by means of environmental disasters. Once they tune up to a certain ecosystem, they generally require a sustainable balance of energy, water, and carbon. Carbon-based (organic)

molecules are crucial for life on Earth. Living organisms need carbon either for structure, energy, or both. The carbon cycle is the biogeochemical cycle by which carbon is exchanged among the Earth's ecosystems. These are key processes to making our planet capable of sustaining life. Carbon dioxide is a greenhouse gas and traps heat in the atmosphere. Without it and other GHGs, Earth would be a frozen world. Learning how to maintain the right balance is the challenge of our time. Since the 1980s, growing international concern about potentially severe consequences of the rising GHG concentrations led to coordinated efforts to develop the scientific basis for understanding the nature of human-induced climate change. The following chapters of this book introduce the geochemistry involved, potential impact of imbalances on climate change, and specifics of the available carbon management options.

To put things into perspective, we are in a midst of the Quaternary ice age that began about 2–3 million years ago (and may last tens of millions of years) while in its relatively warmer interglacial period. The last glaciation ended about 11,500 years ago. The latest interglacials lasted for 10,000–30,000 years, but, according to computer models, it is possible to prolong the current one for up to 500,000 years by slowly burning all potential fossil energy reserves (which is about 5000 Gt of carbon). The glacial periods typically last for 80,000–90,000 years. For the current solar activity, that would require CO_2 concentration in atmosphere to drop down to about 240 ppm. The previous, Karoo ice age occurred during the Carboniferous period of Paleozoic era but it was not as cold as the recent one. However, the Andean-Saharan ice age resulted in mass extinction of species at the end of the Ordovician period of the Paleozoic era. The bituminous coalfields of the Eastern U.S., Europe, and Northern China were primarily deposited during the Upper Carboniferous period, suggesting that lush vegetation persisted even during the ice age.

The Sun's activity fluctuations, periodic changes in the Earth's orbit, axial tilt, magnetic field, and surface reflectivity, continental drifts, volcanoes, fires, and the living things are changing the atmosphere all the time. Long-term changes in the composition of the atmosphere and oceans are linked to the ongoing geophysical changes and the evolution of life. The atmosphere and oceans appeared in the very early stages of the Earth's formation, when gas emissions from lava, erupting through volcano vents, rapidly created a radiation-shielding haze enveloping the young planet, thus allowing a primitive crust to cool to the point where liquid water could condense. Following the massive early escape of volatile gases (helium and hydrogen; facilitated by the very strong solar wind during the heat-up phase of the young Sun, prior to differentiation of the Earth's core and formation of magnetosphere deflecting it) into outer space (4.3 billion years ago) and partial decomposition of ammonia (here comes nitrogen) and methane (one of the most potent greenhouse gases) triggered by sunlight, the Earth's hot and dense atmosphere was primarily made of steam as the entire content of the would-be oceans was up in the air. Yet, as soon as primordial heat had dissipated to space, precipitating masses of water (about 0.023% of Earth's total mass) vigorously came down to the ground, in such a spectacular/cataclysmic fashion that it would make a brick wall (or even a thousand of them) pale in comparison. At the same time, volcanoes were pouring

massive amounts of CO_2 into the atmosphere. Just a few hundred million years later, the atmospheric pressure dropped to nearly its current level; however, after condensation of water into the oceans, CO_2 (along with nitrogen) remained a dominant gas until the advent of photosynthetic (Archean eon) and multicellular (Proterozoic eon) life. Life, right from the onset, started to have a major impact on the environment by reducing CO_2 into carbon-based molecules. Some scientists believe that the first living organisms were self-replicating iron-rich clays which fixed CO_2 into carboxylic acids. With evolution of photosynthetic organisms (3.7–2.5 billion years ago) this process accelerated and simultaneously contributed to ongoing oxygen build-up, which has allowed the evolution of animal life.

For the past 200 million years, the atmosphere has not changed much. However, human activity (e.g., burning fossil fuels and deforestation) is causing it to change. Since the Industrial Revolution, the global annual mean concentration of CO_2 in the atmosphere has increased from 280 to over 400 ppm; thus providing more food (CO_2 that had become relatively scarce, on geological time scale) and energy (GHG effect) to the older, more primitive life forms but endangering the younger, more complex species including humans. The implications of this rapid increase in atmospheric CO_2 concentration are not fully understood, with respect to the stresses that it might impose on the natural environment and the ability of ecosystems to adapt to and attenuate those. One could argue that there is no harm in pushing the atmosphere "ever so slightly" toward the early days (i.e., billions of years ago). After all, the younger Earth's atmosphere was once extremely enriched in carbon dioxide, with CO_2 partial pressure then being several orders of magnitude higher than today (Mojzsis 2001); nevertheless, it did not slow down the continued cooling of the Earth's surface nor did it slow down the condensation of water vapor. In fact, the oceans formation and the origin of life just happened to roughly coincide with the all-time maximum in atmospheric CO_2 concentration, and then the CO_2 had begun to rapidly dissolve in the ocean water and react with sedimentary rocks.

So, apart from a steady increase in the power output of the Sun, what is different now? For one, this is our house now—We have to defend it! Here's the thing: The most likely result of the projected rise of GHG concentration in the atmosphere (granted, with the current models) would be a subsequent rise in mean global temperatures by several degrees. It is increasingly unlikely, but still possible, that such increase will be lost in the natural background. However, the risk that the anomalous temperature increases may cause serious climate disruptions cannot be simply ignored. Prudent carbon management will be needed to continue sustainable economic growth while avoiding major disruptions.

Carbon dioxide, methane and other GHGs, in current concentrations, are not dangerous air pollutants, but they may affect global climate and ecosystems. The detailed weather patterns on Earth are produced by a web of interacting physical, chemical and biological processes. Due to complexity of such interactions, significant changes in one component will affect the other components, thus making accurate weather forecast very challenging. Climate change is a much slower but also very complex process. The challenge is to develop recommendations on how to

avoid the unmanageable and how to manage the unavoidable climate changes, including possible adaptation and mitigation measures.

Is preservation of the existing ecosystems, while maintaining the current rate of economic growth, a sustainable strategy? Or would it be viable if we relied on natural (often dramatic) adaptability of the life forms to ever changing environment? These and other relevant questions cannot be satisfactorily answered without due diligence based on advanced scientific knowledge and understanding.

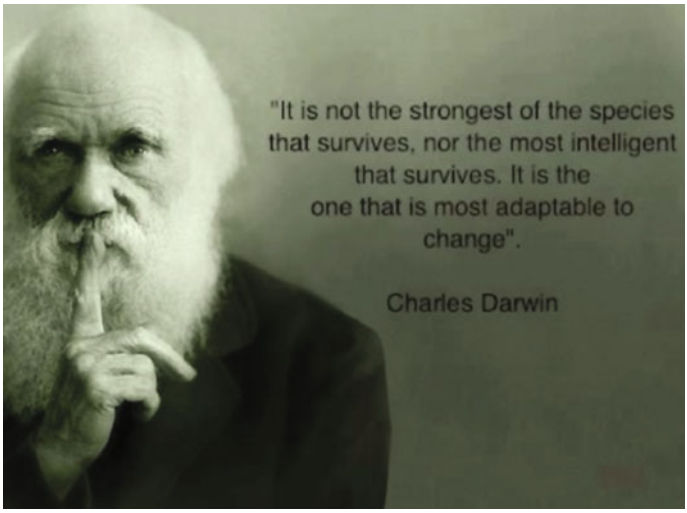

This book invites you to learn the science of carbon management, with particular focus on carbon capture and storage in geological formations. Rather than jumping to any conclusions, we will review the current state of knowledge and discuss the risks, available options and likely scenarios. In the early chapters, students and avid readers who are passionate about the global challenges, can learn the basics about greenhouse gases and their role in the Earth's radiative balance, about natural carbon cycles and the challenges of controlled carbon management (capture, storage a.k.a. sequestration, and utilization) including the role of fossil fuels and common geological materials. More advanced chapters are reserved for recent research developments in understanding the nature of interactions between greenhouse gases and ubiquitous geomaterials, such as clay. Motivation for this exciting effort is to elucidate the state of understanding in the science of clay–CO_2 interactions, to bridge between traditional and modern geoscience perspectives, and to introduce consistent terminology that will facilitate communication between different generations and areas of scientific and technological inquiry.

Natural prevalence of clays makes their research relevant to a broad spectrum of economic sustainability aspects, from energy production to environmental preservation. Not surprisingly, clays have been actively studied. However, natural

heterogeneity due to weathering of clay minerals, combined with rapid advances in fundamental research, all but ensured discovery of some unusual mechanisms of clay interaction with various gases and fluids, which resulted in shifting conceptual paradigms. It naturally triggered a social process to reconcile communication differences between the traditional experts and the scientists attempting to advance new knowledge and understanding. And there clearly is an urgent need to facilitate such a transition. To paraphrase a Chinese proverb: The best time to start was years ago; the next best time is now.

References

Bennett, C. L., et al. (2013). Nine-year Wilkinson Microwave Anisotropy Probe (WMAP) observations: Final maps and results. *Astrophysical Journal Supplement, 208*(2), 20.

Emiliani, C. (1992). *Planet earth: Cosmology, geology, and the evolution of life and environment* (Hardback ed.). Cambridge and New York: Cambridge University Press.

England, J. L. (2013). Statistical physics of self-replication. *Journal of Chemical Physics, 139* (121923), 1–8.

Frank, A., & Sullivan, W. T. (2016). A new empirical constraint on the prevalence of technological species in the universe. *Astrobiology, 16*(5), 359–362.

Hawking, S. (1988). *A brief history of time: from the big bang to black holes* (1st ed.). London and New York: Bantam Dell Publishing Group.

IPCC. (2001). *Climate change 2001: The scientific basis. Contribution of Working Group I to the third assessment report of the Intergovernmental Panel on Climate Change.* New York: Cambridge University Press.

Mojzsis, S. J. (2001). Life and the evolution of earth's atmosphere. In E. A. Mathez (Ed.), *Earth: Inside and Out (American Museum of Natural History Book)* (pp. 32–39). New York: New Press.

Chapter 2
Greenhouse Gases and Their Role in Climate Change

Robert Dilmore and Liwei Zhang

The Sun, with all the planets revolving around it, and depending on it, can still ripen a bunch of grapes as though it had nothing else in the Universe to do.

—Galileo Galilei

Abstract The chapter begins with a comprehensive review of the representative greenhouse gases and their role in the Earth's radiative balance. Eight greenhouse gases (CO_2, CH_4, N_2O, HFC-23, HFC-134a, PFC, SF_6, and NF_3) and their contributions to radiative heating of the atmosphere are analyzed, and the mechanisms associated with global warming potential are discussed. To illustrate the reported evidence of changes in the radiative balance attributed to greenhouse gases, the correlation between the global temperature rise and the increase in atmospheric concentration of CO_2, the most important greenhouse gas, is presented. The primary anthropogenic CO_2 emission sources and the amount of CO_2 emissions by region, and the disturbance of anthropogenic CO_2 emission to global carbon cycle are discussed. At the conclusion of this chapter, a brief review of global actions to mitigate anthropogenic CO_2 emissions is presented.

Human activity since the advent of the Industrial Revolution has contributed to the gradual increase in atmospheric concentration of carbon dioxide (CO_2) and concentrations of other greenhouse gas constituents. These concentration increases, in combination with other human-induced changes, have driven additional retention of solar energy, in the form of thermal infrared radiation, by the atmosphere. This has led to the increase in mean global temperature at the Earth's surface, with significant and impactful effects such as reduction in extent and thickness of Earth's sea

R. Dilmore (✉)
U.S. Department of Energy, National Energy Technology Laboratory (NETL), Pittsburgh, USA
e-mail: Robert.Dilmore@netl.doe.gov

L. Zhang
NETL, Oak Ridge Institute for Science and Education, Oak Ridge, TN, USA

© Springer International Publishing AG 2018

V. Romanov (ed.), *Greenhouse Gases and Clay Minerals*, Green Energy and Technology, https://doi.org/10.1007/978-3-319-12661-6_2

and terrestrial ice, sea level rise, increased incidence of extreme weather events, increased incidence of crop failure and famine, and loss of health and biodiversity in the Earth's ecosystems. Furthermore, atmospheric CO_2 concentration rise also contributes to the acidification of our planet's oceans, with implications for the health and productivity of marine ecosystems, and likely impacts to the contribution of our oceans to the global carbon cycle.

Identifying and implementing ethical and effective approaches to stabilize atmospheric greenhouse gas concentrations at a level that would avoid the worst weather, environmental, and social impacts, and prevent irreparable damage to Earth's climate system is the focus of significant technical and policy research. In this chapter, a general review of the basic physical and chemical phenomena that underpin the Earth's response to the greenhouse gas effect and the role of atmospheric CO_2 in the context of global carbon cycle is provided—to give context to the technical discussion of technology alternatives to mitigate atmospheric GHG concentration rise.

2.1 Radiative Forcing and Greenhouse Gases

Energy from the sun travels to Earth in the form of electromagnetic radiation. In classical electromagnetic wave theory, this radiation is considered to take the form of oscillating waves of various frequencies. While the frequency of solar energy reaching the Earth spans the broader electromagnetic spectrum, most of that energy is in the visible to near-infrared range, with a smaller amount falling in the ultraviolet frequency range. A little less than a third of the energy that reaches the Earth's atmosphere is reflected back into space by the atmosphere itself, clouds, and the Earth's surface, as a function of the reflectivity (the albedo) of those bodies. The remaining approximately 70% of that solar energy passes into the atmosphere and is absorbed by the atmosphere, clouds, and Earth's surface (water and ground). The vast majority of that absorbed radiation is radiated out from those absorbing bodies as infrared energy (energy in the infrared spectrum) (Kiehl & Trenberth, 1997; NASA, 2016a). A portion of that radiated energy is trapped by the Earth's atmosphere—warming the lower atmosphere, moderating the extreme diurnal variations in temperature that would otherwise exist, and allowing our planet to be habitable.

The difference in the balance between the energy entering the Earth's atmosphere and that which is radiated back out to space (Fig. 2.1) drives changes in the mean atmospheric temperature at the Earth's surface (NASA, 2016b). Maintaining equilibrium (zero difference) in that balance means that average surface temperatures will remain stable.

The contribution that a system component makes to disequilibrium in that system is termed 'radiative forcing.' Radiative forcing, as defined by the IPCC (2007), is

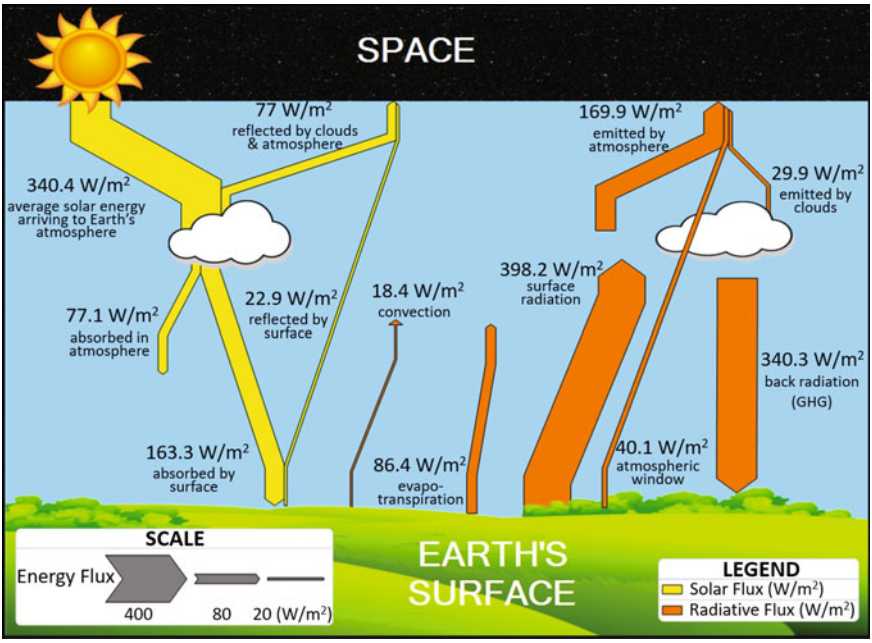

Fig. 2.1 Simplified Sankey diagram illustrating example of the Earth's radiative balance with solar energy input to the Earth and thermal infrared energy in relation to the Earth's surface, its atmosphere, and outer space (modified from NASA, 2014)

> a measure of the influence a factor has in altering the balance of incoming and outgoing energy in the Earth-atmosphere system and is an index of the importance of the factor as a potential climate change mechanism.

The publication (IPCC, 2007) specifies values of radiative forcing as being in terms of changes relative to preindustrial conditions (based on the year 1750 as a selected datum) and reports that in units of Watts per square meter (W/m^2).

Factors contributing to changes in radiative balance (agents of radiative forcing) include changes in the amount of radiation delivered to the Earth from the Sun and changes in the composition or characteristics of the material with which that radiation comes in contact. That includes changes in reflective and absorptive properties of the terrestrial Earth (e.g., changed reflectance and absorbance resulting from deforestation) and changes in the composition of the Earth's atmosphere that impact how the atmosphere behaves in response to incoming solar radiation and infrared radiation emitted by Earth's surface, and the atmosphere itself (e.g., increased reflectance of insolation associated with increased concentration of particulate matter in the upper atmosphere resulting from volcanic activity).

One type of radiative forcing agent that is of significant concern as a contributor to perturbations in radiative balance is the increase in atmospheric (tropospheric and stratospheric) concentrations of certain constituents that lead to the trapping of

thermal infrared energy in our Earth's lower atmosphere, such as carbon dioxide, methane, halocarbons, and nitrous oxide, collectively called "greenhouse gases" (White et al., 2003; IPCC, 2007) because of the blanketing role that they play in trapping thermal energy near the Earth's surface. Increases in the atmospheric concentrations of these gases directly contributes to positive radiative forcing and increases in atmospheric temperature, but can also indirectly cause radiative forcing in response to physical/chemical changes that their increased concentrations in the atmosphere induce (e.g., chemical alteration of ozone concentrations and distribution in the upper atmosphere, and greenhouse effects from increases in atmospheric water vapor concentration resulting from atmospheric warming).

An index has been developed to estimate the contribution of incremental increases in greenhouse gases to the atmosphere. This index, called global warming potential (GWP) allows the relative comparison of the direct global warming effects of different greenhouse gas constituents and is commonly applied in policy and planning related analyses to understand the GWP contribution of various activities. GWP of a greenhouse gas is a function of the amount of time it spends in the atmosphere before being destroyed, the frequency ranges in which it absorbs radiation, and the strength of that absorption, its molecular weight, and the time period over which the GWP analysis is being considered. A convention has been adopted in which the GWP is normalized to that of CO_2, such that the GWP factor is the time integrated radiative forcing of a greenhouse gas divided by the time integrated radiative forcing of CO_2 for the same time interval. Table 2.1 provides a list of calculated GWP values of select GHGs, as reported in the IPCC Fifth Assessment Report (2013). Because GWPs are indexed to CO_2, the GWP of CO_2 is 1.

These values are calculated based on the best-available scientific information; as the research community's understanding of the behavior of these constituents in the atmosphere evolves, these values are revised. Also, it should be noted that there are other, perhaps more technically rigorous approaches for considering the contribution of GHGs to radiative forcing that are advocated by some in the scientific community; consideration of those is outside the scope of this overview. For a far more detailed consideration of radiative forcing and GWP associated with these and

Table 2.1 Summary of 20- and 100-year GWP values of select GHG constituents (IPCC 2013)

	Half-life (years)	GWP time horizon	
		20 years	100 years
Carbon dioxide (CO_2)	Complex	1	1
Methane (CH_4)	12.4	84	28
Nitrous oxide (N_2O)	121	264	265
HFC-23	222	10,800	12,400
HFC-134a	13.4	3710	1300
CF_4 (PFC)	50,000	4880	6630
Sulfur hexafluoride (SF_6)	3200	17,500	23,500
Nitrogen trifluoride (NF_3)	500	12,800	16,100

many other GHG constituents, please refer to the Chap. 8 of the IPCC Fifth Assessment Report (2013).

The greenhouse gas with the largest atmospheric concentration, and the largest volumetric rate of anthropogenic emission, by far, is carbon dioxide, a byproduct of the large-scale use of fossil fuels as an energy source for electricity generation, transportation, and industrial processes. Electricity generation is the largest contributor to CO_2 emissions, which accounted for 37% of CO_2 emissions from 1990 to 2014. Transportation is the second largest contributor to CO_2 emissions, which accounted for 31% of CO_2 emissions from 1990 to 2014 (U.S. Environmental Protection Agency, 2016). Among all GHGs, CO_2 is the largest contributor to global warming. The anthropogenic radiative forcing induced by CO_2 emissions in 2011 was 1.68 relative to a datum radiative forcing value of zero for the year 1750 (IPCC, 2013).

Another greenhouse gas that significantly contributes to global warming is methane (CH_4). In the United States, 33% of CH_4 emissions came from natural gas and petroleum systems from 1990 to 2014, followed by enteric fermentation (22%), landfills (20%), coal mining (9%) and manure management (8%) (U.S. Environmental Protection Agency, 2016). CH_4 is the second largest contributor to global warming. The anthropogenic radiative forcing induced by CH_4 emissions in 2011 was 0.97 relative to a datum radiative forcing value of zero for the year 1750 (IPCC, 2013).

Developing and deploying technology and policy measures to reduce the rate at which these greenhouse gases are being emitted into the atmosphere as a result of human activity and, in some cases, to reduce the concentration of these gases in the atmosphere is the focus of international efforts. These technologies include the capture of anthropogenic CO_2 from large industrial point sources and transportation of that CO_2 to locations where it can be stored away from the atmosphere or beneficially reused.

2.2 Climate Change

Anthropogenic emissions of CO_2 are recognized as the predominant contributor to the observed rise in atmospheric concentrations of CO_2. Atmospheric CO_2 concentration increase was observed after the Industrial Revolution, and the increase was accelerated after 1900. From 1800 to 1900, atmospheric CO_2 concentration increased from 280 ppmv to 290 ppmv. Over the next century from 1900 to 2000, atmospheric CO_2 concentration increased from 290 to 370 ppmv (Halmann & Steinberg, 1999; Keeling et al., 2009).

Detailed consideration of the role that GHGs and anthropogenic emissions of GHGs play in shifting the radiative balance, mean temperature, and related issues of weather patterns, distribution of water in the atmosphere and Earth's surface, and other issues potentially impactful to global stasis, is beyond the focus of this summary.

Corresponding to that trend of increasing CO_2 concentration, the IPCC reported that the Earth's average global surface temperature increased 0.6 ± 0.2 °C, over the twentieth century (IPCC, 2007). A plot of indexed mean land-ocean temperature (an average temperature at the Earth's surface derived from surface air temperature measurements and satellite data-derived estimates of sea surface temperature in regions without sea ice) as reported by the NASA Goddard Institute for Space Studies (GISTEMP Team, 2016; Hansen, Ruedy, Sato, & Lo, 2010) as a function of the atmospheric concentration of CO_2 between 1959 and 2008 (Keeling, Piper, Bollenbacher, & Walker, 2009) shows a strong correlation between CO_2 concentration change and land-ocean temperature change (Fig. 2.2).

Concurrent with observations of the rise of the Earth's average global surface temperature, other related significant effects have been observed with important implications for the health of our planet. A global rise in sea level of 0.1–0.2 m was observed through the twentieth century—with this rise primarily attributed to a decrease in snow and ice cover over the northern hemisphere (NASA, 2016c). Also, as atmospheric concentrations of CO_2 rise, the amount of CO_2 that is absorbed into surface water bodies at the atmosphere/water interface also increase. While this absorption does remove significant amounts of CO_2 from the atmosphere, the dissolution of this gas causes the acidity of that water to increase. Since the beginning of the Industrial Revolution, the pH of surface ocean waters has fallen by 0.1 pH units, which represents approximately a 30% increase in acidity. Future predictions indicate that the oceans will continue to absorb CO_2 and become even more acidic. Estimates of future carbon dioxide levels, based on business-as-usual emission scenarios, indicate that the surface waters of the ocean could be nearly

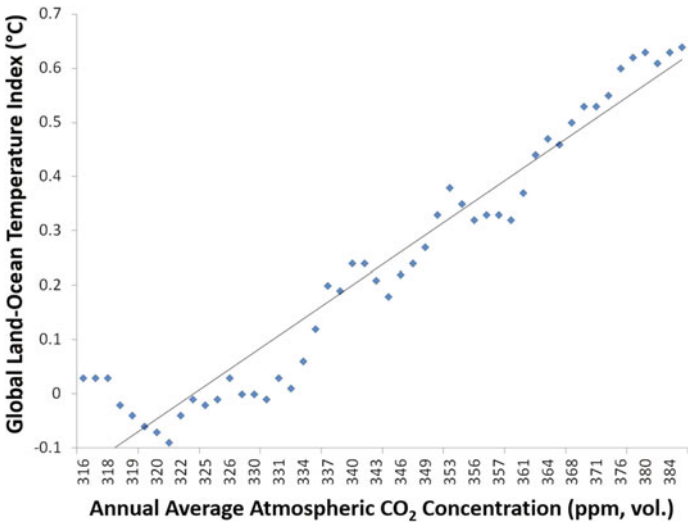

Fig. 2.2 Plot of the mean land-ocean temperature index as reported by the NASA Goddard Institute for Space Studies (GISTEMP Team, 2016; Hansen et al., 2010) as a function of the atmospheric concentration of CO_2 through time, derived from in situ air samples collected at the Mona Loa, Hawaii, USA (Keeling et al., 2009) for years of 1959 through 2008

150% more acidic by the end of this century, resulting in a pH that the oceans have not experienced for more than 20 million years (National Oceanic & Atmospheric Administration, 2016a).

In 2010, countries agreed in Cancún, Mexico, that global temperature rise above preindustrial levels should not be allowed to exceed 2 °C and made pledges to limit their emissions by 2020. However, an analysis by the Intergovernmental Panel on Climate Change (IPCC) published in 2013 concluded that measures called out by that agreement will be insufficient to address this challenge and will likely lead to the warming of more than 3 °C by the end of the twenty-first century.

2.3 Carbon Cycle

The carbon cycle is the biogeochemical cycle by which carbon is exchanged among atmosphere, land, and oceans of the Earth (Wigley & Schimel, 2005). Exchange of carbon between atmosphere and land is mainly achieved by uptake/release of CO_2 by the terrestrial biosphere, and exchange of carbon between atmosphere and oceans is mainly achieved by dissolution of CO_2 into the oceans and uptake/release of CO_2 by marine biota. The carbon cycle is important because carbon is the fundamental building block of life on Earth and an important component of many chemical processes (National Oceanic & Atmospheric Administration, 2015). Moreover, as described previously, CO_2 in the atmosphere acts like a blanket over the planet by absorbing infrared radiation that would otherwise radiate excess heat away from the planet. In short, maintaining the balance of the carbon cycle is crucial to sustain the stability of the Earth's ecosystems.

2.3.1 Exchange of Carbon Between Atmosphere and Land

Carbon in the atmosphere mainly exists in two forms: carbon dioxide (CO_2) and methane (CH_4). Methane exists in much lower concentrations than CO_2 in the atmosphere, and methane is less stable than CO_2 in the atmosphere. Therefore, CO_2 plays a major role in the exchange of carbon between atmosphere and land. Carbon in the atmosphere represents only a small fraction of total carbon on Earth (720 gigatonnes, where a tonne or "metric ton" is equivalent to 1000 kilograms, or approximately 1.1 short tons, and a gigatonne refers to billions of tonnes) of carbon in the atmosphere, representing 1.9% of total carbon in the oceans and less than 0.001% of total carbon in the lithosphere (Falkowski et al., 2000). The atmosphere, however, acts as a "nexus" with respect to the carbon cycle, and the other carbon reservoirs interact with each other primarily by trading carbon through the atmosphere (Archer, 2010; Archer, Buffett, & Brovkin, 2009). The terrestrial biosphere takes carbon from the atmosphere mainly through photosynthesis. Photosynthesis is the process by which plants synthesize organic compounds from carbon dioxide

and other inorganic raw materials in the presence of sunlight (Hall & Rao, 1999). Plants convert about 1.20×10^{17} g carbon per year into hydrocarbons (gross primary production, GPP) via photosynthesis (Ciais et al., 1997).

Photosynthesis occurs in chloroplasts in plant cells. Photosynthesis can be divided into two steps: (1) light reactions, which take energy from light to produce adenosine triphosphate (ATP) for reactions in the next step; (2) Calvin Cycle (dark reactions) which is composed of a series of reactions to convert CO_2 into organics. ATP and protons (supplied by nicotinamide adenine dinucleotide phosphate—NADPH) from light reactions are needed for Calvin Cycle reactions. Specifically, ATP provides energy for Calvin Cycle reactions to reduce CO_2 and convert CO_2 into organic matter rich in chemical energy, and NADPH provides H^+ that will combine with CO_2 to produce H-containing organic matter. Net photosynthesis reaction can be simply written as:

$$6\,CO_2 + 6\,H_2O \rightarrow C_6H_{12}O_6 + 6\,O_2$$

A diagram of simplified photosynthesis processes can be found in Fig. 2.3.

Based on the mechanism of CO_2 fixation via Calvin Cycle, plants can be divided into "C3" plants and "C4" plants. C3 plants have the first measurable CO_2 fixation product in the Calvin Cycle as an organic compound with three carbons [e.g., phosphoglycerate ($C_3H_7O_7P$)]; and C4 plants have the first measurable CO_2 fixation product in the Calvin Cycle as an organic compound with four carbons (e.g.,

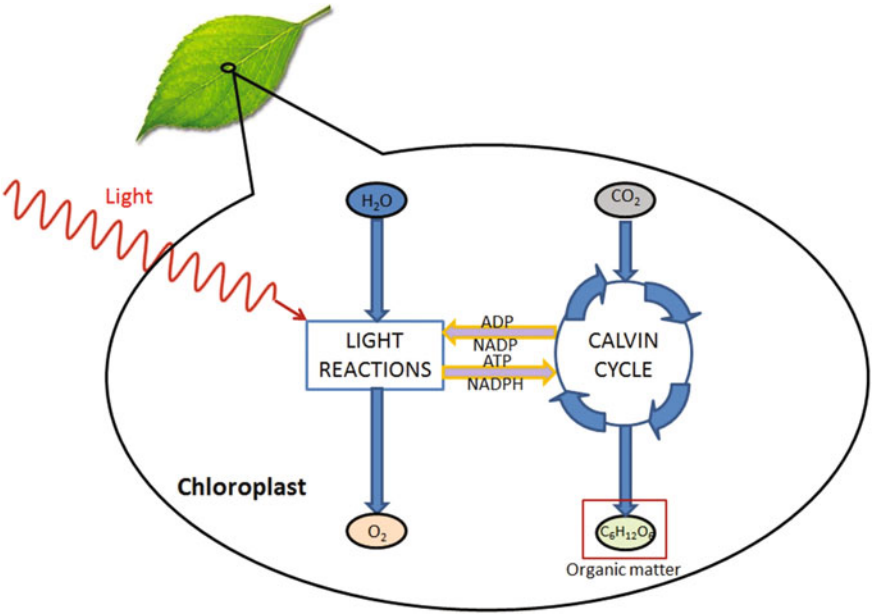

Fig. 2.3 Simplified photosynthesis processes (modified from Hall & Rao, 1999)

malate, aspartate, and oxaloacetate) (Mohr & Schopfer, 1995). Compared with C3 plants, C4 plants possess the ability to greatly reduce photorespiration, and have a higher rate of net photosynthesis and greater light saturation (Mohr & Schopfer, 1995). For more thorough treatment of these complex reactions, the interested reader is directed to textbooks on biology and biochemistry.

A large portion of the organic matter stored via photosynthesis is returned to the atmosphere via numerous respiratory pathways (Falkowski et al., 2000): (1) autotrophic respiration by the plants themselves; (2) heterotrophic respiration, in which plant-derived organic matter is consumed and oxidized by animals and soil microbes; (3) oxidation of organic matter by combustion (e.g., use of biomass as fuel, or forest fire). A small amount of carbon accumulates in the soil in the process of microbial decomposition, becoming organics in the soil. If that accumulated organic carbon remains stable, the terrestrial biosphere globally would represent a carbon sink. Based on the use of atmospheric O_2 and CO_2, and the isotopic signature of atmospheric CO_2, the net (per annum) flux of CO_2 from the atmosphere to the soil was estimated to be $0.2 \pm 0.7 \times 1015$ g C a^{-1} during the 1980s and $1.4 \pm 0.7 \times 1015$ g C a^{-1} during the 1990s (Prentice et al., 2001). A diagram showing the movement of carbon between atmosphere and land can be found in Fig. 2.4.

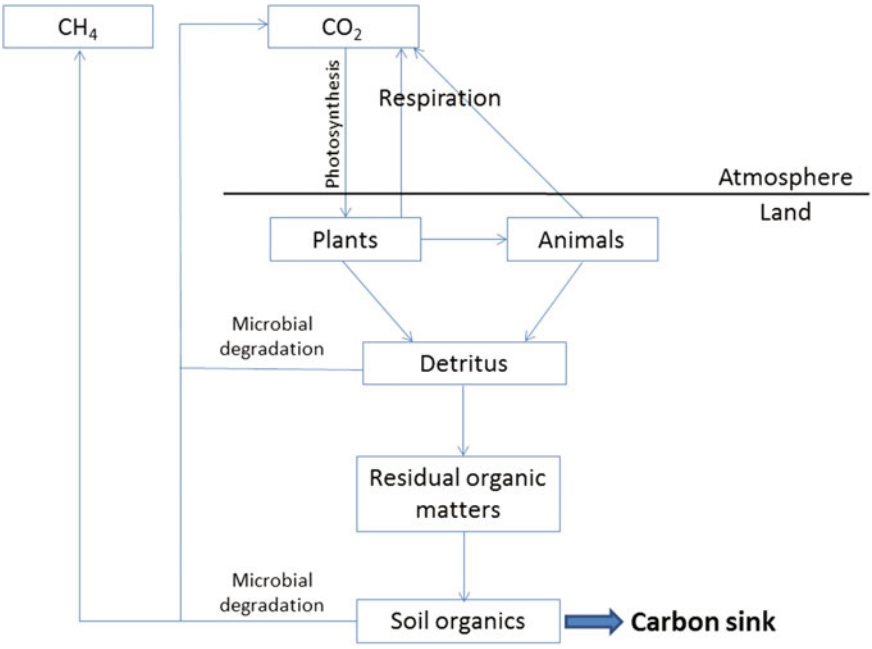

Fig. 2.4 Carbon exchange between atmosphere and land, and carbon cycle in the land (modified from Marini, 2007)

2.3.2 Movement of Carbon Between Atmosphere and Oceans

The oceans play a crucial role in the climate system by redistributing heat and carbon across the planet through a complex interplay of physical, chemical, and biological processes (Williams & Follows, 2011; Burwicz, Rupke, & Wallmann, 2011). The total amount of carbon contained in the oceans is 63 times the carbon contained in the atmosphere, with the large carbon content of the oceans mainly as dissolved CO_2 in the oceans. Due to the particular chemistry of seawater, more than 99% of the dissolved CO_2 in the oceans is in the form of bicarbonate and carbonate ions (hereafter referred to collectively as dissolved inorganic carbon, or DIC). Physical transport of DIC-rich water from the surface to the deep ocean brings a large quantity of DIC to the deep ocean, and more DIC can be held in deep oceans compared with surface oceans, due to the large volume of water, and the high pressure and low-temperature conditions in the deep ocean environment (Williams & Follows, 2011). A certain portion of DIC is taken up by phytoplankton via photosynthesis, which lowers the partial pressure of CO_2 in the upper ocean and thereby promotes the absorption of additional CO_2 from the atmosphere (Falkowski et al., 2000).

CO_2 dissolved in the ocean can directly react with Ca^{2+} in the ocean to form $CaCO_3$, and biologically-mediated processes in the ocean (e.g., uptake of DIC by phytoplankton, zooplankton, shells, and corals) can also catalyze the production of $CaCO_3$. $CaCO_3$ contained within the detritus of marine life contributes to sediment, effectively taking significant amounts of carbon away from the carbon cycle. Export of soft tissue from detritus of phytoplankton and zooplankton produces dissolved organic carbon (DOC), and some DOC forms organic sediment, which takes additional carbon away from the active carbon cycle. Additionally, a significant portion of this detritus is deposited with inorganic sediment and deeply buried—effectively removing it from ocean carbon cycle on a long-term basis. Therefore, the oceans and ocean sediments globally represent a carbon sink. A diagram showing the movement of carbon between the atmosphere and the oceans can be found in Fig. 2.5.

Oceanic absorption of CO_2 is one of the most important forms of carbon sequestration—partially offsetting the human-caused rise of atmospheric CO_2 concentration. However, the capacity of the oceanic carbonate system to uptake CO_2 is limited. Firstly, the CO_2 uptake capacity of the ocean is dependent on the addition of cations from weathering of rocks, which is a relatively slow process. Given several orders of magnitude greater anthropogenic CO_2 emissions than the supply of mineral cations, the ability of the surface oceans to absorb CO_2 will decrease eventually (Falkowski et al., 2000). CO_2 absorption also makes water more acidic, which affects ocean biosystems. The projected rate of increasing oceanic acidity could inhibit the biogeochemical processes associated with conversion of CO_2 to calcium carbonates in the ocean, thus decreasing the ocean's capacity to absorb CO_2 (Kleypas et al., 1999; Langdon et al., 2000). The transfer of

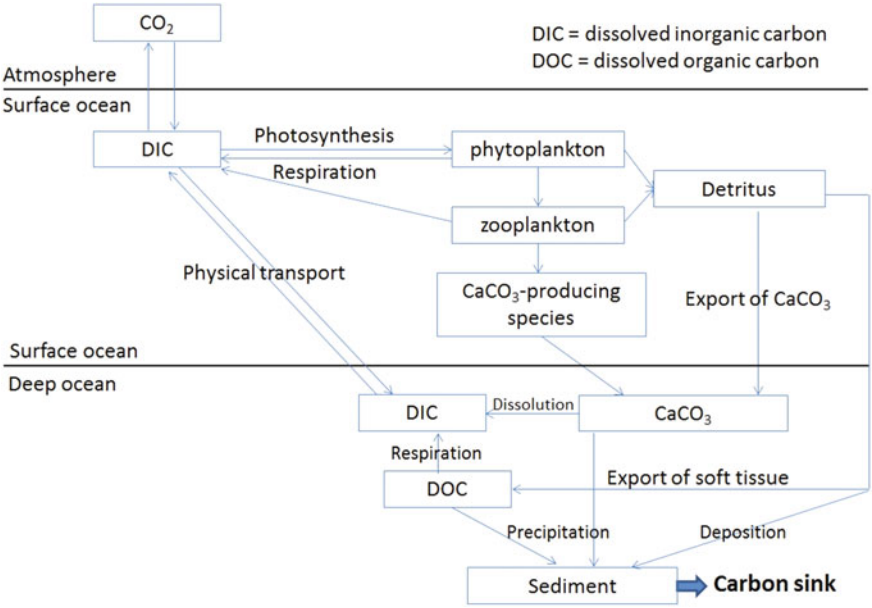

Fig. 2.5 Carbon exchange between atmosphere and the ocean, and carbon cycle in the ocean (modified from Marini, 2007)

organic matter from the land to the oceans via fluvial systems also brings carbon to the ocean, which also impairs the ocean's ability to absorb atmospheric CO_2. In summary, it is not sufficient to rely on the ocean alone to counter CO_2 concentration increase induced by anthropogenic CO_2 emissions.

2.4 Impact of Human Activities on Carbon Cycle

Over the past 200 years, human activities have altered the global carbon cycle significantly. It is crucial to understand the consequences of human activities on the global carbon cycle and to find a clear path to mitigate global carbon-cycle alteration caused by human activities.

Human activities have released half a trillion ton of carbon to the atmosphere in the form of CO_2 since the beginning of the Industrial Revolution (Richardson, Steffen, & Liverman, 2011). These emissions have led to an increase of about 45% in atmospheric CO_2 from 280 ppm in 1750–387 ppm in 2009 and 407 ppm in 2016 (National Oceanic & Atmospheric Administration, 2016b). Major contributors to CO_2 concentration increase includes (Sabine et al., 2004; Field & Raupach, 2004; U.S. Environmental Protection Agency, 2015):

- Carbon emissions from electric power sector. The electric power sector accounted for 32% of U.S. total greenhouse gas emissions in 2012. Greenhouse gas emissions from electricity have increased by about 11% since 1990 as electricity demand has grown and fossil fuels have remained as the dominant source for electricity generation (U.S. Environmental Protection Agency, 2015). Fossil fuel-fired power plants are the largest source of U.S. CO_2 emissions.
- Cement production, which contributes about 6% of the global anthropogenic CO_2 budget. About 50% of CO_2 emissions in cement production sector come from calcination of limestone to produce lime and CO_2, and the remaining emissions are from the energy required to fire the kiln.
- Steel production, which contributes 4–7% of global anthropogenic CO_2 emissions. CO_2 is generated from two processes: energy for steel production by burning of fuel and the use of reducing agents for steel production from iron ore, the most readily available reducing agent being coal (Birat, 2010).
- Transportation, which accounted for 28% of U.S. total greenhouse gas emissions in 2012 (U.S. Environmental Protection Agency, 2015).
- Underground coal fires, some of which are induced by mining activities, are an additional, as-yet unaccounted for, source of carbon to the atmosphere—potentially, as large a contributor as cement production.
- Carbon emissions from land use and land management (deforestation, the expansion of crop land and pasture, infrastructure extension and other effects driven by market growth, and demographic pressures). Prior to 1910, cumulative carbon emissions attributed to land use and land management were larger than cumulative carbon emissions from fossil fuel combustion. Land use and land management still play an important role in carbon emissions, though the contribution as a fraction of total emissions is smaller.

Raupach et al. (2007) have summarized possible global CO_2 emission scenarios based on the actual CO_2 emission data from 1850 to 2005 and various actions that can be taken to mitigate anthropogenic CO_2 emissions (Fig. 2.6). Under the worst-case scenario (F, intensive dependence on fossil fuels) annual global CO_2 emissions reach 23 gigatonnes of carbon per year (GtC/year) in 2050, which is 3.1 times of annual CO_2 emissions in 2005. Under the best-case scenario (T, alternative technologies largely replace fossil fuels) annual CO_2 emissions reach 12 GtC/year in 2050, which is 1.6 times of annual CO_2 emissions in 2005. However, even under the best-case scenario, the annual CO_2 emissions are still more than the CO_2 emission cap considered necessary to reach the International Energy Agency (IEA) CO_2 concentration stabilization goal o f 450 ppm by 2050 (International Energy Agency, 2015). Therefore, switching energy source from fossil fuel to alternative energy is not sufficient to achieve the CO_2 reduction goal, and other approaches (e.g., increasing end-use energy efficiency, implementing carbon capture, and sequestration (CCS) technology need to be taken together with energy source switching (Global CCS Institute, 2014).

It is widely accepted that the global carbon cycle will be further disturbed due to a continuous increase in atmospheric CO_2 concentration given the current rate of

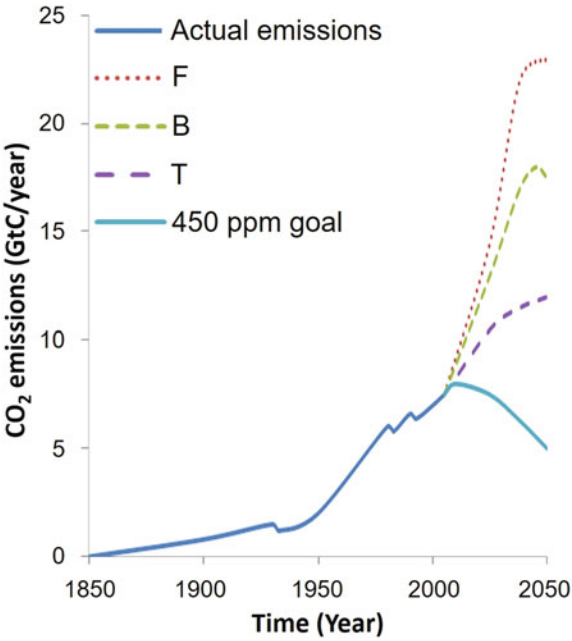

Fig. 2.6 Comparison between different projected CO_2 emission scenarios (Raupach et al., 2007). Projected scenarios: *F* (intensive dependence on fossil fuels), *B* (balanced energy supply between fossil fuels and alternatives), *T* (alternative technologies largely replace fossil fuels), and *450 ppm goal* (CO_2 emission cap to keep atmospheric CO_2 concentration at or below 450 ppm by 2050). *Note:* Units are in terms of gigatonnes of carbon (not of CO_2) per year (GtC/year).

anthropogenic CO_2 emissions. Broecker et al. showed that the oceans only took up to 35% of the CO_2 released from fossil-fuel burning during the period from 1958 to 1980 (Broecker, Peteet, & Rind, 1985; Post et al., 1990). Falkowski et al. conclude that there is no "natural savior" to assimilate all the anthropogenic CO_2 in the twenty-first century. Their global carbon-cycle models suggest that the feedbacks between carbon and other biogeochemical and climatological processes will lead to weakened natural sink strengths in the foreseeable future (Falkowski et al., 2000). Anthropogenic CO_2 emissions will affect Earth's biogeochemical cycles for hundreds of years to come (Joos et al., 1999).

2.4.1 CO_2 Emissions by Region

Since 1990, energy-related CO_2 emissions have grown slower in the mature economies of member countries of the Organization for Economic Cooperation and Development (OECD) as a group, than they have worldwide (OECD, 2015). In 1990, all OECD countries had a total CO_2 equivalent emission of 11.6 gigatonnes (where equivalent CO_2 emissions account for both direct CO_2 emissions and emissions of other greenhouse gases using GWP factors). In 2007, that value reached 13.7 gigatonnes, representing an 18% increase from 1990 to 2007. For non-OECD countries, emissions were 10 gigatonnes in 1990 and 16 gigatonnes in 2007, representing a 60% increase from 1990 to 2007 (Fig. 2.7). The United States

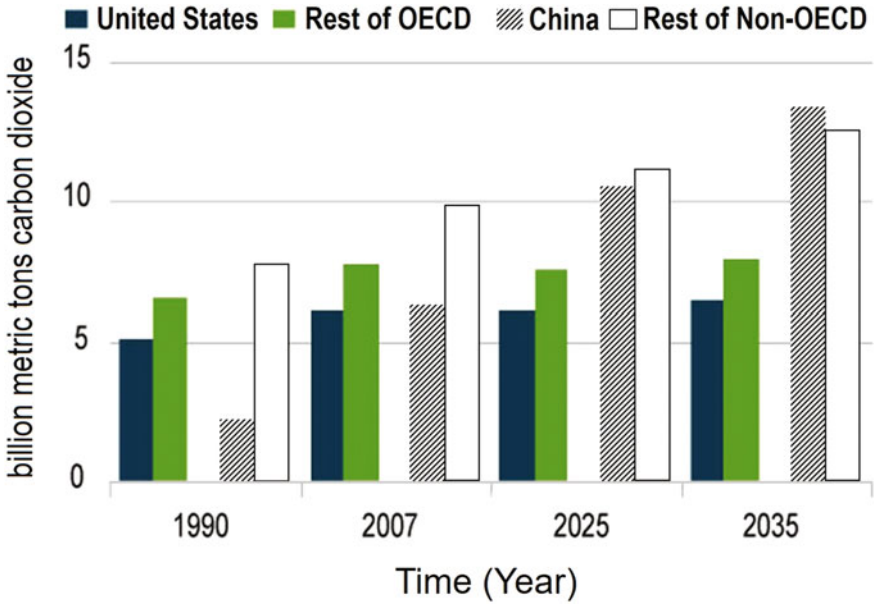

Fig. 2.7 Demonstration of total CO_2 emissions by region (U.S. Energy Information Administration, 2011)

is the biggest contributor to CO_2 emissions among OECD countries, with an annual CO_2 emission of ~5 gigatonnes (CO_2 only, not CO_2 equivalent) in 1990 and ~6 gigatonnes in 2007 (Fig. 2.7). U.S. energy-related CO_2 emissions were projected to increase by an average of 0.2% per year from 2007 to 2035 (U.S. Energy Information Administration, 2011); and in other OECD countries they were projected to increase by an average of 0.08% per year from 2007 to 2035 (see Fig. 2.7). Among the non-OECD countries, China is the biggest contributor to CO_2 emissions, and China has been the biggest CO_2 emitter in the world since 2007 (Rosenthal, 2007). China's share of global energy-related CO_2 emissions is projected to grow from 21% in 2007 to 31% in 2035, and China will account for 56% of the projected increase in world emissions over the period. India accounts for the second largest (7%) share of the projected increase (U.S. Energy Information Administration, 2011).

2.4.2 CO_2 Emissions by End-Use Sector

Based on end-use sector, CO_2 emissions can be classified into residential emissions (CO_2 from direct fuel use in households and CO_2 emissions from purchased electricity for households), commercial emissions (CO_2 from direct fuel use in

buildings for commercial purpose and CO_2 emissions from purchased electricity for commercial activities), industrial emissions (CO_2 from direct fuel use in industrial activities and CO_2 emissions from purchased electricity for industrial activities) and transportation emissions (CO_2 emissions from mobile source combustion). In 2009, industrial emissions account for the largest share in total U.S. CO_2 emissions (2240 megatonnes (million metric tons) equivalent CO_2 or 34.1% of total U.S. equivalent CO_2 emissions), and residential emissions, commercial emissions and Transportation emissions account for 18.0, 19.6, and 28.3% of total equivalent CO_2 emissions in the U.S., respectively, (U.S. Energy Information Administration, 2011).

2.5 Actions to Mitigate CO_2 Emissions and Climate Change

To mitigate greenhouse gas emissions, the U.S. has taken a series of actions at the federal level. The U.S. Environmental Protection Agency (EPA) finalized Rules for Mandatory Reporting of Greenhouse Gases by 31 industries and emissions sources in October 2009. Final rules and methods were proposed in April 2010 for a second group of industries: five industries that emit fluorinated greenhouse gases; oil and natural gas systems; and facilities that inject and store CO_2 underground for the purposes of geologic sequestration or enhanced oil and gas recovery (U.S. Energy Information Administration, 2011). Due to significant emissions of greenhouse gases and other pollutants from light-duty vehicles, the EPA has classified light-duty vehicles as a danger to public health and welfare. In April 2010, the EPA and the U.S. Department of Transportation's National Highway Traffic Safety Administration (NHTSA) jointly published Corporate Average Fuel Economy (CAFE) and GHG emissions standards to regulate emissions from light-duty vehicles of model years 2012–2016. Regarding R&D activities to mitigate CO_2 emissions, the U.S. Department of Energy (DOE) has invested significantly in developing and demonstrating technologies to capture CO_2 from large anthropogenic sources and store it safely and effectively in geologic formations—enabling continued use of our abundant fossil energy resources while reducing emissions from their use (U.S. Department of Energy, 2015).

Climate change is a global challenge and requires a global solution. An effective global strategy to mitigate CO_2 emissions requires commitments and actions by all the world's major economies (Center for Climate and Energy Solutions, 2015). A major step that reflects a global effort to mitigate CO_2 emissions is the Kyoto Protocol, which was agreed upon in 1997 by countries participating in the United Nations Framework Convention on Climate Change (UNFCCC). Under the Kyoto Protocol's first commitment period (2008–2012) developed countries were charged with reducing their emissions by an average of 5% below 1990 levels by 2012. The 15 countries that were the EU Member States at the time that Kyoto Protocol was

agreed upon committed to an 8% cut (European Commission, 2015). A second commitment period of the Kyoto Protocol runs from 2013 until 2020, and the EU has committed to reduce its greenhouse gas emissions by 20% below 1990 levels by 2020 (European Commission, 2015).

On September 16th, 1987, the Montreal Protocol, an international treaty designed to protect the ozone layer by phasing out hydrofluorocarbons (HFCs) and other substances causing ozone depletion, was agreed upon. U.S., Canada, and Mexico released a proposal in 2009 to include a binding schedule for phasing down production and consumption of 20 HFCs. The proposal calls for developed countries to reduce their production and consumption of the 20 HFCs to 15% of a 2004–2006 average baseline by 2033, and for developing nations to meet the same level by 2043 (U.S. Energy Information Administration, 2011).

Other major developing economies, like China and India, have pledged to cut their carbon emissions. On November 11, 2014, the U.S. and China released a joint announcement on climate change and clean energy cooperation. In this announcement, the U.S. set a new target to cut net greenhouse gas emissions 26–28% below 2005 levels by 2025. At the same time, China announced targets to peak CO_2 emissions around 2030, and to increase the nonfossil fuel share of all energy to around 20% by 2030 (The White House, 2014). India filed its climate action plan at the U.N. Climate Secretariat in Germany on October 1, 2015. In this climate action plan, India would reduce carbon emissions relative to its GDP by 33–35% from 2005 levels by 2030. India also pledged that 40% of the country's electricity would come from non-fossil fuel-based sources, such as the wind and solar power, by 2030 (Plucinska, 2015).

References

Archer, D. (2010). *The global carbon cycle*. Princeton, NJ: Princeton University Press.

Archer, D., Buffett, B., & Brovkin, V. (2009). Ocean methane hydrates as a slow tipping point in the global carbon cycle. *Proceedings of the National Academy of Sciences, 106,* 20596–20601.

Birat, J. P. (2010). Carbon dioxide (CO_2) capture and storage technology in the iron and steel industry. *Developments and Innovation in Carbon Dioxide (CO_2) Capture and Storage Technology* (pp. 492–521). Amsterdam: Elsevier.

Broecker, W. S., Peteet, D. M., & Rind, D. (1985). Does the ocean-atmosphere system have more than one stable mode of operation? *Nature, 315*(6014), 21–26.

Burwicz, E., Rupke, L. H., & Wallmann, K. (2011). Estimation of the global amount of submarine gas hydrates formed via microbial methane formation based on numerical reaction transport modeling and a novel parameterization of Holocene sedimentation. *Geochimica et Cosmochimica Acta, 75*(16), 4562–4576.

Center for Climate and Energy Solutions. (2015). *Climate change 101: International action.* Available online at: http://www.c2es.org/publications/climate-change-101/international. Accessed 20 April 2017.

Ciais, P., et al. (1997). A three-dimensional synthesis study of $\delta^{18}O$ in atmospheric CO_2: 1. Surface fluxes. *Journal of Geophysical Research: Atmospheres, 102*(D5), pp. 5857–5872.

European Commission. (2015). *Climate action: Working with international partners.* Available online at: https://ec.europa.eu/clima/policies/international_en. Accessed 20 April 2017.

Falkowski, P., et al. (2000). The global carbon cycle: A test of our knowledge of earth as a system. *Science, 290*(5490), pp. 291–296.

Field, C. B., & Raupach, M. R. (2004). *The global carbon cycle: Integrating humans, climate, and the natural world* (Illustrated ed.). Washington, DC: Island Press.

GISTEMP Team. (2016). *GISS Surface Temperature Analysis (GISTEMP). NASA Goddard Institute for Space Studies.* Available online at: http://data.giss.nasa.gov/gistemp/. Accessed 31 January 2016.

Global CCS Institute. (2014). *The global status of CCS: 2014.* Available online at: http://hub.globalccsinstitute.com/publications/global-status-ccs-2014. Accessed 20 April 2017.

Hall, D. O., & Rao, K. (1999). *Photosynthesis*. Cambridge: Cambridge University Press.

Halmann, M. M., & Steinberg, M. (1999). *Greenhouse gas carbon dioxide mitigation: Science and technology*. Boca Raton: Lewis Publishers.

Hansen, J., Ruedy, R., Sato, M., & Lo, K. (2010). Global surface temperature change. *Reviews of Geophysics, 48*(4), p. RG4004.

International Energy Agency. (2015). *World energy outlook.* Available online at: http://www.iea.org/publications/scenariosandprojections/. Accessed 20 April 2017.

IPCC. (2007). *Climate change 2007: The physical science basis. Working Group I contribution to the fourth assessment report of the Intergovernmental Panel on Climate Change*. Cambridge and New York: Cambridge University Press.

IPCC. (2013). *Climate change 2013: The physical science basis. Contribution of Working Group I to the fifth assessment report of the Intergovernmental Panel on Climate Change*. Cambridge and New York: Cambridge University Press.

Joos, F., et al. (1999). Global warming and marine carbon cycle feedbacks on future atmospheric CO_2. *Science, 284*(5413), 464–467.

Keeling, R. F., Piper, S. C., Bollenbacher, A. F., & Walker, S. J. (2009). *Atmospheric CO_2 values (ppmv) derived from in situ air samples collected at Mauna Loa, Hawaii, USA*. Available online at: http://cdiac.ornl.gov/ftp/trends/co2/maunaloa.co2. Accessed 20 April 2017.

Kiehl, J. T., & Trenberth, K. E. (1997). Earth's annual global mean energy budget. *Bulletin of the American Meteorological Society, 78*(2), 197–208.

Kleypas, J. A., et al. (1999). Geochemical consequences of increased atmospheric carbon dioxide on coral reefs. *Science, 284*(5411), 118–120.

Langdon, C., et al. (2000). Effect of calcium carbonate saturation state on the calcification rate of an experimental coral reef. *Global Biogeochemical Cycles, 14*(2), 639–654.

Marini, L. (2007). *Geological sequestration of carbon dioxide: Thermodynamics, kinetics, and reaction path modeling*. Amsterdam: Elsevier.

Mohr, H., & Schopfer, P. (1995). *Plant Physiology*. Berlin: Springer-Verlag Publishing.

NASA. (2014). *Wikipedia: Earth's energy budget.* Available online at: https://en.wikipedia.org/wiki/Earth%27s_energy_budget. Accessed 19 April 2017.

NASA. (2016a). *Surface energy budget.* Available online at: https://www.earthobservatory.nasa.gov/Features/EnergyBalance/page5.php. Accessed 21 April 2017.

NASA. (2016b). *The atmosphere's energy budget.* Available online at: https://www.earthobservatory.nasa.gov/Features/EnergyBalance/page6.php. Accessed 21 April 2017.

NASA. (2016c). *Climate change: How do we know?* Available online at: https://climate.nasa.gov/evidence/. Accessed 21 April 2017.

National Oceanic & Atmospheric Administration. (2015). *NOAA—Carbon cycle science.* Available online at: https://www.esrl.noaa.gov/research/themes/carbon/. Accessed 21 April 2017.

National Oceanic & Atmospheric Administration. (2016a). *NOAA—What is ocean acidification?* Available online at: https://pmel.noaa.gov/co2/story/What+is+Ocean+Acidification%3F. Accessed 21 April 2017.

National Oceanic & Atmospheric Administration. (2016b). *NOAA—Up-to-date weekly average CO2 at Mauna Loa.* Available online at: https://www.esrl.noaa.gov/gmd/ccgg/trends/weekly.html. Accessed 21 April 2017.

OECD. (2015). *Environment at a glance 2015: OECD indicators*. Paris: OECD Publishing.

Plucinska, J. (2015, 1 October). India pledges to reduce carbon emissions 33%-35% by 2030. *Time*.

Post, W. M., et al. (1990). The global carbon cycle. *American Scientist, 78*(4), 310–326.

Prentice, I. C., et al. (2001). The carbon cycle and atmospheric carbon dioxide. In J. Houghton et al. (Eds.), *Climate change 2001: The scientific basis* (pp. 183–238). Cambridge and New York: Cambridge University Press.

Raupach, M. R., et al. (2007). Global and regional drivers of accelerating CO_2 emissions. *Proceedings of the National Academy of Sciences of the United States of America, 104*(24), 10288–10293.

Richardson, K., Steffen, W., & Liverman, D. (2011). *Climate change: Global risks, challenges and decisions*. New York: Cambridge University Press.

Rosenthal, E. (2007, 20 June). China overtakes U.S. in greenhouse gas emissions. *The New York Times*.

Sabine, C. L., et al. (2004). Current status and past trends of the global carbon cycle. In C. B. Field & M. R. Raupach (Eds.), *The global carbon cycle: Integrating humans, climate, and the natural world* (Illustrated ed., pp. 17–44). Washigton, DC: Island Press.

The White House. (2014). *Fact sheet: U.S.-China joint announcement on climate change and clean energy cooperation.* Available online at: https://obamawhitehouse.archives.gov/the-press-office/2014/11/11/fact-sheet-us-china-joint-announcement-climate-change-and-clean-energy-c. Accessed 21 April 2017.

U.S. Department of Energy. (2015). *Carbon storage atlas* (5th ed.). Washington, DC: U.S. Department of Energy.

U.S. Energy Information Administration. (2011). *EIA—Emissions of greenhouse gases in the U.S.*. Available online at: https://www.eia.gov/environment/emissions/ghg_report/ghg_overview.cfm. Accessed 20 April 2017.

U.S. Environmental Protection Agency. (2015). *Learn about carbon pollution from power plants.* Available online at: https://archive.epa.gov/epa/cleanpowerplan/learn-about-carbon-pollution-powerplants.html. Accessed 21 April 2017.

U.S. Environmental Protection Agency. (2016). *Greenhouse gas emissions: overview of greenhouse gases.* Available online at: https://www.epa.gov/ghgemissions/overview-greenhouse-gases. Accessed 21 April 2017.

White, C. M., et al. (2003). Separation and capture of CO_2 from large stationary sources and sequestration in geological formations—coalbeds and deep saline aquifers. *Journal of the Air and Waste Management Association, 53*(6), 645–715.

Wigley, T. M. L., & Schimel, D. S. (Eds.). (2005). *The carbon cycle*. Cambridge : Cambridge University Press.

Williams, R. G., & Follows, M. J. (2011). *Ocean dynamics and the carbon cycle: Principles and mechanisms*. New York: Cambridge University Press.

Chapter 3
Clay: Geologic Formations, Carbon Management, and Industry

Daniel J. Soeder

Any sufficiently advanced technology is indistinguishable from magic.

—Arthur C. Clarke

Abstract The term clay is used interchangeably for the particles and the minerals, the latter commonly referred to as clay minerals to distinguish them from the clay particle size. Clay sediments are typically deposited in quiet-water environments, settling out as fine-grained mud, which may then be buried and lithified into shale. The quiet-water depositional environments are favorable for deposition of organic material as well, which over geologic time, may result in the shale becoming a source rock for petroleum and natural gas. Hydrocarbons have traditionally been produced from porous and permeable reservoir rock, where they had migrated from source rock and become concentrated in geologic traps. The recent development of "unconventional resources" like shale gas and tight oil has allowed hydrocarbons to be produced directly from the source rock. Conventional natural gas and oil reservoirs that have been depleted of hydrocarbons provide a viable option for secure carbon storage because there is a known trap and seal. CO_2 can potentially be used for enhanced recovery of the hydrocarbons and for pressure management in shale, to minimize the loss of permeability that comes from increased net stress during drawdown. As a side note, natural clay-rich geomaterials can be used in agriculture, industrial processes, and for clay liners in chemical and radioactive waste disposal sites. The purpose of addressing geomaterials here is to give the readers an idea of the enormous breadth of each subject and point them toward other resources for additional information.

In Greek mythology, Gea (*Γαῖα*)—the goddess of the Earth and the ancestral mother of all life, a divine character created as a holistic representation of our planet's ecosystem as well as the Humans' connection to it (and more generally,

D.J. Soeder (✉)
U.S. Department of Energy, National Energy Technology Laboratory (NETL), Pittsburgh, USA
e-mail: Dan.Soeder@sdsmt.edu

© Springer International Publishing AG 2018

V. Romanov (ed.), *Greenhouse Gases and Clay Minerals*, Green Energy and Technology, https://doi.org/10.1007/978-3-319-12661-6_3

mythical personification of the material component of life in the universe)—was born after Chaos (*Χάος*) from the great void of emptiness within the universe. In modern English, the root "Ge" relates to terms such as geology (*γῆ/λόγος* = discourse about the land) preserving that ancient connection.

In geology, the term clay is used to describe both very small, clastic sediment particles, and a type of mineral called a phyllosilicate (from Greek *φύλλον*—leaf) or "sheet" silicate, related to mica. Although the term clay is used interchangeably for both the minerals and particles, the minerals are commonly referred to as "clay minerals" to distinguish them from the clay particle size (2 micrometers or smaller). Clay minerals typically form as tiny sheets or flakes and a stack of clay flakes is known as a "book."

Clay is a secondary mineral, formed as a weathering product of primary minerals like feldspar or biotite that crystallized from an igneous melt. Water is required for the formation of clay minerals and they are in fact, commonly described as "hydrous aluminosilicates" because water is incorporated into the lattice as part of the structure (Kerr, 1955). Hypogene processes create clay minerals under hydrothermal conditions, usually in volcanic regions in the presence of hot water, steam, or vapors from magma. Supergene processes are those that form clay minerals under conditions of atmospheric temperatures and pressures during long-term weathering (Kerr, 1955).

3.1 Geology of Clays

The most common rock type containing abundant quantities of clay is called shale, a class of sedimentary rocks composed of tiny grains of quartz, flakes of clay, organic material, and carbonate minerals such as calcite. Shale is essentially made from the mineral components of mud and the generic term for this rock is "mudstone." Mudstones may be classified as (1) predominantly silt or (2) predominantly clay. Silt-rich rocks are called siltstone.

The term "shale" itself is not well-defined. Some geologists apply it only to those fine-grained rocks composed of clastic sediments and exhibiting a property of splitting into thin sheets, known as fissility (Fig. 3.1). Fissility (or fissibility) comes from a preferred alignment of the clay flakes during deposition, when they tend to stack together flat, one on top of another like a deck of cards that imparts a finely layered structure to the resulting rock. However, not all clay-rich rocks are fissile and some geologists use the more generic term "claystone."

Rocks composed of something as simple as mud may not seem to be very exotic, but a closer look often reveals some interesting features. Shale contains complex and often rather strange-looking grain and pore structures (Schieber, 2010; Goral, Miskovic, Gelb, & Kasahara, 2015); and laboratory experiments using low-velocity flumes (Schieber, 1994) have shown that the depositional environments of fine-grained clastic sediment are often far more complicated than many people suppose.

Fig. 3.1 Outcrop of the Middle Devonian-age Millboro Shale (Marcellus equivalent) at Sugar Grove, WV, showing *vertical* natural fractures, fine layering, and fissility (in foreground). The *white* sample bag is approximately 10 cm (4″) long. Photographed in 2010 by Daniel J. Soeder

The proportion of the three primary mineral components of mudrocks (clay, quartz, and carbonate) varies in any particular shale, but most are composed of some combination of these end members. Shale also typically contains minor mineral components, such as feldspars, oxide minerals, and sulfides (Chermak & Schreiber, 2014). The bulk of the fine-grained sediment making up shale is clastic in nature. Similar, fine-grained, but non-clastic carbonate rocks like chalk are classified as limestones. Intermediate rocks composed of both clastic and carbonate minerals are known as shaly limestones or calcareous shales, depending on the proportion of the constituents. Shales also contain diagenetic minerals, such as siderite and dolomite that precipitated from fluids trapped within the rock after deposition of the clastic sediments over geologic time.

Clay minerals as a class are composed of two broad structural groups—the layer or sheet silicates and the chain silicates (Brindley, 1955). Chain silicate clays are the hydrated, weathered byproducts of primary inosilicate minerals such as pyroxenes and amphiboles, and include palygorskite or attapulgite, and possibly sepiolite (Brindley, 1955). The sheet-like or layered phyllosilicates are usually classified into four main groups: serpentine, clay minerals, mica, and chlorite.

Clay minerals fall into two main classes: swelling and non-swelling. The water incorporated into clay minerals as part of the crystal structure is known as water of hydration, and removing it, such as when a clay pot is fired in a kiln, causes the material to recrystallize into a ceramic. Water of hydration is bound between the phyllosilicate layers that make up the clay structure. Clays that contain a single layer of bound water between sheets is dimensionally stable, but those with multiple layers of bound water can gain or lose layers of hydration, causing the clay to expand or contract. These are known as swelling clays.

Swelling clays (e.g., smectites) can expand or contract in response to changes in salinity, temperature, or pressure. Smectites are commonly found in younger sediments and more shallow-buried rocks. In the context of sedimentary geology, a clay rock made of volcanic ash is classified as bentonite if the smectite content is very considerable (e.g., 70% or more) but it may contain considerable amounts of illite and/or kaolinite, just as well. You may also find carbonates, pyrite, quartz, feldspar, calcite, and gypsum in it. Bentonite, originally found in weathered volcanic ash at Fort Benton (Eastern Wyoming) is often used in oil and gas drilling because of its ability to swell up and seal leaky boreholes. Drillers are cautious about encountering swelling clay in the rock formations they are drilling, however, because it can shut off oil and gas flow if it swells, or cause the borehole wall to collapse if it contracts. Drillers monitor the downhole salinity, temperature, and pressure very carefully when penetrating formations that contain swelling clay.

Non-swelling clay is typically found in more deeply buried rocks where heat and pressure over geologic time have driven off excess water layers and compressed the sheets. The bulk of more deeply buried, thermally-mature shale consists of non-swelling clays such as chlorite, illite, and kaolinite. A third, intermediate class of clay with both swelling and non-swelling layers is known as mixed-layer clay. Depending on the structure, some of these can swell significantly. The dominant clay minerals in shale include illite, mixed layer illite-smectite, smectite, kaolinite, and chlorite (Chermak & Schreiber, 2014).

3.1.1 Fossil Fuels

The quiet-water depositional environments that allowed fine-grained sediments to settle out of the water column to create shale were also favorable for the deposition of organic matter. Most organics in sediment originated as plant material from

either marine or terrestrial sources (Chen et al., 2015). If aerobic bottom conditions prevailed, much of the deposited organic matter was consumed by benthic organisms and bacteria, resulting in an organic-lean or "gray" shale. However, if anoxic bottom conditions were present, the organic material was often preserved from decay, creating dark colored or "black" shale (Fig. 3.2). Organic carbon contents of only a few percent are needed to turn the rock noticeably dark, and at carbon contents of about 4% and greater, the rock is black, and does not become any darker with the addition of more organic material (Hosterman & Whitlow, 1980, 1981). When the black muds were buried and lithified into shale, the organic material was subjected to heat and pressure in the absence of oxygen over geologic time periods, slowly becoming hydrocarbons, such as petroleum, natural gas, and coal.

Fig. 3.2 Contact between the *black* Cleveland Shale and the underlying gray Chagrin Shale in a drill core from Ohio. There is a *yellowish* layer of pyrite at the contact (2040.54 ft.)—Depths are marked in tenths of a foot, and the *vertical* ink line down the front of the core is the North side. Heavy *black arrows* point downward. Photograph by Daniel J. Soeder

For many years, the bulk of commercial oil and gas was produced from what are known as "conventional" resources. The high-grade, concentrated hydrocarbons in a conventional oil and gas reservoir were usually created elsewhere, and migrated into the porous, permeable reservoir rock, typically sandstone or limestone, where they accumulated and were trapped. Conventional reservoirs can typically be produced at economic rates with standard vertical well drilling technologies.

Shale gas, shale oil, gas-bearing coal seams, tight gas sandstones, and methane hydrates (Guggenheim & Koster van Groos, 2003) are known as "unconventional" resources. These resources typically consist of low to very low permeability materials with dispersed hydrocarbons created in-place from organic material deposited with the sediment. Special engineering techniques, such as horizontal drilling and high-volume hydraulic fracturing (HVHF) are required to produce economic quantities of oil and gas from these formations. Unconventional resources tend to be less concentrated and lower grade than conventional hydrocarbons, but total quantities are often very large, sometimes extending throughout almost the entire volume of the formation (Soeder, Randolph, & Matthews, 1988).

Hydrocarbon resources in conventional reservoirs are created through a complex process that includes a number of conditions and events that must occur in a specific order and with proper timing. If anything goes wrong, the end result is a dry hole with no production. This is why exploration for conventional oil and gas requires a deep knowledge of geology, volumes of data, and a significant amount of luck. The five things needed, in order, are a source rock, thermal maturity, a reservoir rock, a trap and seal, and a migration pathway (Soeder, 2012). These are described in detail below.

1. Source rock: Two common sources of organic material in sediments are algae or other water plants and woody land plants. Some animals may have contributed as well, but most fossil fuel is derived from preserved plant material, known as sapropel, not from dead dinosaurs. Organic material is easily suspended in water and does not settle out until encountering the same quiet water conditions that deposit clays and mud. The decay process typically requires oxygen, so if the organic material settles to the bottom in water that contains low levels of dissolved oxygen, it will often be preserved. As such, source rocks are usually composed of fine-grained sediments and organic material deposited under anoxic bottom conditions in quiet water, such as black shale.

2. Thermal maturity: In addition to containing a few percent of preserved organic matter, the source rock had to be buried deeply, and subjected to heat and pressure within the Earth over geologic time periods in the absence of oxygen. This process is called thermal maturation and it breaks down the organic carbohydrates into fossil fuel hydrocarbons. Temperatures within the Earth increase with depth along geothermal gradients, thus deeper burial of a source rock means exposure to higher temperatures.

3. Reservoir rock: Rocks that produce conventional oil and gas usually consist of coarse-grained sandstones or limestones with high porosity and permeability. The coarse grain size results in larger pore sizes, and larger pores allow hydrocarbons in the rock to flow freely into a well. The high water energy needed to

entrain and transport coarse clastic material is not favorable for the deposition of fine-grained sediment and particles of organic matter, which tend to remain suspended until encountering a low energy, quiet water environment. Good reservoir rocks usually make poor source rocks and vice versa.

4. Trap and seal: To contain the gas and oil in a conventional reservoir, there must be some kind of a trap, such as a fold or a fault, to displace the rock layers and create an underground structure that acts as a container to hold the hydrocarbons in the reservoir rock. To be effective, the trap must also include an impermeable caprock, such as shale, gypsum, or salt to seal the reservoir. A body of reservoir rock without a trap and seal will not retain any hydrocarbons. Traps can be either structural, such as a closed fold like a dome, or stratigraphic, such as a sandstone lens overlain by shale.

5. Migration pathway: Because the source rocks and reservoir rocks are usually completely different formations, a migration path is needed for hydrocarbons to get from the source rock to a reservoir rock. This can be a through-going fracture, such as a fault that allows movement through the intervening rocks, or just tilted beds that will let hydrocarbons slowly seep updip (up the slope of a dipping geologic reservoir plane/surface). Timing is everything: if the migration pathway is in place before a reservoir rock is available, the oil and gas will be lost. Likewise, if the reservoir rock is present, but no migration path ever develops, the reservoir stays empty. It is a tribute to the talents of the petroleum geologists and engineers that virtually all of the oil and gas produced throughout history, until the first decade of the twenty-first Century, has been found in conventional reservoirs.

3.1.2 Unconventional Resources

Although the term "unconventional" is on the way to becoming "conventional" in the minds of some people, it does have a specific definition, in that the target formation must be engineered with some type of reservoir stimulation (such as hydraulic fracturing) to produce economical amounts of hydrocarbons. Shale gas was generated in-place from thermally-mature organic material that had been deposited with the shale. This is a new concept in petroleum geology: the source rock is also the reservoir rock. The USGS refers to gas shales as "continuous resources," to distinguish them from hydrocarbons in traditional traps and seals (Charpentier & Cook, 2011). One can drill and stimulate a well almost anywhere in a continuous resource with the proper production technology and expect to produce economical amounts of hydrocarbons. By developing the lower-grade hydrocarbon resources in U.S. shale formations, industry has significantly increased the amount of recoverable oil and gas in the nation. Unconventional resources vastly exceed conventional resources.

The key to producing economical quantities of gas from shale is to drill horizontally or "laterally" through the rock, which contacts much more formation volume than drilling vertically (Soeder, 2012). The typical black shale thickness of

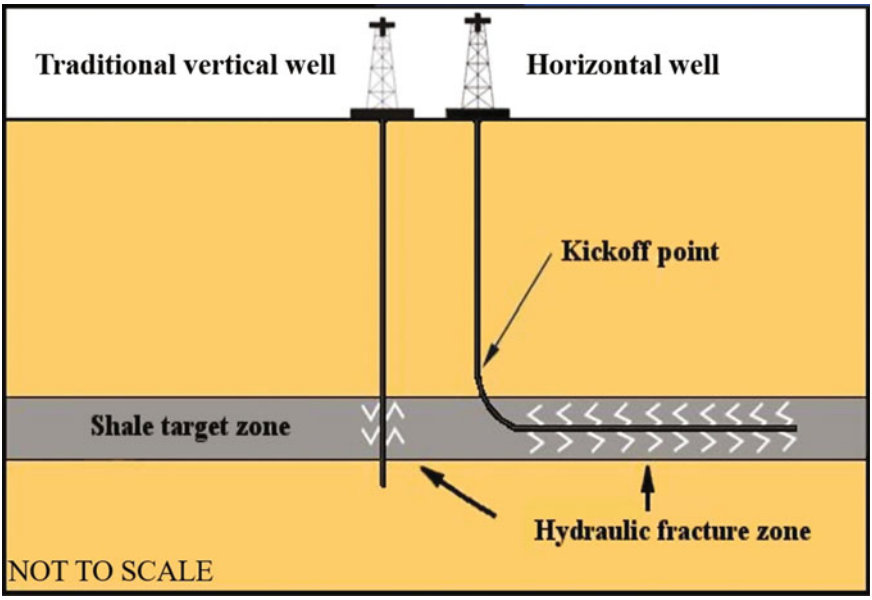

Fig. 3.3 Illustration of the combination of *horizontal* drilling and hydraulic fracturing technology used for gas production from the Marcellus Shale in the Appalachian Basin. Horizontal wells have a much greater contact area with the shale than *vertical* wells, which are limited by the formation thickness. Not to scale (Soeder & Kappel, 2009)

only a few dozen meters (a few hundred feet) limits the amount of contact a single vertical well can have with the formation. Drilling horizontally, however, allows the wellbore to remain within the shale for long distances, penetrating hundreds of meters or thousands of feet of rock (Fig. 3.3).

Engineering developments in the 1990s with hydraulically powered downhole drilling motors that did not require the entire drill string to be turned from the surface helped directional drilling technology advance significantly (Soeder, 2012). As offshore rigs began drilling in increasingly deeper water and became more expensive to move, the oil and gas industry focused on directional drilling as a method for penetrating multiple reservoir traps from an anchored, semi-submersible tension leg platform. The big players in the deepwater drilling game were willing and able to spend the sums of money needed to develop and improve directional drilling equipment to make this a reality, including better motors and more accurate methods for determining the location of the borehole and the end of the drill string. Some deepwater platforms now routinely drill as many as 60 different wells from a single anchorage.

A modern downhole motor uses hydraulic power, supplied by drilling mud pumped down the inside of the drill pipe under high pressure. There are several designs for providing power to the motor from the mud, ranging from spiral grooves built into the drill pipe to turbine-like spinning blades. The motor then

turns the bit, which cuts the rock by using rotating steel and carbide teeth and applied pressure (Soeder, 2012). The impeller, motor, and bit together are known as the "bottomhole assembly," and it is the only part of the drill string that rotates. With this configuration, wells can be drilled in virtually any direction, including horizontally.

Long lateral boreholes drilled using this new technology were coupled with hydraulic fracturing to create high permeability flowpaths into the shale. Instead of the single "frac" (a well stimulation technique in which rock is fractured by a pressurized liquid) done in vertical wells, the long horizontal boreholes allow for an entire series of hydraulic fractures to be spaced a few dozen meters (a few hundred feet) apart. There can be ten or more of these so-called staged hydraulic fracs in a horizontal borehole, resulting in large volumes of gas production. Drilling costs for a horizontal well are approximately two–three times higher than for a vertical well, but the initial gas production potential can be three–four times greater (Engelder & Lash, 2008).

3.2 Carbon Management

The ability of carbon dioxide gas to trap heat has been known since Joseph Fourier first developed the physics of radiative heat transfer in 1827 (Pierrehumbert, 2011). The steady increase in the atmospheric concentration of the gas since regular measurements began in 1957 (Fig. 3.4); the monthly updates can be viewed by

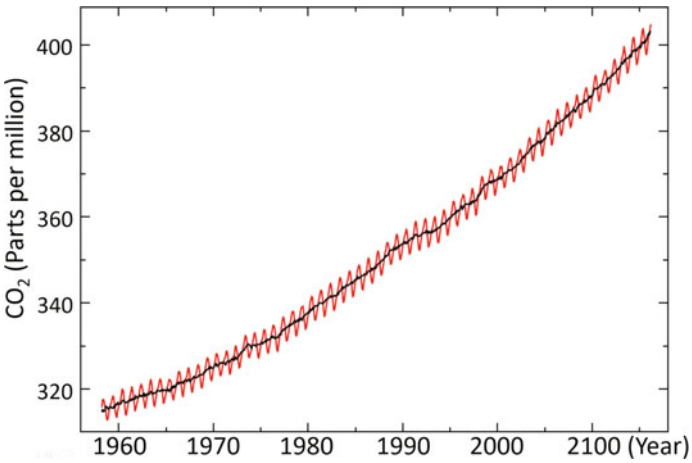

Fig. 3.4 Atmospheric carbon dioxide levels measured since 1957 at Mauna Loa, Hawaii. The saw-tooth pattern is caused by a seasonal fluctuation as plants bloom in the spring and take up CO_2. Data from NOAA and Scripps

anyone interested at http://www.esrl.noaa.gov/gmd/ccgg/trends/ as of the time of this writing (2017). Note that the trend line is not straight, but is growing steeper over time.

The details of anthropogenic climate change are discussed in other chapters of this book, but readers are reminded that climate is a complex and chaotic system; so much so that mathematical models of climate change often require the largest, fastest supercomputers in the world to run. Translating the observed and predicted increases in atmospheric carbon dioxide into potential climate change includes a significant amount of uncertainty, which inevitably leads to variability in the model outputs, including how such changes might result in environmental risk. As such, environmental risk is most often assessed and presented in terms of probabilities. (As an example, consider the daily weather report, where the forecast for rain is presented as a probability due to complexities in weather prediction models.)

A report by the Intergovernmental Panel on Climate Change (IPCC, 2007) states that if carbon dioxide emissions are not reduced by industrial nations (i.e., if nothing is done and emissions continue to increase under a baseline business-as-usual scenario) concentrations of the gas in the atmosphere will likely increase from 390 parts per million (ppm) in 2007 to about 1250 ppm by 2100. The IPCC scientists determined that the most probable result of the projected carbon dioxide increase would be a rise in mean global temperatures by approximately 3.4 °C (6.1 °F). Lower probability results give a one-in-six chance that temperature increases will exceed 5.4 °C (9.7 °F) causing serious climate disruptions. There is also a one-in-six chance that it will be less than 2.0 °C (3.6 °F) and be lost in the natural background.

Risk is defined as the probability of an event multiplied by the consequences (Soeder et al., 2014). A one-in-six probability that global temperature rise could exceed 5.4 °C may not sound like that great of a risk to some people, but these are the same odds as Russian roulette. No one considers that activity to be low risk, given the possible consequences. Likewise, the possible consequences of a 5.4 °C temperature rise include the potential melting of the polar ice sheets (Poore, Williams, Tracey, 2000), which could raise sea levels by up to 76 m (250 feet). This would inundate large parts of low-lying countries such as Bangladesh, or Holland and neighboring countries around the North Sea and Baltic Sea. Some nations like Micronesia, composed of coral atolls only a few meters above sea level, might disappear altogether. In the U.S., nearly all of Florida (mean elevation 30 m or 100 ft.) would be underwater, with only a few small strips of dry land remaining.

One needs only to trace the 250-foot contour line on topographic maps of the U.S. Gulf and East coasts to see the amount of land that would be inundated. Sea level rise will especially affect large coastal cities like Boston, New York, Philadelphia, Baltimore, Washington, Charleston, Miami, Tampa, New Orleans, and Houston. On the West Coast, the shoreline areas of San Diego, Los Angeles, Portland, and Seattle would be submerged, as would large parts of the San Francisco Bay area, if not the city itself. Anchorage and Seward in Alaska, and Honolulu and Hilo in Hawaii would also be inundated. The list goes on around the world. Clearly, the probabilities and possible consequences of human-induced

climate change are dire. Whether this is enough to justify efforts to reduce anthropogenic carbon dioxide levels in the atmosphere is a policy question, not a technical issue.

Two options are available for atmospheric carbon management. The first is to add less CO_2 to the atmosphere from energy-related sources by improving the efficiency and economics of carbon-neutral technology like solar, geothermal, wind, nuclear power, or biomass. Solar, geothermal, nuclear, and wind generate no carbon dioxide at all. Biomass fuel recycles carbon that is already part of the terrestrial carbon cycle and does not add "new" carbon from geologic sources into the atmosphere. Carbon-neutral energy sources at present are expensive and inefficient, and the world is expected to continue to obtain at least 80% of all energy from fossil fuels through 2035. Some economic models suggest that abruptly outlawing the use of fossil fuels would be more disruptive to the world economy than the storms, droughts, and sea level rise predicted to result from climate change (Adair, 2012).

The other carbon management option, mentioned in Chap. 2 is to remove CO_2 from the atmosphere using engineering techniques known as "carbon capture and storage," or CCS to lock down and "sequester" the carbon someplace to keep it isolated. Rather than removing the dilute gas from the air, this technology usually focuses on capturing concentrated carbon dioxide from fossil fuel combustion exhaust at the source before it enters the atmosphere. As such, CCS generally works best on carbon dioxide generated by large, non-mobile facilities, such as coal-fired electric power plants.

One of the major challenges to CCS is the cost of the technology, and how that might be reflected in the cost of electricity. Carbon capture is usually done either chemically by using a technique called "pressure-swing adsorption," or cryogenically by freezing the gas out of the combustion exhaust as dry ice. Adding carbon capture technology to existing coal fired or natural gas power plants may as much as double the cost of electricity (U.S. Energy Information Administration, 2017). Most carbon capture and storage schemes try to find a beneficial use for the carbon dioxide in industrial applications to improve the economics.

A second challenge to CCS is where to store the captured carbon dioxide to keep it isolated from the atmosphere. A research group in California, among others (Romanov et al., 2015) are working on ways to convert carbon dioxide into carbonate, or CO_3, and then use this substance to create useful products like concrete and cement. Construction materials made from waste carbon dioxide may keep it out of the atmosphere for quite a long time while providing a beneficial use that reduces costs. Other ideas include growing plants like trees, algae, or hemp under atmospheres high in CO_2 to sequester the gas as wood, fuel, fiber or other plant products, which can then be used as construction materials or fuel. These are only temporary fixes, however, because when the wood is burned or the plant material rots, the carbon will once again be in the atmosphere.

A large-scale technology for sequestering significant volumes of atmospheric carbon dioxide is called geologic storage, which involves pumping the captured carbon dioxide underground and isolating it for geologic time periods (potentially millions of years) in the pores and fractures of deep rock formations. CO_2—which

is normally more buoyant than preexisting liquids that might be present in the pore space—may percolate up through the porous rocks until it reaches the top of the geological storage reservoir, where it is structurally (or stratigraphically) trapped by an impermeable layer of cap-rock and then by slow dissolution. As the CO_2 plume migrates so, the initially displaced liquid (such as oil or brine) again replaces it, but some of the disconnected CO_2 droplets become immobilized in the pore spaces via residual trapping. Rock units under consideration for such storage include depleted, conventional natural gas or oil fields, deep saltwater aquifers, unmineable coal seams, depleted gas shales, and basalts (U.S. Department of Energy, 2015). Each has advantages and disadvantages in terms of practicality and cost.

Conventional natural gas and oil reservoirs that have been depleted of hydrocarbons provide good storage for CO_2 because there is a known trap and seal in the geology. Otherwise, there would not have been gas or oil there in the first place. A beneficial use for captured carbon dioxide in conventional reservoirs is to sweep out residual oil in a process called enhanced oil recovery or EOR. This has been done successfully in a number of vintage oil fields in Texas, Louisiana, and Wyoming, and CO_2 has also been injected into depleted conventional gas reservoirs with some success, notably the Frio Formation on the Gulf Coast. An additional advantage of using depleted conventional oil and gas reservoirs is that the infrastructure of wells and surface pipelines may still be in place, saving the costs of installing these.

The presence of existing wells, especially older wells, can also be a disadvantage at a carbon storage location. When carbon dioxide gas is injected into the ground at depths below 800 m (2500 ft.) the hydrostatic pressure transforms it into a state known as a "supercritical fluid," which has the properties of both a gas and a liquid. Some field demonstrations suggest that storing carbon dioxide in conventional rocks as a supercritical fluid is more efficient because it takes up less space than a compressed gas. However, supercritical CO_2 is a powerful organic solvent, and it will also form carbonic acid when dissolved in subsurface formation waters and brines. The solvent may deteriorate wellbore packers and O-ring seals, and the acid can damage cement, steel casing, and even the formation seal itself (Watson & Bachu, 2009). On older wells where the cement may already be deteriorated and the casing corroded, exposure to supercritical CO_2 and water can require major well repairs.

Storing captured CO_2 in deep saltwater aquifers, unmineable coal seams, or basalt formations requires the installation of injection wells, in some cases to great depths. An additional challenge is the requirement to displace preexisting pore fluids like water or brine to make room underground for storing the CO_2 (Goodman et al., 2011, 2013). In deep, saline aquifers the supercritical fluid is stored as a plume in a manner similar to injected chemical waste. Coal seams store the CO_2 in pores and fractures, and also as an adsorbed phase on active carbon sites. Coals may swell when charged with CO_2, potentially blocking flowpaths, although at the geologic basin scale this is probably negligible (Goodman et al., 2011). Basalts undergo a mineral transformation of calcium-rich feldspars into calcium carbonate, and store CO_2 as a carbonate solid phase (U.S. Department of Energy, 2015). The challenge with these generally fractured and well-jointed igneous rocks is retaining

the CO_2 in place until the relatively slow mineral transformations can occur, although field experiments in Iceland have shown significant calcium carbonate mineralization within two years of CO_2 injection (Matter et al., 2016).

Several groups of researchers have been considering the potential for carbon storage in depleted gas shale (Curtis, 2002; Nuttall, Ebble, Drahovzal, & Bustin, 2005; Busch et al., 2008; Jarvie, 2012; Tao & Clarens, 2013; Kulga, Dilmore, Wyatt, & Ertekin, 2014; Levine et al., 2016) and even suggested utilizing liquid or supercritical CO_2 as an alternative fluid for shale fracturing (Middleton et al., 2015)—akin to CO_2 utilization in enhanced coalbed methane and enhanced oil recovery. Black shales have an adsorbed component of gas, and preliminary data indicate that adsorption may be significantly stronger for carbon dioxide than for methane (Godec, Koperna, Petrusak, & Oudinot, 2013). Both the clay minerals and organic carbon in shale appear to contribute to the adsorption and storage of gas (Busch et al., 2009). Many if not most gas shales also contain a non-mobile water phase (Soeder et al., 1986) suggesting that the corrosion problems experienced with supercritical carbon dioxide storage in conventional reservoirs will be much less of an issue in gas shale.

An economic advantage of using a depleted gas shale for carbon storage is the same as for depleted conventional oil and gas reservoirs: the pads, wellheads, hydraulically fractured boreholes, distribution pipelines and other infrastructure needed to transport and inject the gas will already be in place. When production ends, the well becomes a liability with additional costs to plug and abandon per state regulations. This liability can be transformed into an asset by utilizing the well for carbon dioxide injection (Levine et al., 2016). Another potential economic advantage is that the stronger adsorption of CO_2 into the shale will displace residual methane, enhancing natural gas recovery (Hong et al., 2016).

The responses of shale matrix pores and flowpaths to increases in net confining stress caused by drawdown during natural gas production are not well understood. Rocks at depth are under an overburden pressure, caused by the weight of the rock above pressing down with a typical lithostatic (overburden) pressure gradient of about one psi per foot of depth. This overburden pressure is offset to some degree by the pressure of fluids in the fractures and pores pushing back. The "pore pressure" typically follows a hydrostatic pressure gradient of about 0.5 psi per foot of depth. When fluids and gases are produced from the rock, however, the pore pressure decreases, causing the "net" overburden pressure to go up. Gas shale formations are not expected to be made available for CO_2 storage until virtually all of the natural gas and liquids have been withdrawn from the rock pores. Thus, an excursion into a high net stress regime prior to CO_2 storage appears unavoidable (Hong et al., 2016).

So why does this matter? Laboratory data indicate that shales are sensitive to high stress: e.g., doubling net confining stress can result in a 70% reduction in matrix permeability (Soeder, 1988). Analyses of the Klinkenberg-corrected permeability data indicate that flowpath tortuosity increases under elevated net stress, as does the median pore size in the matrix. This has been interpreted as the smaller pores being preferentially compressed and closed off under high net stress, leading to the observed permeability losses (Soeder et al., 1986).

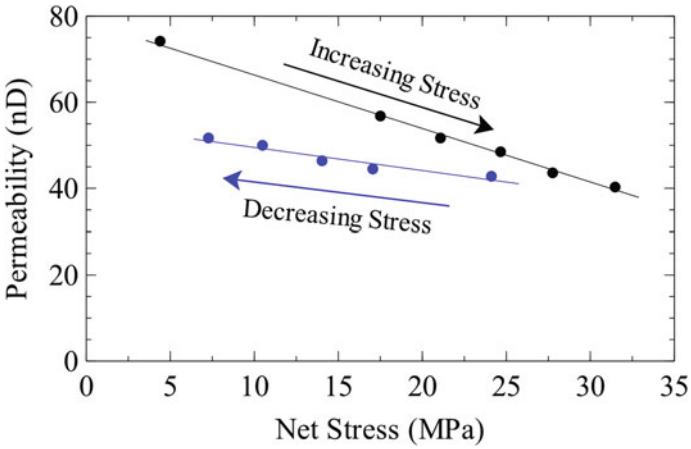

Fig. 3.5 A series of dry nitrogen gas permeability measurements were made on a sample of Marcellus Shale during a high net stress excursion. The *upper black line* shows permeability decreasing to the *right* as net confining stress increases, and the *lower blue line* shows permeability increasing back toward the left as net stress is later reduced. Data from Dilmore et al. (2015)

Laboratory experiments also show hysteresis in shale after high net stress excursions. As displayed in Fig. 3.5, reducing the stress on the rock after taking it to high net stress did not restore the original permeability within the time frame of the laboratory experiment (Dilmore et al., 2015). This is probably due to the crushing of the asperities that prop open the flat or slot-like pores (Randolph & Soeder, 1986). Similar studies on the Barnett Shale have suggested that stress-induced alterations of the rock are likely permanent (Vermylen, 2011).

Despite these lab results, modeling simulations indicate that permeability hysteresis may not significantly impact the CO_2 storage potential of very low permeability shale (Kulga et al., 2014). This is because the movement of gas in or out of these extremely tight rocks is already so difficult that any further reduction in permeability after an excursion to high net stress is likely to make little difference. Shale matrix permeability is typically in the nano-Darcy (nD) range, which is a million times lower than the milli-Darcy (mD) permeability typical of a conventional oil or gas reservoir. As an example, if a one meter length of exposed milli-Darcy conventional reservoir rock in a wellbore is able to accept one cubic meter of CO_2 per second, a similar length of exposed nano-Darcy shale in a wellbore would require a million seconds, or about 11.6 days, to accept the same cubic meter of CO_2. This drastic difference in flow rates is what makes both natural gas production and CO_2 storage so challenging in shale.

Along with a reduction in matrix permeability with increasing net stress, the permeability of propped hydraulic fractures and natural fractures also decreases under high stress (Ahn, Dilmore, & Wang, 2014). Because fractures provide an important pathway for the movement of fluids into shales, the loss of fracture

permeability represents a significant potential reduction in the amount of CO_2 that may be stored in these rocks.

Permeability reductions under high net stress and the resulting flowpath hysteresis may or may not eliminate the utility of depleted gas shales for carbon dioxide storage. Reservoir pressure management during the earlier natural gas production phase may help to preserve permeability for later CO_2 storage. Pressure management strategies might include injecting carbon dioxide along the perimeter of a shale gas reservoir at an earlier stage of drawdown to help maintain reservoir pressures and keep flowpaths open. If done carefully, such an injection could also help sweep the natural gas more efficiently from the shale and increase recovery. If it improves the economics, operators are more likely to adopt it as a practice.

It is generally believed that hydraulic fracturing is behind the recent spate of earthquakes in regions not usually associated with seismic activity (Bao & Eaton, 2016; Frazier, 2017) but the underlying processes are still poorly understood. Between the years of 1973–2008, there was an average of 21 earthquakes of magnitude three and larger (on the Richter scale) in the central and eastern United States. This rate has ballooned to over 1000 after 2014 (U.S. Geological Survey, 2016). However, the main culprit is injection of wastewater and salt water into the subsurface, which can actually cause man-made earthquakes that are large enough to be felt and that may cause damage. Seismicity can be induced at distances of 10 miles (16 km) or more away from the injection point and at significantly greater depths than the injection point (U.S. Geological Survey, 2016). There are concerns that pumping fluids into the ground near the storage reservoir might trigger small earthquakes that can breach the CO_2 storage system, allowing the gas back into the atmosphere (Zoback & Gorelick, 2012).

3.3 Other Clay Applications

Clay minerals are primarily utilized as geologic materials in three industries: agriculture, ceramics, and oil & gas development (Pask & Turner, 1955). Scientific studies covering these areas encompass the vast fields of soil science, ceramics and materials engineering, and petroleum engineering. Each study area is enormous in its own right, with hundreds of reference books and thousands of peer-reviewed papers. The purpose of addressing geomaterials here is to give the reader an idea of the breadth of each subject and then point him or her toward some other resources for additional information. As a side note, natural clay-rich geomaterials such as bentonite, an absorbent aluminium phyllosilicate clay, can also be used in many other industrial processes and for clay liners in chemical and radioactive waste disposal sites—specifically, bentonite/sand mixtures are the favored option for clay-based engineered barriers for nuclear waste repositories due to their self-sealing capacity driven by swelling pressure and low hydraulic conductivity at full saturation.

Agriculture: Clay in soil, especially in combination with organic material, exerts a strong influence on soil properties. Soil grains clumped together in aggregates with small amounts of clay have a more open structure, allowing air and water to move freely to plant roots. Soils with excessive amounts of clay tend to be heavy and impervious, and unfavorable for plant growth (Page, 1955). Clay soils can be improved by the addition of coarser material, such as sand, and organic material or compost. These form aggregates that give the soil a more open structure, yet still retain the water needed for plant growth. Clay soils with added aggregate and no organics tend to drain too quickly and can harden into a brick-like adobe when dry.

Not all soils are suitable for growing crops, and must be balanced in terms of mineral components (sand/silt/clay), soil organic matter, air, and water (Parikh & James, 2012). Farmers strive to achieve this balance to provide sufficient water retention for plant roots while allowing excess water to drain, maintain oxygen in the root zone, ensure the movement of nutrients through the soil, and supply the physical support for plants. The structure and composition of the soil is influenced by the parent material, the age of the soil, the climate, organisms living within the soil, and topography.

As an interesting aside, polyacrylamide, the surfactant material used as a friction reducer for "slickwater" (freshwater to which a friction-reducing agent is added) hydraulic fracturing in shale is also a common agricultural chemical applied to silty loam and clay loam soils in irrigation canals to reduce the amount of water infiltration into the soil. The treatment helps to ensure that the water remains in the canal until it reaches the agricultural field where it is needed (Lentz, 2003).

Ceramics: Because clay is easy to shape when wet, and hardens into a rigid solid when dried, it has been used since the earliest times to make ceramic materials. A ceramic is a nonmetallic, inorganic solid (Kingery, Bowen, & Uhlmann, 1976), which is generally (but not always) produced by heating or "firing" the soft material to drive off water and recrystallize the mineral components, creating a rigid and (usually) brittle solid when cooled to room temperature. The word "ceramic" comes from the Greek word *keramikos*, for "pottery." Ceramics include everything from simple clay pots to delicate Chinese porcelain figurines to high-temperature superconductors (Carter & Norton, 2007).

Sociologists, educators, city planners, psychologists, architects, and artists are considering the potential impact of large-scale shale gas production on society. Jennie Shanker, an artist and art professor at the Tyler School of Art at Temple University in Philadelphia has been focusing on the origin of materials, and how objects are perceived by the population. She has been producing figures and objects using clay from the Marcellus Shale as sculpting medium, including a sculpture of an everyday foam coffee cup (Fig. 3.6) showing the replacement of a common but manufactured material (plastic foam) with a natural but artistically rare material (Marcellus Shale clay). The cup motif was used to emphasize the link between the shale and water issues.

Ceramics are usually made up of arrays of interconnected atoms in covalent, ionic, and sometimes metallic bonds (Carter & Norton, 2007). The minerals comprising ceramics are often oxides, nitrides, and carbides, in addition to silica

Fig. 3.6 Philadelphia artist Jennie Shanker's sculpture of a foam coffee cup executed in clay from the Marcellus Shale, sitting on a slab of the same material. Cup motif is intended to show a connection between the shale and water. Photograph by Daniel J. Soeder; sculpture shown with permission from the artist

and clay. As a nonmetallic, inorganic fused solid, glass may also be considered a type of ceramic material (Carter & Norton, 2007). Ceramics are often used for reinforcement or as a bonding medium in composite materials. Bricks, for example, are an ancient ceramic composite consisting of a fired clay matrix bonding together filler materials—straw thousands of years ago, replaced by coarse sand in modern times. Other examples of composite ceramics include the heat-shielding tiles on spacecraft and the radar-absorbing materials used on "stealth" military aircraft.

Ceramics are divided into the "traditional" and the "advanced." Traditional ceramics are usually based on clay and silica, and are used for a wide variety of applications, including glass and glassware, porcelain and porcelain enamel (the white coatings on steel sinks, bathtubs, etc.), refractory materials, and structural clay (Carter & Norton, 2007). Monthly sales of structural clay in the form of bricks, roofing tile, and sewer pipe are valued at hundreds of millions of dollars, but the traditional ceramics market is dominated by glass, which is worth billions. A higher-tech application of traditional ceramics consists of crystallizing special glasses to make strong, vitreous, glass-ceramic composites, such as certain types of "unbreakable" dinner plates. The process is called "ceramming" the glass (Carter &

Norton, 2007). These products are known as whiteware, and in addition to dishes, they also include things like sinks and toilet bowls, which must have greater strength than traditional, glazed porcelain.

Advanced ceramics are primarily used in electrical applications as insulators, capacitors, substrates, and other uses (Carter & Norton, 2007). Other advanced ceramics are called engineering ceramics, and include wear-resistant parts such as bearings, cutting edges, or spray nozzles. Bioceramics are used for dental crowns and bone implants. High-temperature ceramic superconductors also fall into the area of advanced ceramics, and although significant growth in this application has been predicted, it has not yet materialized.

Oil and Gas: Clay is a critical ingredient in a fluid known as "drilling mud," which is needed to construct the wells that extract oil and gas from the ground. This mud consists of a watered-down, moderately syrupy liquid with a number of important functions in a drill hole. First, it is used to lubricate and cool the bit downhole to prevent heat buildup from friction while cutting the rock. Second, it transports the drill cuttings up and out of the borehole to keep it clear. Finally, it supports the sides of the borehole wall to prevent it from collapsing until steel casing can be set in place. When used with a downhole motor, the pressurized mud also supplies hydraulic power to turn the drill bit.

Drilling mud is more than just a simple mixture of clay and water. It contains various stabilizers, lubricants, corrosion inhibitors, polymers, viscosity control agents, and other compounds, most of which are highly specialized and closely guarded trade secrets. Mud can be water-based or oil-based, including synthetic oil. One of the common clays used in drilling mud is the swelling clay bentonite. Drillers use it to form a "cake" or seal on the bare rock walls that prevents drilling fluid leak-off into the formations. This is especially critical when drilling encounters a fractured zone, where a "loss of circulation" can cause large volumes of the downhole fluids to go missing and may result in a collapsed borehole.

Mud is typically pumped downhole through the inside of the drill pipe. It jets out around the cutter head through special vent holes, cooling the drill bit and sweeping away the drill cuttings (Fig. 3.7). The mud then returns to the surface through the annulus (the ring-like space between the outside of the drill pipe and the borehole wall). It is captured at the surface and stored in a pit or tank until it is recirculated. The drill cuttings are filtered out through a series of vibrating screens called shale shakers and are analyzed by an onsite geologist or mud-logging engineer to confirm the geology of the formation being drilled. This can be tricky because it is difficult to pinpoint the exact depth where the cuttings originated. It depends on the penetration rate of the bit and the travel time needed for the mud to return to the surface.

The unit density or "weight" of the drilling mud is important for controlling the stability of a wellbore, and it is monitored and adjusted carefully. This is called balanced drilling. Mud weight is adjusted by adding minerals, typically barite, into the mud mix to increase the weight, or water to reduce it. Mud engineers track the pore pressures in the rocks, and the fracture gradient or rock strength. If the mud weight is underbalanced, or too low, oil and gas in the rocks can escape prematurely into the borehole, or the borehole walls could collapse. On the other hand, if the mud

Fig. 3.7 A Polycrystalline Diamond Composite (PDC) drill bit used on the Niobrara Shale in Colorado. The raised "buttons" are the cutting surfaces, which are in fact an advanced ceramic. The holes on the hub are jets for the pressurized drilling mud to flush away cuttings and cool the bit. The copper coin in the center for scale is 2 cm (0.75″) in diameter. Photograph by Daniel J. Soeder

weight is too high, or overbalanced, it might exceed the hydraulic fracture gradient and crack the rock. This can result in lost circulation of drilling fluids. The frac gradient and pore pressure vary with location and can even vary with depth in the same hole. Mud engineering is a precise science that requires detailed planning and a thorough understanding of downhole conditions to maintain a proper borehole.

References

Adair, R. K. (2012, March). Another exchange on climate change. *Physics Today, 65*(3), p. 8.

Ahn, C. H., Dilmore, R., & Wang, J. Y. (2014). Development of innovative and efficient hydraulic fracturing numerical simulation model and parametric studies in unconventional naturally fractured reservoirs. *Journal of Unconventional Oil and Gas Resources, 8,* 25–45.

Bao, X., & Eaton, D. W. (2016). Fault activation by hydraulic fracturing in Western Canada. *Science, 354*(6318), pp. 1406–1409.

Brindley, G. W. (1955). Structural mineralogy of clays. *California Division of Mines Bulletin, 169,* 33–43.

Busch, A., et al. (2008). Carbon dioxide storage potential of shales. *International Journal of Greenhouse Gas Control, 2*(3), 297–308.

Busch, A., et al. (2009). Effects of physical sorption and chemical reactions of CO_2 in shaly caprocks. *Energy Procedia, 1*(1), 3229–3235.

Carter, C. B., & Norton, M. G. (2007). *ceramic materials science and engineering*. New York: Springer Science and Business Media.

Charpentier, R. R., & Cook, T. A. (2011). *USGS methodology for assessing continuous petroleum resources*. Reston, VA: U.S. Geological Survey.

Chen, R., et al. (2015). Comparison of isotopic and geochemical characteristics of sediments from a gas- and liquids-prone wells in Marcellus Shale from Appalachian Basin, West Virginia. *Applied Geochemistry, 60,* 59–71.

Chermak, J. A., & Schreiber, M. E. (2014). Mineralogy and trace element geochemistry of gas shales in the United States: environmental implications. *International Journal of Coal Geology, 126,* 32–44.

Curtis, J. (2002). Fractured shale-gas systems. *AAPG Bulletin, 86*(11), 1921–1938.

Dilmore, R., et al. (2015). *Experimental characterization of Marcellus Shale outcrop samples, and their interactions with carbon dioxide and methane*. Morgantown, WV: U.S. Department of Energy.

Engelder, T., & Lash, G. G. (2008, May). Marcellus Shale play's vast resource potential creating stir in Appalachia. *The American Oil and Gas Reporter*, p. 7.

Frazier, R. R. (2017). *Pennsylvania confirms first fracking-related earthquakes.* Available online at: http://www.alleghenyfront.org/pennsylvania-confirms-first-fracking-related-earthquakes/. Accessed 3 May 2017.

Godec, M., Koperna, G., Petrusak, R., & Oudinot, A. (2013). Potential for enhanced gas recovery and CO_2 storage in the Marcellus Shale in Eastern United States. *International Journal of Coal Geology, 118,* 95–104.

Goodman, A., et al. (2011). U.S. DOE methodology for the development of geologic storage potential for carbon dioxide at the national and regional scale. *International Journal of Greenhouse Gas Control, 5*(4), 952–965.

Goodman, A., et al. (2013). Comparison of methods for geologic storage of carbon dioxide in saline formations. *International Journal of Greenhouse Gas Control, 18,* 329–342.

Goral, J., Miskovic, I., Gelb, J. & Kasahara, J. (2015). *Pore network investigation in Marcellus Shale Rock Matrix: Paper SPE-176988-MS.* Brisbane, Australia: Society of Petroleum Engineers.

Guggenheim, S., & Koster van Groos, A. (2003). Experimental investigation of methane gas production from methane hydrate. *Geology, 31*(7), 653–655.

Hong, L., et al. (2016). Factors affecting the interaction of CO_2 and CH_4 in Marcellus Shale from the Appalachian Basin. *Journal of Unconventional Oil and Gas Resources, 14,* 99–112.

Hosterman, J. W., & Whitlow, S. I. (1980). *Munsell color value as related to organic carbon in Devonian Shale of the Appalachian Basin*. Reston, VA: U.S. Geological Survey.

Hosterman, J. W., & Whitlow, S. I. (1981). Munsell color value as related to organic carbon in Devonian Shale of Appalachian Basin. *AAPG Bulletin, 65*(2), 333–335.

IPCC. (2007). *Climate change 2007: The physical science basis. Working Group I contribution to the fourth assessment report of the Intergovernmental Panel on Climate Change.* Cambridge and New York: Cambridge University Press.

Jarvie, D. (2012). Shale resource systems for oil and gas: Part 1—Shale-gas resource systems. *AAPG Memoir, 97,* 69–87.

Kerr, P. F. (1955). Formation and occurrence of clay minerals. *California Division of Mines Bulletin, 169,* 33–43.

Kingery, W. D., Bowen, H. K., & Uhlmann, D. R. (1976). *Introduction to ceramics* (2nd ed.). New York: Wiley.

Kulga, B., Dilmore, R., Wyatt, C., & Ertekin, T. (2014). *Investigation of CO_2 storage and enhanced gas recovery in Depleted Shale gas formations using a dual-porosity/dual-permeability, multiphase, reservoir simulator*. Morgantown, WV: U.S. Department of Energy.

Lentz, R. D. (2003). Inhibiting water infiltration with polyacrylamide and surfactants: Applications for irrigated agriculture. *Journal of Soil and Water Conservation, 58*(5), 290–300.

Levine, J. S., et al. (2016). U.S. DOE NETL methodology for estimating the prospective CO_2 storage resource of shales at the national and regional scale. *International Journal of Greenhouse Gas Control, 51,* 81–94.

Matter, J. M., et al. (2016). Rapid carbon mineralization for permanent disposal of anthropogenic carbon dioxide emissions. *Science, 352*(6291), 1312–1314.

Middleton, R. S., et al. (2015). Shale gas and non-aqueous fracturing fluids: Opportunities and challenges for supercritical CO_2. *Applied Energy, 147,* 500–509.

Nuttall, B., Ebble, C., Drahovzal, J. A., & Bustin, R. M. (2005). *Analysis of Devonian black shales in Kentucky for potential carbon dioxide sequestration and enhanced natural gas production*. Lexington, KY: University of Kentucky.

Page, J. B. (1955). Role of physical properties of clays in soil science. *California Division of Mines Bulletin, 169,* 167–176.

Parikh, S. J., & James, B. R. (2012). Soil: The foundation of agriculture. *Nature Education Knowledge, 3*(10), 2.

Pask, J. A. & Turner, M. D. (Eds.) (1955). *Clays and clay technology: Proceedings of the First National Conference on Clays and Clay Technology* (1st ed.). San Francisco: State of California, Division of Mines.

Pierrehumbert, R. T. (2011, March). Infrared radiation and planetary temperature. *Physics Today, 64*(1), pp. 33–38.

Poore, R. Z., Williams Jr., R. S. & Tracey, C. (2000). *Sea level and climate: U.S. Geological Survey Fact Sheet 002–00.* Available online at: https://pubs.usgs.gov/fs/fs2-00/pdf/fs002-00/. Accessed December 2013.

Randolph, P. L., & Soeder, D. J. (1986). *Rock matrix analysis of eastern gas shale and western tight gas sands. Final report, October 1, 1983–December 31, 1984*. Institute of Gas Technology: Chicago, IL.

Romanov, V., et al. (2015). Mineralization of carbon dioxide: A literature review. *ChemBioEng Reviews, 2*(4), 231–256.

Schieber, J. (1994). Evidence for high-energy events and shallow-water deposition in the Chattanooga Shale, Devonian, central Tennessee, USA. *Sedimentary Geology, 93*(3–4), 193–208.

Schieber, J. (2010). *Common themes in the formation and preservation of intrinsic porosity in shales and mudstones—illustrated with examples across the Phanerozoic: Paper SPE-132370-MS* (pp. 1–10). Richardson, TX: Society of Petroleum Engineers.

Soeder, D. J. (1988). Porosity and permeability of Eastern Devonian Gas Shale. *SPE Formation Evaluation, 3*(1), 116–124.

Soeder, D. J. (2012). Shale gas development in the United States. In H. Al-Megren (Ed.), *Advances in natural gas technology* (pp. 3–28). Rijeka, Croatia: InTech.

Soeder, D. J. & Kappel, W. M., 2009. *Water resources and natural gas production from the Marcellus Shale: U.S. Geological Survey Fact Sheet 2009–3032.* Available online at: https://pubs.usgs.gov/fs/2009/3032/. Accessed 24 April 2017.

Soeder, D. J., Randolph, P. L., & Matthews, R. D. (1986). *Porosity and permeability of Eastern Devonian Gas Shale*. Chicago, IL: Institute of Gas Technology.

Soeder, D. J., et al. (2014). An approach for assessing engineering risk from shale gas wells in the United States. *International Journal of Coal Geology, 126,* 4–19.

Tao, Z., & Clarens, A. (2013). Estimating the carbon sequestration capacity of shale formations using methane production rate. *Environmental Science and Technology, 47*(19), 11318–11325.

U.S. Department of Energy. (2015). *Carbon storage Atlas* (5th ed.). Washington, DC: U.S. Department of Energy.

U.S. Energy Information Administration. (2017). *Annual Energy Outlook 2017: USEIA report DOE/EIA-0383(2017).* Available online at: https://www.eia.gov/outlooks/aeo/index.cfm. Accessed 23 April 2017.

U.S. Geological Survey. (2016). *Induced earthquakes.* Available online at: https://earthquake.usgs.gov/research/induced/. Accessed 3 May 2017.

Vermylen, J. P. (2011). *Geomechanical studies of the Barnett Shale, Texas, USA [Ph.D. dissertation]*. Stanford, CA: Stanford University, SRB (Vol. 125).

Watson, T. L., & Bachu, S. (2009). Evaluation of the potential for gas and CO_2 leakage along wellbores: Paper SPE-106817-PA. *SPE Drilling & Completion, 24*(1), 115–126.

Zoback, M. D., & Gorelick, S. M. (2012). Earthquake triggering and large-scale geologic storage of carbon dioxide. *Proceedings of the National Academy of Science of the United States of America, 109*(26), 10164–10168.

Chapter 4
Clay Mineralogy

Bret H. Howard and Jonathan W. Lekse

Abstract When discussing clays, it is important to understand what they are, their origins, their chemical and physical properties, and their crystal structures. Clay minerals, a subgroup of the phyllosilicates, are a major and important type of mineral in the Earth's crust. Phyllosilicates exist over a crystal-size range from traditional clay-size range to very large crystals. However, in terms of their impact on everyday life, small grain-sized geomaterials are of most importance. Chemical weathering of primary minerals is one of the processes of principal interest when fine-grained crystalline hydrous aluminosilicates are considered. There are a variety of detailed approaches for the orderly classification of clay minerals, which is outside the scope of this work; for simplicity, the two principal layer types and three clay mineral families—kaolin, smectite, and chlorite—are discussed here. Importance of pillared and lateritic (a source of rare-earth elements) clays is also highlighted. While there is no comprehensive nomenclature for mixed-layer clays, statistical treatment of the binary mixed systems can be simplified by assuming three standard sequences: random, ordered, and segregated. The primary analytical tool used to sort out all these structural variations is powder X-ray diffraction. Though the structure of clay will inform many of the physical properties and allows for differentiation of the various clay minerals, substitution into the individual clay layers can alter the base physical properties and provides variation within the clay families. For more precision in clay mineral identification, additional analytical information is required (as further discussed in this book).

Clay materials have had a large impact on the history of human civilization stretching all the way back in time to the darkest days of our hunter-gatherer ancestors. The first definition of "clay" or *lutum* (Latin) as related to "earth" in the earth-air-fire-water system was formalized by Agricola (1546) but only since the advent of X-ray diffraction studies have satisfactory mineral classification groupings

B.H. Howard (✉) · J.W. Lekse
U.S. Department of Energy, National Energy Technology Laboratory (NETL), Pittsburgh, USA
e-mail: Bret.Howard@netl.doe.gov

© Springer International Publishing AG 2018

V. Romanov (ed.), *Greenhouse Gases and Clay Minerals*, Green Energy and Technology, https://doi.org/10.1007/978-3-319-12661-6_4

been obtained. The term "clay mineral" may refer to phyllosilicate minerals and to minerals which impart plasticity to clay and which harden upon drying or firing. It is useful when applied to clay constituents, though many accessory minerals that occur in clay are not characteristic of bulk clay properties (Mackenzie, 1962).

The exact definition of "clay" depends on the discipline: geologists associate it with grain size smaller than 2 μm, engineers with plasticity, and ceramicists with hardening upon firing. Indeed, in many literature sources, one can find clay defined by not only chemistry and structure but also by particle size. This is due to the processes that lead to the formation of many natural clay deposits resulting in relatively small particles. In rock terms, a conventional size limit for a clay particle is less than two microns. However, many clay minerals actually exist over a large crystal size range from within the clay size definition to orders of magnitude larger, depending on the mechanism of formation and growth. However, in terms of their impact on everyday life, the small grain sized materials are probably of most importance. In order to facilitate a greater understanding of where the physical properties of clays originate, this work is going to define and differentiate clays by their chemistry and structure. It is predominantly the atomic structure of these materials that will dictate the physical properties that are observed at a macro scale.

4.1 Origins of Clay

Clay minerals are a major and important type of mineral in the Earth's crust. They make up a large portion of the crust, estimated at up to 10% by volume (Ronov & Yaroshevsky, 2013). When discussing clay it is important to understand where it comes from. To do that, we must first define the term mineral. A mineral is a naturally occurring solid inorganic (usually) substance with a definite chemical formula and an ordered atomic structure. A mineral is different from a rock which does not necessarily need to be defined by a specific chemical formula. In fact, many rocks contain multiple minerals. For example, the very familiar rock, granite, often seen in counter tops, is comprised of three principal minerals: feldspar, mica, and quartz. Minerals can be classified into two general categories; primary and secondary minerals. Primary minerals are formed by geologic processes, typically the crystallization of molten lava under various temperature/pressure regimes. Many of these minerals are found in igneous rocks such as the granite just mentioned. Secondary minerals form from the alteration of primary minerals and other secondary minerals through a variety of processes such as metamorphic alteration and chemical weathering.

The chemical weathering of primary minerals is one of the processes of principal interest when fine-grained crystalline hydrous aluminosilicate clay minerals are considered. During chemical weathering, water breaks down the primary minerals through oxidation and hydrolysis. In addition to water, oxygen and biological agents can also contribute to the weathering process. The mechanism of formation accounts for the small crystal size of many clay minerals. These types of clay minerals are

crystallized from chemically released building blocks, not mechanically reduced to small size from a larger source crystal (Eberl, 1984). In clay deposits, the chemical weathering process often results in fine-grained mixtures of one or more of the clay minerals and residual metal oxides/hydroxides. Fine-grained illite, chlorite, and vermiculite can be formed via mild weathering of primary aluminosilicate minerals, whereas kaolinite and residual metal oxides/hydroxides are typically produced by intense weathering. Intermediate weathering conditions lead to formation of smectite (montmorillonite). In each case, clay genesis (Fig. 4.1) is accompanied by the removal in solution of such elements as K, Na, Ca, and Mg. Also, clay deposits often contain organic matter and detrital mineral particles such as quartz. These deposits are not necessarily homogenous, which can lead to difficulties in later applications. Additionally, these clay deposits are usually not mineralogically static (Hazen et al., 2013; Srodon, 1999). As they are buried, under relatively mild temperature/pressure conditions they can experience diagenesis, converting into other clay minerals and, under more extreme conditions, can be metamorphosed into other minerals completely.

Clay minerals are also formed through a variety of other mechanisms (Eberl, 1984). These can include crystallization from a melt, for example, the mica in a granite as mentioned above. Other important formation and growth mechanisms include medium-grade metamorphic alteration, crystallization from hydrothermal systems and growth in pegmatites. These growth mechanisms usually result in coarse-grained crystals ranging from microns to hundreds of millimeters.

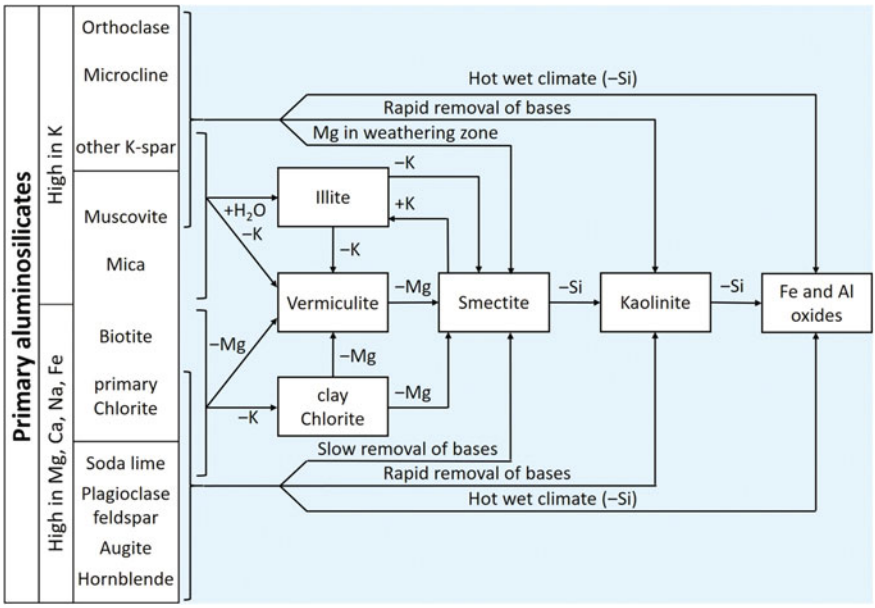

Fig. 4.1 Paragenesis of clay minerals (common weathering schemes) (Brady & Weil, 2010)

Clay minerals can also convert into other clay minerals when the proper weathering conditions are present. Heat-induced (at temperatures > 200 °C) transformation of low-charge smectite (montmorillonite) to high-charge smectite (a.k.a. beidellization) is frequently observed as the first step in transformation of smectite-to-illite (illitization process). In geothermal fields, beidellitic and saponitic smectites are formed in the hot fluids in volcanic rocks and then transformed to illite-smectite mixed layers and clay-sized chlorite. Also, steep thermal gradients (50–130 °C) during the early (< 50 years) radioactive-waste repository evolution, when the near-field is being water re-saturated, may induce internal mass redistribution (i.e., dissolution and re-precipitation of accessory minerals) in the smectite-rich bentonite buffer (refer to Chap. 3) resulting in some cementation of the bentonite matrix (Leupin et al., 2014). In the long run (100–10,000 years), if the elevated temperature persists, smectite may undergo mineralogical changes: e.g., transformation of smectite-to-illite may be facilitated by increased temperature and potassium activity (Srodon, 1999).

4.2 Crystal Structure of Clay

There are a variety of detailed approaches for the orderly classification of mineral species including clay minerals. Probably the best known is the Dana classification which is based on both chemistry and structure (Gaines et al., 1997). Clay minerals generally fall into Dana Class 71-Phyllosilicate Minerals. Clay minerals are divided into different principal groupings or families based primarily on their structural details. Discussion of all the groups, divisions, and specific clay minerals is outside the scope of this work; therefore, for simplicity, the two principal layer types and three important clay mineral families from the two types, kaolin, smectite, and chlorite, will be discussed here. The selection of these three mineral groups will become apparent when their structures are defined below. There are many detailed reviews of clay mineral structures available in the literature (Moore & Reynolds, 1997; Bailey, 1984, 1988; Brown & Brindley, 1980) that go into great detail discussing the many structural variations and subtle nuances of clay structures that result in the over 50 clay minerals currently recognized by the International Mineralogical Association.

Understanding both the similarities and differences between the multiple clay minerals fundamentally starts with an examination of the crystal structures of these materials. The clay mineral groups all have layered structures so are termed phyllosilicates. These layered structures are often apparent in clay mineral morphologies and can be observed directly by analytical techniques such as scanning electron microscopy for the micron size-range clays (Fig. 4.2) and simply by visual examination for hand-sized specimens of minerals such as muscovite (Fig. 4.3). The composition and number of these layers is what differentiates one clay grouping from another. There are two principal components of each layer: tetrahedral and octahedral sheets. These types of sheets are named for the coordination

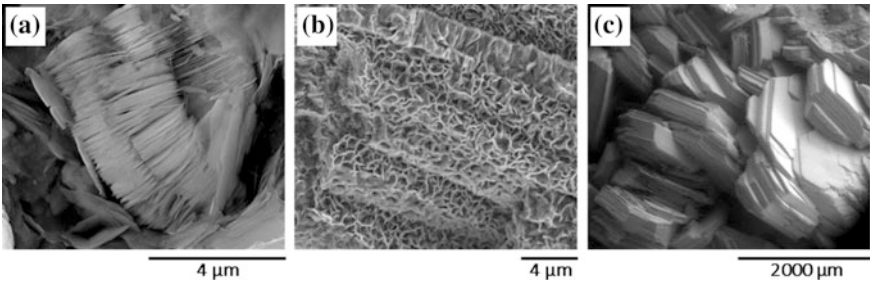

Fig. 4.2 **a** Kaolin group clay—Kaolinite from Jackson County, Mississippi; **b** Smectite group clay—Montmorillonite from Apache County, Arizona; **c** Chlorite group clay—Clinochlore from Marki Khel, Nangarhar Province, Afghanistan; secondary electron images obtained using FEI Quanta 600F SEM

Fig. 4.3 Muscovite (*dark* crystals) exhibiting the phyllosilicate sheet structure. Specimen (≈6 cm size) is from the North American Emerald Mine, Hiddenite, Alexander County, North Carolina, USA

of the cations that comprise them. For example, typical tetrahedral sheets are composed primarily of silicon atoms that are coordinated to four anions which form the corners of a tetrahedron. Similarly, the octahedral sheets typically comprise aluminum atoms coordinated to six anions which form the corners of an octahedron. The ratio of tetrahedral-to-octahedral sheets as well as the amount of

Table 4.1 Abundances of common elements in Earth's crust (Evangelou, 1998)

Element	Percent in earth's crust
O	46.5
Si	27.6
Al	8.1
Fe	5.1
Ca	3.6
Na	2.8
K	2.6
Mg	2.1
Ti	0.6
P	0.12
Mn	0.09
S	0.06
Cl	0.05
C	0.04

elemental substitutions into the sheets are what gives rise to the differences between the two primary clay families. Each site, either tetrahedral or octahedral, can be occupied by several different cations; however, the most common elemental components are Si^{4+} on the tetrahedral sites and Al^{3+} on the octahedral sites. This is predictable when one considers that many clays are produced by the weathering of rocks and the global crustal abundance of silicon and aluminum is right behind oxygen (Table 4.1).

Though the sheets are primarily composed of silicon and aluminum, there are frequent substitutions of varying amounts of other elements into one or both of the sheet types. When either silicon or aluminum is replaced by a cation with a different valence, the result is a permanent charge on the sheet. The most common type of substitution in naturally occurring clays is a lower valence cation substituting for silicon or aluminum, which results in negatively charged sheets. Nature tends to eliminate or compensate for permanent charges and clays are no exception with the permanent charge being compensated for through cation occupations in either the interlayer or, in some cases, within the structure of the layers themselves. The interlayer is the space between the layers in the clay structure. The amount of structural substitutions that are not compensated for by other substitutions within the structural units results in an overall negative layer charge that is usually compensated for by cations/hydrated cations occupying the interlayer. These interlayer-charge-compensating cations are usually mobile and can be exchanged for other cations. The experimentally measurable amount of exchangeable cations is defined (Chap. 7) as the cation exchange capacity (CEC) often expressed as milliequivalents of positive charge per 100 g of dried clay (meq/100 g). Because exchangeable cations can also occupy sites other than the interlayer sites, essentially all clays have some degree of CEC. The CEC strongly influences the physical

Table 4.2 Comparison of several common clays

Name (subgroup)	Chemical formula (Gaines et al., 1997)	Layer type (Guggenheim et al., 2006)	CEC (Evangelou, 1998)
Kaolinite (Kaolin)	$Al_2Si_2O_5(OH)_4$	1:1	3–15
Montmorillonite (Smectite)	$(Na, Ca)_{0.3}(Al, Mg)_2(Si_4O_{10})(OH)_2 \cdot n(H_2O)$	2:1	60–100
Clinochlore (Chlorite)	$(Mg, Fe^{2+})_5Al(AlSi_3O_{10})(OH)_8$	2:1	10–30
Illite (Mica)	$(K, H_3O)(Al, Mg, Fe)_2(Si, Al)_4O_{10}[(OH)_2 \cdot (H_2O)]$	2:1	20–40
Vermiculite (Vermiculite)	$(Mg, Fe^{2+}, Al)_3(Al, Si)_4O_{10}(OH)_2 \cdot 4(H_2O)$	2:1	110–160

properties that are observed in the clay minerals, especially the ability to swell and degree of swelling possible in the presence of water or water vapor.

While the composition of the individual sheets is important to the properties of the clay, the ratio of tetrahedral-to-octahedral sheets in each layer is what truly differentiates the clay minerals from one another (Table 4.2). Layers can be defined as structural units that are composed of tetrahedral and octahedral sheets, in varying ratios, coordinated through corner-shared anions. Two basic stacking arrangements are commonly defined. A layer unit with one tetrahedral sheet and one octahedral sheet is commonly referred to as a 1:1 layer type and one with two tetrahedral sheets and one octahedral sheet is commonly referred to as a 2:1 layer type. A third layer unit was used in the past and often encountered in the literature. It consists of two tetrahedral sheets and one octahedral sheet per layer with an additional octahedral sheet associated with the layer, commonly referred to as a 2:1:1 or 2:2 layer type. This layer type is now considered a variation of the 2:1 family (Guggenheim et al., 2006). The structures of 1:1 and 2:1 layer types as well as the 2:2 are illustrated in Fig. 4.4. Not only are the structures of these materials affected by the differing layer arrangements, but the mineral properties (such as surface functional groups, interactions with solution species, ability to swell, and surface charge) can also be quite different.

Further division of clay minerals into subgroupings is based on cation site occupancy within the octahedral sheets. The cationic sites can be occupied by divalent and/or trivalent cations, commonly Al^{3+}, Mg^{2+}, and/or Fe^{3+} although other cationic species are possible. Two octahedral designations are defined based on the cation-to-anion ratio. If all sites are filled by divalent cations, the sheet is referred to as trioctahedral. At the other extreme, trivalent cations can occupy two-thirds of the sites which is designated as a dioctahedral sheet. Figure 4.5 schematically illustrates these two sheet geometries. Of course, occupancies between the two extremes are also possible. Table 4.3 summarizes the various groups and specific clay minerals organized by layer type, octahedral sheet type, and layer charge. Typically observed interlayer species are also listed.

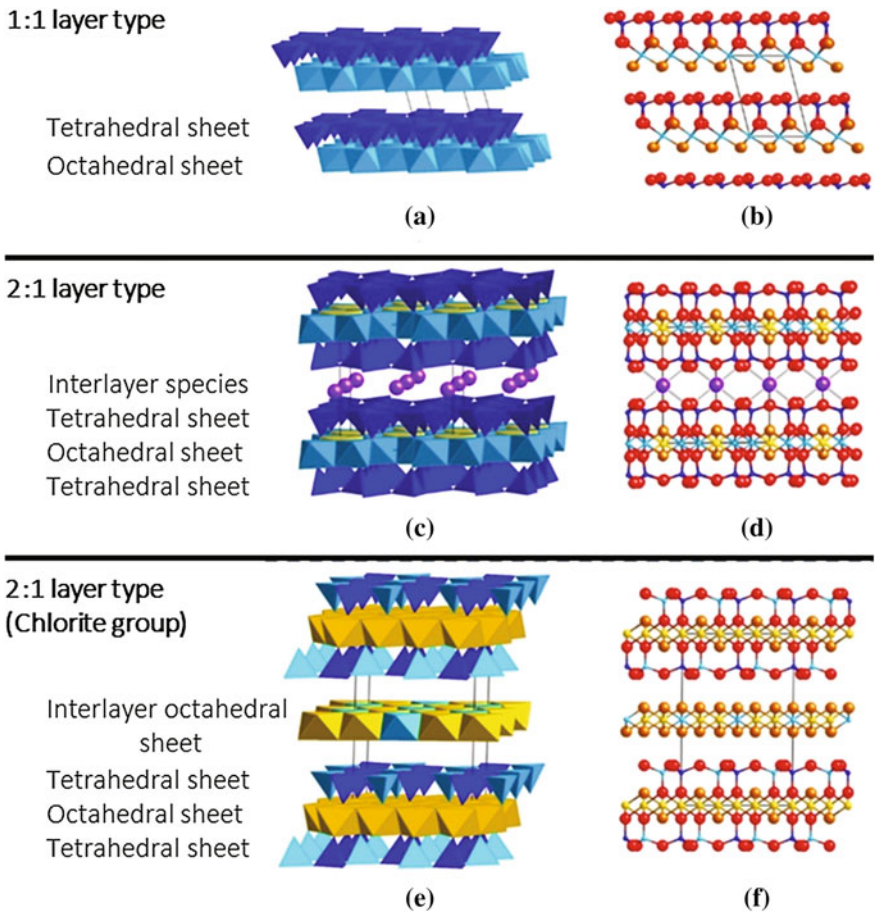

Fig. 4.4 Simplified structures of the 1:1 layer type, 2:1 layer type and the 2:1 layer type with an interlayer octahedral sheet (also known as a 2:1:1 or 2:2 layer type)

Just to make things even more interesting, Mother Nature likes to mix it up. Mixed layer type stacking sequences occur because the layers comprising many clay minerals are similar enough in structure that they can substitute for each other in the crystal stacking sequence. These clays are often referred to as mixed-layer or interstratified clays. Typically only two types of clay layers are involved, although there can be more, and the sequence can be repeating or random. If the sequence is regular and repeating, a unique mineral name is often applied such as rectorite (alternating layers of dioctahedral mica and dioctahedral smectite) (Moore & Reynolds, 1997). For randomly interstratified clays, if enough information is known of the composition, they are often referred to by a compound name designating the clay layers comprising the structure, for example illite/smectite. It has been proposed that interstratified clays often form as a clay evolves from one end member

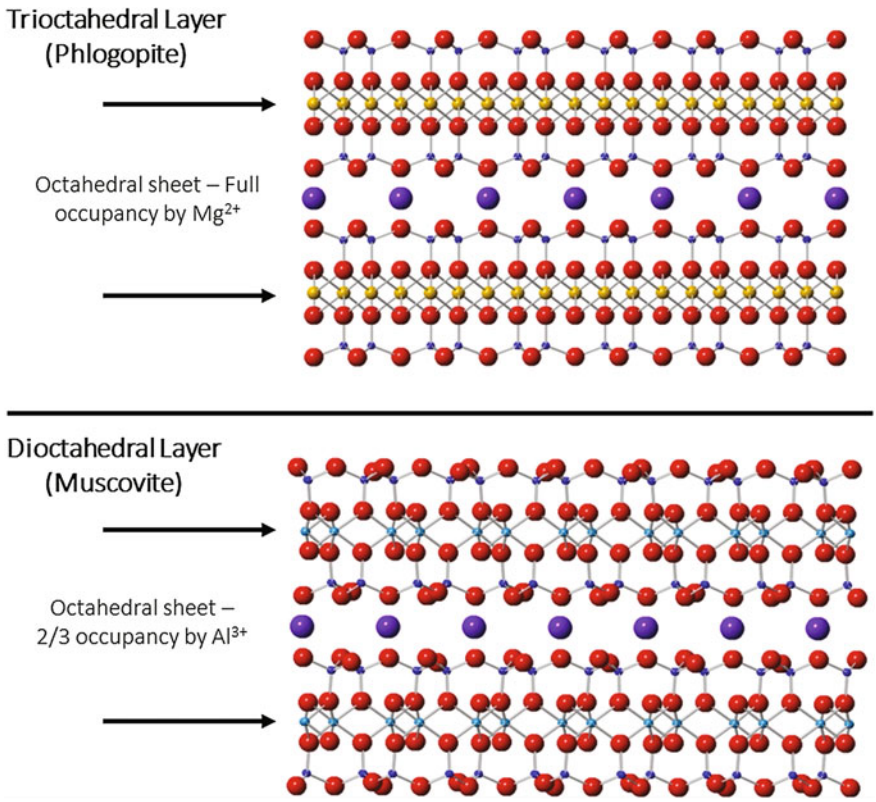

Fig. 4.5 Simplified structures of tri- and di-octahedral sheets. The specific octahedral occupancy sites are indicated by the arrows

clay mineral into another through alteration associated with the burial process (Srodon, 1999). For example, a correlation was observed between the percentage of illite interlayered with smectite and the depth of burial.

Another variation frequently found in clay structure is associated with the perfection of the alignment of the layers in the stacking sequence. The layers can be rotated and/or translated relative to each other in the sequence. This type of disorder can be random or systematic and is related to the strength of the interaction between the layers. Weak interaction resulting in more layer separation tends to result in more stacking disorder. No stacking alignment between layers is termed turbostratic disorder and is common in smectites due to the weak attraction between layers and large layer separations. When there is a systematic order to the layer displacements in the stacking sequence, polytypes result. Polytypes are common in micas due to the strong layer attraction with non-hydrated cations between the layers, commonly potassium, and small interlayer separation. A simple way to look at polytypism in micas is to imagine the K^+ cations occupying the regularly spaced hexagonal holes

Table 4.3 Classification of common clay minerals /hydrous phyllosilicates (after Guggenheim)

Layer type	Group	Layer [1] charge	Interlayer species	Octahedral [2] sheet type	Representative clay mineral
1:1	Serpentine-kaolin	≈0	None, water	Tri	Lizardite, amesite
				Di	Kaolinite, dickite, nacrite
2:1	Talc-pyrophyllite	≈0	None	Tri	Talc
				Di	Pyrophyllite
	Smectite	≈0.2–0.6	Hydrated cations, exchangeable	Tri	Saponite, hectorite
				Di	Montmorillonite, nontronite
	Vermiculite	≈0.6–0.9	Hydrated cations, exchangeable	Tri	Trioctahedral-vermiculite
				Di	Dioctahedral-vermiculite
	Micas	≈0.6–2.0	Non-hydrated cations (+1, +2), non-exchangeable	Tri	Lepidolite, phlogopite, illite
				Di	Muscovite
	Chlorite	Variable	Octahedral sheet, hydroxide	Tri	Clinochlore, chamosite
				Di	Donbassite
2:1	Regularly interstratified	Variable	Regularly interstratified	Tri	Corrensite
				Di	Rectorite

Note Table is not exhaustive
[1]Approximate negative layer charge
[2]*Tri* trioctahedral, *Di* dioctahedral

at the surfaces of the tetrahedral sheets of the layer. These cations act as "pins" limiting the rotational orientations of the layers relative to each other to 60° increments resulting in specific ordered stacking sequences. These specific stacking arrangements are given polytype identifiers. There are many detailed discussions of polytypism in micas and other clays available (Brown & Brindley, 1980; Moore & Reynolds Jr., 1997).

4.2.1 Clay Mineral Identification

The primary analytical tool used to sort out all these structural variations is powder X-ray diffraction (XRD). XRD utilizes X-rays to probe the details of the crystal structures of clay minerals. Detailed information on the XRD technique is widely available (Moore & Reynolds Jr., 1997; Klug & Alexander, 1974) and the specifics of utilizing XRD for clay mineral identification are very well documented (Brown & Brindley, 1980; Moore & Reynolds Jr., 1997). For more precision in clay mineral identification, additional analytical information is usually required (see Chap. 5 for details) such as chemical composition, infrared analysis, morphological examination by electron microscopy (SEM/TEM) with elemental information obtained by energy dispersive spectroscopy (EDS). At a basic level of characterization, the layer stacking arrangements in clays result in specific layer stacking repeat units in the crystal structure which are observed as diagnostic XRD peak ranges for the clay groups, commonly referred to as the basal spacing. Depending on the clay, the basal spacing may be more or less constant or, for expanding clays like smectites, the basal spacing is variable depending on the degree of hydration.

An "individual or free" particle which yields a single-crystal, 2D hk0 selected-area electron-diffraction pattern (a hexanet reciprocal lattice) is commonly defined as a 'fundamental particle' (fp) (Nadeau, Wilson, McHardy, & Tait, 1984) —not to be confused with the XRD usage of "primary particle"—even though substantial uncertanty is expressed over whether such particles are primary crystallization products or artifacts of sample preparation (Ahn & Buseck, 1990), which was a subject of heated debates fueled by different interpretations of XRD and high-resolution TEM data (Chap. 5). Fundamental particles can be considered as fragments (sub-units) of larger coherent sequences, one-dimensional MacEwan crystallites (MacEwan, 1958) formed as fp stacks (aggregates where the fp interfaces behave like smectite interlayers).

Miller indices form a notation system in crystallography (Miller, 1839) for crystals/Bravais (1850) lattices. They are whole numbers, written (hkℓ)—negative integers are written with a bar placed above the symbol—and denoting the family of planes orthogonal to [h $\boldsymbol{a}^* + k\,\boldsymbol{b}^* + \ell\,\boldsymbol{c}^*$]; *where* $\boldsymbol{a}^*$, $\boldsymbol{b}^*$, and $\boldsymbol{c}^*$ are the basis of the reciprocal-lattice vectors. The plane is not always orthogonal to the linear combination of direct lattice vectors because the reciprocal lattice vectors need not be mutually orthogonal. When the indices describe a crystal face, they are written without brackets; when they describe a crystal form, they are enclosed in brackets: (h, k, ℓ) represents a point; [hkℓ]—a direction; <hkℓ>—a family of

directions; (hkℓ)—a plane; {hkℓ}—a family of planes. When using Bragg's law, it is important to distinguish between lattice and reflecting planes—Laue indices for reflecting planes are written without brackets.

If a crystal structure exactly repeats its basal reflections at periodic spacing, the produced X-ray diffraction pattern obeys Bragg's law:

$$\ell\lambda = 2d_{00\ell} \sin\,\theta \tag{4.1}$$

where λ is the wavelength of incident X-ray radiation and θ is the scattering/observation angle that satisfies the condition for strongest constructive interference; the basal distances $d_{00\ell}$ occur as integral series, referred to as a rational series of reflections. Bailey (1982) suggested that any such series of at least ten *00ℓ* spacings—unless calculations show that intensities of odd suborders are too low to be observed—should be considered a manifestation of a discrete phase, if a coefficient of variation (CV) for ($\ell \times d_{00\ell}$) values is less than 0.75%. While there is no comprehensive nomenclature for mixed-layer clays, statistical treatment of the binary mixed systems can be simplified by assuming three standard sequences: random, ordered, and segregated. The random sequence is defined by equal junction probabilities of layer type A (the smaller d-spacing mineral/phase) being followed by any layer (type A or B): $P_{A\cdot A} = P_{A\cdot B}$ which are then equal to the relative amount/probability of finding layer type A (i.e., P_A). The ordered sequence is specified by the case when $P_{A\cdot A} = 0$, if $P_A < 0.5$ or $P_{B\cdot B} = 0$ if $P_A > 0.5$. The segregated sequence is specified by the condition of $P_{A\cdot A} = 1$, if $P_{A\cdot A} > P_A$. Statistics for non-nearest neighbors is more complicated but follows the same logic with an addition of the parameter *Reichweite* (German: reach/range) or *S* to define the most-distant number of layers that affect a probability of the final layer; for example, the R1 ordering scheme represents the nearest-neighbor layer only dependence. The Fourier series technique of predicting XRD patterns for interstratified clay minerals requires the calculation of a matrix of frequency factors—overwhelmingly, by using a quasi-homogeneous model that assumes Markovian statistics (Reynolds, 1980)—but it can be simplified for faster computing (Bethke & Reynolds, 1986).

Figure 4.6 illustrates an experimental XRD pattern for a system that is best modeled by a combination of a predominant (81 wt%) structure and a binary mixed-layer structure that results from the random interstratification of 0 W and 1 W layers (70%/30%). Standard deviation of the departure from rationality of the *00ℓ* reflection series in such systems was proposed to qualitatively characterize heterogeneity of clay minerals (Ferrage, Lanson, Sakharov, & Drits, 2005). Junction probability diagrams conveniently illustrate the overall variation of layer arrangements in the mixed-layer minerals. Figure 4.7 shows the R1 layer arrangements in I/S (illite-smectite) system (Bethke, Vergo, & Altaner, 1986). Most I/S samples show *Reichweite* 0, 1, or 3 (i.e., R0, R1, or R3) ordering by XRD, but the TEM analysis may yield differing results (Chap. 5).

Diagnostic treatments are often used to modify the basal spacing which can help in the identification of clay groups. Heat treatments can be used to remove interlayer water and controlled exposure to organic materials such as ethylene glycol can

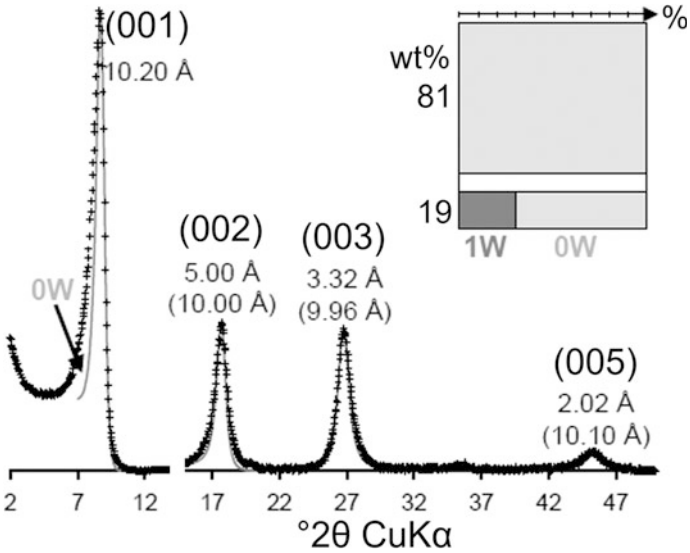

Fig. 4.6 Strategy used to fit XRD patterns: *light grey*—0 W layer hydration fit to experimental data (Ferrage et al., 2005); insert—two-phase (0 W and mixed 0 W/1 W) best-fit model

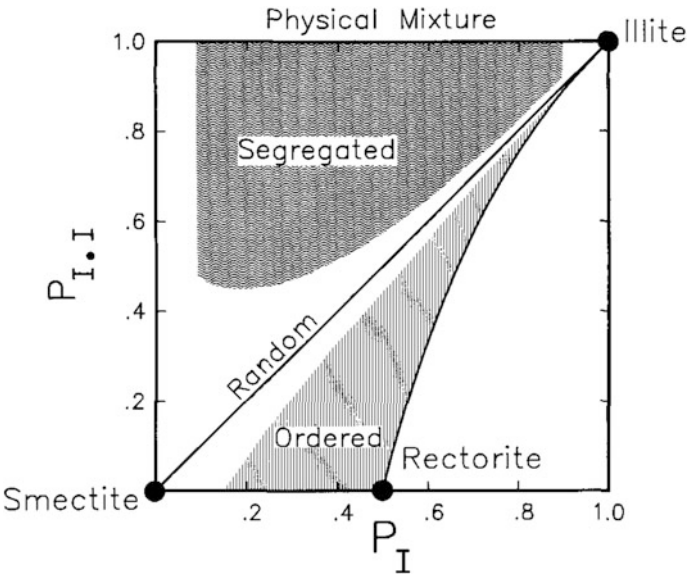

Fig. 4.7 Junction probability diagram showing pathways for smectite (S) transformation to illite (I); the direct transitions to rectorite represent the ideal ordering whereas either $P_{I \cdot I}$ or $P_{I \cdot S}$ equal zero—reproduced with kind permission of The Clay Minerals Society, publisher of *Clays and Clay Minerals* (Bethke, Vergo, & Altaner, 1986)

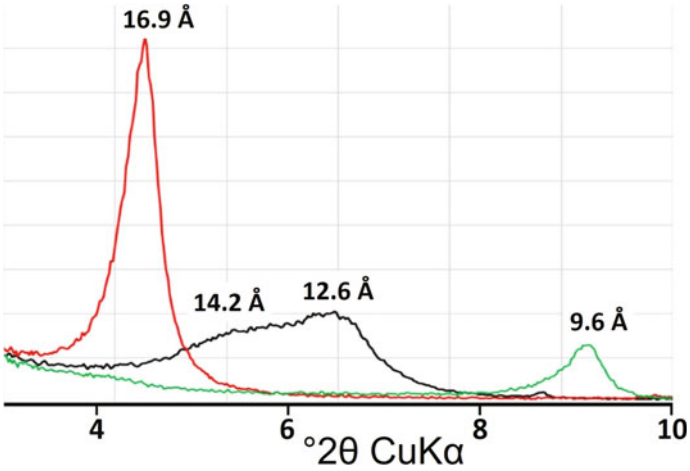

Fig. 4.8 XRD scan of the (001) peak of a Wyoming montmorillonite (SWy-3): *black*—in ambient air (double-peak: 12.6 Å—one interlayer-H_2O layer; 14.2 Å—two interlayer-H_2O layers); *green* (color version)—after dehydration at 400 °C (collapsed to 9.6 Å—no interlayer-H_2O); *red*—after ethylene glycol treatment (expanded to 16.9 Å)

give a specific basal spacing expansion. Ethylene glycol treatment can be used to fix the layer-to-layer space in swelling clay samples with basal spacing sensitive to ambient humidity (Steudel et al., 2017) and is especially useful to distinguish smectites from other clays. For example, montmorillonite has a basal {001} spacing in the range of 14–15 Å depending on the degree of hydration, however, after ethylene glycol treatment, the basal {001} spacing shifts to about 16.9 Å and becomes much sharper (Fig. 4.8).

NEWMOD (Reynolds & Reynolds, 1996) software and its adaptations are commonly employed as the standard method for quantitatively evaluating one-dimensional XRD patterns of oriented mixed-layer clay-mineral specimens, given a set of parameters that describe instrumental factors, chemical composition and structural parameters (crystallite size distribution, the nature of ordering, proportions of the different layer types, etc.) of the system. Such computations can be particularly difficult for systems with flocculation at the edges or turbostratic arrangements of the sheets (Chap. 5).

4.2.2 Common Clays—Characteristic Attributes Arising from Their Structure

Kaolinite, a member of the kaolin-serpentine group, is a 1:1 layer type clay. This means that in each clay layer there is one tetrahedral sheet and one octahedral sheet. In general, kaolinite has very little or no substitutions in either the tetrahedral or

octahedral sheets, so the layers generally have very little charge that needs to be balanced. For this reason, the interlayer width in most kaolinite group members is relatively small and stable, and it is rare to find any ions or molecules in the interlayer of these minerals. As a consequence, most members of the kaolin group have very low shrink-swell capacity. This is also evidenced in the low CEC for 1:1 clays which tend to be in the range from 3 to 15 (Table 4.2).

The chemical and physical characteristics resulting from kaolinite's structure govern its properties, and subsequently, its industrial applications. The most common uses for kaolinite are in paper coatings and ceramics. Since kaolinite typically has very few substitutions in its structure, it can have high brightness (whiteness) which is a desirable characteristic for applications in the paper industry as well as in the production of high-quality ceramics. The property of very low swelling results in lower viscosity dispersions at high loadings which is a valuable characteristic when it is used in coatings. This property also helps reduce shrinkage during ceramic firing. It is also used as a high-quality filler component in a variety of products including paints, polymers, and pharmaceuticals. In some applications, it is used as mined, however, it is often chemically modified to improve dispersibility, especially in organic materials and enhance suspension stability. There are a vast number of other applications of kaolinite in addition to these (Murray, 2000).

Smectite group clays, of which montmorillonite is the best-known member, are 2:1 clays that consist of two tetrahedral sheets sandwiching one octahedral sheet. Originally, montmorillonite was a specific clay mineral that was discovered in Montmorillon (France) and named by Mauduyt (1847). However, it is currently used both as a group name for all clay minerals with an expanding lattice, except vermiculite, and as a name of the representative mineral of the smectite group (low-charge dioctahedral smectite). Many 2:1 clays are known for their swelling potential and for the presence of cations and water in the interlayer of these materials. For example, in an idealized montmorillonite clay each unit of two tetrahedral and one octahedral layers is separated by a layer of sodium cations. Smectite clays tend to have the largest CEC and greatest potential for expanding the interlayer width and associated basal distance. This structural flexibility, especially in the case of montmorillonite, has resulted in a great interest in these clays for a variety of applications such as sorbents, catalysts, fillers, and drilling mud additives.

Interestingly, the capability of these clays to absorb molecules and expand their interlayer is affected by the location of substitution in the layers. Substitution occurring in one of the tetrahedral sheets will restrict the interlayer expansion. This is due to the physical proximity of the tetrahedral layers to the charge compensating cations. When one examines the structure of a typical 2:1 clay, the tetrahedral sheets are adjacent to the interlayer while the octahedral sheets are bordered on both sides by the tetrahedral sheets. When a substitution occurs in the tetrahedral sheet, the resulting charge-balancing-cation can arrange itself very close to the induced negative charge. The induced charge is also more localized due to there not being as many oxygen anions nearby to share the excess charge.

Unlike substitution into the tetrahedral sheets, substitution in octahedral sheets results in a more diffuse induced charge due to the greater distance between the substituted atom and the charge compensating anions as well as the presence of six oxygen atoms (instead of four) to share the excess charge. As a result of the more diffuse nature of the charge, the substitution into octahedral layer results in clays that have a greater capacity for expansion.

Montmorillonite, the most common clay of the group and the one that probably has generated the most interest, has a very flexible structure. The sodium and calcium varieties, referring to the primary exchangeable cationic species, are the common naturally occurring forms. However, the exchangeable cations can be replaced by many other cations, simple metal cations through complex organic cations, enabling control of chemistry, expandability, surface area and structure.

The expansion of montmorillonite and other clays in the presence of humidity/water have been studied for many years (MacEwan & Wilson, 1980; Moore & Hower, 1986; Moore & Reynolds Jr., 1997). Under controlled humidity conditions with different cations exchanged into the same clay, specific basal spacing expansions were noted. Several factors influence the observed expansion behavior including the charge and size of the predominant interlayer cation and the location (tetrahedral versus octahedral sheet) and concentration of the anionic sites. A study by Moore and Hower (1986) using Na-montmorillonite indicated the (almost) discrete spacings observed were due to integral layers of water, depending on the relative humidity present (see Chap. 7 for details). Of course, to complicate this, at low relative humidity, an interstratified structure can form where some interlayers are occupied by a single water layer and some are not, thus resulting in intermediate basal spacing values. Interstratification of montmorillonite with other nonexpanding clay layers such as illite can also lead to variations in the observed hydration basal expansion. Due to the importance of the expanding characteristics of smectites for various industrial applications and the problems that can arise when it is encountered in the natural world such as during road construction, there have been many studies of the interactions of water with these clays (Brown & Brindley, 1980; Moore & Reynolds Jr., 1997).

The exceptionable expandability of the smectite structure and freely exchangeable cations enables the synthesis of a collection of modified clay materials with useful properties—the pillared clays. The pillaring process has been recognized, studied, and utilized for many years, and many reviews have appeared in the literature (Vicente, Gil, & Bergaya, 2013). These materials are synthesized relatively easily by exchanging a bulky cation for the existing simple cation, typically the Na^+ of a Na-montmorillonite. The bulky cation acts as a prop or pillar holding the clay layers apart after drying, resulting in a micro- or meso-porous structure as shown in Fig. 4.9. An early pillared clay study (Barrer & MacLeod, 1955) reported materials preparation using bulky organo-ammonium cations exchanged into a montmorillonite. The resulting pillared clays had increased basal spacing and porosities but were not thermally stable above the decomposition temperature of the pillaring organo-cation, limiting their applications. Pillaring with large inorganic cationic species overcame the thermal limitation and opened up more possible

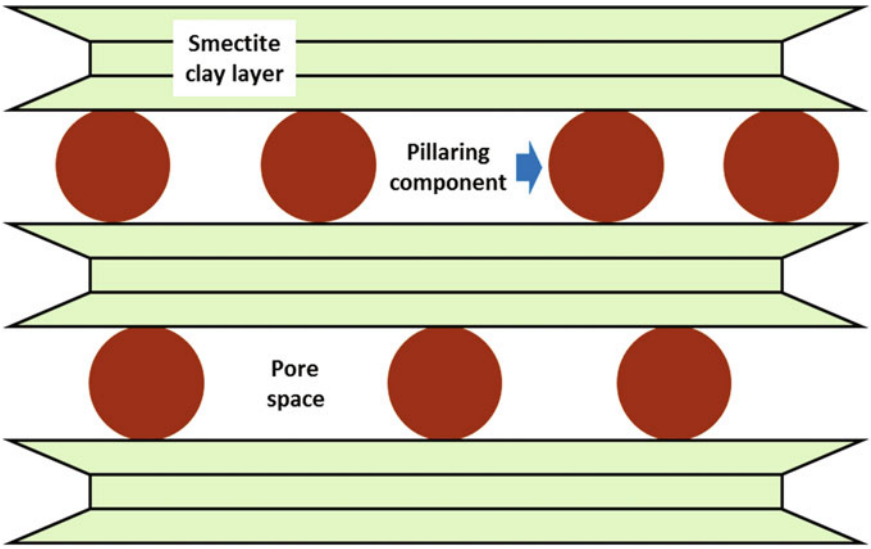

Fig. 4.9 Schematic showing the general structure of a pillared smectite clay

applications. Brindley and Sempels (1977) reported the preparation of a smectite pillared with aluminum oxide which was prepared by exchanging large Al-oxyhydroxide cations (the Al_{13}-Keggin ion, $[Al_{13}O_4(OH)_{24}(H_2O_{12}]^{7+}$) into the clay and thermally treating the exchanged material. The resulting structure was thermally stable with a relatively high surface area. Since these early pillared clays were reported, there have been many more oxide variants synthesized and studied with pillars containing Al combined with Ga, Fe, Cr, Ce, Zr, and others as well as non-Al pillaring materials such as Ti, Mn, and Cr. The process has been expanded to non-oxide pillars as well. Pillared clays are of most interest as catalysts and sorbents and have been widely studied for uses in these areas (Gil, Korili, Trujillano, & Vicente, 2010).

A relatively recent and important use for ion exchangeable clays is as an ore for rare earth elements (REE). These ores, also known as lateritic ores or lateritic clay deposits, occur over a large region of southern China and have been mined for REEs since the 1970s. These deposits contribute to China's dominance of the world supply of REEs. While these lateritic clays only contain 0.05–0.2 weight percent REEs, they are attractive because they are found in easily mined shallow surface deposits covering large areas and the REEs are easily extracted by ion exchange using ammonium salts. Additionally, these ores are naturally enriched in the more valuable and rarer heavy rare earth elements (HREE) through the adsorption-desorption fractionation processes taking place during their formation. HREEs have a higher charge to size ratio, so are more readily adsorbed by the ion exchangeable clays and preferentially concentrated relative to the light REEs. Although lateritic clay deposits are common in tropical regions worldwide, a specific set of conditions

have combined to result in China's REE-enriched laterites. The protolith from which the laterite formed must contain REE minerals that are susceptible to weathering. Felsic rocks, in this case, contain accessory minerals such as monazite, apatite, bastnäsite, and others. Weathering of the protolith in this area of China resulted in lateritic deposits from about 5–10 m in thickness containing REE-enriched kaolinite, halloysite and smectite (Kynicky, Smith, & Xu, 2012).

Two clay species worth mentioning briefly are vermiculite and illite. Both are clay minerals with a 2:1 structure that have some structural similarities to smectites but different chemical characteristics. Vermiculite is typically singled out due to its prominence as a commercially available material that has been marketed to have hundreds of applications such as the familiar expanded vermiculite used as a packing material and soil additive. It is also valuable as insulation since it is fire-proof. This variety of vermiculite occurs in much larger crystals that are outside the "size limit" for a clay because it is formed through the alteration of non-clay-sized micas. Clay-sized vermiculites commonly found in soils form through the alteration of other clays such as illite. Vermiculites are also expandable similarly to smectites but usually have a higher layer charge. Most of the commercial applications utilize the expanded or exfoliated form of the mineral which is produced by a rapid heating to high temperature, typically 900 °C or higher (Potter, 2001). The rapid heating vaporizes the interlayer water expanding the crystal into the familiar form. Illite, though a 2:1 clay, is considered to be a non-expanding clay. It is probably more accurate to consider illite to be a family of clays rather than a specific, well-defined species. It also differs from smectites in that it has a smaller CEC and a higher layer charge. The structure of illite is very similar to muscovite so it is difficult to distinguish them based on XRD alone. Also, illite is commonly interstratified, most often with montmorillonite layers. Illite is an important clay species because it is one of the primary clay components in common sedimentary rocks like shales and mudstones, and in many soils.

The structure and descriptions of chlorite group members are slightly more complicated than those of kaolin or smectite clays (Bailey, 1988). Chlorites have been referred to as 2:1, 2:1:1, and 2:2 phyllosilicates. This is due to an interesting arrangement of sheets in the chlorite structure. As a simple description, chlorites are 2:1 clays with two tetrahedral sheets sandwiching one octahedral sheet with a positively charged brucite-like (ideally $Mg_2Al(OH)_6^{1+}$) octahedral sheet occupying the interlayer space. Most chlorites are trioctahedral containing Mg and Fe in the octahedral sheet although other substitutions are very common. The nearly ubiquitous presence of Fe in the structure leads to the green coloration of most common species, ranging from pale (Mg-dominant) to nearly black (Fe-dominant). In fact, the name, chlorite, is derived from *chloros* (Greek: *χλωρός*) for "*green*" (Dana & Ford, 1941). Many mineral names have been proposed and used for the different chlorite varieties. To bring some order to the group, Bayliss (1975) proposed naming the trioctahedral chlorites based on the dominant divalent cation present: Mg^{2+}-dominant—clinochlore (Fig. 4.2), Fe^{2+}-dominant—chamosite, the more rare varieties of Ni^{2+}—nimite, Mn^{2+}—pennantite, and Zn^{2+}—baileychlore. Other substitutions are possible as well as mixtures of cations, which makes assigning the

correct mineral name challenging. Chlorites are very common clay minerals in a variety of geologic settings. Most commonly, chlorites occur in low- to medium-grade metamorphic rocks and can be the dominant mineral is some metamorphic rock deposits. In these rocks, chlorite is often the origin of their green coloration. It also forms through other processes such as crystallization of pegmatites and hydrothermal alteration of host rocks. These formation mechanisms often result in macrocrystalline chlorites. In fact, the chlorite group of phyllosilicates is generally not considered with the customary clay minerals because of its typically larger crystal size. However, chlorites are quite commonly found in sedimentary rocks as well, usually at lower concentrations, where they can fall in the "clay" size range. These occurrences are often linked to low-grade metamorphic alterations of these sedimentary formations.

The chemistry of the chlorite group is in some ways similar to the 1:1 clay group. Chlorite clays demonstrate relatively little expansion potential, which is tied to the interlayer containing a complete sheet instead of a mixture of cations and neutral molecules such as water and it has a relatively low CEC. Chlorite itself does not have any significant industrial uses. However, indirectly, chlorite has some importance in decorative stone applications, for example, the green coloration in some slates used in construction.

Though the structure of clay will inform many of the physical properties and allows for differentiation of the various clay minerals, substitution into the individual clay layers can alter these "base" physical properties and provides variation within the clay families. The layered structure of clays and the existence of an interlayer are the two primary structural features that give rise to the macro properties that can be exploited for a wide variety of applications. Currently, clays are routinely characterized through a combination of computational analysis and experimental research as discussed in the following chapters.

References

Ahn, J. H., & Buseck, P. R. (1990). Layer-stackings equencesa nd structural disorder in mixed-layer illite/smectite: Image simulations and HRTEM imaging. *American Mineralogist, 75*(3–4), 267–275.

Bailey, S. W. (1982). Nomenclature for regular interstratifications. *Clay Minerals*, *17*(2), 243–248.

Bailey, S. W. (1984). *Reviews in mineralogy, Volume 13: Micas.* Chantilly, VA: Mineralogical society of America.

Bailey, S. W. (1988). *Reviews in mineralogy, Volume 19: Hydrous phyllosilicates (exclusive of Micas).* Chantilly, VA: Mineralogical Society of America.

Barrer, R. M., & MacLeod, D. M. (1955). Activation of montmorillonite by ion exchange and sorption complexes of tetra-alkyl ammonium montmorillonites. *Transactions of the Faraday Society, 51,* 1290–1300.

Bayliss, P. (1975). Nomenclature of the trioctahedral chlorites. *Canadian Mineralogist, 13,* 178–180.

Bethke, C. M., & Reynolds, R. C. (1986). Recursive method for determining frequency factors in interstratified clay diffraction calculations. *Clays and Clay Minerals, 34*(2), 224–226.

Bethke, C. M., Vergo, N., & Altaner, S. P. (1986). Pathways of smectite illitization. *Clays and Clay Minerals, 34*(2), 125–135.

Brady, N. C., & Weil, R. R. (2010). *Elements of the nature and properties of soils* (3rd ed.). London: Pearson.

Brindley, G. W., & Sempels, R. E. (1977). Preparation and properties of some hydroxy-aluminum beidellites. *Clay Minerals, 12*(3), 229–237.

Brown, G., & Brindley, G. W. (1980). X-ray diffraction procedures for clay mineral identification. In G. Brindley & G. Brown (Eds.), *Crystal structures of clay minerals and their X-ray identification* (3rd ed., pp. 305–360). London: Mineralogical Society.

Dana, E. S., & Ford, W. E. (1941). *Dana's manual of mineralogy (revised by Hurlbut, C. S.)* (5th ed.). New York: Wiley.

Eberl, D. D. (1984). Clay mineral formation and transformation in rocks and soils [and discussion]. *Philosophical Transactions of the Royal Society of London. Series A: Mathematical, Physical, and Engineering Sciences,* 311(517), 241.

Evangelou, V. (1998). *Environmental soil and water chemistry: Principles and applications* (1st ed.). New York: Wiley.

Ferrage, E., Lanson, B., Sakharov, B. A., & Drits, V. A. (2005). Investigation of smectite hydration properties by modeling experimental X-ray diffraction patterns: Part I. Montmorillonite Hydration Properties. *American Mineralogist*, *90*(8–9), 1358–1374.

Gaines, R. V., et al. (1997). *Dana's new mineralogy* (8th ed.). Hoboken: Wiley.

Gil, A., Korili, S. A., Trujillano, R., & Vicente, M. A. (Eds.). (2010). *Pillared clays and related catalysts*. New York: Springer.

Guggenheim, S., et al. (2006). Summary of recommendations of nomenclature committees relevant to clay mineralogy: Report of the Association Internationale pour l'Etude des Argiles (AIPEA) Nomenclature Committee for 2006. *Clay Minerals, 41*(4), 863–877.

Hazen, R. M., et al. (2013). Clay mineral evolution. *American Mineralogist, 98*(11–12), 2007–2029.

Klug, H. P., & Alexander, L. E. (1974). *X-Ray diffraction procedures: For polycrystalline and amorphous materials* (2nd ed.). New York: Wiley.

Kynicky, J., Smith, M. P., & Xu, C. (2012). Diversity of rare earth deposits: The key example of China. *Elements, 8*(5), 361–367.

Leupin, O. X., et al. (2014). *Montmorillonite stability under near-field conditions*. Wettingen, Switzerland: National Cooperative for the Disposal of Radioactive Waste.

MacEwan, D. M. C. (1958). Fourier transform methods for studying X-ray scattering from lamellar systems: II. The calculation of X-ray diffraction effects for various types of interstratification. *Kolloid-Zeitschrift,* 156(1), 61–67.

MacEwan, D. M. C., & Wilson, M. J. (1980). Interlayer and intercalation complexes of clay minerals. In G. Brindley & G. Brown (Eds.), *Crystal structures of clay minerals and their X-ray identification* (3rd ed., pp. 197–248). London: Mineralogical Society.

Mackenzie, R. (1962). De natura lutorum. *Clays and Clay Minerals, 11*(1), 11–28.

Mauduyt, L. (1847). Un mot sur un morceau de quartz d'une variété particulière, ainsi que sur une substance minérale trouvée dans le département de la Vienne. *Bulletin de la Société Géologique de France*, *4*, 168–170.

Miller, W. H. (1839). *A treatise on crystallography* (1st ed.). Cambridge, UK: J. & J. J. Deighton.

Moore, D. M., & Hower, J. (1986). Ordered interstratifrcation of dehydrated and hydrated Na-montmorillonite. *Clays and Clay Minerals, 34*(4), 378–384.

Moore, D. M., & Reynolds, R. C., Jr. (1997). *X-Ray diffraction and the identification and analysis of clay minerals* (2nd ed.). New York: Oxford University Press.

Murray, H. H. (2000). Traditional and new applications for kaolin, smectite, and palygorskite: A general overview. *Applied Clay Science, 17*(5), 207–221.

Nadeau, P. H., Wilson, M. J., McHardy, W. J., & Tait, J. M. (1984). Interstratified clays as fundamental particles. *Clay Minerals, 19*(5), 757–769.

Potter, M. J. (2001). Vermiculite. In *Minerals Yearbook* (Vol. 1, pp. 82.1–82.5). Online: U.S. Geological Survey.

Reynolds, R. C. (1980). Interstratified clay minerals. In G. Brindley & G. Brown (Eds.), *Crystal structures of clay minerals and their X-ray identification* (3rd ed., pp. 249–303). London: Mineralogical Society.

Reynolds, R. J., & Reynolds, R. I. (1996). *NEWMOD for Windows©: The calculation of one-dimensional X-ray diffraction patterns of mixed-layered clay minerals*. Available online at: http://www.newmod-for-clays.com/home.html. Accessed 21 June 2017.

Ronov, A. B., & Yaroshevsky, A. A. (2013). Chemical composition of the earth's crust. In P. J. Hart (Ed.), *The earth's crust and upper mantle (geophysical monograph series)* (pp. 37–57). Online: American Geophysical Union.

Srodon, J. (1999). Nature of mixed-layer clays and mechanisms of their formation and alteration. *Annual Review of Earth and Planetary Sciences, 27,* 19–53.

Steudel, A. et al., 2017. Characterization of a fine-grained interstratification of turbostratic talc and saponite. *Minerals,* 7(1), 5.1–14.

Vicente, M. A., Gil, A., & Bergaya, F. (2013). Pillared clays and clay minerals. In F. Bergaya & G. Lagaly (Eds.), *Handbook of clay science* (2nd ed., pp. 523–557). Amsterdam: Elsevier.

Chapter 5
Advanced Experimental Techniques in Geochemistry

Vyacheslav Romanov

Gentlemen, now you will see that now you see nothing. And why you see nothing you will see presently.
—Quotations by Sir Ernest Rutherford

Do we see reality as it is? A third of the brain's cortex is engaged in vision. The eye has a retina with 130 million photo-receptors but there are even more neuro-receptors.
—"Decoding Bursts of Light" by Moona Perrotin, Science Rhymes, Australia, 2015.

Abstract Has anyone wondered why clay is the most ubiquitous geomaterial in earth's crust but we still are in need of developing more sophisticated methods and techniques to properly characterize it? The main reason is: it is not well defined; in fact, the variations in local clay structure and composition are virtually infinite. Geological origin descriptions provide an important foundation for clay models needed for interpretation of the experimental data collected on heterogeneous samples. Chemical analysis is the most essential step in mineral analysis; it usually follows structural analysis, in order to identify the major crystalline phases and impurities. Non-destructive techniques that are complementary to crystallography are electron microscopy and NMR spectroscopy for structure determination and study of dynamics. Some of the important methods in clay mineral identification are determination of coherent scattering domain size from XRD, Bertaut-Warren-Averbach analysis, counting layers on TEM lattice-fringe images, Pt-shadowing, and calculation of the average number of fundamental particles per MacEwan crystallite. A combination of the X-ray and neutron diffraction can be used for advanced model refinement, by utilizing a technique devised by Rietveld. Synchrotron radiation can be advantageous to laboratory sources. Several other advanced techniques are described in this chapter as well. Advances (including in situ analysis) in experimental methods go hand-in-hand with advances in conceptual understanding of the experimental observations.

V. Romanov (✉)
U.S. Department of Energy, National Energy Technology Laboratory (NETL), Pittsburgh, USA
e-mail: romanov@netl.doe.gov

© Springer International Publishing AG 2018

V. Romanov (ed.), *Greenhouse Gases and Clay Minerals*, Green Energy and Technology, https://doi.org/10.1007/978-3-319-12661-6_5

5.1 Heterogeneity Challenge

Has anyone wondered why clay is the most ubiquitous weathered geomaterial in earth's crust but we still are in need of developing more and more sophisticated methods and techniques to properly characterize it? The main reason is: it is not well defined; in fact, the variations in local clay structure and composition are virtually infinite. This is caused not only by differences in primary inorganic components of soil but also by historical changes in the local environments. When magma (which is a high-temperature, high-pressure reactive multicomponent system, involving multi-phase eutectics, solid solutions, and dissolved water) incongruently crystallizes upon cooling, it forms igneous rock, the principal constitutive material of the planet's crust. Depending upon the surroundings and the rate of cooling, a great variety of textures and compositions of igneous rock can be formed. When crystallization is complete, the result is a solid mass of interlocking crystals of different sizes. The major structural elements of this rock are silicate groups, SiO_4^{4-} tetrahedra interspersed with mutually soluble metal (commonly, Al, Fe or Mg) cation substitutions, which tend to polymerize by sharing one or more oxygen atoms at the adjacent tetrahedral vertices. Higher degrees of polymerization are associated with higher Si:O ratios and smaller fractions of the foreign metal inclusions. Positive ions that are too large, too small, or too highly charged to be accommodated in silicate structures remain in magma as it solidifies, and form solid minerals during the later stages of cooling. All the silicates are molten at about 1200 °C and all are solid when cooled to about 600 °C. Consolidation of the solidified geological materials caused by weathering, chemical and biological processes in the pedosphere produces sedimentary rocks (shale, sandstone and limestone).

The primary inorganic components of soil are sand and silt particles that come directly from the parent rocks. This fraction is dominated by quartz and feldspars (aluminosilicates). However, under the influence of heat and pressure, particularly at tectonic plate boundaries, solid crustal material may undergo partial or complete re-melting, followed by cooling and transformation into metamorphic rocks such as quartzite and mica. The secondary soil components such as clays are formed by chemical changes within the soil itself or in the sediments from which the soil is derived (Chap. 4). Clay is a sedimentary rock made of tiny particles which come from the weathering of other rocks and minerals. The particles can be transported by rivers or ice and then deposited. Soil is a product of the interaction of water, air, and living organisms with exposed rocks or sediments at the earth's surface. A typical soil contains about 45% inorganic solids and 5% organic solids by volume. Water and air each make up about 20–30%. A simple way of classifying soils is based on the relative quantities of clay, silt and sand in the solid component (Fig. 5.1) separated by the grain size (as specified by the U.S. Department of Agriculture). Several grain-size scales are in use, but the Udden-Wentworth scale (commonly called the Wentworth scale) is the one that is most frequently used in geology.

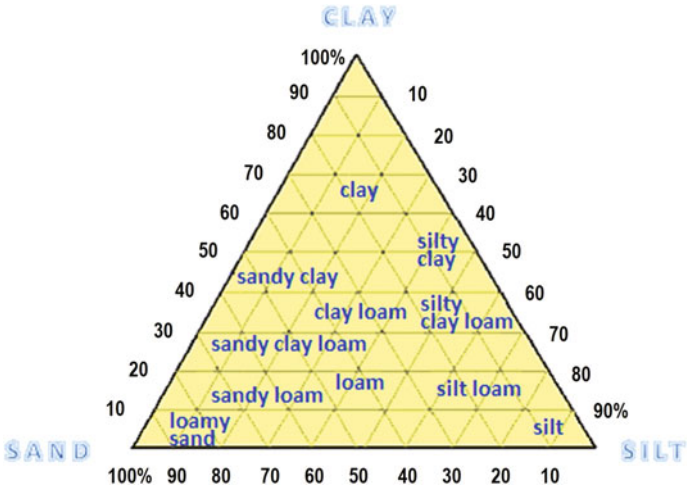

Fig. 5.1 Soil classification diagram (Udvardi et al., 2014)

The ion-exchange properties of clays help to maintain the pH balance of soils, through the exchange of H^+ and cations such as Ca^{2+}. The soil pH, in turn, strongly affects the solubility of cations. Organic matter of soil consists of living organisms such as bacteria and fungi as well as of fulvic and humic acids in association with a variety of smaller organic molecules. Both acids are polyelectrolytes strongly interacting with inorganic ions. Once organic carbon gets incorporated into humic substances, it is locked into a slow (hundreds of years) recycling process. Organic matter binds to the cation components of clay colloids thus acting as cementing agents of soil. The organisms' activity significantly affects the gas-phase composition of soil, thus resulting in oxygen depletion, generation of CO_2 concentration within soil pores at the levels of 5–50 times greater than in the atmosphere, and under conditions of poor aeration (controlled by water) substantially increased concentrations of the secondary gaseous components such as N_2O, NO, H_2, CH_4, C_2H_6, and H_2S. Soil water is held by capillary action and adsorption. The water binding strength is traditionally expressed in terms of pressure or "tension" that would be required to force the water out of soil. The capillary pressure in soil varies over a range of 0.01–3.2 MPa (plants can produce osmotic pressure of about 1.5 MPa). Water in excess of the capillary capacity ("gravitational" water) fills larger voids and reduces soil aeration.

Weathering of rocks at the earth's surface is a complex process involving both physical and chemical changes: dissolution, hydration, hydrolysis, reaction with carbonic acid, and oxidation. Among the main causes of physical weathering are the abrasive action of windborne material and glacier movements, rapid temperature changes promoting fracturing by differential expansion, and penetration of water into the voids, with its subsequent freezing. Expansion of water upon freezing can exert pressure of up to 15 MPa, more than the tensile strength of a typical rock.

In chemical weathering, the reaction products are not well characterized, thermodynamic data is lacking and the reactions are not entirely understood. The problem with quantifying it in the laboratory is that such reactions occur very slowly and may never reach equilibrium. The rocks that crystallized from magma at higher temperatures (Ca-feldspar and olivine) tend to weather more rapidly than the rocks with lower melting temperature (Fig. 5.2). In general, sodium, calcium and magnesium seem to leach before potassium and silicon, while iron and aluminum can only be released very slowly. Individual rates depend on the structural units containing the element and vary with grain size and conditions of the ambient environment. Chemical weathering of rock minerals generally occurs more rapidly in hot, humid climatic regions.

Mineral dissolution usually results in ionic species, some of which may react with water to yield acidic or alkaline solutions. Dissolution of silica, however, results in the neutral species of H_4SiO_4. Reactions involving hydration and dehydration are associated with minor free-energy changes and hence reversible under slightly different conditions. Solid carbonates tend to dissolve in acidic solutions, including those produced when atmospheric carbon dioxide dissolves in water. Thermodynamics can predict the most stable oxidation state of metal ion under given conditions of pH and oxidant concentration. However, the reaction mechanisms tend to be uncertain for a variety of reasons: the reactant and product can exist in various states of hydration and the dissolved species are a mix of poly-cations and complexed species undergoing oxidation.

The chemical composition of rocks tends to be complex and variable as well; often it can only be defined in a more precise manner at the structural level—traditionally, in terms of the mass percent of oxides of the elements present in the

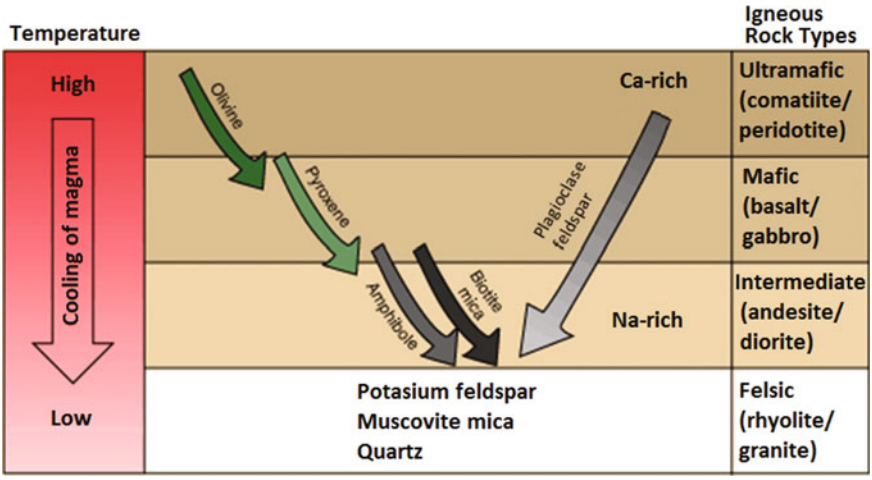

Fig. 5.2 Lutgens and Tarbuck's (2014) perspective of the N.L. Bowen's reaction series (originally patterned by Carl R. Nave)

rock, even though the oxides may not be present as structural units. In the chemical analysis of rocks, oxygen is generally not determined separately, though neutron activation analysis may be utilized to determine its content quite accurately; it is expected to combine stoichiometrically with the other elements, including hydration and structural 'water' (H_2O^- that evolves below 105 °C and H_2O^+ that evolves between 105 and 1000 °C). In clay studies, even the same locality may contain a multitude of subtly different minerals, with substantial variations in mineral assemblage and the composition of individual clay minerals. As a result, the data from different laboratories on ostensibly the same clay may not be comparable. Several coherent attempts have been made, however, to collect samples of representative clays, homogenize and analyze them, and publish the baseline study results. As any processing may affect the material properties, it is necessary to carefully take into consideration its implications as well as the primary objectives of a given research, to properly assess the tradeoffs and choose the most appropriate options. For example, even partial homogenization (sample scale uniformity) alters clay fabric and cation exchange; and drying may result in irreversible changes in lamellar or globular microcrystalline aggregation.

5.2 Preliminary Sample Characterization

The basic clay properties that are conventionally characterized are its geological origin, chemical composition, structural patterns, layer charges, cation-exchange capacity, thermal behavior, and colloid and surface properties. Although geological origin descriptions may seem somewhat speculative, they provide an important foundation for developing clay models (a combination of fundamental theory and statistics) that are inevitably called upon for interpretation of the experimental data collected on heterogeneous samples. Chemical analysis is the most essential step in mineral analysis; however, it usually follows the structural analysis, in order to identify the major crystalline phases and impurities which can also be removed by selective dissolution—without removing the impurities (such as crystalline silica) it is not possible to accurately derive the formation-specific structural composition (e.g., of the Gonzales County, TX smectite-rich bentonite STx-1). If purification is required, it must be done in a manner that does not significantly alter the physical or chemical properties of the sample. As mentioned in Chap. 4, clay minerals are usually fine-grained (<2 μm); this physical property can be utilized to separate them from coarse-grained minerals (such as quartz, feldspar, or calcite). The textures of smectite, illite, and mixed layer I/S, which are important mineral components in sediments and soil, are very different in sandstones, bentonites and other rock type. However, some characteristics of the clay particles and their interfaces could be altered during the separation and subsequent evaporation due to proton exchange and surface charge alteration.

An important problem in clay mineralogy has been the understanding of the structure of clay particles and how that structure is perceived by XRD of sedimented

(onto glass slides) aggregates. The sedimented aggregates consisting of clay suspensions dried onto a flat surface (see Sect. 5.3) are useful because the preferred orientation of the sheet-like clay particles enhances the $d_{00\ell}$ diffraction maxima, thus resolving the diagnostic (c^*-axis) dimension of various clay minerals. It is generally accepted that clay particles are of the order of 0.1 μm in length and width (i.e., in a and b dimensions) but the number of associated unit-cells (N) along the c direction can be debatable. This is particularly true for smectite, illite, and interstratified clays (e.g., I/S—see Chap. 4). The controversy arises from the relationship between the shape and intensity of the XRD maxima and N as defined by the interference function (Guthrie & Reynolds, 1998). For the Debye-Scherrer geometry:

$$B = K\lambda/N\,d\,\cos\theta \tag{5.1}$$

where K is a dimensionless particle's shape-factor with a value close to unity (e.g., 0.89 for a sphere), d—the layer spacing, λ—the wavelength of radiation, θ—the Bragg angle, and B—the diffraction peak breadth measured in radians 2θ (at half-height). The maxima broaden and their intensity decreases as N decreases.

The fp concept (as defined in Chap. 4) assumes that particles separated for XRD analysis were either separate units (stacks) in original rocks, or thin sub-units of MacEwan crystallites (thick stacks) with incoherent and coherent /semi-coherent (e.g., turbostratically stacked owing to rotational disorder) interfaces (Peacor, 1998; Guthrie & Reynolds, 1998). Cleavage is assumed to occur on the incoherent interfaces—e.g., polar, smectite-like terminations (acting as smectite interlayers) in I/S systems—thus separating the stack into fp's within each of which the interfaces are coherent (illite-like). Although the term "coherent" was not used in the original definition, the crystallographic implication of experimentally observed single-crystal hk0 patterns is that the layers be related by three-dimensional (3D) periodicity (rotations of multiples of 60° around the c^* axis, which occur periodically) or by stacking faults that are random variations in the sequence of 60° rotations (Peacor, 1998).

> One of the touchstones of crystallography, Nicolaus Steno's (born Niels Stensen) Law of Interfacial Angles (1669) concerning the appearance of crystals, reflects a regular arrangement of atoms from which a notion of 3D periodicity is derived.

This paradigm may cause confusion (regarding the usage of the terms crystal, crystallite, coherent domain, particle, and layer) because a coherent 1D arrangement of layers is no longer a mixed-layered crystal. The concept's evolution to account for experimental (TEM) evidence of lattice-fringe images—the spacing of such set of fringes is proportional to the mineral's lattice spacing when the corresponding lattice planes meet the Bragg condition, viewed in direct space—and the polar character of I/S (Nieto & Cuadros, 1998) has brought it closer to the traditional mixed-layer view in MacEwan or Markovian interpretive models (Reynolds, 1980) which consider the I/S crystallites as composed of smectite and illite layers (also with polar character)—the remaining difference lying only in the crystallographic (3D) coherence across fundamental particles (particularly, across smectite interlayer).

To resolve the fp—MacEwan crystallites controversy, it was necessary to observe the above coherence while using samples of sedimentary origin that are indeed representative of sedimentary sequences, and to take into account clay heterogeneity, which is implicit in the Markovian statistics used to model I/S (Drits, 1987) and was described in the mathematical decomposition of diffraction patterns (Lanson & Champion, 1991). The consensus is that I/S mixed-layer (ML) stacking is generally different from complete disorder ($1M_d$) polytypism (Ahn & Buseck, 1990).

The earlier (prior to 1990) TEM investigations of ion-milled specimens showed large regions containing clay mineral lattice fringes with periodicities that were suggested as representing mixed layering of illite and smectite. However, the lattice-fringe images do not contain information regarding structural coherency between stacked 2:1 layers. To address this problem, there are several methods available, in addition to the determination of coherent scattering domain size (*N*) from XRD patterns (Eq. 5.1): Bertaut-Warren-Averbach (BWA) analysis of XRD patterns collected on I/S intercalated with high molecular weight polyvinylpyrrolidone; counting layers on high-resolution TEM (HRTEM) lattice-fringe images; Pt-shadowing; and calculation of the average number of fundamental particles per MacEwan crystallite by using the fixed cation content (Mieunier, Lanson, & Beaufort, 2000).

Electron diffraction patterns and lattice images (interference patterns between the direct and diffracted beams, viewed in direct space) are two forms of data which allow crystallographic analysis in TEM. Two types of electron diffraction patterns in TEM are referred to as selected area electron diffraction (SAED) and convergent beam electron diffraction (CBED). Nano-diffraction using CBED is useful in studies of very small crystallites. Kikuchi diffraction (Nishikawa & Kikuchi, 1928) and the crystal orientation-dependent fringe-visibility maps (Fraundorf, Qin, Moeck, & Mandell, 2005) can be realized via both SAED and CBED. Proof of coherency between two or more contiguous interlayers occurs where the corresponding 001 lattice fringes are cross-cut by non-001 (e.g., 020) fringes included in the objective lens aperture; then those 001 layers must have the non-001 plane in common and be related by multiples of 60° rotation around c^* (i.e., they must be coherent interfaces). As the focal conditions are different for imaging the 001 fringes and cross fringes, through-focus series of images are obtained, normally from 100 nm under-focus to 100 nm over-focus. Coherency across even smectite interlayers is commonly demonstrated in original rocks by: TEM lattice-fringe images with "cross-fringes"; euhedral crystals of I/S, smectite, and illite; and SAED patterns with discrete, but non-periodic hkl reflections—In the latter case, cross fringes are the Fourier transform of ill-defined, non-00ℓ reflections in SAED patterns (Peacor, 1998).

SAED pattern must include $\mathbf{c}^*$ (in reciprocal space), an orientation promoted by preparation of TEM samples as thin sections normal to bedding, that is, with (001) planes parallel to the electron beam (Dong & Peacor, 1996). The second vector must then lie in the $\mathbf{a}^*$–$\mathbf{b}^*$ plane and the rotation around $\mathbf{c}^*$ may become either $\mathbf{a}^*$ or $\mathbf{b}^*$ or one of their pseudo-symmetrically-related, 60° rotation-equivalents. Although $\mathbf{a}^*(\mathbf{b}^*)$ and its rotation-equivalents have nearly equal d-values, the angle between $\mathbf{c}^*$ and the equivalents is different from the one between $\mathbf{c}^*$ and $\mathbf{a}^*(\mathbf{b}^*)$. TEM images

show that montmorillonite particles exhibit thin-plate and curly-flake morphologies (Roberson, Weir, & Woods, 1968; Nadeau, Tait, McHardy, & Wilson, 1984), with long, parallel but undulated layers, which complicates the 3D image reconstruction (Malla et al., 1993).

Caution must be exercised when interpreting the XRD and TEM results. The dispersion processes for XRD and TEM analyses would easily disarticulate originally-undisturbed crystallites into "fundamental particles" with no geological meaning with respect to the original sample (Nieto & Cuadros, 1998). While fp observed in particles separated for XRD are assumed to be related by incoherent interfaces in original rocks, implying that the sites of coherent and incoherent interfaces in separates are identical to those in original rocks; that must depend critically on the severity of sample treatment (Peacor, 1998). It has been shown that 3D periodicity of I/S can be induced through smectite interlayer-ion saturation and thermal effects. HRTEM methods of sample preparation require that the bulk-rock specimen be sectioned, polished, and subjected to ion-milling (a beam of high-energy ions). In the high-vacuum environment during the latter procedure, effects of ion-milling illitic or micaceous specimens could result in potassium fixation in nearby ion-exchange sites, and increases susceptibility to alteration of three-dimensional periodicity (Nadeau, 1998).

As the abundance of any mineral is determined by the availability of its constituent elements in the Earth's crust, its chemical composition combined with the mineralogical information is important in shedding the light on the mineral's origin and transformation history. The clay elemental composition analysis by a combination of atomic absorption (AA) and atomic emission (ICP/ICP-MS or flame emission, particularly for alkali metals) spectroscopy methods is routinely performed following the microwave-assisted acid digestion, and sometimes after the subsequent neutralization. ICP-MS (i.e., inductively-coupled-plasma mass-spectrometry) is ideally suitable for rapid qualitative elemental analysis of clays and other geomaterials; however, the quantitative analysis requires the use of external calibration standards and corrections applied for mass-dependent matrix effects, mass spectral interferences, and drift. The quantities of multivalent element fractions (such as Fe^{3+} vs. Fe^{2+}) are determined separately. The main principle of atomic emission spectroscopy—a unique emission spectrum corresponding to a unique atomic structure—is utilized in a variety of spectroscopic techniques with different excitation sources (electron beam excitation in electron microscopes; X-ray beam excitation in X-ray fluorescence spectrometers) and emission spectra (e.g., Auger electron spectroscopy). Accurate estimation of the elemental composition from the measured X-ray emission spectrum also requires the application of quantitative correction procedures (matrix corrections for the emitted X-rays' re-absorption by the sample). Laser-induced breakdown spectroscopy (LIBS) is another type of atomic emission spectroscopy which uses a highly energetic laser pulse as the excitation source; it was employed to identify various phyllosilicates such as Martian clay analogs (Humphries et al., 2011).

Thermal analysis involving a dynamic phenomenological approach can also be used to study solid state reactions (chemisorption, reduction/oxidation, desolvation/

dehydration, and decomposition) and phase transitions (crystallization, glass transition, melting and sublimation, vaporization, absorption, adsorption, and desorption) by monitoring a variety of physical properties: mass in thermo-gravimetric analysis (TGA), mass changes as function of pressure in pressurized TGA (PTGA), temperature difference in differential thermal analysis (DTA), heat difference in differential scanning calorimetry (DSC), gaseous decomposition products in evolved gas analysis (EGA/TGA-MS), deformations and dimension in thermo-mechanical analysis, and volume in dilatometry. Often different properties can be measured simultaneously. For example, TGA-MS can be used to characterize desorption of various species (water and adsorbed gases) from geomaterials; alternatively, CO_2 coulometer can be used for total carbon determination by measuring the amount of CO_2 evolved, when coupled with thermal decomposition of the sample (by heating up to 1000 °C) or for carbonate carbon determination by using complementary acid digestion technique. For gas or supercritical fluid sorption studies, specialized sorption isotherm techniques of quantitative manometric or gravimetric measurements (convoluted by sample swelling) can be combined with semi-quantitative Raman and infrared (IR) spectrometry studies.

IR spectroscopy is a powerful tool for mineralogical, composition, and structural analysis of clay (Madejová, 2003). In combination with a polarizer placed between interferometer and the IR reflectance cell, it provides enhanced capabilities to study preferred orientation of clay layers and even specific chemical bonds; which is particularly useful for monitoring and analyzing clay–fluid interactions (Amarasinghe, Katti, & Katti, 2008; Ras et al., 2003; Johnston, Sposito, & Erickson, 1992). Optical microscopy, on the other hand, can be used for preliminary characterization of the lateral swelling of clay aggregates to complement the X-ray diffraction (XRD) studies. Laser scanning microscopy was used to investigate bentonite swelling in NaCl solution (Suzuki, Prayongphan, Ichikawa, & Chae, 2005).

5.3 Analysis of Crystalline Phases

Qualitative identification of the crystalline phases in multicomponent clay samples can be performed using conventional laboratory XRD methods and equipment (Chap. 4). The amount of sample available and what a researcher hopes to reveal about the sample will determine how the sample is prepared and/or mounted; for example, small specimens of oriented clay particles can be mounted on the zero background (off-axis-cut) quartz plates to improve signal-to-noise ratio. Semi-quantitative evaluation of the mineral abundances (amorphous components are not quantified, though the recent development of techniques that interpret both Bragg and diffuse elastic scattering has extended the use of XRD to amorphous materials) requires the use of external standards, accounting for variations in degree of preferred orientation of the crystallites (for the random mount) or the finite sample thickness (for the oriented samples), Lorentz-polarization effects, and relative humidity during the analysis. The latter is particularly important for smectite

samples whose basal 00ℓ-diffraction pattern varies as a function of numerous factors, which prompts some researchers to explore the environmental cell options. High-pressure rated cells are particularly useful for studies on clay interaction with greenhouse gases for as long as the cell's window is sufficiently transparent and does not convolute the observed diffraction patterns. Hence, they may not be suitable for all laboratory X-ray machines and may even require the use of synchrotron (Kulipanov, 2007) light-source beamlines.

Synchrotron radiation can be advantageous to laboratory sources for several reasons: orders of magnitude higher brightness and intensity (for 3rd generation sources, brilliance larger than 10^{18} photons/s/mm^2/mrad^2/0.1%BW, where 0.1% BW is a bandwidth of $f \times 10^{-3}$ centered around frequency f; and for 4th generation, X-ray free electron lasers, brilliance larger than 10^{24} photons/s/mm^2/mrad^2/0.1% BW); higher collimation; higher degree of polarization; lower emittance (product of source cross-section and solid angle of emission); larger wavelength tunability (use of monochromators); pulsed light emission (pulse durations may be below one nanosecond in 3rd generation sources and close to picoseconds in 4th generation sources) allows ultra-fast time-resolved studies.

The advanced light-source (beamline) facilities (see examples in Figs. 5.3 and 5.4) are naturally equipped with a variety of probes that fall into three broad categories: diffraction and scattering (like X-ray reflectivity, including resonant anomalous and standing wave) techniques, spectroscopy (X-ray and low-energy) and imaging (X-ray and IR). Simultaneous recording of both small and wide angle X-ray scattering (SAXS and WAXS) in combination allows users to probe length scales ranging from a few Angstroms to several micrometers, with high resolution. HRTEM in conjunction with SAXS can be used to study the effect of interlayer cations, hydration state, and applied pressure on organization of clay layers including the size of crystallites. The unique properties of synchrotron radiation are its high collimation and coherence, high flux and brightness (brilliance) essential for SAXS studies of oriented samples, continuous (high resolution, tunable) spectrum that enables studies of anomalous SAXS close to the absorption edges of the element. Synchrotrons' major advantages over laboratory XRD is high-volume event counting statistics (millions of counts in just a few seconds)—in reflection (Bragg-Brentano) and transmission (Debye-Scherrer) modes; transmission geometry, fast data acquisition and high-frequency sample spinning contribute to reduced preferential orientation effects; polarization and the pulsed nature of these sources can also be harnessed in special experiments.

Advances in developing environmental pressure cells with X-ray transparent windows (Giesting, Guggenheim, Koster van Groos, & Busch, 2012; Loring et al., 2012) produced a number of high-pressure X-ray diffraction reactors which allow conducting in situ observation of swelling clay as it interacts with active gases/fluids like CO_2. Such reactors can be used to precisely control humidity as well as simultaneously observe infrared spectra of the gas and solid phases, along with XRD patterns. Controlled humidity experiments are particularly important for highly hygroscopic samples like clays.

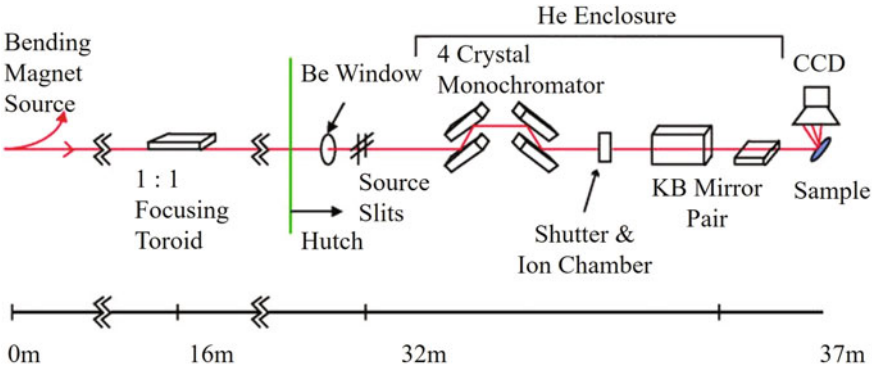

Fig. 5.3 Schematic layout of a beamline at the advanced light source, Berkeley Lab (http://www-esg2.lbl.gov/microdif/beamline733.htm accessed 19 May 2017)

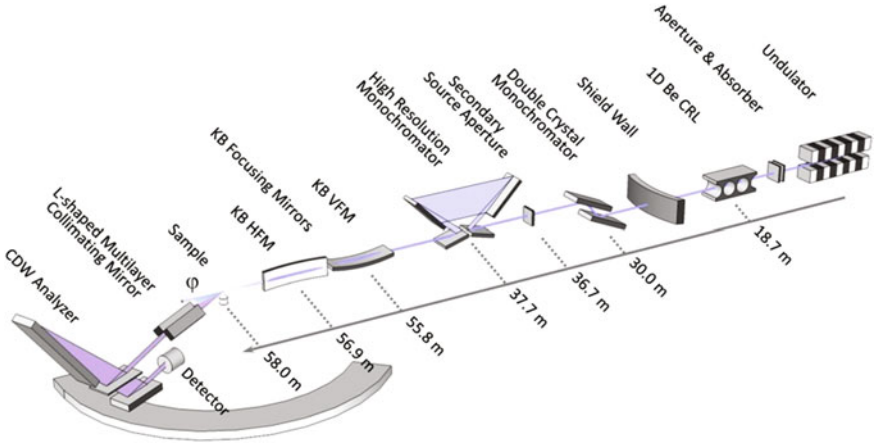

Fig. 5.4 Inelastic X-ray scattering beamline at Brookhaven National Laboratory world-brightest light source, NSLS II (Suvorov, Cai, Sutter, & Chubar, 2014); CRL = compound refractive lenses, KB = Kirkpatrick-Baez focusing with independent *vertically* and *horizontally* focusing mirrors (VFM and HFM), CDW = charge-density-wave phase deformation

5.4 Element-Specific Advanced Analytic Techniques

Molecular structure in the clay interlayer has been studied experimentally using a variety of techniques: IR spectroscopy, incoherent neutron scattering, nuclear magnetic resonance (NMR) spectroscopy, dielectric relaxation, neutron and X-ray diffraction, and others (Sposito & Prost, 1982). Among the chemical element-specific, soft X-ray/vacuum-ultraviolet spectroscopy techniques based on the measurement of absorption, transmission, or reflectivity of a sample as a function of

the incident photon's energy, electron photoemission (XPS/UPS), fluorescence and inelastic photon scattering (viable only at brilliant synchrotron sources) are most common. XPS (Fig. 5.5) was reported to detect carbonate formation near clay surfaces, though it is difficult to resolve the broadened (due to differential surface charging) chemical shift distributions and identify specific kind of carbonate species among others or to detect whether they are in the interlayer or at the external surfaces. There are several semi-quantitative XPS depth-profiling methods, including ion etching, surface charging, angle-resolved (for oriented samples) and QUASES (developed by Sven Tougaard) methods, but all suffer from various limitations. The ion beam etching (for depth profiling) leads to destructive chemical and topographical modifications; hence difficulties with data interpretation. 3D atom probe tomography (APT) is an alternative technique for imaging and chemical composition analysis at atomic scale, based on progressive electrostatic-field evaporation of atoms from a sample prepared in the form of a very sharp tip, time-of-flight detection and 3D reconstruction.

Non-destructive techniques that are complementary to crystallography are electron microscopy (EM) and NMR spectroscopy for structure determination and the study of dynamics. Advanced methods of non-destructive imaging include soft X-ray imaging (with the use of photon or electron optics to achieve high spatial resolution) and hard X-ray tomography (with raster scanning of the sample through the illuminated spot). X-ray tomography can be performed in situ (with the sample placed in controlled gas and temperature environment). Hard X-ray imaging non-destructively visualizes samples, frequently the internal or hidden components of the samples. The contrast can be due to changes in absorption, elemental composition, or refractive index of the sample.

The X-ray standing wave (XSW) technique, briefly mentioned in Sect. 5.3, provides another non-destructive element-specific structural probe by using X-ray reflectivity (XR) setup to generate a "two-beam" interference field that in turn induces a spatial dependence to spectroscopic (fluorescence or photoelectron) yields from atoms within the field. XR is extremely powerful for obtaining in situ information about structural properties of surfaces and interfaces on the atomic

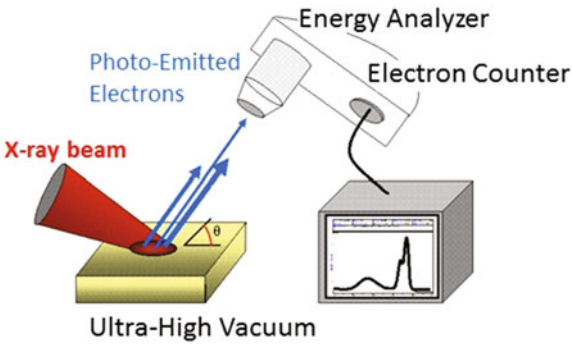

Fig. 5.5 X-ray photoelectron spectroscopy (wikimedia)

scale, with high spatial resolution and chemical selectivity (Fenter & Lee, 2014). Despite insensitivity toward hydrogen atoms, the X-ray techniques have proven their efficiency in assessing the clay interlayer electron density profiles and in determining the conditions with minimum hydration heterogeneity required for neutron diffraction (ND) experiments.

Advancements in small-angle scattering of neutrons—interacting with atom cores—provide more reliable data for indirect determination of the physical dimensions of clay particles, compared to more traditional techniques like electron-optical birefringence, ultra-centrifugation, viscosity, and UV-Vis (ultraviolet-visible) light scattering (Nadeau, 1985). ND also represents a step forward in the validation of clay and H_2O models, because contribution to the diffracted intensities of interlayer species increases from $\sim 25\%$ for X-ray to $\sim 40\%$ (using H_2O) and $\sim 47\%$ (using D_2O) for neutron diffraction (Ferrage et al., 2011). However, strong divergence of neutron beams broadens 00ℓ reflections and leading to an apparent decrease of the coherent scattering length (from about 12–16 layers for XRD to 5–7 for ND). This, in combination with short wavelength and large angular steps, makes calibration of experimental data difficult to perform; and modification of ND reflection intensity distribution induced by the presence of minor hydration heterogeneity may lead to erroneous assessment of the interlayer models.

A comprehensive dataset provided by a combination of the XRD and ND can be used for advanced model refinement, by utilizing a technique devised by Rietveld (1969) for use in the characterization of crystalline materials, to deal reliably with strongly overlapping reflections. Layer stacking faults in clay minerals may hamper the Rietveld refinement and require specific algorithms (Brigatti & Mottana, 2011).

UV-Vis spectroscopy is not as widely used in chemical-selectivity research because of molecular absorption band overlap. However, UV-Vis spectroscopic measurements are not detector noise limited as are IR measurements. For this reason, advances in phase-, time-, and space-resolution using step-scan as well as rapid-scan spectroscopy were first made in the UV-Vis region and only later followed by the Fourier-transform IR (FTIR). Time-resolved FTIR is a spectroscopic technique whereby transient processes, including non-cyclic (Rammelsberg, Boulas, Chorongiewski, & Gerwert, 1999) can be measured; with these advances, transient (in the range of a couple of seconds to nanosecond range) species can be identified from parent species by a specific change in vibrational properties.

Mid- and far-infrared microprobes using synchrotron radiation are used to address heterogeneity problems such as multiple mineral phases in geological specimens and for chemical identification and molecular conformation studies. Infrared radiation from a synchrotron is more intense than that from a conventional laboratory source, but it is still nondestructive. A variety of high-pressure IR cells (transmission, reflectance, and advanced combinations) are available for in situ studies of the interaction between geomaterials and fluids at relevant temperature and pressure conditions. At high concentrations of the active species in the gas/fluid

phase, the attenuated total reflection (ATR) is a natural choice to study surface phenomena; it became a routine, high-throughput laboratory technique in combination with FTIR spectrometry, despite the need to de-convolute the spectra. In advanced applications, it can be paired with the transmission technique used to simultaneously monitor concentration of the gaseous water molecules. Similar to X-ray techniques, it can be used to study orientation-dependent properties. Additionally, micro-ATR (in conjunction with microscope optics) imaging has opened up the areas of study that were previously precluded by inadequate spatial resolution of conventional (macro-) ATR cells. This has applications in analyses of heterogeneous samples with small domain sizes. In practice, micro-spectroscopic mapping is limited to 10–15 μm spatial resolution in traditional laboratory settings.

The effects of the ATR technique on observed spectrum are well characterized. The near-field penetration depth is inversely proportional to the wavelength; therefore, the peak intensity is relatively more attenuated on the higher wavelength side of the spectrum. This may cause a skewed baseline, peak's distortion and changes in its position (shifted toward lower wavenumber side, compared to transmission spectra) and intensity, commonly in spectra of the samples with higher refractive index. The observed change in peak width is attributed to the change in refractive index as a function of wavenumbers, which is more prominent in the case of strong absorption and higher refractive index of the prism. In any case, the prism must have a relatively high (compared to the sample) refractive index for this technique to work properly. When using the ATR technique to measure solid samples, it is necessary to press the sample against the prism. If there is any change in the physical state of the sample due to pressure, these changes will be manifested in obtained spectrum.

IR/Raman spectra can serve as a fingerprint for mineral identification, but they can also provide unique information about the mineral structure, the degree of regularity within the structure, the nature of isomorphic substituents, the distinction of molecular water from structural hydroxyl, and the presence of either crystalline or non-crystalline impurities. Most of the spectroscopic studies on source clays (Clay Minerals Society specimens) have been done in mid-IR (MIR) region but some information about structural OH groups and H_2O was gleaned from overtones

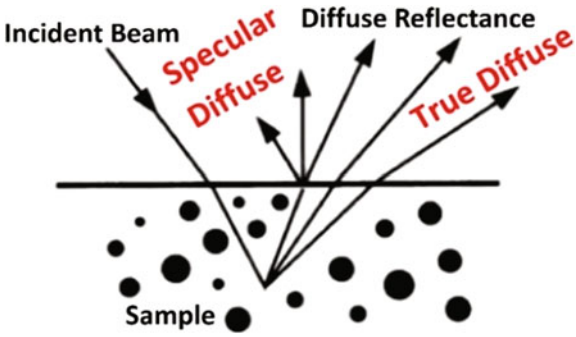

Fig. 5.6 DRIFT spectroscopy

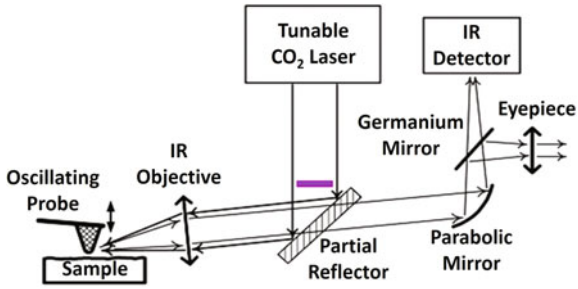

Fig. 5.7 Example of ANSOM design (University of Pittsburgh)

in near-IR (NIR) reflectance spectra as well. Diffuse reflectance infrared Fourier-transform (DRIFT, Fig. 5.6) spectroscopy is most suitable for studies of hydroxyl vibrations of clays in both MIR and NIR regions. Coal and soil samples may also be analyzed by diffuse reflectance as neat powders. To minimize interference effects created by particle sizes (of some larger aggregates) matching the incident IR radiation wavelength, the analyte is mixed with KBr to obtain high quality DRIFT spectra toward the low-frequency region (for clay powder: below 1200 cm^{-1}); however, interaction between the clay sample and KBr may even occur at room temperature. Diffuse reflectance can also be used to study the effects of temperature by configuring the accessory with a heating chamber. The sample should be loosely but evenly packed in the cup to maximize IR beam penetration and minimize spectral distortions.

An advanced variation of the ATR is nearfield scanning optical (or infrared) microscopy (NSOM) taking advantage of the evanescent waves' perturbation near precision-positioned subwavelength features. For example, in the apertureless (ANSOM) mode of operation (Fig. 5.7) such a feature is the atomic force microscope (AFM) cantilever tip. Hence the resolution is limited by the effective radius of curvature and quality of the tip and not by the wavelength of p-polarized illuminating light used in such applications. Lateral resolution of 10–20 nm and vertical resolution of 2–5 nm has been demonstrated for the contrast imaging at a fixed (infrared or visible) excitation wavelength (Romanov & Walker, 2007). As a bonus, AFM is used to measure sub-nano Newton forces (strength of atomic bonding, single-molecule stretching and rupture forces, van der Waals and Casimir-Polder forces, and dissolution forces in liquids)—with demonstrated spatial resolution on the order of fractions of a nanometer.

Although high-contrast ANSOM images have been observed using infrared (1650–1950 cm^{-1}) laser excitation, the interpretation of the near-field spectral features is not straightforward and generally requires rigorous simulations. Several advancements in experimental techniques and instrumentation (such as second-harmonic detection, homo- and heterodyning, and phase-shifting interferometry) simplified the methodology and improved the signal-to-noise ratio; but the near-field infrared detection remains in its nascent state and is primarily limited to advanced scientific experimentation.

The above techniques can provide a wealth of information about a variety of the natural materials; and methodology for examination of the structure and composition of minerals keeps advancing rapidly. However, classification of 2:1 phyllosilicates (packets of the discrete layers composed of two tetrahedral sheets coordinated to a central octahedral sheet, with shared oxygens) remains a problem. The scientists still do not fully understand the interactions that occur at the surfaces or interfaces. Clay mineralogists emphasize importance of the layer charge for their characterization—arguably, the most significant characteristic of such minerals. For homoionic clay minerals, the charge distribution between the sheets as well as the total layer charge may be estimated from the occupancy of elements in the tetrahedral and octahedral sheets, based on the structural formula. Determination of the layer charge based on the basal spacing expansion after cation exchange (e.g., with alkylammonium cations of varying chain lengths) proved to be a more practical (albeit time-consuming) approach, as it is not always possible to accurately derive the structural composition due to persistent contaminants. Alternatively, infrared spectroscopy permits semi-quantitative determination of the total layer charge for NH_4^+-exchanged clays via measurement of the NH_4^+ ν_4 deformation band intensity using a calibration curve. However, it is important to remember that any procedure involving cation exchange in solution, with subsequent drying may change the aggregate properties of the specimen.

Differentiation between the octahedral and tetrahedral charges is possible but requires advanced scientific studies tailored to specific mineral structures. For example, saturation of dioctahedral (but not trioctahedral!) smectite with Li^+ and heating at 200–300 °C may lead to migration of the small Li cations towards free octahedral (but not tetrahedral!) vacancies where they neutralize the negative charge imbalance arising from isomorphous ionic substitutions in the structure of octahedral sheet. This experimental evaluation is compromised, to some extent, by the variable (pH-dependent) positive charge of the crystal-edge sites.

When a solid mineral comes into contact with a liquid, its surface acquires an electric charge due to unsatisfied structural charge imbalance, ionization, broken bonds, differential dissolution, and sorption of charged species from the liquid. Generally, behavior of the fine (colloid-sized) solid particles in the solution is controlled by the ζ-potential (the electric potential at the slipping plane that separates mobile fluid from fluid attached to the particle's surface) which indicates the degree of electrostatic repulsion between adjacent, similarly-charged particles in a dispersion.

In practice, researchers tend to modify available experimental techniques to suit particular systems and phenomena under investigation. Frequently, multiple techniques are intertwined in a complex experimental setup to simultaneously collect as much relevant information as possible. Such advances generally go hand-in-hand with advances in conceptual understanding of the experimental observations. In the following chapters, that will be demonstrated on research examples related to interaction of greenhouse gases with clay systems.

References

Ahn, J. H., & Buseck, P. R. (1990). Layer-stacking sequences and structural disorder in mixed-layer illite/smectite: Image simulations and HRTEM imaging. *American Mineralogist, 75*(3–4), 267–275.

Amarasinghe, P. M., Katti, K. S., & Katti, D. R. (2008). Molecular hydraulic properties of montmorillonite: A polarized fourier transform infrared spectroscopic study. *Applied Spectroscopy, 62*(12), 1303–1313.

Brigatti, M. F., & Mottana, A. eds. (2011). Layered mineral structures and their applications in advanced technologies. *EMU Notes in Mineralogy* (Vol. 11). ISBN: 978-0-903056-29-8.

Dong, H., & Peacor, D. R. (1996). TEM observations of coherent stacking relations in smectite, I/S and illite of shales; evidence for MacEwan crystallites and dominance of 2 M polytypism. *Clays and Clay Minerals, 44*(2), 257–275.

Drits, V. A. (1987). Mixed-layer minerals: Diffraction methods and structural features. In *Proc. International Clay Conference, Denver, 1985* (pp. 33–45). Bloomington, IN: The Clay Minerals Society.

Fenter, P., & Lee, S. S. (2014). Hydration layer structure at solid–water interfaces. *MRS Bulletin, 39*(12), 1056–1061.

Ferrage, E., et al. (2011). Hydration properties and interlayer organization of water and ions in synthetic Na-smectite with tetrahedral layer charge. Part 2. Toward a precise coupling between molecular simulations and diffraction data. *Journal of Physical Chemistry C, 115*(5), 1867–1881.

Fraundorf, P., Qin, W., Moeck, P., & Mandell, E. (2005). Making sense of nanocrystal lattice fringes. *Journal of Applied Physics, 98*(114308), 1–10.

Giesting, P., Guggenheim, S., Koster van Groos, A. F., & Busch, A. (2012). X-ray diffraction study of K- and Ca-exchanged montmorillonites in CO_2 atmospheres. *Environmental Science and Technology, 46*(10), 5623–5630.

Guthrie, G. D., & Reynolds, R. C. (1998). A coherent TEM- and XRD-description of mixed-layer illite/smectite. *The Canadian Mineralogist, 36*(6), 1421–1434.

Humphries, S. D., et al. (2011). Investigation of Mars clay analogs by remote laser induced breakdown spectroscopy (LIBS). In *Proc. 42nd Lunar and Planetary Science Conference (LPSC)* (p. 1851). The Woodlands, TX: Lunar and Planetary Institute.

Johnston, C. T., Sposito, G., & Erickson, C. (1992). Vibrational probe studies of water interactions with montmorillonite. *Clays and Clay Minerals, 40*(6), 722–730.

Kulipanov, G. N. (2007). Ginzburg's invention of undulators and their role in modern synchrotron radiation sources and free electron lasers. *Physics Uspekhi, 50*(4), 368–376.

Lanson, B., & Champion, D. (1991). The I/S-to-illite reaction in the late stage diagenesis. *American Journal of Science, 291*(5), 473–506.

Loring, J. S., et al. (2012). In situ molecular spectroscopic evidence for CO_2 intercalation into montmorillonite in supercritical carbon dioxide. *Langmuir, 28*(18), 7125–7128.

Lutgens, F. K., & Tarbuck, E. J. (2014). *Essentials of geology* (12th ed.). Upper Saddle River, NJ: Pearson Education Inc.

Madejová, J. (2003). FTIR techniques in clay mineral studies. *Vibrational Spectroscopy, 31*(1), 1–10.

Malla, P. B., et al. (1993). Charge heterogeneity and nanostructure of 2:1 layer silicates by high-resolution transmission electron microscopy. *Clays and Clay Minerals, 41*(4), 412–422.

Mieunier, A., Lanson, B., & Beaufort, D. (2000). Vermiculitization of smectite interfaces and illite layer growth as a possible dual model for illite-smectite illitization in diagenetic environments: A synthesis. *Clay Minerals, 35*(3), 573–586.

Nadeau, P. H. (1985). The physical dimensions of fundamental clay particles. *Clay Minerals, 20* (4), 499–514.

Nadeau, P. H. (1998). Fundamental particles and the advancement of geosciences; response to Implications of TEM data for the concept of fundamental particles. *The Canadian Mineralogist, 36*(6), 1409–1414.

Nadeau, P. H., Tait, J. M., McHardy, W. J., & Wilson, M. J. (1984). Interstratified XRD characteristics of physical mixtures of elementary clay particles. *Clay Minerals, 19*(1), 67–76.

Nieto, F., & Cuadros, J. (1998). Evolution, current situation, and geological implications of the "fundamental particle" concept. *The Canadian Mineralogist, 36*(6), 1415–1419.

Nishikawa, S., & Kikuchi, S. (1928). Diffraction of Cathode rays by mica. *Nature, 121*(3061), 1019–1020.

Peacor, D. R. (1998). Implication of TEM data for the concept of fundamental particles. *The Canadian Mineralogist, 36*(6), 1397–1408.

Rammelsberg, R., Boulas, S., Chorongiewski, H., & Gerwert, K. (1999). Set-up for time-resolved step-scan FTIR spectroscopy of noncyclic reactions. *Vibrational Spectroscopy, 19*(1), 143–149.

Ras, R. H. A., et al. (2003). Polarized infrared study of hybrid Langmuir—Blodgett monolayers containing clay mineral nanoparticles. *Langmuir, 19*(10), 4295–4302.

Reynolds, R. C. (1980). Interstratified clay minerals. In G. Brindley & G. Brown (Eds.), *Crystal structures of clay minerals and their X-ray identification* (3rd ed., pp. 249–304). London: Mineralogical Society.

Rietveld, H. M. (1969). A profile refinement method for nuclear and magnetic structures. *Journal of Applied Crystallography, 2*(2), 65–71.

Roberson, H. E., Weir, A. H., & Woods, R. D. (1968). Morphology of particles in size-fractionated Na- montmorillonites. *Clays and Clay Minerals, 16*(3), 239–247.

Romanov, V., & Walker, G. C. (2007). Infrared near-field detection of a narrow resonance due to molecular vibrations in a nanoparticle. *Langmuir, 23*(5), 2829–2837.

Sposito, G., & Prost, R. (1982). Structure of water adsorbed on smectites. *Chemical Reviews, 82* (6), 553–573.

Suvorov, A., Cai, Y. Q., Sutter, J. P., & Chubar, O. (2014). Partially coherent wavefront propagation simulations for inelastic x-ray scattering beamline including crystal optics. In *Proc. SPIE 9209, Advances in Computational Methods for X-Ray Optics III* (p. 92090H). Bellingham, WA: SPIE.

Suzuki, S., Prayongphan, S., Ichikawa, Y., & Chae, B. G. (2005). In situ observations of the swelling of bentonite aggregates in NaCl solution. *Applied Clay Science, 29*(2), 89–98.

Udvardi, B., et al. (2014). Application of attenuated total reflectance Fourier transform infrared spectroscopy in the mineralogical study of a landslide area, Hungary. *Sedimentary Geology, 313,* 1–14.

Chapter 6
Experimental Studies: Molecular Interactions at Clay Interfaces

Lei Hong and Vyacheslav Romanov

We must be clear that when it comes to atoms, language can be used only as in poetry. The poet, too, is not nearly so concerned with describing facts as with creating images and establishing mental connections.

—Quotations by Niels Bohr.

Science is the belief in the ignorance of experts.

—Quotations by Richard P. Feynman.

Abstract Water vapor, carbon dioxide, and methane have extensively been studied because of their significant impact on energy security and environmental sustainability. Interaction of water with clay minerals strongly depends on the exchangeable cations in the interlayer. Interlayer H_2O forms a coordination shell around cation through temperature-dependent interaction between the cation and water oxygen—three distinct mechanisms have been identified. Various forms of CO_2 and its interaction with geomaterials include supercritical fluid, gas dissolved into brine, and (bi-) carbonate species. Due to the heterogeneity of geological formations, the interactions between geomaterials and injected fluids (and gas-in-place) are very complex and may result in dramatic changes in the rock formations. Mineral precipitation and dissolution reactions under low-water conditions have not received much attention so far, although water-bearing CO_2 can mediate important geochemical reactions; which is also true for water-saturated samples exposed to dry CO_2. In swelling smectites, the term "nano-confinement" was introduced to characterize the initial trapping of CO_2 molecules in the inter-

L. Hong (✉)
U.S. Department of Energy, NETL–AECOM, Pittsburgh, USA
e-mail: Lei.Hong@netl.doe.gov

V. Romanov
U.S. Department of Energy, National Energy Technology Laboratory (NETL), Pittsburgh, USA
e-mail: romanov@netl.doe.gov

© Springer International Publishing AG 2018

V. Romanov (ed.), *Greenhouse Gases and Clay Minerals*, Green Energy and Technology, https://doi.org/10.1007/978-3-319-12661-6_6

layer, with subsequent conversion to carbonates. The nano-confined CO_2 is distinguished by the red-shift in asymmetric-stretch vibration, which depends on the hydration state as confirmed by exposure to elevated temperatures. The presence of CO_2 and H_2O has a considerable effect on CH_4 sorption on clays. The idea of utilizing competitive sorption of CO_2 and CH_4 on shales in depleted reservoirs for enhanced gas recovery and concomitant carbon storage has been gaining momentum and for a good reason as discussed in this chapter.

Of all the greenhouse gases, water vapor, carbon dioxide and methane are the three gases which have extensively been studied because of their significant impact on energy security and environmental sustainability. Methane (CH_4) is the primary component of natural gas, a common fuel source. Many studies have proven that CO_2 more strongly adsorbs on clays than CH_4 does. Therefore, geologic sequestration of anthropogenic CO_2 could provide dual benefits: an environmental benefit from long-term CO_2 storage, and an economic benefit from the enhanced gas recovery (EGR) due to displacement of CH_4 by CO_2 from adsorption sites (Chap. 3). However, the reality is more complex because of the presence of water. Ubiquitous water molecules are present in clays (clay minerals) in a variety of states, such as free water, structural hydroxyl groups, water molecules adsorbed on clay surfaces, and interlayer water. Water has a substantial effect on interaction of CO_2 and CH_4 with clay minerals in geologic formations.

To better understand the mechanisms of H_2O, CO_2 and CH_4 sorption on clay minerals let us compare the physical properties of these molecules. As shown in Table 6.1 the three molecules have distinctly different physical properties. Water is a polar molecule which can form hydrogen bonds on the mineral surfaces and be attracted by the cations forming hydration shell. On the other hand, CO_2 is a nonpolar but highly polarizable molecule with large quadrupole moment, whereas CH_4 is none of the above; which leads to CO_2 having preferred adsorption on clay mineral surfaces over CH_4. More interestingly, a possible electron donor-acceptor affinity can be formed between CO_2 and ions. In comparison, association between CH_4 and clays is a result of van der Waals forces.

Specific features of clay minerals, such as the active ion's size, valence, electronegativity, and hydration energy, directly and indirectly, affect their interaction with the nature molecules.

Table 6.1 Physical properties of H_2O, CO_2 and CH_4 (Li, Kuppler, & Zhou, 2009)

Molecule	Kinetic diameter (Å)	Polarizability volume (10^{-25} cm^3)	Dipole moment (D)	Quadrupole moment ($\times 10^{-11}$ B)
H_2O	2.65	14.8	1.85	N/A
CO_2	3.30	29.1	0	–41
CH_4	3.80	25.9	0	0

6.1 Water and Clay Minerals

Interaction of water with clay minerals has been extensively studied for over a century. It strongly depends on the exchangeable cations located in the interlayer. Water molecules form a coordination shell around the cations through interaction between the metal ion and water oxygen. The dynamic motion of water molecules in the interlayer, such as stretching and bending, can be detected using spectroscopic methods (Moore & Reynolds, 1997).

It has long been known that the adsorbed water in clay interlayer is different from regular liquid water. For example, the density of water in the interlayer space is different from bulk liquid water. Monte Carlo simulations showed that density of water in the interlayer space of Mg- and Na-smectites changes from 0.85 at zero pressure to 1.91 g/cm^3 at 1000 MPa, at 26.84 °C. Experimental measurements (Table 6.2) confirmed that at low water content, the adsorbed water density in clay exceeds liquid water density at 25 °C. Freezing-point measurements also suggested that supercooling is very common in clay-water system (Martin, 1960). All these simulations and experimental results indicate that the adsorbed water on clays has a different structure from bulk liquid water.

Table 6.2 Density of adsorbed water on clay minerals at 25 °C (Martin, 1960)

Minerals	Relative humidity (%)	Water content (mg/g clay)	Density of adsorbed water (g/cm^3)
Montmorillonite	25	116	1.41
	50	166	1.37
	75	284	1.32
	100	460	1.16
	–	2440	1.02
	–	3010	1.02
Kaolinite	25	4	1.68
	50	8	1.12
	75	9	1.03
	100	65	0.99
Illite	25	30	1.36
	50	49	1.17
	75	69	1.08
	100	188	1.04
	–	1038	1.00

6.1.1 Hydroxyl Groups in Water and Clay Structure

Gaseous H_2O molecules have three vibrational modes detected by IR, asymmetric stretch (ν_2), symmetric stretch (ν_1) and bending of the covalent bonds (ν_3), which are 3756, 3657, and 1595 cm^{-1}, respectively (Eisenberg & Kauzman, 1969). However, the fundamental vibrations of water molecules adsorbed on clay are slightly different. Comparing to the free H_2O, both asymmetric (ν_2) and symmetric (ν_1) stretch shift to lower wavenumbers at around 3400 cm^{-1}, while the bending band shifts to higher wavenumbers at around 1630 cm^{-1} (Madejov, Komadel, & Madejová, 2001; Madejová, 2003). However, it is extremely difficult to differentiate the spectrum of OH in water from hydroxyl groups composing clay structure (Heller-Kallai, 2001). The vibrations of structural hydroxyl groups are strongly affected by the local environments, including the cations forming coordination patterns with OH, hydrogen bonding, and specific electronic fields induced by the surrounding ions (Farmer, 1968). It is also interesting to observe that the absorption bands of water shift along with the changes in strength of hydrogen bonding. When hydrogen bonding is stronger, the stretching bands move to lower wavenumbers; reversely, the bending band moves to higher wavenumbers (Fukuda, 2012; Fukuda & Shinoda, 2008). The water absorption spectrum in clay is very complex depending on the local environment around the water molecules (Steiner, 2002). Simply put, there are two major types of H_2O molecules in minerals, either coordinating to a cation or forming a hydrogen bonding with structural oxygen (Fukuda & Shinoda, 2011; Fukuda, Yokoyama, & Kirino, 2009). In general, the stretching frequency of O–H increases with the increase of the O···O and O···H distance (Steiner, 2002). It can be fitted to exponential regression function, with the O···O and O···H distance (Libowitzky, 1999). Beside hydrogen bond distance, another preeminent factor determining the position of OH stretching band of water is how many hydrogen bonds a water molecule can form with adjacent molecules. The coordination number of a given water molecule can be as high as five at room temperature; however, most molecules in liquid water participate in two hydrogen-bonded configurations with one strong donor and one strong acceptor hydrogen bond (Head-Gordon & Johnson, 2006; Wernet et al., 2004).

Formation of hydrogen bonds generally weakens OH oscillator strength. As a result, the frequency of OH stretching band shifts to a lower frequency region (Brubach et al., 2005). As shown in Fig. 6.1, the shift of absorption band of structural OH in chalcedony to higher frequency is ascribed to a slight increase in hydrogen bond distance as temperature increases. In contrast, a relatively steeper shift (15 cm^{-1}/50 °C) of the water OH vibration with temperature increase can be the result of a hydrogen bond breakdown at elevated temperature. With reduction in hydrogen-bonds density, the water stretching band shifts to a higher frequency region (Fukuda & Nakashima, 2008; Lu, Brown, Liotta, & Eckert, 2001; Lu et al., 2002).

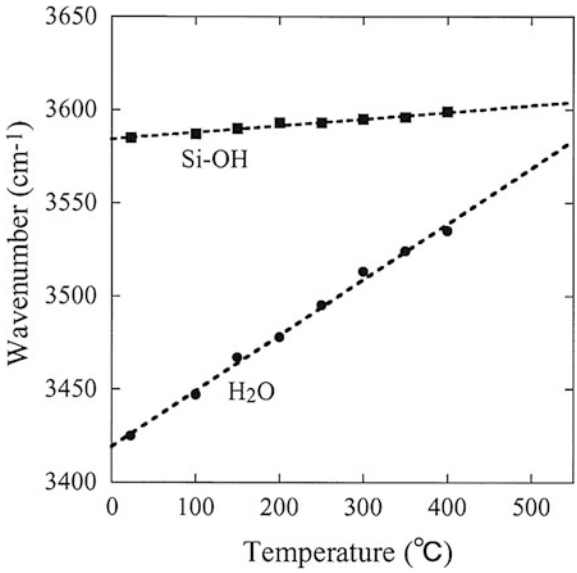

Fig. 6.1 The absorption bands of Si-OH and water in chalcedony, shift with temperature (Fukuda & Nakashima, 2008)—used with permission

6.1.2 Interactions of the Lattice Oxygens and Water Molecules

In montmorillonite and hectorite, with weak hydrogen bonds between the interlayer water and surface oxygens, there is a minor OH stretching peak observed near 3620 cm^{-1}. A broad absorption band near 3400 cm^{-1} is ascribed to the hydrogen bonds between the water molecules. A shoulder near 3250 cm^{-1} is due to the overtone of water bending vibration at 1630 cm^{-1}. The strength of hydrogen bonds to the lattice oxygens is highly dependent on the ability of electron donation by silicate layers, which is determined by isomorphous substitutions. A substitution in a tetrahedral layer, e.g., in saponite or vermiculite, creates a negative charge distribution over at least three surface oxygen atoms coordinated to tetrahedral Al^{3+}, which is more localized than in the case of the substitution occurring in octahedral layer, e.g., in montmorillonite and hectorite, where the negative charge is distributed over at least ten surface oxygen atoms of Si–O framework (Farmer & Russell, 1971; Farmer, 1971). A typical absorption pattern of H_2O molecules interacting with lattice oxygens includes a high-frequency band above 3500 cm^{-1} ranging from 3570 to 3650 cm^{-1}, a relatively lower frequency band below 3500 cm^{-1} located at 3350–3430 cm^{-1}, and a low-frequency shoulder at 3230 cm^{-1}. The bands of the highest frequency, i.e., above 3500 cm^{-1}, are ascribed to the OH groups which are forming weak hydrogen bonds to surface oxygens, evidenced by the high angle of O–H bond to the plane of the silicate sheet. The bands below 3500 cm^{-1} are attributed to the OH groups bonded to lattice oxygens and are stronger than those observed above 3500 cm^{-1}. These OH groups are found

to be nearly parallel to the plane of the silicate sheets. The lowest frequency, usually a shoulder, is due to the overtone of water bending band at 1630 cm^{-1} (Farmer, 1971).

In case of saponite, hydrogen bonds formed between water and the oxygens involved in Si–O–Si framework give rise to absorption band near 3610 cm^{-1}. The hydrogen bond is weak because oxygen in the linkage is not a strong electron donor. However, oxygens in Al–O–Si linkage, after Si is replaced by Al in tetrahedral layer, have highly concentrated negative charges and form stronger hydrogen bonds; which gives an absorption band near 3400 cm^{-1}. This band is overlapping with the vibration band of OH, associated with water-water linkages. As a result, saponite shows a similar absorption bands with montmorillonite and hectorite, but with an enhanced intensity near 3400 cm^{-1}. Vermiculite, similarly, has highly concentrated negative charges of oxygens of the Al–O–Si linkages in tetrahedral layer; however, this charge also distributes over the adjacent oxygens of the Si–O–Si linkages. The spread negative charge over the silicate layer makes the band near 3610 cm^{-1} disappear, distinguishing it from saponite. Similar to saponite though, the main band near 3400 cm^{-1} was identified; which corresponds to hydrogen bonds forming between water molecule and the surface oxygens and/or other water molecules. It is noted that this principal band is sensitive to the nature of the exchangeable cations in the interlayer, which is explained as follows (Farmer, 1974).

6.1.3 Interactions of the Interlayer Cations and Water Molecules

There are three distinct mechanisms of water interaction with the interlayer cations (Farmer, 1971):

(a) Water molecules directly coordinate to inorganic cations. The position of OH vibration band was found to be related to the polarizability of cations. Using infrared spectroscopy, Russell and Farmer (1964) investigated water properties in smectites with two types of exchangeable cations based on polarizing power. The first cation group including Na^+, K^+, and NH_4^+ has lower polarizability. Water molecules were found to directly bond to these cations, giving rise to an unusually strong IR absorption at 1630 cm^{-1}. This type of water can be removed by heating at 150–200 °C in montmorillonite and at 150–300 °C in saponite. The other cation group including Li^+, Ca^{2+}, and Mg^{2+} has higher polarizability. The water molecules directly coordinated to these cations retain in that position at high temperature up to 350 °C. However, displacement of water molecules from the outer coordination sphere begins at about 100 °C (Russell & Farmer, 1964).

Each type of the interlayer cation forms a distinct coordination sphere with water, which is reflected in the changes of IR absorption bands. Figure 6.2 illustrates the IR absorption bands of montmorillonite, MX-80 samples saturated with

different electrolytes solutions, KCl, NaCl, $CaCl_2$, and $MgCl_2$, using ATR. All the spectra have a band near 3618 cm^{-1} which belongs to the OH stretching of structural hydroxyl groups. The band near 3400 cm^{-1} is attributed to OH stretching of water. Figure 6.2 shows that the position of OH stretching of water shifts to lower wavenumber in the order of K^+, Na^+, Ca^{2+} and then Mg^{2+}. The order corresponds to the increase of ion polarizing power, which is an indicator of the ability of a cation to distort an anion's configuration. Mg^{2+} has the strongest polarizing power of all four cations and forms stronger hydrogen bonds with water molecules, causing the OH stretching band shift by about 50 cm^{-1} to lower wavenumber compared to the K^+ saturated samples. Cations with stronger polarizing power promote more water adsorption in the interlayer, which is evidenced by the increasing intensity of the water band (Madejová, 2003).

(b) Water molecules act as a bridge to other water molecules and to organic molecules. The strength of the hydrogen bond again is a function of polarizing power of a cation. The fact that water in the outer coordination sphere in Ca- and Mg-saponite persists up to 100 °C suggests that a structure of double-layers of water molecules hydrating Ca^{2+} and Mg^{2+} is particularly stable in saponite (Russell & Farmer, 1964). The same group studied stretching vibrations of water in hectorite

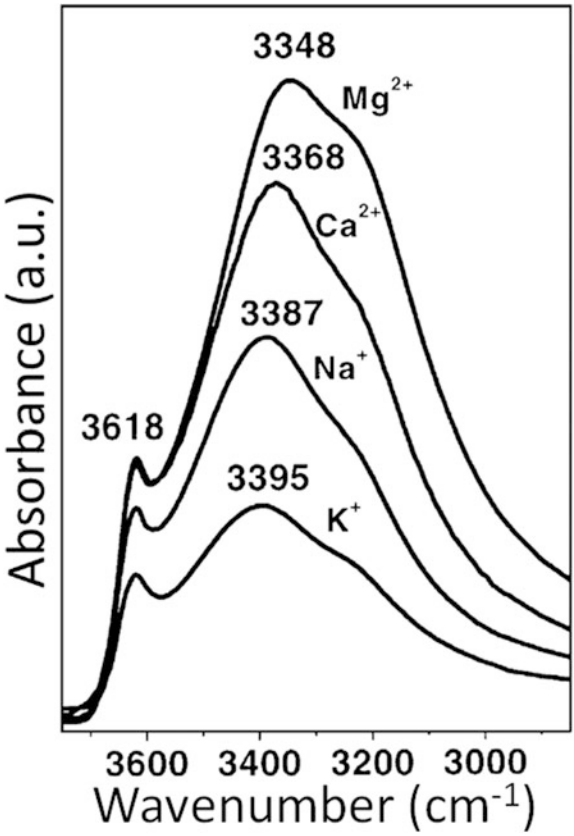

Fig. 6.2 Absorption bands of OH stretching of montmorillonite MX-80 samples, saturated with different cations; reprinted from (Madejová, 2003) Copyright (2003) with permission from Elsevier

saturated with different interlayer cations. The bands observed near 3630 cm^{-1} were attributed to a weak hydrogen bond to the oxygen of the silicate lattice and the bands near 3425 cm^{-1} correspond to water-to-water hydrogen bonds. However, there are strong broad bands developed below 3300 cm^{-1} as well, at 3234 cm^{-1} for Mg^{2+} and at 3230 cm^{-1} for Cu^{2+}. In K-hectorite, a relatively stronger band at 3424 cm^{-1} as compared to the one at 3632 cm^{-1} is ascribed to the water molecules directly bonded to K^{+} cation. These hydrogen bonds are like those in liquid water. However, Mg^{2+} and Ca^{2+} have stronger polarizing power and form stronger hydrogen bonds to water in the outer sphere. As a result, the broad bands below 3300 cm^{-1} are observed for Mg^{2+} and Ca^{2+} hectorite.

This hydrogen bond to the outer-sphere water molecules is relatively weak in the presence of polar organic molecules such as pyridine and nitrobenzene. Immediately after having been removed from pyridine, Mg-hectorite shows a band at 3049 cm^{-1}, indicating a double hydrogen bond formed between the protons of the directly coordinated water molecules on Mg^{2+} and two pyridine molecules as shown in Fig. 6.3a. One of the two pyridines is promptly lost after exposure to air. Accordingly, the d-spacing decreases from 23 to 14.8 Å during the loss of the pyridine molecule in Fig. 6.3b (Farmer & Russell, 1967).

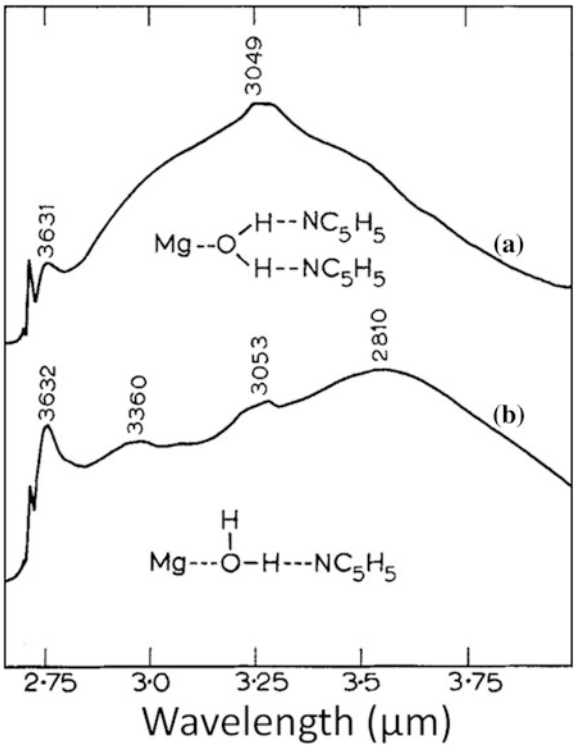

Fig. 6.3 Stretching vibrations of water in Mg-hectorite: **a** double hydrogen bonds to pyridine; **b** single hydrogen bond to pyridine—reproduced with kind permission of the clay minerals society, publisher of *Clays and Clay Minerals* (Farmer & Russell, 1967)

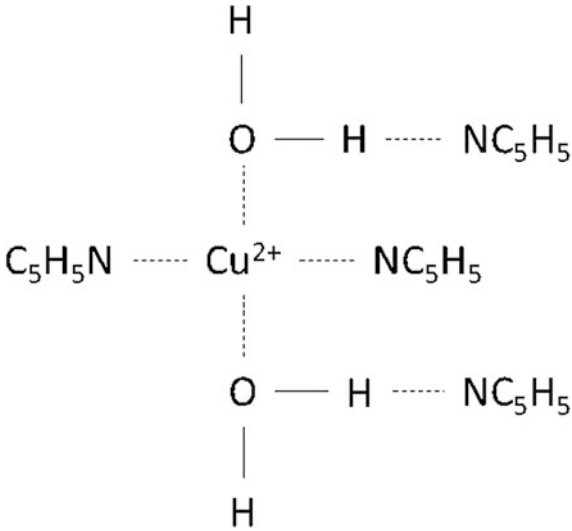

Fig. 6.4 Complex formed between Cu^{2+} with pyridine through direct coordination or through a water molecule by hydrogen bonding (Farmer & Mortland, 1966)

Water molecules acting as hydrogen bonding bridge for pyridine were also identified for montmorillonite saturated with Mg^{2+} and Ca^{2+}. Another complex is formed by Cu^{2+} and pyridine as shown in Fig. 6.4, in which pyridines are linked to Cu^{2+} through direct coordination as well as hydrogen bonding via water molecules (Farmer & Mortland, 1966).

(c) Water molecules can protonate adsorbed bases in the interlayer space of layer silicates. When water molecules coordinate to polarizing cations (hydrated metal cations) their ability to donate protons is enhanced compared to a liquid water molecule. The overall protonation reaction can be explained by the following equation

$$M(\mathrm{H_2O})_x^{+n} + B \leftrightarrow \left[M\,\mathrm{OH}(\mathrm{H_2O})_{x-1}\right]^{+n-1} + BH^+,$$

where M is a metal (cation) and B is an adsorbed base, such as urea or ammonia. The protonation power of hydrated cations is dependent on the nature of the cation. The cations with higher electronegativity tend to have a stronger ability of proton donation than those with lower electronegativity. For example, hydrated Al^{3+} is more prone to donate a proton than hydrated Na^+ is. It was found that urea can be protonated at montmorillonite surfaces that are saturated with H^+, Al^{3+}, or Fe^{3+}, but not if by Na^+ or Ca^{2+} (Mortland, 1970). Another important factor affecting the water's proton-donation ability is the amount of water adsorbed in the clay. It is interesting that the more water is adsorbed, the less proton-donating capability water molecules have. Mortland and Raman (1968) suggested that the polarizing power of cations might be highly distributed and diminished with a large amount of water. Oppositely, less water makes the polarizing power more concentrated, accordingly enhancing proton-donating capabilities (Mortland & Raman, 1968).

Farmer and Mortland (1966) reported that pyridine was associated with Mg^{2+} through the water molecules directly coordinated to the cation in hydrated montmorillonite; however, pyridinium ions were observed in the condition of dehydration. In another study, Ca-montmorillonite samples were exposed to NH_3. Only 16 meq of NH_4^+ per 100 g of clay was identified when there was 40.7% water in the clay; in contrast, 80 meq of NH_4^+ per 100 g was identified when the water content decreased to 5.9% (Mortland & Raman, 1968). These studies confirmed that water content has a substantial effect on the proton-donating capability in clay.

6.1.4 Temperature Effects

Interaction between water molecules and the cations can be diminished at elevated temperatures. Figure 6.5 shows IR spectra of SAz-1 montmorillonite samples that were heated and held at 50 °C for 5, 10, 15, 20, and 60 min (from top to bottom, beginning with the unheated sample) (Madejová, 2003). The interlayer cation in the SAz-1 samples was Li^+. In Fig. 6.5a the sharp and strong band at 3616 cm^{-1} is due to the OH stretching vibration of the structural OH groups in clay mineral. The broader band at 3423 cm^{-1} refers to the overlapping asymmetric (ν_2) and symmetric (ν_1) stretching vibrations of OH in adsorbed water. Figure 6.5b shows a change in the bending vibration related to ν_3 (H–O–H) band of the water adsorbed on

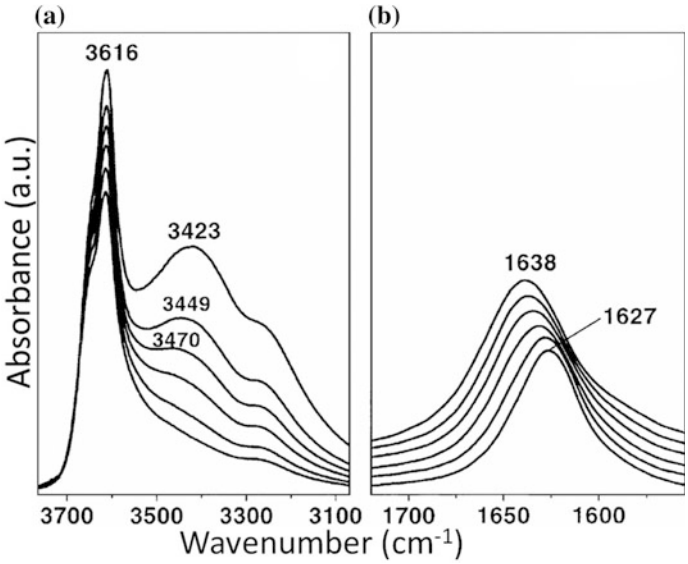

Fig. 6.5 IR absorption bands of water in Li–SAz-1 montmorillonite at 50 °C with changing hold time: **a** OH stretching vibration bands and **b** OH bending vibration bands; reprinted from (Madejová, 2003) Copyright (2003) with permission from Elsevier

montmorillonite. The IR bands of both stretching and bending vibrations fade with increasing treatment time at 50 °C. Simultaneously, the stretching vibration band shifts to higher wavenumber and bending vibration band shifts to lower wavenumber. This observation indicates that dehydration was taking place during the heat treatment at 50 °C (Madejová, 2003). With the removal of water molecules from the outer coordination sphere, the evidence of direct water coordination to the cations as well as to clay layer oxygens can be seen more clearly, with FTIR spectroscopy.

Instead of holding the samples at a constant temperature and changing the hold time, Hur et al., (2013) investigated the dehydration of SWy-2 montmorillonite (after exposure to CO_2) with FTIR spectroscopy using a diffuse-reflectance (DRIFT) mode in a temperature-controlled environmental chamber—at each step, the sample was allowed to equilibrate for 10 min in high-purity helium flow, before the spectra were collected. Intensity of the absorption band around 1630 cm^{-1}, owing to the bending vibration of adsorbed water, steadily decreased with temperature and became almost undetectable at 450 °C, indicating complete dehydration of the clay. Similar to the band shift in Fig. 6.5, the H_2O absorption band shifted to lower wavenumbers as the temperature was increasing.

Clay dehydration upon heating results in predominantly direct water molecules coordination to the interlayer cations and the surface oxygens of the clay layer. For example, Fig. 6.6 demonstrates a possible configuration of Mg^{2+} and three water

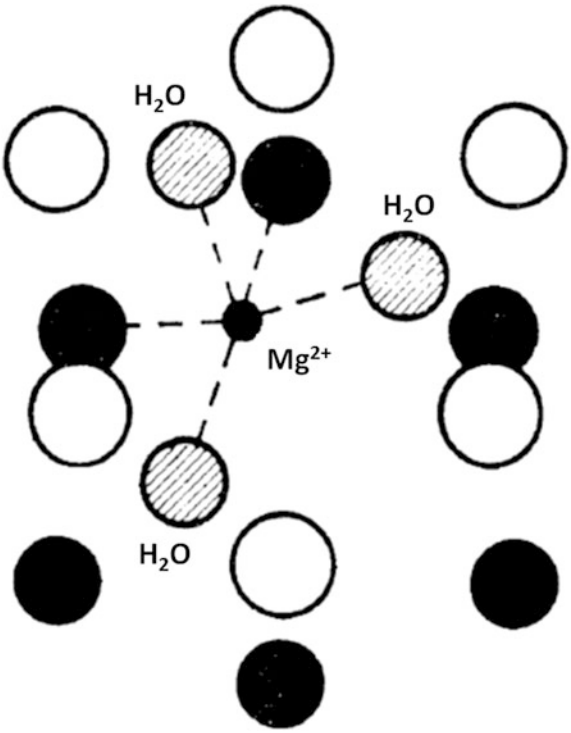

Fig. 6.6 The interlayer Mg^{2+} and water molecules coordinated to clay oxygens; *open circles* and *filled circles* represent the upper and lower surface oxygens of the silicate layer

molecules coordinating to the surface oxygens on two successive silicate interlayers. Mg^{2+}, located between two silicate layers, directly coordinates to two neighboring oxygens on one silicate interlayer and three water molecules which could form hydrogen bonds to each of the six charge-bearing surface oxygens on the opposing layer. This is a relatively lower energy configuration compared to the one in which Mg^{2+} directly binds to three oxygens. The proposed structure agrees with the thermo-gravimetric and spectroscopic results reported by Farmer and Russell (Farmer & Russell, 1971; Russell & Farmer, 1964).

6.2 CO_2 and Clay Minerals

Various forms of CO_2 and its interaction with geomaterials, investigated with the goal of storage of anthropogenic CO_2 in geologic formations, include single-phase supercritical fluid ($scCO_2$), gas dissolved into brine, bicarbonate species, and carbonate solids. Due to heterogeneity of the geological formations, with a wide variety of complex natural environments, the interactions between geomaterials and injected fluids (as well as gas-in-place) are very complex and may result in dramatic changes in the rock formations as discussed in Chap. 3. This can be of major concern if the natural seals of the geological storage formation are affected (Busch et al., 2016) by either mineral dissolution or precipitation, or by various CO_2-induced mechanical strains, volumetric and structural changes in clay minerals as discussed in the next chapter. The focus of the environmental and geo-science research has been on CO_2 sorption and dissolution within potential storage formations and its role in geochemical reactions (Romanov et al., 2015). Renewed interest in such research is fueled by recent successes with CO_2 mineralization in basalt formations, particularly in the U.S. and Iceland. Most of the bedrock, on land and offshore Iceland consists of basalt that can be used for injection of CO_2, fully dissolved in water. Alternatively, scientists are increasingly interested in flood basalts (formed from lava flows millions of years ago) as potential sites for the permanent storage of CO_2, due to their vast presence, particularly in North America.

Recent studies on CO_2 adsorption on shales provided evidence of significant storage potential of shaly caprock that could not be attributed to CO_2 dissolution in water or sorption on organic matter alone. Earlier, Nuttall et al., (2005) found a positive correlation between CO_2 sorption capacity and organic carbon content, but no correlation with the clay mineral content. Some portion of CO_2 uptake is most likely related to sorption on clay minerals. The exact processes and mechanisms are not quite understood yet. For example, water molecules usually compete with CO_2 for active surface sites. Yet, CO_2 sorption capacity of certain (particularly, kaolinite-rich) shales tends to decrease with decreasing moisture content. CO_2 adsorption onto kaolinite surface initially increases with increasing CO_2 density in free phase, reaching a peak near 0.4 g/cm^3, before declining rapidly due to a competition between the surface kinetics and energetics of the CO_2–mineral surface

and CO_2–CO_2 interactions; DFT (density functional theory) studies confirmed that CO_2 adsorption at kaolinite surface is favored over CO_2 clustering up to the density of ~ 0.34 g/cm^3 (Schaef et al., 2014a).

Mineral precipitation and dissolution reactions under low-water conditions have not received much attention so far, although the water-bearing CO_2 (water dissolved in liquid or supercritical CO_2) fluids can mediate important geochemical reactions; which is also true for water-saturated samples exposed to dry CO_2. Busch et al., (2009) observed rapid mineralogical changes, predominantly transformation of illite into smectite, in moist mixed clay/shale samples with small particle sizes (<200 μm) after exposure to (initially) dry $scCO_2$. In a study by the Romanov group (NETL) accelerated carbonation was observed in smectites exposed to dry, high-pressure liquid and supercritical CO_2, predominantly within the first 2 days of the exposure. Romanov & Soong (2008) also observed a combination of the manometric sorption isotherm hysteresis, diffuse-reflectance infrared spectroscopy of the trapped-CO_2 fingerprints, irreversible X-ray diffraction pattern changes for the clay interlayer in intermediate hydration state, and HF acid digestion apparently resulting in formation of non-extractable F:CO_2 adducts. The observations corroborated a hypothesis that carbon dioxide molecules can intercalate between the clay layers and become irreversibly trapped there via extreme confinement, which results in formation of carbonates in the longer term. The subsequent validation on montmorillonite lumps suggested that such processes may occur in natural clay deposits at a different rate.

6.2.1 Intercalation of CO_2 in Clay

Intercalation is a process that clay sorbs ions and molecules into the interlayer, frequently resulting in its volume expansion (as further discussed in Chap. 7). CO_2 intercalation in clay/shale had not been sufficiently investigated until the relatively recent findings by the Romanov group (Romanov & Soong, 2008; Romanov, 2013) and others (Michels et al., 2015) showed that it can be significant and even irreversible. The magnitude of near-surface molecular interactions, including intercalation between the surfaces, is governed by surface availability, surface accessibility, and competitive affinity of molecular species under specific temperature and pressure conditions, in a specific environment.

External (micropore) surface areas are typically determined by the B.E.T. method (developed by Brunauer, Emmett, and Teller in 1938) using chemically inert gas sorption isotherms. Availability of clay surfaces for sorption is significantly affected by cation exchange, which tends to first occur at edge sites (making up roughly 20% of the total exchange capacity of montmorillonite, illite and vermiculite—subject to debate) and the outer layer surfaces of the clay aggregates, before affecting the interlamellar sites. Multivalent cations can bind the edges together resulting in wider clay aggregates with corresponding smaller external surface area. Ordering of the clay platelets' orientation by aqueous dispersion or by

smaller cations, like Na^+ and Ba^{2+}, may restrict access to surface areas internal to such "quasi-crystalline" regions and thus dramatically decrease the surface area accessible for sorption of nonpolar molecules. However, experimental evidence suggests that CO_2 molecules are sufficiently polarizable to be able to penetrate between overlapping montmorillonite or illite crystals, thanks to the separation of these regions by residual water molecules.

The B.E.T. surface areas were observed to depend on the nature of clay and on the water content. Internal micropore volume in aggregate particles of clays, such as kaolinite, pyrophyllite, illite, and bentonite is practically inaccessible for the van der Waals type of adsorption at very low (−183 °C and below) temperatures; in halloysite and bentonite, internal pore accessibility may vary with the state of hydration though. The presence of even a few residual water molecules, coordinated with the interlayer cations, greatly facilitates the entry of CO_2 into quasi-crystalline regions of montmorillonite. In vermiculite, with stronger interlayer forces resulting from substitution of Al for Si in the outer tetrahedral sheets of this mineral which is structurally similar to montmorillonite, increasing the size of the interlayer cations does not weaken the forces between layers (unlike in montmorillonite) but coordinated water does facilitate slight edge penetration between the platelets. In fact, large exchangeable cations may clog the clay interlayer access points.

In organoclays (with bentonite or hectorite base) CO_2 molecules adsorb to the surfaces which they can access without appreciably separating the clay platelets. In some (bentonite-based) organoclays' preheating to 100 °C results in sharp increase in the nitrogen surface area. Upon their thermal decomposition, hydrocarbon chains are dehydrogenated and the resulting carbon can separate the clay platelets enough to permit gas molecules to penetrate the interlayer. The hectorite structure slightly favors the hydrogenation step over the montmorillonite's, because of the lower activation energy.

The (scarce but) available excess sorption isotherm data show that CO_2 sorption capacity of the montmorillonite powder is high, comparable to sorption capacity of coal—from multiple geologic formations that were considered a suitable target reservoir for CO_2 sequestration (injection and long-term storage)—but the adsorption-desorption hysteresis is much more pronounced in the clay isotherms. Reproducibility of the clay sorption data is generally poor with respect to the exact amount of residual sorption (Busch et al., 2008; Romanov et al., 2010b) but the hysteresis during the isothermal (55 °C) portion of the test, for the 20% RH equilibrated samples and long (several hours at each pressure step) CO_2-equilibration times, was consistently observed to varying extent (Romanov, Ackman, Soong, & Kleinm, 2009) except for sorption on the clay powder dried by heating in vacuum prior to the tests. The sample weight gain due to CO_2 exposure was much smaller than the weight gain that would correspond to the residual sorbed amount of CO_2 (without accounting for clay dehydration). Hence at least some interlayer water molecules should have been displaced by the CO_2 molecules.

DRIFT spectra provide further evidence that at high pressure (>7 MPa) some CO_2 molecules enter the interlayer and become trapped there for at least several months. The vibrational frequency shifts for CO_2 antisymmetric (asymmetric)

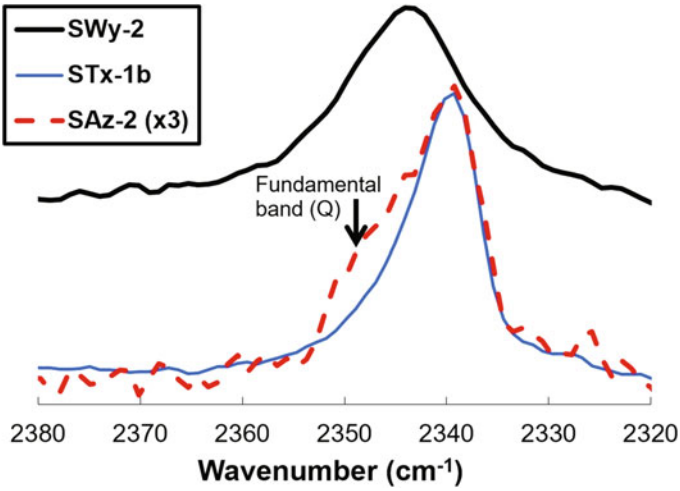

Fig. 6.7 The post-scCO_2 SAz-2 IR reflectance as compared to STx-1b and SWy-2 reprinted from (Romanov, 2013) Copyright (2013) with permission from Elsevier

stretching (ν_3) are quite stable and reproducible, at -5 cm^{-1} for SWy-2 and -10 cm^{-1} (with positive skewness in shape of the peak) for STx-1b; however, the IR-active trapped-CO_2 modes are not as readily detected in the similarly treated lump samples of Arizona montmorillonite, SAz-2 as its spectrum is convoluted by slowly degassing free-phase CO_2 (Fig. 6.7). The relatively small frequency shifts indicate some form of physical trapping. In the long term, the intensity of the shifted (ν_3^*) peaks significantly drops, while the intensity of a carbonate band near 1430 cm^{-1} significantly increases over time in the SWy-2 sample, several months after exposure to CO_2. Persistence of the trapped-CO_2 vibrations in SWy-2 and STx-1b suggests some form of extreme (molecular or nanoscale) confinement that prevents some of the CO_2 molecules from diffusing out of molecular-scale traps, presumably located in the interlayer. The term "nano-confinement" was tentatively introduced to distinguish this trapping mechanism from reversible physisorption. Boiling in hydrofluoric acid at 250 °C (in a failed attempt to chemically release the trapped-CO_2) did not affect the magnitude but shifted the corresponding IR peaks further, in both clays to the wavenumber of 2315 cm^{-1}, identified as asymmetric-stretch vibrational frequencies of the matrix-isolated CO_2 fluoride anion complexes. Remarkably, no distinct CO_2 bending-mode vibrations (ν_2) were detected in these tests (Romanov et al., 2010a).

The rotational features are suppressed as well but do reveal themselves at elevated temperatures (above 200 °C). However, it is not clear if they belong to the same "nano-confined" CO_2 species. The original spectrum of the trapped CO_2 is fully restored upon cooling below 200 °C, in case of the ($\sim$1 W) SWy-2 samples. However, NETL researchers (2014, unpublished data) observed that IR spectrum for the ($\sim$2 W) STx-1b samples appears to blue-shift by $\sim$5 cm^{-1} and broaden

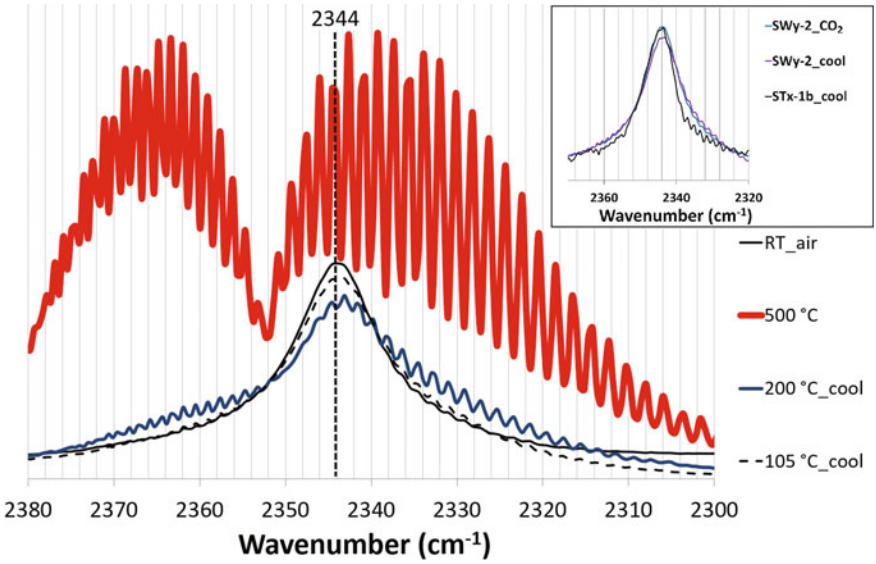

Fig. 6.8 Effect of the heating-cooling cycle on CO_2 spectra in SWy-2; inset: comparison of the spectra for the heated and then cooled SWy-2 and STx-1b ("SWy-2_CO_2"—spectrum collected before heating)

after the heating to 500 °C and subsequent cooling cycle (in dry helium or nitrogen environment) to become almost identical (yet, still positively skewed) to the room temperature (RT) IR spectrum for the SWy-2 montmorillonite (Fig. 6.8). This is attributed to dynamic loss of interlayer water controlled by hydraulic conductivity (Amarasinghe, Katti, & Katti, 2008) eventually resulting in a collapsed ($\sim$1 W) STx-1b configuration; which was indirectly supported by our observation of progressively higher H–O–H bending (deformation) frequency—an indication of the increased mean molecular polarization associated with the increase in surface acidity at reduced basal spacing (Johnston, Sposito, & Erickson, 1992). As the irreversible blue-shift was observed at the temperatures above 200–250 °C, while most of the interlayer water loss occurs below 200-250 °C, it is likely that this phenomenon is primarily related to interlayer width (cf. hysteresis in Chap. 7) rather than cation valence or molar ratio of H_2O/CO_2 in the interlayer.

As mentioned earlier, the (ν_3^*) band of the trapped-CO_2 vibrations is less conspicuous in SAz-2 smectite exposed to $scCO_2$. However, its shape is quite like that of the absorption band in STx-1b, with an extra shoulder peak in the vicinity of the fundamental Q-band (Fig. 6.7). STx-1b has the Ca^{2+}/Na^+ concentration ratio (6.75:1) much higher than that of SAz-2 (1.08:1) and even more so compared to SWy-2 (1:2.67). This trend correlates positively with the relative intensities of the fundamental band (ν_3) and the band (ν_3^*) red-shifted by 10 cm^{-1}, which is associated with the Ca^{2+} interlayer cations (Romanov, 2013). Another band, red-shifted by $\sim$5 cm^{-1}, observed in SWy-2, as a shoulder on the Q-band (ν_3) in Li-smectite

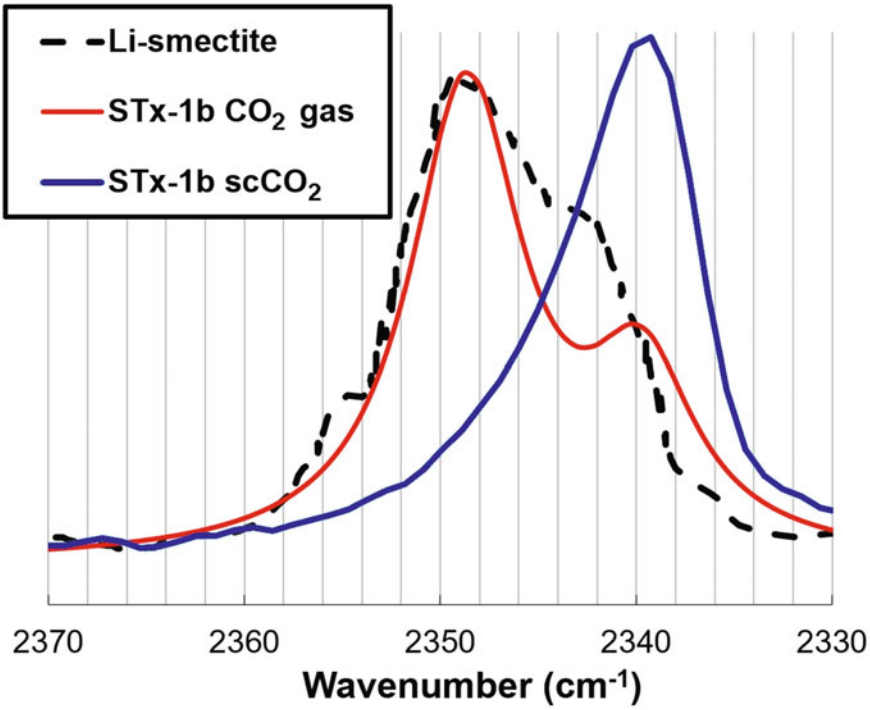

Fig. 6.9 IR absorbance spectrum of Li smectite after exposure to low-pressure CO_2 (Fripiat et al., 1974) as compared to spectra of STx-1b after exposure to gaseous and supercritical CO_2

(Fripiat, Cruz, Bohor, & Thomas, 1974), and even as a very subtle, secondary shoulder in SAz-2 is likely associated with single-charged interlayer cations such as Li^+ and Na^+ (Fig. 6.9). In STx-1b, a similar shape is observed after exposure to gaseous CO_2 but with the shoulder peak shifted by $\sim 10\ cm^{-1}$. After exposure to supercritical CO_2, this shoulder turns into a well-defined, narrow peak with distinct skewness suggestive of anharmonic oscillations.

Even after exposure to lower-pressure (<3.5 MPa) gaseous CO_2, STx-1b and SWy-2 experiments (Romanov et al., 2010b) as well as the Li-smectite systems' IR transmission spectra (Fripiat et al., 1974) already indicate some presence of the trapped CO_2 fingerprint (ν_3^*) that is red-shifted relative to the fundamental Q-band (ν_3) position as a shoulder peak (as shown in Fig. 6.9). The relative peak intensities do change with increasing CO_2 pressure (Romanov et al., 2010b); in STx-1b and SWy-2, only the red-shifted (ν_3^*) absorption peak is observed after exposure to supercritical CO_2 (Fig. 6.7). The in situ absorption band of the CO_2-Cs-smectite system (Fripiat et al., 1974) has only one (ν_3) peak that is slightly broader than in the Li- and Ca-smectites (Fig. 6.9). This may indicate that the red-shifted (ν_3^*) peak is associated with the nano-confined CO_2 molecules, in closer proximity of the clay surface than the CO_2 molecules that are weaker physisorbed onto the clay surface

via dispersive interaction. The confinement in the Cs-smectite interlayer may not be sufficiently close-packed for a noticeable absorption-band splitting. Interestingly though, the in situ data (Fripiat et al., 1974) suggest that CO_2 molecules are much better aligned parallel to the interlayer surfaces in the less-hydrated Cs-smectite, despite the larger spacing insured by the large Cs^+ cations—which implies the cation's proximity to the surface.

Orientation of CO_2 molecules in clay interlayer was simulated as illustrated in Fig. 6.10. Different configurations of CO_2 molecules in the interlayer are corresponding to certain orientation parameter, S(z) values. Configurations of CO_2 molecules perpendicular to clay surface, parallel to the surface and randomly oriented correspond to the values of 0.5, −0.5, and 0, respectively. Per Fig. 6.10, the CO_2 molecules close to interlayer surface are more prone to be oriented parallel to the surface. This is ascribed to the sodium cations being attracted to the charged surface, which would then more likely to result in CO_2 alignment parallel to the surface. When the spacing (H) is smaller than 2 nm, CO_2 molecules in the middle of the interlayer tend to have an angle to the surface. However, when the spacing width becomes larger than 3 nm, CO_2 molecules approach the bulk limit evidenced

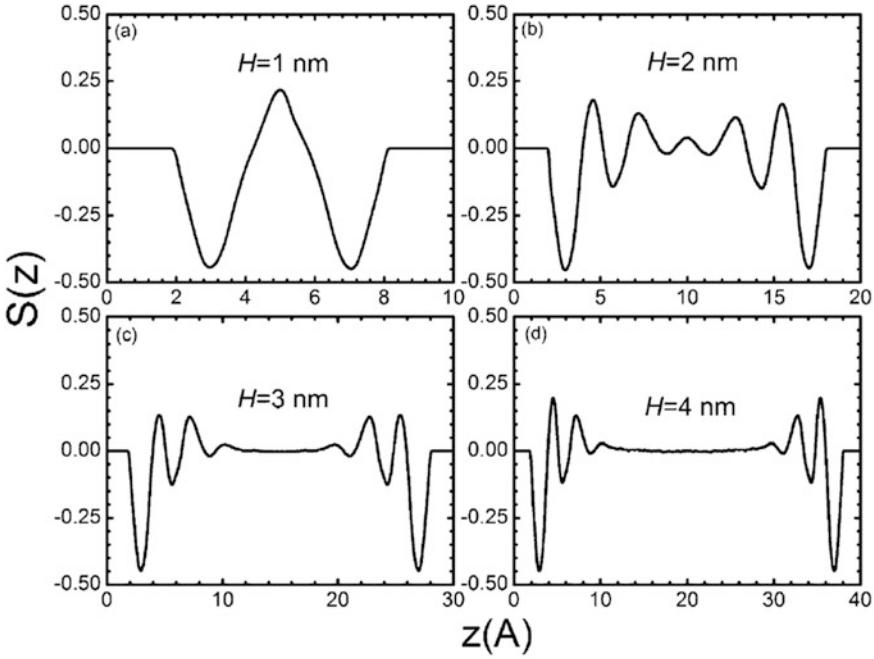

Fig. 6.10 The plot of the orientation order parameters of CO_2 versus spacing distance of interlayer at 4 MPa and 25 °C; reproduced from (Jin & Firoozabadi, 2013) Copyright (2013) with permission from Elsevier

by randomly oriented configuration, because the correlation between charges of the two clay surfaces becomes weaker (Jin & Firoozabadi, 2013).

For understanding CO_2 behaviors in clays and clay minerals, the degree of hydration of clays cannot be ignored and, in most of situations, plays a critical role in the interaction between CO_2 and clays. (This topic is further explored in Chap. 7) Kaolinite (KGa-2) and Ca^{2+} saturated montmorillonite (Ca–STx-1) in $\sim$1 W hydration state were similarly exposed to anhydrous supercritical CO_2 (50 °C and 90 bar) and were studied by in situ analytical techniques, including magic-angle spinning nuclear magnetic resonance (MAS NMR), attenuated total reflection infrared spectroscopy (ATR-IR), and X-ray diffraction (Loring et al., 2012). The in situ techniques demonstrated that there were no identified changes of KGa-2 before and after the interaction with supercritical CO_2. On the other hand, the intercalation of CO_2 in montmorillonite was confirmed by the Pacific Northwest National Laboratory (PNNL) group as well. For example, Fig. 6.11 shows in situ IR spectra of the ion-exchanged STx-1 before and after exposure to supercritical CO_2. The black curve represents the C–O stretching band from bulk supercritical CO_2, which is asymmetric and has a peak at 2336 cm^{-1}. The shoulder at 2360 cm^{-1} and the asymmetric shape are the result of CO_2 rotational-vibrational peaks at high pressure. More frequent collisions of molecules occur at high pressure compared to low pressure, consequently, resulting in rotational relaxation and broadening of P- and R-branch peaks. The C–O stretching bands for KGa-2 exposed to anhydrous supercritical CO_2 nearly overlap with that obtained for bulk CO_2 at the same temperature and pressure, indicating that there is no interaction between CO_2 and

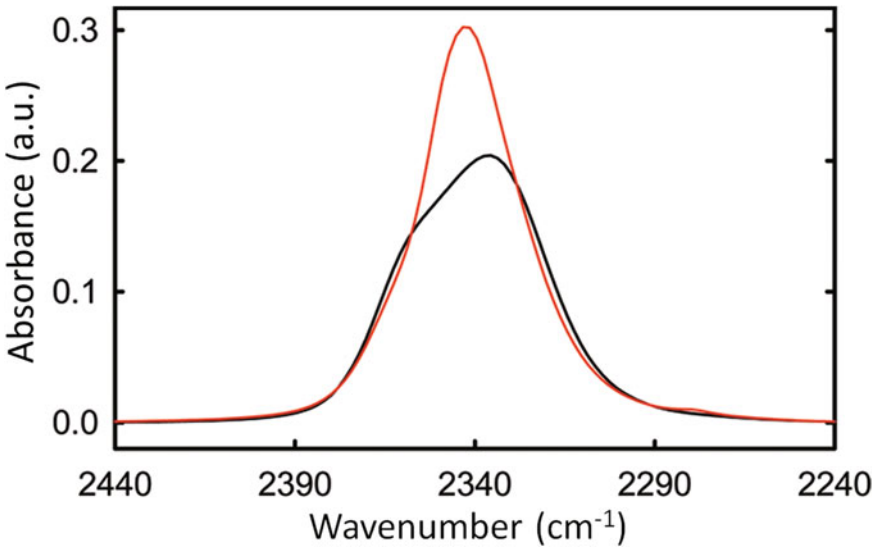

Fig. 6.11 ATR-IR spectra of C–O stretching band of CO_2 before (—) and during (–) the contact with Ca-STx-1—reprinted with permission from (Loring et al., 2012) Copyright (2012) American Chemical Society

KGa-2. However, Ca–STx-1 showed a more intense, symmetric, and sharp peak after exposure to supercritical CO_2. It was suggested that the rotation of CO_2 molecules is constrained due to their intercalation in the interlayer.

6.2.2 *Chemical Reactivity of CO_2 at the Clay Mineral Surfaces*

Among the most common reactions between CO_2 and minerals are reactions to form metal carbonates, especially in the presence of water. In general, carbonation on clay is preceded by a dissolution process in which dissolved cations and bicarbonate anions are formed. Verifiable and permanent nature of in situ mineralization (e.g., mineral carbonation) is likely to lead to its greater public acceptance as carbon storage mechanism (IPCC, 2005) but most researchers agree that the fraction of CO_2 mineralized under typical reservoir conditions will be minor in the first few hundred years (Romanov et al., 2015). Several studies (by the Romanov group and others) have indicated that even dry CO_2 interaction with clay may result in some form of chemical change (such as carbonation) detectable as early as after a few days of exposure. Availability of reactive cations such as Ca^{2+} is the key driver of the process.

Water film on clay mineral's surface affects these processes in a significant way (Miller et al., 2013; Schaef et al., 2013; Loring et al., 2011). It can act as acidified (via formation of carbonic acid) bulk water to facilitate formation of bicarbonate ions, metal cation dissolution, and carbonation followed by precipitation of secondary minerals—the process known as CO_2 mineralization or mineral trapping. The molecular dynamics simulations demonstrated that condensation of the water film on clay mineral surface from the water contained in wet $scCO_2$, especially at high water concentration, is an energetically favorable process (Glezakou, Rousseau, Dang, & McGrail, 2010; Kerisit, Weare, & Felmy, 2012).

Hur et al. (2013) examined formation and stability of the carbonate phase by in situ monitoring of montmorillonite exposed to supercritical CO_2 at 70 °C, for up to 2 weeks. FTIR measurements were performed in transmittance mode using a pelleted sample as well as in diffuse-reflectance mode using an environmental chamber with the clay powder sample. The CO_3^{2-} asymmetric-stretch vibrational band observed within spectral range of 1375–1550 cm^{-1} (Fig. 6.12) was attributed to carbonation. The intensity of the band gradually increased with increasing CO_2 exposure time. This broad band, reflecting a large field-splitting of the ν_3 mode, can be separated into two bands. The primary band at ~ 1420 cm^{-1} was relatively well-defined, but a shoulder band at ~ 1476 cm^{-1} was irregular due to a broadening associated with the field-splitting of the mode (Farmer, 1974; White, 1971).

After exposure to liquid CO_2 ($liqCO_2$) the primary asymmetric stretching band (ν_3) was observed at a relatively smaller wavenumber, ~ 1417 cm^{-1}. The second band, at ~ 1476 cm^{-1} became significantly weaker (after the liquid CO_2) as part of a long tail extending to ~ 1550 cm^{-1}. The corresponding difference between the

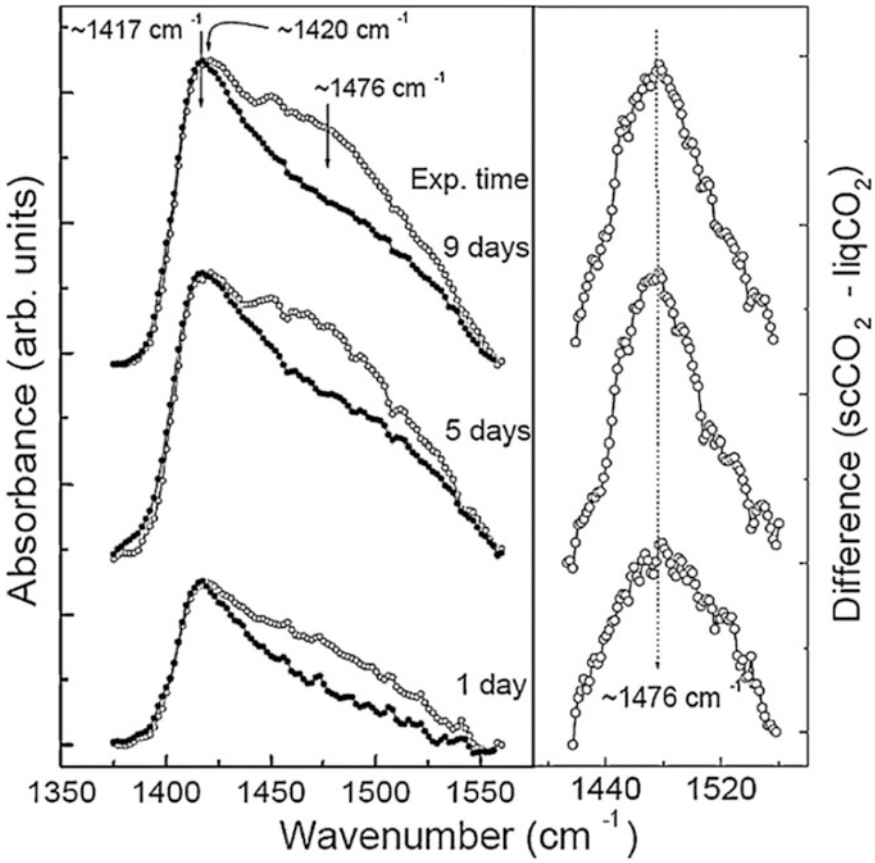

Fig. 6.12 **a** Infrared spectra of SWy-2 exposed to $liqCO_2$ (•) and $scCO_2$ (○); **b** baseline supplementary absorbance at $scCO_2$ versus $liqCO_2$ conditions (difference between the spectra) reprinted from (Hur et al., 2013) Copyright (2013) with permission from Elsevier

two spectra, as shown in Fig. 6.12b reveals a distinct field-splitting band centered at $\sim 1476\ cm^{-1}$. It is well-known that supercritical CO_2 fluid has lower viscosity, higher diffusivity, and near-zero surface tension (Horsch et al., 2006; Serhatkulu, Dilek, & Gulari, 2006; Zhao & Samulski, 2003) compared to liquid CO_2. However, it is not clear how the difference between the CO_2 phases affects the carbonation reactions in clays. The difference between the spectra of the carbonate phases formed under supercritical and liquid CO_2 may be attributed to different sites at which the reaction occurs at different temperatures (White, 1971; Adler & Kerr, 1963; Zhang et al., 2006; Liu et al., 2005; Barriga et al., 2002). It is likely that the elevated temperature provides more favorable conditions for carbonate formation at the surfaces less accessible to the liquid CO_2 phase, such as interlayer galleries or isolated micro-pore voids between the crystals. Interestingly, in other samples exposed to supercritical CO_2 for 3 days, carbonate formation (accompanied by the

matching, up to 15% reduction in intensity of the IR band around 1630 cm^{-1}, associated with the bending vibration of interlayer water molecules) NETL researchers (2010–2012) observed in STx-1b and the cation-exchanged Ca–SWy-2 (Ca-rich) but not in Na–SWy-2 (Na-rich) clay. This suggests that the interlayer cations play a crucial role in this phenomenon. Silicate minerals that contain divalent cations such as Ca^{2+}, Mg^{2+}, and Fe^{2+} can make the formation of carbonate phase to be energetically favorable (Lackner, 2002; Seifritz, 1990). This phase appeared to remain stable while SWy-2 was heated from 22 to 450 °C in environmental chamber filled with high-purity He.

Semi-quantitative measurements of the near-surface carbonate phase concentrations were done using XPS (Hur et al., 2013). Binding energies were referenced to the C 1s peak for adventitious carbon at 285.0 eV. Figure 6.13 shows the representative C 1s spectra obtained from the natural (as received) SWy-2 clay exposed to supercritical CO_2 as a function of the exposure time. The XPS spectrum includes an initially weak peak at 289.7 eV due to carbonate carbon, indicating that the as-received clay already contains some surface carbonate impurities. As the total

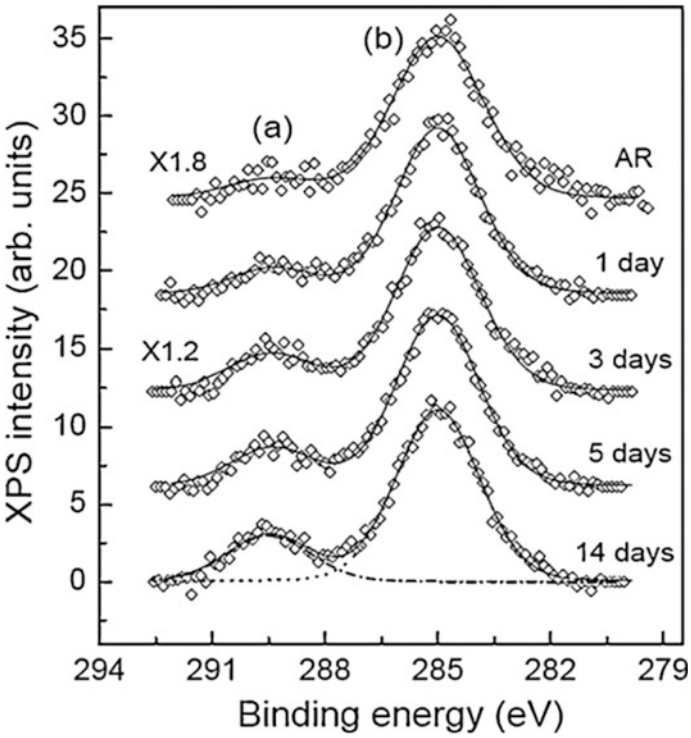

Fig. 6.13 XPS profiles of the clay samples exposed to $scCO_2$. *Solid lines* indicate the best fit of the raw data (♦) to a pseudo-Voigt function: **a** C 1s spectral line for carbonate; **b** C 1s spectral line for adventitious carbon. The *bottom* profile shows components of a representative best fit to the spectrum. Reprinted from (Hur et al., 2013) Copyright (2013) with permission from Elsevier

time of exposure to the CO_2 phase increased, the relative intensity of the C 1s spectral line for the carbonate phase increased as well. Estimated 0.35 mmol-C/g-clay was captured in 2 weeks. The relative amount of carbonate in each sample was calculated by measuring the area of C 1s peak due to carbonate and normalizing by the area of Si 2p peak; the relative contribution of Si from the clay was assumed to be similar for all the samples. Atomic concentrations were further estimated based on the peak areas, with the appropriate sensitivity factors.

The behavior of the carbonation reaction can be described by the Elovich equation (Bansal, Vastola, & Walker, 1970; Bulut, Özacar, & Şengil, 2008; Polyzopoulos, Keramidas, & Pavlatou, 1986):

$\frac{dq}{dt} = \alpha e^{-\beta q}$ or $q = \frac{1}{\beta}\ln(1 + \alpha\beta t)$ in integral form,

where q is the amount chemisorbed, t is the length of exposure time, and α and β are constants.

6.3 CH_4 and Clay Minerals

CH_4 adsorption on clay and clay minerals is dominated by physisorption due to the nonpolarizable nature of the molecule. Methane is a neutral (with zero electric charge) molecule, with zero dipole and quadrupole moments (Table 6.1). There is no long-range electrostatic interaction between methane and clay, which is but dominated by van der Waals force. Therefore, methane sorption capacity on clay is strongly related to the surface area of clay minerals. As shown in Fig. 6.14, CH_4 adsorption capacity on clay minerals linearly correlates with BET surface area—which is greatly dependent on the type of clay mineral—in the order of montmorillonite > illite/smectite mixed layer > kaolinite > chlorite > illite. In shale formations, the organic matter contributes to a large amount of methane adsorption (Zhang et al., 2012); however, adsorption on clay minerals, constituting most of the inorganic matter in shale, may not be ignored when estimating the gas-in-place of methane (Jin & Firoozabadi, 2013).

The presence of CO_2 and H_2O, which are abundant in the natural systems, has a considerable effect on CH_4 sorption on clays and clay minerals (Jin & Firoozabadi, 2014). In general, CH_4 sorption capacity can be substantially reduced by competitive adsorption of CO_2 and H_2O, mostly because the adsorption sites on the clay surfaces are preferentially occupied by CO_2 and H_2O molecules. Water molecules engage in the most preferred interaction, compared to CO_2 and CH_4, with the surface sites on hydrophilic clay minerals; it may lead to clay swelling and hence to blocking of the pore throats. Water sorption can greatly reduce porosity and permeability and restrict access to active sites for methane (Ji et al., 2012; Zhang et al., 2012).

CO_2 and CH_4 sorption isotherms were measured for 0 W Na–SWy-2 and sub-1 W Ca–SWy-2 at 50 °C (Schaef et al., 2014b). CH_4 sorption on Na–SWy-2

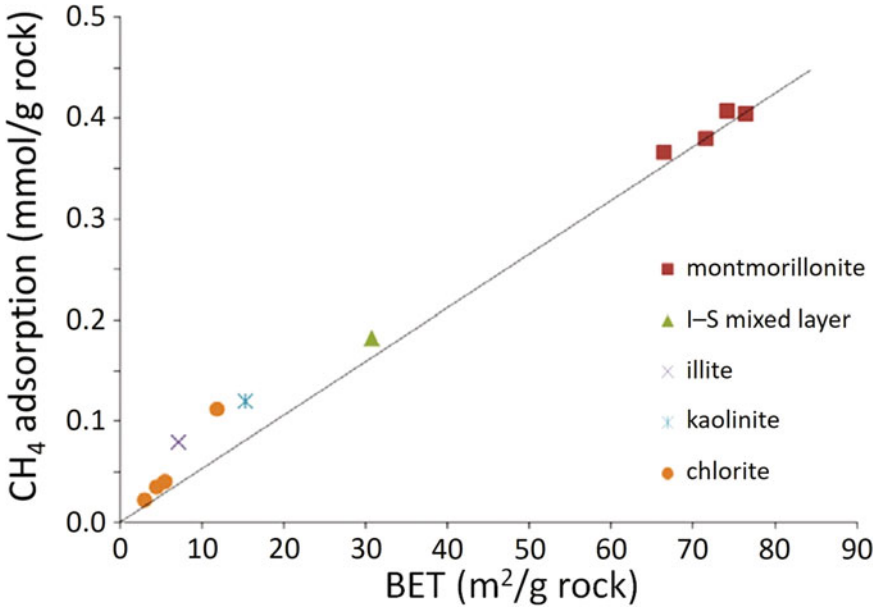

Fig. 6.14 Langmuir maximum capacity of CH_4 adsorption plotted versus BET surface area of clay-rich rocks; I-S refers to illite/smectites mixed layer. Reproduced from (Ji et al., 2012) Copyright (2012) with permission from Elsevier

was linear with pressure up to 12.5 MPa, whereas sorption on Ca–SWy-2 reached a maximum value at 6 MPa and maintained it up to 12.5 MPa, as shown in Fig. 6.15. CH_4 sorption on Na–SWy-2 was higher than that of CO_2 until pressure reached 6 MPa. As expected, sub-1 W Ca–SWy-2 has higher CO_2 sorption than 0 W Na–SWy-2; because CO_2 only absorbs onto external surfaces of Na–SWy-2, in contrast, it can reach both external surfaces and interlayer spaces of Ca–SWy-2. After excess CO_2 sorption on the two montmorillonite samples reaches a maximum around 9 MPa, further pressurization leads to a decrease in CO_2 sorption. Ignoring for a moment the role of (unknown) changes in void volume, this would imply that the interaction between the condensed and bulk CO_2 molecules eventually becomes stronger than the near-surface interactions between the CO_2 and clay. Computational simulations have indicated that this could be associated with a minimum of adsorption energy at 1 W Ca–SWy-2, for CO_2 but not for CH_4. The authors suggested an "ideal" pressure window, which is up to 7.5 MPa, to maximize CO_2 adsorption and CH_4 recovery based on this research.

The idea of utilizing competitive sorption of CO_2 and CH_4 on shales in depleted reservoirs for the sake of achieving enhanced gas recovery (CO_2-EGR) and concomitant carbon storage has been gaining momentum (Busch et al., 2008, 2009; Kang et al., 2011; Shukla, Ranjith, Haque, & Choi, 2010; Zhang et al., 2014) and for a good reason. In addition to improving the economics of the baseline CO_2 storage project and cost savings on infrastructure, CO_2-EGR also contributes to

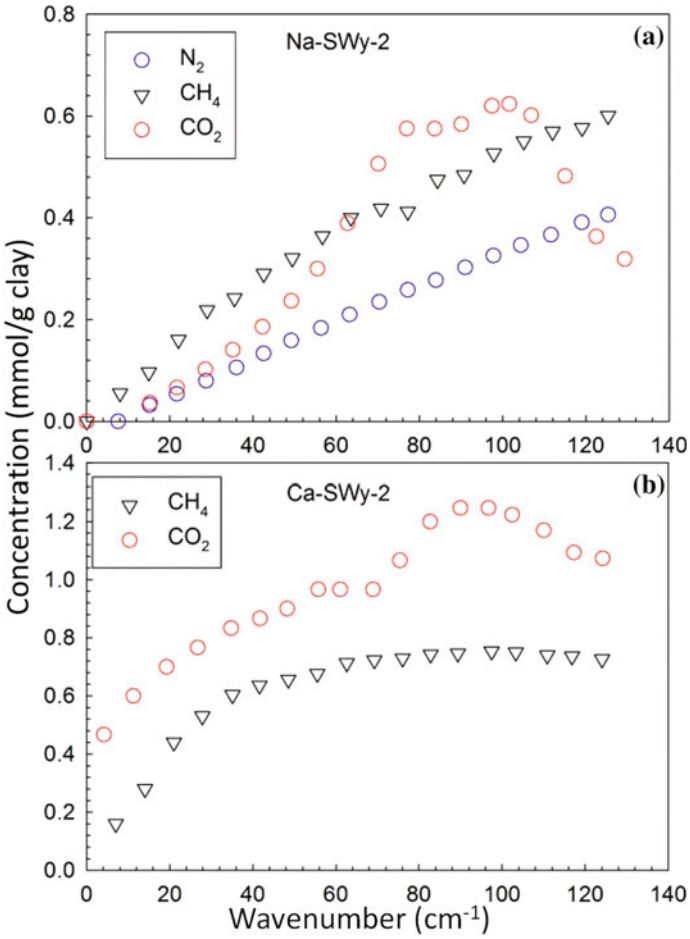

Fig. 6.15 Sorption isotherms (at 50 °C) of CO_2 and CH_4 on **a** 0 W Na–SWy-2, **b** sub-1 W Ca–SWy-2; reprinted from (Schaef et al., 2014b) Copyright (2014) with permission from Elsevier

natural assurance of the seal integrity for the gas storage reservoir (de Jong, Spiers, & Busch, 2014). Reestablishment of pressure in the gas reservoirs by the injected CO_2 would actually remedy the deformation of geologic networks caused by release of natural gas, thus leading to assured long-term carbon storage (Hong et al., 2016). The storage potential available for CO_2-EGR has already been reaffirmed by nature as well, because adsorption capacity of CO_2 on shale is generally several orders of magnitude greater than that of CH_4. Nuttall et al., (2005) reported that CO_2 adsorption capacity is five times greater than that of CH_4 on Devonian black shales from Kentucky (Nuttall et al., 2005). Kang et al. (2011) also observed that

CO_2 adsorption is five to ten times larger than adsorption of CH_4 on the Barnett Shale (Kang et al., 2011). The experimental data suggest that such organic-rich black shale could act as a long-term storage formation for CO_2.

References

Adler, H. H., & Kerr, P. F. (1963). Infrared absorption frequency trends for anhydrous normal carbonates. *American Mineralogist, 48*(1–2), 124–137.

Amarasinghe, P. M., Katti, K. S., & Katti, D. R. (2008). Molecular hydraulic properties of montmorillonite: A polarized Fourier transform infrared spectroscopic study. *Applied Spectroscopy, 62*(12), 1303–1313.

Bansal, R. C., Vastola, F. J., & Walker, P. L., Jr. (1970). Studies on ultraclean carbon surfaces: II. Kinetics of chemisorption of oxygen on graphon. *Journal of Colloid and Interface Science, 32* (2), 187–194.

Barriga, C., et al. (2002). Hydrotalcites as sorbent for 2,4,6-trinitrophenol: Influence of the layer composition and interlayer anion. *Journal of Materials Chemistry, 12,* 1027–1034.

Brubach, J. B., et al. (2005). Signatures of the hydrogen bonding in the infrared bands of water. *Journal of Chemical Physics, 122*(18), 184509.

Bulut, E., Özacar, M., & Şengil, İ. A. (2008). Equilibrium and kinetic data and process design for adsorption of Congo Red onto bentonite. *Journal of Hazardous Materials, 154*(1–3), 613–622.

Busch, A., et al. (2008). Carbon dioxide storage potential of shales. *International Journal of Greenhouse Gas Control, 2*(3), 297–308.

Busch, A., et al. (2009). Effects of physical sorption and chemical reactions of CO_2 in shaly caprocks. *Energy Procedia, 1*(1), 3229–3235.

Busch, A., et al. (2016). On sorption and swelling of CO_2 in clays. *Geomechanics and Geophysics for Geo-Energy and Geo-Resources, 2*(2), 111–130.

de Jong, S. M., Spiers, C. J., & Busch, A. (2014). Development of swelling strain in smectite clays through exposure to carbon dioxide. *International Journal of Greenhouse Gas Control, 24,* 149–161.

Eisenberg, D., & Kauzman, W. (1969). *The structure and properties of water*. Oxford: Oxford University Press.

Farmer, V. C. (1968). Infrared spectroscopy in clay mineral studies. *Clay Minerals, 7*(4), 373–387.

Farmer, V. C. (1971). The characterization of adsorption bonds in clays by infrared spectroscopy. *Soil Science, 112*(1), 62–68.

Farmer, V. C. (1974). *The infrared spectra of minerals*. London: Mineralogical Society.

Farmer, V. C., & Mortland, M. M. (1966). An infrared study of the co-ordination of pyridine and water to exchangeable cations in montmorillonite and saponite. *Journal of the Chemical Society A: Inorganic, Physical, Theoretical,* 344–351.

Farmer, V. C., & Russell, J. D. (1967). Infrared absorption spectrometry in clay studies. *Clays and Clay Minerals, 15*(1), 121–142.

Farmer, V. C., & Russell, J. D. (1971). lnterlayer complexes in layer silicates, the structure of water in lamellar ionic solutions. *Transactions of the Faraday Society, 67,* 2737–3749.

Fripiat, J. J., Cruz, M. I., Bohor, B. F., & Thomas, J., Jr. (1974). Interlamellar adsorption of carbon dioxide by smectites. *Clays and Clay Minerals, 22*(1), 23–30.

Fukuda, J.-I. (2012). Water in rocks and minerals—species, distributions, and temperature dependences. In T. M. Theophanides (Ed.), *Infrared Spectroscopy—materials science, engineering and technology* (pp. 77–96). Princeton: InTech.

Fukuda, J., & Nakashima, S. (2008). Water at high temperatures in a microcrystalline silica (chalcedony) by in-situ infrared spectroscopy: Physicochemical states and dehydration behavior. *Journal of Mineralogical and Petrological Sciences, 103*(2), 112–115.

Fukuda, J., & Shinoda, K. (2008). Coordination of water molecules with Na^+ cations in a beryl channel as determined by polarized IR spectroscopy. *Physics and Chemistry of Minerals, 35* (6), 347–357.

Fukuda, J., & Shinoda, K. (2011). Water molecules in beryl and cordierite: High-temperature vibrational behavior, dehydration, and coordination to cations. *Physics and Chemistry of Minerals, 38*(6), 469–481.

Fukuda, J., Yokoyama, T., & Kirino, Y. (2009). Characterization of the states and diffusivity of intergranular water in a chalcedonic quartz by high-temperature in situ infrared spectroscopy. *Mineralogy Magazine, 73*(5), 825–835.

Glezakou, V.-A., Rousseau, R., Dang, L. X., & McGrail, B. P. (2010). Structure, dynamics and vibrational spectrum of supercritical CO_2/H_2O mixtures from ab initio molecular dynamics as a function of water cluster formation. *Physical Chemistry Chemical Physics, 12*(31), 8759–8771.

Head-Gordon, T., & Johnson, M. E. (2006). Tetrahedral structure or chains for liquid water. *Proceedings of the National Academy of Sciences of the United States of America, 103*(21), 16614–16615.

Heller-Kallai, L. (2001). Protonation-deprotonation of dioctahedral smectites. *Applied Clay Science, 20*(1–2), 27–38.

Hong, L., et al. (2016). Factors affecting the interaction of CO_2 and CH_4 in Marcellus Shale from the Appalachian Basin. *Journal of Unconventional Oil and Gas Resources, 14,* 99–112.

Horsch, S., Serhatkulu, G., Gulari, E., & Kannan, R. M. (2006). Supercritical CO_2 dispersion of nano-clays and clay/polymer nanocomposites. *Polymer, 47*(21), 7485–7496.

Hur, T.-B., et al. (2013). Carbonate formation in Wyoming montmorillonite under high pressure carbon dioxide. *International Journal of Greenhouse Gas Control, 13,* 149–155.

IPCC (2005). *Climate change 2005: Carbon dioxide capture and storage. A special report of Working Group III of the fourth assessment report of the Intergovernmental Panel on Climate Change,* Cambridge and New York: Cambridge University Press.

Ji, L., et al. (2012). Experimental investigation of main controls to methane adsorption in clay-rich rocks. *Applied Geochemistry, 27*(12), 2533–2545.

Jin, Z., & Firoozabadi, A. (2013). Methane and carbon dioxide adsorption in clay-like slit pores by Monte Carlo simulations. *Fluid Phase Equilibria, 360,* 456–465.

Jin, Z., & Firoozabadi, A. (2014). Effect of water on methane and carbon dioxide sorption in clay minerals by Monte Carlo simulations. *Fluid Phase Equilibria, 382,* 10–20.

Johnston, C. T., Sposito, G., & Erickson, C. (1992). Vibrational probe studies of water interactions with montmorillonite. *Clays and Clay Minerals, 40*(6), 722–730.

Kang, S. M., et al. (2011). Carbon dioxide storage capacity of organic-rich shales. *SPE Journal, 16* (4), 1–14.

Kerisit, S., Weare, J. H., & Felmy, A. R. (2012). Structure and dynamics of forsterite–$scCO_2/H_2O$ interfaces as a function of water content. *Geochimica et Cosmochimica Acta, 84,* 137–151.

Lackner, K. S. (2002). Carbonate chemistry for sequestering fossil carbon. *Annual Review of Energy and the Environment, 27,* 193–232.

Libowitzky, E. (1999). Correlation of O–H stretching frequencies and O–H···O hydrogen bond lengths in minerals. *Monatshefte, 130*(8), 1047–1059.

Li, J.-R., Kuppler, R. J., & Zhou, H.-C. (2009). Selective gas adsorption and separation in metal-organic frameworks. *Chemical Society Reviews, 38*(5), 1477–1504.

Liu, Z., et al. (2005). Selective and controlled synthesis of α- and β-cobalt hydroxides in highly developed hexagonal platelets. *Journal of the American Chemical Society, 127*(40), 13869–13874.

Loring, J. S., et al. (2011). In situ infrared spectroscopic study of forsterite carbonation in wet supercritical CO_2. *Environmental Science and Technology, 45*(14), 6204–6210.

Loring, J. S., et al. (2012). In situ molecular spectroscopic evidence for CO_2 intercalation into montmorillonite in supercritical carbon dioxide. *Langmuir, 28*(18), 7125–7128.

Lu, J., et al. (2002). Solvatochromic characterization of near-critical water as a benign reaction medium. *Industrial and Engineering Chemistry Research, 41*(12), 2835–2841.

Lu, J., Brown, J. S., Liotta, C. L., & Eckert, C. A. (2001). Polarity and hydrogen-bonding of ambient to near-critical water: Kamlet-Taft solvent parameters. (R828130). *Chemical Communications, 7,* 665–666.

Madejová, J. (2003). FTIR techniques in clay mineral studies. *Vibrational Spectroscopy, 31*(1), 1–10.

Madejov, J., Komadel, P., & Madejová, J. (2001). Base line studies of The Clay Minerals Society source clays: Infrared methods. *Clays and Clay Minerals, 49*(5), 410–432.

Martin, R. T. (1960). Adsorbed water on clay: A review. *Clays and Clay Minerals, 9*(1), 28–70.

Michels, L., et al. (2015). Intercalation and retention of carbon dioxide in a smectite clay promoted by interlayer cations. *Scientific Reports, 5*(8775), 1–9.

Miller, Q. R. S., et al. (2013). Insights into silicate carbonation processes in water-bearing supercritical CO_2 fluids. *International Journal of Greenhouse Gas Control, 15,* 104–118.

Moore, D. M., & Reynolds, R. C., Jr. (1997). *X-Ray diffraction and the identification and analysis of clay minerals* (2nd ed.). New York: Oxford University Press.

Mortland, M. M. (1970). Clay-organic complexes and interactions. *Advances in Agronomy, 22,* 75–117.

Mortland, M. M., & Raman, K. V. (1968). Surface acidity of smectites in relation to hydration, exchangeable cation, and structure. *Clays and Clay Minerals, 16*(5), 393–398.

Nuttall, B., Ebble, C., Drahovzal, J. A., & Bustin, R. M. (2005). *Analysis of Devonian black shales in Kentucky for potential carbon dioxide sequestration and enhanced natural gas production. Kentucky Geological Survey*. Lexington: University of Kentucky.

Polyzopoulos, N. A., Keramidas, V. Z., & Pavlatou, A. (1986). On the limitations of the simplified Elovich equation in describing the kinetics of phosphate sorption and release from soils. *European Journal of Soil Science, 37*(1), 81–87.

Romanov, V. N. (2013). Evidence of irreversible CO_2 intercalation in montmorillonite. *International Journal of Greenhouse Gas Control, 14,* 220–226.

Romanov, V. N., Ackman, T. E., Soong, Y., & Kleinman, R. L. (2009). CO_2 storage in shallow underground and surface coal mines: Challenges and opportunities. *Environmental Science and Technology, 43*(3), 561–564.

Romanov, V. N., et al. (2010a). *Mechanisms of CO_2 interaction with expansive clay*. Poster presented at the SEA-CSSJ-CMS Trilateral Meeting on Clays, Seville, Spain.

Romanov, V. N., et al. (2010b). *CO_2 interaction with geomaterials*. Paper presented at the AGU Fall Meeting (p. H11 J-01, Invited), San Francisco, CA.

Romanov, V., & Soong, Y. (2008). *Multi-scale modeling of carbon dioxide sequestration in unmineable coal seams.* Poster presented at the 7th Annual Conference on Carbon Capture & Sequestration, Pittsburgh, PA.

Romanov, V., et al. (2015). Mineralization of carbon dioxide: A literature review. *ChemBioEng Reviews, 2*(4), 231–256.

Russell, J. D., & Farmer, V. C. (1964). Infra-red spectroscopic study of the dehydration of montmorillonite and saponite. *Clay Minerals Bulletin, 5*(32), 443–464.

Schaef, H. T., et al. (2013). Forsterite [$Mg_2{\cdot}SiO_4$] carbonation in wet supercritical CO_2: An in situ high-pressure X-ray diffraction study. *Environmental Science and Technology, 47*(1), 174–181.

Schaef, H. T. et al. (2014a). CO_2 Utilization and storage in shale gas reservoirs: Experimental results and economic impacts. *Energy Procedia, 63,* 7844–7851.

Schaef, H. T. et al. (2014b). Surface condensation of CO_2 onto Kaolinite. *Environmental Science and Technology Letters, 1*(2), 142–145.

Seifritz, W. (1990). CO_2 disposal by means of silicates. *Nature, 345*(6275), 486.

Serhatkulu, G. K., Dilek, C., & Gulari, E. (2006). Supercritical CO_2 intercalation of layered silicates. *Journal of Supercritical Fluids, 39*(2), 264–270.

Shukla, R., Ranjith, P., Haque, A., & Choi, X. (2010). A review of studies on CO_2 sequestration and caprock integrity. *Fuel, 89*(10), 2651–2664.

Steiner, T. (2002). The hydrogen bond in the solid state. *Angewandte Chemie International Edition, 41*(1), 49–76.

Wernet, P. et al. (2004). The structure of the first coordination shell in liquid water. *Science, 304* (5673), 995–999.

White, W. B. (1971). Infrared characterization of water and hydroxyl ion in the basic magnesium carbonate minerals. *American Mineralogist, 56*(1–2), 46–53.

Zhang, T., et al. (2012). Effect of organic-matter type and thermal maturity on methane adsorption in shale-gas systems. *Organic Geochemistry, 47,* 120–131.

Zhang, Y., et al. (2014). Experimental investigation of CO_2–CH_4 displacement and dispersion in sand pack for enhanced gas recovery. *Energy Procedia, 61,* 393–397.

Zhang, Z., et al. (2006). Temperature- and pH-dependent morphology and FT-IR analysis of magnesium carbonate hydrates. *Journal of Physical Chemistry B, 110*(26), 12969–12973.

Zhao, Q., & Samulski, E. T. (2003). Supercritical CO_2-mediated intercalation of PEO in clay. *Macromolecules, 36*(19), 6967–6969.

Chapter 7
Experimental Studies: Clay Swelling

Vyacheslav Romanov and Evgeniy M. Myshakin

We are like dwarfs on the shoulders of giants, so that we can see more than they, and things at a greater distance, not by virtue of any sharpness of sight on our part, or any physical distinction, but because we are carried high and raised up by their giant size.
—Quotations by Bernard of Chartres (XII century)

We don't know one millionth of one percent about anything.
—Quotations by Thomas Alva Edison

Abstract The best-known characteristic of clay is a dramatic change in its morphological and geomechanical properties: from hard, dense, and brittle upon drying or firing to soft, pliable, and swelling upon exposure to water. Chemical properties of the 1:1 and 2:1 clay minerals are significantly different, which is mainly related to the bonds between individual layers. The interlayer environment is determined by the chemical nature of clay layers, the layer charge, interlayer cations, and water molecules forming hydration shells around the cations and H-bonding with clay surfaces. Mechanisms of water sorption and cluster organization are electrochemical in nature and fundamental to the swelling process. Some researchers also observed irreversible CO_2-induced swelling with smectite in 1–2 W hydration state, but the others reported only shrinking attributed to drying effects of high-pressure CO_2, for the cation-exchanged smectite with partly filled second hydration layer. The current interpretation of swelling phenomena evolves rapidly, following advances in experimental techniques and Monte Carlo and MD simulations of the structured fluid behavior. MD simulations show that the interlayer molecules do not organize themselves in a strictly tilted or strictly parallel to the surface configuration, which may result in fairly steep but gradual rather than stepwise increase in the

V. Romanov (✉)
U.S. Department of Energy, National Energy Technology Laboratory (NETL), Pittsburgh, USA
e-mail: romanov@netl.doe.gov

E. M. Myshakin
U.S. Department of Energy, NETL–AECOM, Pittsburgh, USA

© Springer International Publishing AG 2018

V. Romanov (ed.), *Greenhouse Gases and Clay Minerals*, Green Energy and Technology, https://doi.org/10.1007/978-3-319-12661-6_7

basal spacing as the interlayer is filled with the solvent molecules. The magnitude of swelling hysteresis varies with the hydration energy of the interlayer cations and is generally more pronounced for vermiculite than montmorillonite.

7.1 Clay Plasticity and Ancillary Properties

Probably, the best-known characteristic of clay is a dramatic change in its morphological and geomechanical properties: from hard, dense, and brittle upon drying or firing to soft, pliable, and swelling upon exposure to water. The disadvantages of such behavior are encountered by construction industries as swelling clay minerals are often responsible for the failure of buildings and highways. Wellbore instabilities—a serious problem for oil industries—are partially caused by swelling clay minerals due to the uptake of water from drilling fluid, and the associated costs are of the order of millions of dollars per year. Whereas clays are used to the benefit as drilling mud lubricants during oil extraction, the replacement of oil-based by water-based muds induces unwanted swelling in clay-rich shales as well as mudrock damage or even well collapse. In many applications, clay plasticity and low hydraulic conductivity are advantageous properties. Ubiquitous clay minerals are featured as liner materials in the containment of waste, paint, drug, agrochemical delivery agents, and catalytic materials.

Advances in experimental research and practical application of clay go together with the advances in theoretical interpretations. The understanding, modeling, and predicting the interaction of clays with water and other environmental fluids is important in the field of geotechnical and geo-environmental engineering as well as industrial applications such as muds for oil well drilling (see Chap. 3) and water treatment. The ability of certain clay minerals to sorb water between the layers, driven by hydration of interlayer ions and resulting in clay expansion, is of particular interest to geoscientists. Water is essential for clay mineral formation and most clay minerals are described as hydrous aluminum phyllosilicates. As stated in Chap. 4, structurally, clay minerals are composed of sheets made of planes of metal cations tetrahedrally or octahedrally coordinated (with oxygen); which in turn are arranged into layers, often described as a 2:1 stacking pattern if they involve units (layers) composed of one octahedral and two tetrahedral (silicate-based) sheets, or 1:1 if they involve units of alternating tetrahedral and octahedral sheets (Hillier, 2003).

A perfect tetrahedral (T) sheet consists of four-valent cations (typically Si^{4+}) surrounded by four oxygen atoms, whereas a "perfect" octahedral (O) sheet consists of trivalent (typically Al^{3+}) or divalent (e.g., Mg^{2+}) cations surrounded by six oxygen atoms and/or OH groups. Isomorphic substitutions of those cations with a metal of lower valency create a negative charge distributed over clay sheets. The neutral subgroups of the 1:1 dioctahedral and trioctahedral phyllosilicates with ideal cation site occupancy in both T and O sheets are kaolin that forms from weathering of the 2:1 minerals and unstable serpentine, respectively. In the 1:1 clay minerals

isomorphic substitutions only happen to a small extent. For the 2:1 stacking, the neutral subgroups are pyrophyllite and talc. Only 2/3 of trivalent cations are required to obtain a neutral clay layer, and consequently, vacancies occur in the octahedral sheet (Moore & Lockner, 2007). All octahedra are filled with Mg in the trioctahedral talc structure, but only two of every three octahedra are occupied by Al in the dioctahedral pyrophyllite structure. Micas and smectites are charged (due to isomorphous substitutions) members of the 2:1 class. The negative charge of a clay platelet (made of stacked layers) arising from isomorphous substitution is manifested in the interlayer as an equivalent anionic field (parameter susceptible to empirical assessment as well as theoretical calculation, ignoring small entropy difference between various cations at the interlayer surfaces) (Eisenman & Horn, 1983; Eberl, 1980). The net negative layer charge is balanced by adsorption of cations, like Li^+, Na^+, K^+, Cs^+, Ca^{2+}, or Mg^{2+}, which can be present in the interlayer between individual clay layers, or on the outer surface of the clay minerals. When micas weather into illite and vermiculite, the interlayer progressively becomes hydrated as K^+ is released from the structure. After advanced weathering, smectites occur as packets of discrete T-O-T layers, weakly bonded by hydrated interlayer cations. Bonding between the tetrahedral and octahedral sheets requires that the tetrahedral sheet becomes corrugated or twisted, causing ditrigonal distortion to the hexagonal array; and the octahedral sheet is flattened. This minimizes the overall bond-valence distortions of the crystallite (Moore & Reynolds Jr., 1997). Each layer has two tetrahedral sheets that are coordinated to a central octahedral sheet. The apical oxygens of the tetrahedra are shared with adjacent octahedra. Four of these shared oxygens combine with two unshared hydroxyls to form the octahedra. The hydroxyls are centered above ditrigonal voids formed by the arrangement of tetrahedra. The two outstanding properties of smectites and vermiculites are the exchangeability of their interlayer cations and their ability to expand in the direction orthogonal to the layers by intercalation of water or polar organic molecules. Both properties are dependent on the interlayer environment.

The chemical properties of 1:1 and 2:1 clay minerals are significantly different, which is mainly related to the bonds between individual layers. In case of 1:1 clay minerals, the outer surfaces of a single layer have basal oxygen atoms on the tetrahedral site and hydroxyl groups on the octahedral site. The hydroxyl groups of the octahedral sheet form strong H-bonds with the tetrahedral oxygen atoms of an adjacent layer. In case of the dioctahedral kaolinite structure, a maximum of one layer of water molecules can occur between the platelets, giving the mineral halloysite. The interaction between layers of the 2:1 group is dominated by electrostatic and van der Waals forces, because the outer surfaces on each side of the layer consist of basal oxygen atoms only. The 2:1 clay platelet can be expanded by penetration of polar (or polarizable) molecules into the interlayer.

The extent of isomorphous substitution is greater in vermiculites than smectites; as a result, vermiculites have higher layer charge densities than smectites. The layer charge and associated cation exchange capacity (CEC) introduced in Chap. 4 are important criteria to classify clay minerals. Per half unit-cell $[O_{10}(OH)_2]$, the charge is on the order of 0.25–0.6 *e* (electron charge) for montmorillonite, beidellite, and

saponite; 0.50–0.90 *e* for illite and vermiculite; and approximately 1.0 and 2.0 *e* for micas (biotite and muscovite) and brittle micas, respectively.

For the purpose of expressing CEC, an equivalent of ionic charge may be defined as the quantity of the ion that contains one mole of that ion divided by its valence. In soil science, the CEC is conventionally expressed in terms of milliequivalent (meq) of exchangeable cations per 100 g of soil. Alternatively, the CEC is expressed in SI units in terms of the molar amount of charge (i.e., in Faraday units) per unit mass of soil. For the convenience of being able to express CEC so that it is numerically equivalent to [meq/100 g] one can use [cmol (+) kg^{-1}] where "+" refers to the proton charge and thus specifies a fraction of cationic charge (per unit of its valence). Hence, the above numbers for layer charge, σ can be converted to CEC (meq/100 g) as follows

$$CEC = 1000 \times \frac{2\sigma/e}{FW/100} \tag{7.1}$$

where *FW* is the formula weight (atomic units).

The classification of smectites is based on both the extent of octahedral cation occupancy, and the dominance of either tetrahedral or octahedral charge. However, only tetrahedrally charged vermiculites are recognized. Smectites and vermiculites are sometimes separated based on the structural charge per formula unit. There are two major problems with calculated structural formulas. First, the specimens must be monomineralic. Very few smectites or even vermiculites are truly monomineralic; most contain traces of mica, kaolinite, quartz, carbonates, and/or metal hydrous-oxides. Structural formulas and the estimated layer charge densities will reflect these contaminants. Metal hydroxides may also exist as separate entities or as external or even internal coatings. They reduce the apparent permanent charge by either blockage or electrostatic cancellation and increase the variable charge due to surface reactions with potential-determining ions. The second problem results from the assumption of anionic charge being exactly "−22" per formula unit. It is nearly impossible to accurately determine the anionic charge of clay, and even a slight deviation from −22 will have a major impact on estimated layer charge densities.

7.2 Charge Density Alteration and Its Role in Clay Swelling

Layer charge density is one of the ever-changing properties of clay minerals. The weathering of micas to vermiculites and smectites is normally accompanied by a decrease in layer charge, evidently resulting from an authigenic recrystallization process where protonation of tetrahedral oxygens facilitates the substitutions of Al^{3+} and Fe^{3+} with Si^{4+} in the tetrahedral layers. There is substantial evidence indicating that iron oxidation is accompanied by stoichiometric hydroxyl deprotonation, a

process which leaves the layer charge unchanged (Laird, 1987). The artificial weathering of micas involves the replacement of interlayer potassium by other cations. Both laboratory and field observations indicate that trioctahedral micas release potassium more readily than dioctahedral micas (Dreher & Niederbudde, 1994; Bassett, 1960; Norrish, 1973a) because of the proximity of hydroxyl protons as structural hydroxyls are oriented normal to the cleavage planes in trioctahedral minerals, while they are near parallel to the plane in dioctahedral minerals. Electrostatic calculations suggest that octahedrally charged micas may exhibit stronger attraction for interlayer potassium than tetrahedrally charged micas (Giese Jr., 1977). The importance of structural hydroxyls is substantiated by oxidized biotites which hold potassium more tightly than unoxidized biotites. Upon oxidation, it appears that either hydroxyl protons are lost during oxidation or some octahedral cations are ejected, which is accompanied by a shift in hydroxyl orientation. Both mechanisms would strengthen the interlayer anionic field, resulting in greater potassium affinity. Consensus based on artificial-weathering experiments, is that during mica alteration some ferrous iron is oxidized, a few divalent octahedral cations are ejected and either structural hydroxyls are lost or protons are adsorbed. The net result is a reduction in layer charge. Alternatively, reduction of structural iron in expandable 2:1 phyllosilicates should directly increase the layer charge density. However, the process is complicated by the loss of structural hydroxyls during reduction. In experiments by Stucki and Roth (1977) nontronite exchange capacity (layer charge) increased linearly with the extent of iron reduction; then above a ferrous iron content of 53 mmol per 100 g, the layer charge remained constant—in the Garfield nontronite, where the greatest amount of reduction occurred, the layer charge actually decreased after reaching a maximum—due to the elimination of structural hydroxyls. However, the precise mechanism remains in question (Komadel, Madejová, & Stucki, 1995). The observed increase in layer charge was easily reversible by exposure of the clay to oxygen (Stucki & Roth, 1977).

Natural smectites typically have a layer charge near 0.33 *e* and only rarely more than 0.40 *e* (per half unit-cell). Vermiculites by contrast, exhibit a wider range in layer charge. According to published structural formulas for vermiculites and hydro-biotites, their layer charge ranges continuously from 0.42 *e* to 1.08 *e* per half unit-cell. In the 1950s, experimental evidence began to accumulate that seemingly homogeneous smectites actually had heterogeneous layer charge densities (Laird, 1987). Layer charge heterogeneity is a rule rather than an exception, even among reference clays. The layer charge of expandable 2:1 phyllosilicates is distributed among three domains: external planar surfaces, internal planar surfaces, and lateral broken edges. The charge due to isomorphous substitution is manifested on the planar surfaces and is said to be "permanent" because the planar surfaces do not react with potential-determining ions (H^+ or OH^-) while the charge due to broken bonds along lateral edges is "variable" charge. At low pH, broken edge radicals are associated with protons and do not contribute to the net negative layer charge. At high pH, the broken edge radicals associate with solution cations. Although the variable charge is important, the permanent charge is clearly the dominant type of layer charge associated with expanding 2:1 phyllosilicates.

Experimental studies of the surface and hydration properties of reduced-charge montmorillonites showed that all layers retain some exchangeable cations until the charge has been reduced by about half (below 0.20 *e*) when collapsed (<1 nm) layers begin to appear (Clementz & Mortland, 1974). Charged clay layers and counterions in the interlayer of swelling clay minerals attract water molecules, depending on the pressure, temperature, and relative humidity. The total amount of water adsorbed on the reduced-charge montmorillonites increases but the amount of water adsorbed per exchangeable cation tends to decrease with increasing layer charge density. Interlayer water molecules are coordinated to both the exchangeable cations and negatively charged sites on the adjacent siloxane surfaces thus forming a complex H-bonding network. In tetrahedrally charged clays, the interlayer cations tend to be localized above the substitution sites, presumably because of a more localized charge on the silicate surfaces. However, the lateral position of interlayer cations is not so well established for octahedrally charged clays. In a direction perpendicular to the layer surface, the midway positioning of interlayer cations (particularly, in expanding 2:1 phyllosilicates) is generally accepted as more stable, but there are well-documented exceptions to this rule.

The type of counterion, total layer charge, and its distribution over the tetrahedral and octahedral sheets significantly influence the swelling properties (Giese, 1978). As the 1:1 layer charge is very small and individual clay platelets are very strongly hydrogen-bonded, swelling of kaolinite usually does not occur. Swelling of 2:1 clay minerals was not reported for the neutral minerals like dioctahedral pyrophyllite and trioctahedral talc. However, the clay minerals with a negative charge on their platelets due to isomorphic substitution can swell to a certain extent. In general (an apparent exception is the reduced-charge smectite) the swelling of clay minerals with a lower layer charge, such as montmorillonite, occurs to a larger extent than the swelling of clay minerals with a much higher layer charge, for example mica.

Ultimately, the interlayer environment is determined by the chemical nature of clay layers, the layer charge and effective electric-field strength (as represented by equivalent anionic radius), interlayer cations, and water molecules forming hydration shells around the cations and H-bonding with clay surfaces. The strength of the interlayer anionic field is described by Coulomb's law (Eberl, 1980; Eisenman & Horn, 1983) and thus must vary directly with layer charge density. However, both the structure and composition of the framework silicate also influence the strength of the interlayer anionic field, and thus swelling and cation exchange phenomena. In micas, hydroxyl orientation, fluorine-hydroxyl substitution and the source of layer charge have been shown to influence cation exchange and swelling properties (Laird, 1987). Hydroxyl orientation dominantly controls the rate of potassium exchange, but the source of charge is more important in controlling swelling. Fluorine, with the same charge and nearly the same radius as hydroxyl, substitutes readily into hydroxyl lattice positions. Fluorine has the strongest electronegativity of all ions and lacks the dipolar character of hydroxyls. Fluorine-hydroxyl substitution results in an increase in potassium affinity. Swelling behavior of potassium systems markedly depends on history and preparation of the clay (Laffer, Posner, & Quirk, 1966). Controversy remains about the relative

importance of the various factors and even the directions of their influence. It is possible that structural distortions, such as tetrahedral rotations, influence interlayer bonding energies. Turbostratic disordering of 2:1 clay layers inherently presented in natural smectites also influences energetics and distributions of interlayer species (Myshakin et al., 2014). Among expandable 2:1 phyllosilicates there is less evidence for the influence of structure and composition on the interlayer anionic field strength. However, it was observed that both the source (tetrahedral versus octahedral) and the amount of charge influenced the extent of vermiculite and smectite swelling (Harward, Carstea, & Sayegh, 1969).

7.3 Electro-Chemistry and Structure of Water Species Near Clay Surfaces

Mechanisms of water sorption and cluster organization are electro-chemical in nature and are fundamental to the process of swelling. Since the early work by Norrish, Posner, and Quirk (1954–1964), it has been recognized that swelling in compacted clays develops in two distinct phases (or regimes). First, at the lowest interlayer H_2O contents, there is "crystalline" swelling, during which the interlamellar space adsorbs water. Second, after the interlamellar space has sufficiently expanded due to intercalation of several molecular water layers, water starts to adsorb to external surfaces of the splitting clay particles, thus producing more voluminous osmotic (entropic) swelling (Fig. 7.1). Eventually, smectite becomes a thixotropic gel and then a sol regarded as the third stage of water uptake (Norrish, 1954).

The crystalline swelling is strongly influenced by the layer charge density, with the generally accepted tendency of clay layers to collapse with increasing layer charge density. However, the apparent spacing between the mineral layers (associated with basal spacing as defined in Chap. 4) may increase with increasing layer-charge density in reduced-charge montmorillonites, if inferred without taking an effort to account for random interstratification of expanded and collapsed layers (mixed layering). Heterogeneity of smectites can lead to coexistence of layers with substantially different degrees of hydration, within the same crystallite (platelet). The effect of layer charge density on the second-range (osmotic) swelling appears minimal, but there is a strong relationship between swelling and the degree of octahedral substitution. Low (1979–1981) argued that clay surface acts as a template on which water molecules propagate (Low, 1982). Thus, structure and composition of the framework silicate influence second-range swelling, but layer charge density does not.

The initial hydration of expandable 2:1 phyllosilicates occurs in a stepwise fashion corresponding to the formation of discrete layers of water molecules in the interlayer of clay platelets. The packing arrangement of interlayer water molecules may influence both the extent of hydration and, as a result, the apparent basal spacing. The molecular structure in the interlayer has also been studied

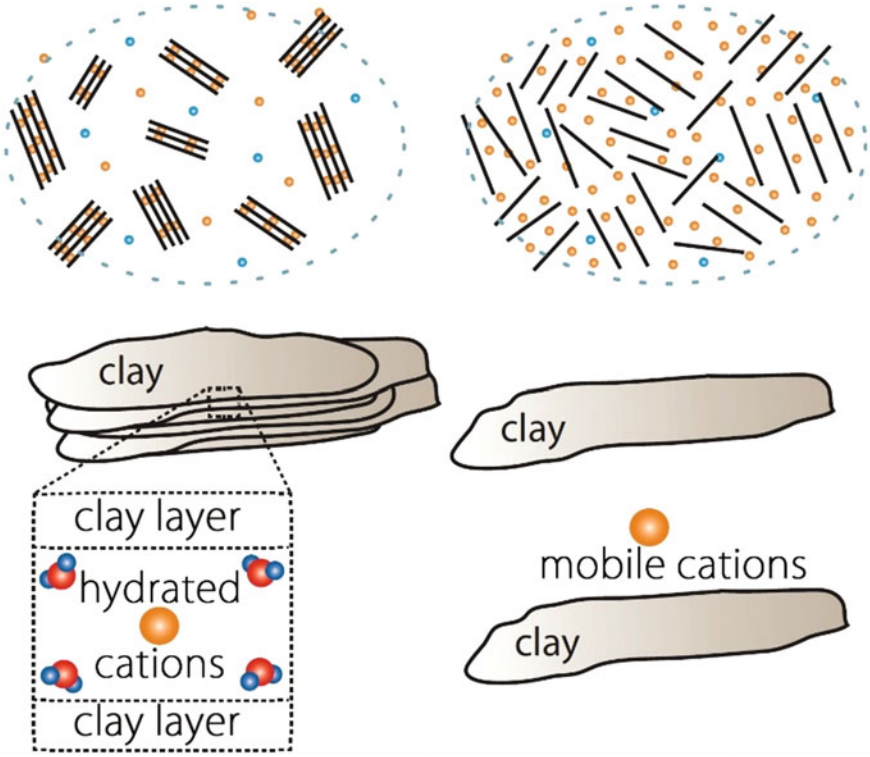

Fig. 7.1 Clay particle transition from crystalline to osmotic swelling—adapted by permission from Macmillan Publishers Ltd: Hansen et al. (2012) copyright (2012)

experimentally using a variety of advanced "in situ" techniques (as discussed in Chap. 5). Experimentally measured basal spacing (also known as d-spacing) of approximately 10, 12, 15, and 18 Å (for montmorillonite) corresponding to dehydrated (no water layers) and one-, two-, and three-layered hydration states, has been reproduced with Molecular Dynamics (MD) simulations (refer to Chaps. 8 and 9 for details). MD simulations show that the interlayer molecules do not organize themselves in a strictly tilted or strictly parallel to the surface configuration, which may result in fairly steep but gradual rather than stepwise increase in the basal spacing as the interlayer is filled with the solvent molecules. Occasionally, this transition range is interpreted as representing intermediate hydration states, especially when multiple interlayer fluids are involved (for example, a mix of CO_2 and H_2O). More advanced discussion on MD simulations of clay systems is forthcoming in Chap. 8.

In most swelling experiments, it was observed that the adsorption pathway is distinctively different (with some exceptions like for Cs-montmorillonite) from the desorption pathway, a phenomenon known as swelling hysteresis (Laffer et al., 1966). The magnitude of this hysteresis varies with the hydration energy of the

interlayer cations and is generally more pronounced for vermiculite than montmorillonite. The hysteresis for the one-to-two-layer transition is generally much less pronounced than that for the zero-to-one and two-to-three transitions. The crystalline-range swelling and shrinking hysteresis can be explained by a free-energy barrier that separates the stable hydration states. The temperature and external pressure influence the magnitude of this (activation) free-energy barrier. The molecular origin of the activation energy barrier is associated with changes in the dynamic water orientation in H-bonding network and the arrangement of counter-ions, including the formation of inner and outer-sphere hydration complexes (as elaborated in Chap. 6).

In neutral (generally nonexpandable) pyrophyllite, immobilized water molecules are believed to be part of a structure determined by the silicate surface and by the formation of the hydrogen bonds nearly orthogonal to it. The MD density profiles and snapshots reveal that water oxygens preferentially point to the pyrophyllite's surface (Zarzycki & Gilbert, 2016). However, in montmorillonite, the presence of counterions promotes the formation of the cation hydration shells in which one of the water molecule's OH bonds is oriented roughly toward the clay surface. The remaining OH bond in each water molecule tends to point to the oxygen of adjacent water molecule residing in the same layer and to form a hydrogen bond between them. According to the ideal schemes (Tambach, 2005; Tambach, Bolhuis, Hensen, & Smit, 2006) as illustrated in Fig. 7.2, during the swelling, hydrogen bonds between the two water layers are broken and new hydrogen bonds are formed in each layer. The type of counter-ion influences the free-energy barrier and swelling. It was found that due to its small size and large hydration energy, Li^+ counter-ions can stabilize an intermediate hydration state, with basal spacing ranging between those of one- and two-layer hydration states. In that intermediate configuration, lithium cations are, ideally, detaching from the surface and moving to the interlayer midplane; while the hydrogen bonds between the water molecules of the two partial layers are yet preserved. The larger cations like Na^+ and K^+ require increasingly larger interlayer spacing (i.e., higher hydration state) to move toward the midplane where they are coordinated by water molecules from the two distinct layers (Fig. 7.2b and c).

The swelling (disjoining) pressure exerted by the hydrated interlayer can be estimated using steered MD. Steered (or interactive) MD is used to accelerate and explore the transition from one equilibrium state to another, on the time scales accessible to MD simulations, through the addition of external forces which reduce the energy barriers. This approach corresponds to molecular-scale manipulation with atomic force microscopy (AFM) or optical tweezers. It was shown that significant compression of the interlayer can only be achieved at external pressure on the order of 1 GPa (Schmidt, Katti, Ghosh, & Katti, 2005; Katti, Schmidt, Ghosh, & Katti, 2005). In dry montmorillonite, it causes smaller cations to be drawn closer to the sites of isomorphous substitutions in the adjacent clay layers. In Na-montmorillonite with one hydration layer, compression primarily occurs in the silica–water interaction zones on each side of the layer. When 0.5–1.0 GPa compressive stress is applied to Na-montmorillonite with two monolayers of water molecules, its interlayer effectively reduces to a single monolayer configuration.

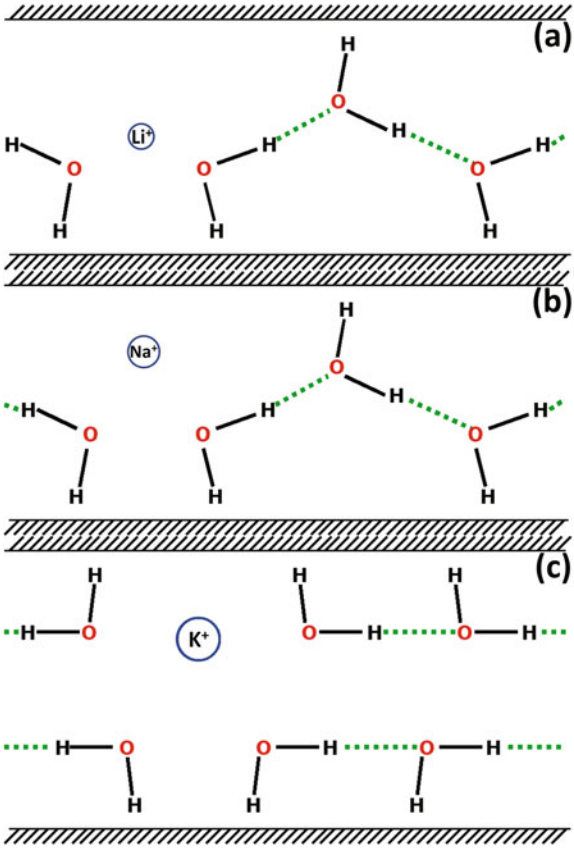

Fig. 7.2 Water and cation arrangements during T-O-T clay swelling from 1- to 2-layer hydration state: **a** "ideal" intermediate state with Li^+ at midplane; **b** Na^+ in intermediate configuration; **c** K^+ adsorbed to the surface while being coordinated by water molecules from two distinct layers—adapted with permission from (Tambach et al., 2006) Copyright (2006) American Chemical Society

Like dioctahedral smectites, saponites (trioctahedral smectites) exhibit discrete-layer hydration (or solvation) states (with water, ethylene glycol and glycerol as solvents) in the crystalline-swelling range, over a wide range of layer charge and a variety of interlayer cations, with increasing tendency to collapse as the layer charge density increases (Suquet, Iiyama, Kodama, & Pezerat, 1977). Swelling of smectite in electrolyte solutions (Norrish & Quirk, 1954a) proceeds in a stepwise fashion up to about three or four layers of water molecules, and then jumps to over 4 nm (Norrish, 1954). The sudden jump apparently results from a reversal in the role of the cation-surface forces (Norrish & Quirk, 1954b). At spacing less than 2 nm, anions are excluded from the interlayers, and the cations are generally positioned in the midplane between two adjacent layers. Electrostatic cation-surface interactions provide the binding energy between the charged clay layers. Since 1954, there has been a general agreement that crystalline swelling is controlled by a balance between forces of attraction due to both Coulombic and van der Waals interactions between clay layers and forces of repulsion arising from hydration of the interlayer cations and negative-surface-charge sites (Laird, 1996, 2006). At

spacing greater than 4 nm, anions penetrate the interlayer and the interlayer ionic distribution forms an overlapping diffuse double-layer. Under these conditions, the concentration gradient between the interlayer and the bulk solution results in diffuse double-layer (DDL) (osmotic) swelling pressure; this is opposed by frictional forces generated by edge-face bonding between the clay particles (Norrish, 1973b). The second-range swelling (>4 nm) is generally restricted to Li-, Na-, or freshly prepared (highly acidic) H-smectites in water or dilute (with the electrolyte concentration reduced to about 0.1 molar) electrolyte solutions. It was also observed in swelling of Li-vermiculite in dilute (<0.15 molar) LiCl solution, after the basal spacing had jumped explosively from 1.5 to 8.2 nm (Laird, 1987).

7.4 Holistic Model Development Issues

Theoretically, salt content in clay soils affects the size of the DDL developing near charged surfaces in aqueous solutions. The difference in the salt concentration between the free macro- or meso-pore fluid and that adjacent to the clay particle gives rise to the osmotic pressure. The swelling response of montmorillonite clay and corresponding development of swelling pressure when swelling is restrained is a result of complex clay-water interactions between particles and within the particle itself (Katti & Shanmugasundaram, 2001; Laird, 2006). As a result, it is possible to observe irreversible shrinking behavior at elevated pressures in the subsurface, depending on relative humidity or, equivalently, on the chemical potential of underground water. The classical effective-stress approach to the behavior of saturated soil has proven to be sufficient for many problems in engineering practice, except for geomechanical problems that involve changes in the pore-fluid chemistry of the soil. In multi-phase continuum mechanics, the stress state and volume change behavior can be described by the combination of effective mechanical stress and thermodynamically induced stress controlled by osmotic pressure. A change in the net electrostatic (repulsive minus attractive) forces between clay particles directly affects the osmotic volume change, while the fluid flow in response to osmotic gradients induces the longer term (typically, minor) volumetric changes (Barbour, Fredlund, & Pufahl, 1992).

The electrical double-layer is conventionally described by the Poisson–Boltzmann (PB) model (Debye & Hückel, 1923). This model can be used to evaluate double-layer forces occurring between charged objects across liquids. Within this double-layer, one of the layers corresponds to the charged surface. The other one corresponds to the diffuse layer which contains the neutralizing charge consisting of counterions and locally depleted co-ions. The resulting electrostatic potential profile between two charged surfaces leads to differences in the ionic concentrations within the gap between the charged particles (platelets) with respect to the bulk solution. These differences generate osmotic pressure, which in turn generates a force between these particles. The strength of this force increases with the magnitude of the surface charge density (or the electrical surface potential). For

two similarly charged objects, this force is repulsive and decays exponentially at larger distances. When the ions' energy due to electric potentials (Φ) is small relative to their kinetic energy (i.e., $|q\Phi| << kT$ where q is ionic charge, T is temperature, and k is the Boltzmann constant) the PB equation can be simplified (linearized) to the Debye-Hückel (DH) equation.

The classical approach to expansive clay structure modeling is DDL (osmotic pressure) theory by van't Hoff, based on a concept of semi-permeable membrane between interparticle pores and mesopores, which accounts for maintaining a difference in cation concentrations between the different pores, by precluding or limiting cation transport through it. The solvent transfer between the pores is assumed to be proportional to the gradients of chemical potential for each species. The thickness of double-layer is characterized by Debye length, depending only on the properties of the liquid, such as temperature, dielectric constant and ionic strength.

However, pure osmotic analysis (without any calibration to match experimental findings) leads to underestimation of the swelling pressure or free-swelling deformation up to two orders of magnitude from the values directly measurable on clays (Mitchell & Soga, 2005; Bolt, 1956). A number of factors can be cited as a cause of such discrepancies, including the failure of the continuous-fluid assumption near the particle surface where the fluid becomes highly structured (Fenter & Lee, 2014) as confirmed by experiments and Monte Carlo and MD simulations. For example, the way in which the charge in the fluid partitions between the mobile and immobile layers (Fig. 7.3) strongly affects the overall flow rate. Moreover, computational models of clay particle suspensions indicate that a nonparallel arrangement of clay particles plays a major role in the resulting overall deformation (Anandarajah & Lu, 1991). An alternative point of view is that the initial (crystalline) swelling from a very dry state involves only the interlamellar space and is widely seen as driven by mechanisms of hydration of the charged clay surface and hydration/solvation of the counterions (either positioned in the midplane between two adjacent layers or imbedded in the charged clay surface); and thus, it is critically affected by the constraining geometry of clay platelets, by turbostratic disorder and structural distortions, and by the presence of voids (cavities) in interfacial sheets, where the charges generated by isomorphic substitutions are more localized. For example, according to Hoffmann, Endell, & Wilm, (1933) structure, hexagonal holes in the silicate sheet surface are 3.3 Å in "free diameter" not occupied by the surrounding oxygen atoms (Hoffmann et al., 1933). Hence ions up to 2.4 Å in diameter could sink entirely below the sheet surface thus leading to cation fixation.

The current interpretation of these phenomena evolves rapidly, following advances in experimental techniques and Monte Carlo and MD simulations of the interlayer structure. Still, the issue of the dominant mechanism remains controversial. While the distribution of solvating ions and forces involved in interlayer H_2O-content organization are simulated with success, the mechanisms of changes in the hydration states are not unraveled. Particularly, the mechanisms of water transport into the interlamellar space are rarely addressed.

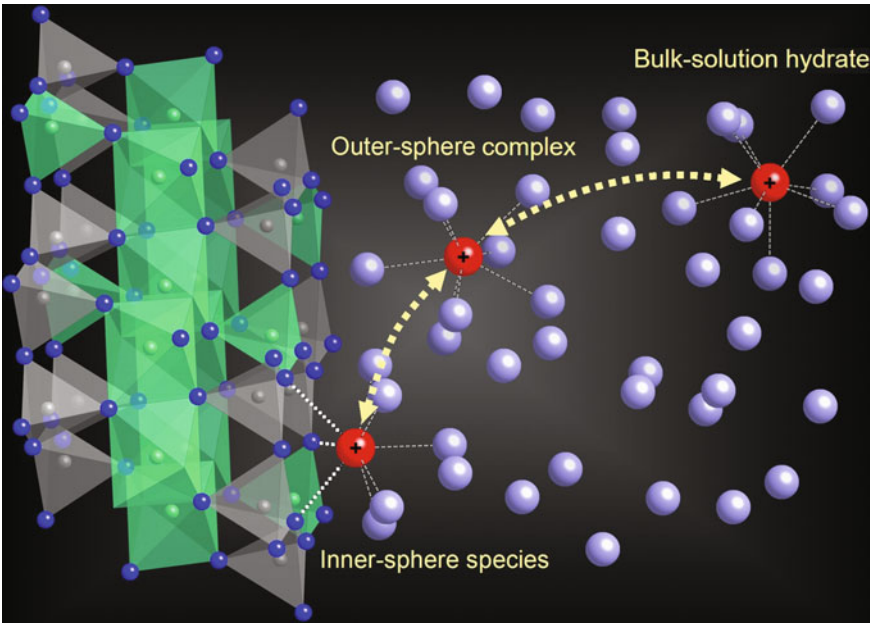

Fig. 7.3 Cation hydration geometries near Muscovite mica (001)–aqueous solution interface (Lee et al., 2010): *red circled plus* = cation; *filled violet circle* = water molecule; *filled blue circle* = oxygen

There are two major approaches used for modeling of crystalline swelling. With the microscopic approach, a modeler attempts energy minimization calculations considering all basic interactions for a system of stacked phyllosilicate layers (two half-platelets) with, typically, a few interlayer cations and several dozen water molecules. It has considerable potential for elucidating fundamental mechanisms, even though it is limited by the complexity of the mathematics and the need for significant computational resources. Experimental verification of microscopic models is difficult because most analytical techniques (particularly, XRD, TGA and chemical analysis) measure macroscopic properties. Alternatively, the macroscopic approach requires spatial averaging of properties and draws governing equations from thermodynamics, mechanics, and empirical relationships. Although this approach is fundamentally less rigorous, the mathematics is reduced to generally more accessible; and it provides a greater level of conceptual understanding. Macroscopic, reduced-order models are amenable to direct experimental verification. However, macroscopic theories have so far failed to adequately describe crystalline swelling, because the relevant properties of a structured fluid near the surface are different from those of the bulk liquid. In this regime (at the lowest interlayer H_2O content) swelling strongly depends on the packing of molecules intercalated between the layers; so far, statistical-mechanical simulations have

unveiled many details of the confined fluid's structure but not of the swelling mechanism, due to their limitations to predict clay H_2O content.

The extent of the interlayer hydration tends to decrease with increasing size of the exchangeable cations, and changes in basal spacing within the crystalline swelling range are related to both the size and hydration energy of the interlayer cations. It is generally accepted that the extent of crystalline swelling depends on a balance between the cation-surface electrostatic energy of attraction and the interlayer hydration energy. The attractive forces cannot be described accurately with simple electrostatic calculations (Kittrick, 1969); and the enthalpy-of-attraction approach using the equivalent-anion estimation cannot account for intermediate crystalline swelling, because the layers are assumed to be either fully contracted or infinitely expanded. Norrish (1954) suggested that the binding energy between adjacent clay layers could be estimated using a blend of a model depicting the layers as thick plane conductors and a model regarding them as condensers. The influence of layer charge density on the energy of attraction is essentially the same in all of these models—The attraction energy increases as the layer charge increases. Three fundamental problems are yet to be tackled before the balance-of-energy models will be able to predict crystalline swelling behavior. For once, the interlayer permittivity (dielectric constant) is known only within broad limits. Besides, the relationship between the energy of interlayer hydration and the extent of interlayer hydration is poorly understood. And when all is said and done, the significance of adsorption–desorption hysteresis has not been addressed with respect to the balance-of-energy models.

Several explanations were proposed for the hysteresis, but there seems to be no consensus. The attractive force is weaker during desorption because the layers are initially farther separated and the attractive force between layers decreases with an inverse power of the separation distance. Thus, the layers cannot come together until the disjoining pressure is reduced enough for the attractive forces to cause the collapse of one layer of solvent. Moreover, the swelling (disjoining) pressure depends not only on molality (or ionic strength) of the ambient medium and not even purely on the surface density of interlayer H_2O content, but also on the (quasi-) steady-state molecular arrangements in the interlayer (Fig. 7.2) which are a function of the interlayer width as well. The latter creates a pre-condition for possibly multiple quasi-equilibrium states in the clay system surrounded by the same environment. Alternatively, the adsorbate nucleation (clustering) around the periphery of quasi-crystals may also contribute to hysteresis in adsorption and desorption of various gases on montmorillonite (Barrer & MacLeod, 1954).

The hydration-dehydration transition temperatures are a measure of the difference between the forces of expansion and contraction. Heating increases the kinetic energy of the interlayer molecules, thus facilitating interlayer dehydration and even the entropy-driven partial liberation of the counterions (Hansen et al., 2012). The narrow temperature range over which the transitions occur and the stability of a dehydrated sample—experimentally observed just above a critical temperature—indicate an equilibrium-controlled process. No matter which explanation of adsorption–desorption hysteresis we accept, from a thermodynamic perspective a

potential energy barrier must be overcome, before layer contraction or expansion can proceed. An alternative perspective is that the stepwise hydration or dehydration of 2:1 phyllosilicates is a sequence of phase transitions (Laird, 1987). The activation energy can then be described as the latent energy associated with a phase transition. This activation energy stabilizes the basal spacing over a limited range of swelling pressures. Thus, in any balance-of-energy model the total swelling energy is only approximately equal to the electrostatic energy of attraction, within a range of uncertainty defined by the activation energy. Overall, crystalline swelling must be modeled using an open system theory (Laird, 1996). During expansion, mass (solvent) is transferred from the ambient solution into the clay platelet and the layers move farther apart while displacing the surrounding media. During the collapse, mass is transferred from the clay to the surroundings, the layers move closer together and solvent molecules must fill the void left by the retreating layers. Each step (in either interlayer expansion or collapse) requires that mass be transferred from one location to another and this mass transfer requires work, which makes crystalline swelling irreversible. The energy that must be transferred into a clay-water system to effect irreversible work during crystalline swelling has been described as "free energy of transition" and accounts for both hysteresis and the stepwise nature of crystalline swelling (Laird, Shang, & Thompson, 1995).

7.5 Experiments on Gas Intercalation in Swelling Clay

It was suggested that initial wedge-like penetration of water molecules bends the unit layers and that resulting elastic forces must be overcome before hydration can proceed (van Olphen, 1965). Once the interlayer is propped up by at least one water layer (1 W hydration state) the work required for further clay layers' separation to accommodate various other (gas) molecules present in surrounding media is thus reduced. This has been confirmed experimentally. XRD, neutron diffraction (Rother et al., 2013) and (indirectly) excess sorption studies showed that the spacing between the mineral layers of montmorillonite expands upon interaction with gaseous CO_2 and supercritical CO_2 ($scCO_2$) and that the degree of expansion depends on the initial water content in the interlayer as well as on water content in the mixed-gas environment (Loring et al., 2014; Schaef et al., 2015). The measurements indicated that the largest expansion is accompanied by an increase in the basal d-spacing of Na-rich montmorillonite from 11.3 to 12.3 Å, the number corresponding to a stable monolayer (the 1 W hydration state conventionally characterized with d-spacing in the range of 11.5–12.5 Å; upon incorporation of more water, the d-spacing increases to 14.5–15.5 Å to the stable 2 W (two water layers) hydration state where water forms a bilayer structure). Interaction of anhydrous $scCO_2$ with smectite clay in the 2 W and higher hydration states may lead in a collapse of the d-spacing to that of the 1 W state (Schaef et al., 2012). However, interaction of Na-exchanged Wyoming montmorillonite (SWy) and Ca-exchanged Texas montmorillonite (STx) samples with variably wet $scCO_2$ (2–100% saturation

of H_2O) induces swelling even to the values equal to the 3 W state with a d-spacing of 18.8 Å (Schaef et al., 2012). Thus, dry $scCO_2$ injected into a target reservoir has the capacity to dehydrate clay and to promote fracturing of caprock. On the other hand, after CO_2 becomes saturated by brine, it can induce further swelling of clay.

It is important to note here that the degree of sample's "swelling" deduced from the shape of the excess sorption plots is not always a good indicator of the changes in clay particle's structure. As earlier mentioned in Chap. 6, the DFT studies of CO_2 interaction with kaolinite surface by Schaef et al. (2014) indicated that surface adsorption on kaolinite is favored up to ~ 0.34 g/cm^3 of CO_2; showing distorted T-shaped CO_2–CO_2 clustering, typical of supercritical CO_2 aggregation over the surface at higher densities (Schaef et al., 2014). Beyond that point, the adsorption energy gain for any additional CO_2 becomes smaller than the CO_2–CO_2 interaction energy (~ 0.2 eV) in the supercritical medium, resulting in desorption of CO_2 from the kaolinite surface. The quartz crystal microbalance (QCM) data indicated linear adsorption of CO_2 (0–0.3 mmol of CO_2/g of KGa-2) onto the kaolinite surface up through the gaseous state (0.186 g/cm^3). However, in the supercritical region, the extent of CO_2 adsorption increases dramatically, reaching a peak (0.9–1.2 mmol of CO_2/g of KGa-2) near 0.40 g/cm3, before declining rapidly. This is by no means an indication of CO_2-induced clay swelling because of non-swelling nature of kaolinite.

Original (1970) debates around the CO_2 intercalation hypothesis stemmed from interpretations of the B.E.T. (Brunauer, Emmett, & Teller, 1938) surface area measurements on cation-exchanged montmorillonites, related to differences in sample preparation, sensitivities of cryogenic (−78 °C) adsorption apparatus, and theoretical assumptions about organization of the lamellae in the clay matrix being affected by the cation exchange, dialysis, and drying procedures. The first report that CO_2 can penetrate the interlamellar space of Cs-smectite (Thomas Jr. & Bohor, 1968) was initially challenged on the grounds of scientific merit, but was later reaffirmed by additional evidence using an infrared (IR) transmission spectrometer (at room temperature and at −78 °C) and X-ray goniometer (20 to −70 to 20 °C) experiments on the same clays. Despite the very low CO_2 pressure (<1 atm.) used in their work, Fripiat, Cruz, Bohor, and Thomas Jr. (1974) reported noticeable orientation dependency of the asymmetric stretching (ν_3) band in the 2350 cm^{-1} region of the absorbed IR spectra of K- and Cs-smectite and significant swelling of Na- and Ca-smectite due to CO_2 condensation during the cooling cycle (Fripiat et al., 1974). Loring et al. (2012) confirmed intercalation of CO_2 by means of NMR spectroscopy and attenuated total reflection infrared spectroscopy. Interestingly, the changes in d_{001} spacing were reversible in both Na-exchanged (10.0 to 12.3 to 10.0 Å) and Ca-exchanged (13.2 to 14.2 to 13.2 Å) smectites, but the changes in d_{002} and d_{003} peak positions appeared to be irreversible with the Ca-smectite (Loring et al., 2012). Fahmy, Paulaitis, Johnson, and McNally (1993) observed that the magnitude of saturated swelling of Mg-montmorillonite is not monotonically dependent on CO_2 pressure at 45 °C, which they attributed to a competition between the swelling caused by increasing solubility of added water in CO_2-rich phase and the hydrostatic pressure compaction effect, but the exact mechanisms were not

determined (Fahmy et al., 1993). More recently, molecular-scale phenomena related to CO_2 interaction with swelling clays have drawn the attention of environmental scientists.

In 2008, researchers at the United States Department of Energy observed that CO_2 molecules may permanently intercalate between the clay lamellae and suggested a sorption mechanism akin to nano-confinement; independently, Busch et al. (2008) conducted experiments on well-characterized shale samples and reported a relatively high CO_2 sorption capacity compared to coal as well as poor reproducibility which they attributed to strong CO_2 interaction with clay minerals present in the shale (Busch et al., 2008). Romanov et al. (2009a, b) reported irreversible swelling of Ca-smectite after exposure to CO_2 in prolonged pressure build-up experiments, with preliminary results suggesting a subsequent carbonate formation in the interlayer (Romanov, 2013; Romanov et al. 2009a). The sorption of volatile fluids in swelling clay was further investigated using *ab initio* and classical MD and MC simulations, which showed that the hydrated clay system is capable of sorbing linear-shaped CO_2 molecules via intercalation (for more details, refer to Chaps. 8 and 9). The disposition of CO_2 molecules and density profiles of atoms within interlayer of Na-montmorillonite from MD simulations reported by the same group were consistent with earlier Monte Carlo simulations for lower CO_2 content. Comparison of the preliminary experimental and theoretical results was followed by advanced complementary studies. It was reported that the modeling results and experimental observations indicate that sufficient presence of water species in the interlayer region is necessary for intercalation of CO_2 (Romanov et al., 2010a, b). The ensuing XRD studies focused primarily on changes in d_{001} basal spacing during and after the CO_2 treatment. The in situ (Giesting et al., 2012a) measurements replicating the group's pressure build-up experiments (Romanov et al., 2009b) confirmed the extent and irreversibility of matrix swelling observed ex situ. The reported XRD results indicate that the nature of the interlayer cations, degree of hydration, and the length of exposure to CO_2 can significantly affect the experimental outcome. However, the outcomes of these studies were inconsistent and specific nature of the CO_2-clay interactions governing this process was not established. Among proposed mechanisms was the formation of carbonate complexes that can be trapped in the interlayer via hydrogen bonding or as part of the interlayer cation hydration shell. Specific nature of CO_2–clay interaction was further investigated by theoretical studies discussed in the following chapters of this book.

Both Romanov et al. (2009a, b) and Giesting et al. (2012a, b) observed irreversible swelling up to 15–15.5 Å in the long-term pressure build-up experiments with Ca-rich smectites in 1–2 W hydration state, which suggests some reorganization of the interlayer content (Giesting et al., 2012a) that increases stability of the CO_2-clay system over time; but Schaef et al. (2012) reported only shrinking, attributed to drying effects of high-pressure CO_2, for the Ca-STx (cation-exchanged) samples (Schaef et al., 2012) with partly filled second hydration layer and initial $d_{001} > 13$ Å (Fig. 7.4). One possible explanation for the lack of consistency in these data is importance of the differences in methods of the CO_2 pressure build-up that may result in various degrees of CO_2–H_2O mixing in the

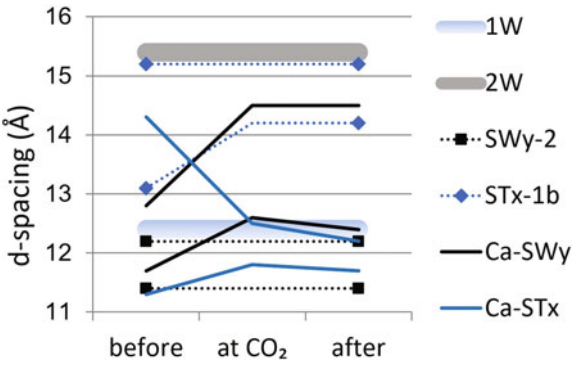

Fig. 7.4 Observed chronological d_{001} changes in SWy-2 and STx-1b based montmorillonites (natural and cation-exchanged), before (ambient), at and after (outgassing to ambient) the exposure to $scCO_2$—data from Romanov (2013)

interlayer as opposed to sheer mechanical displacement of H_2O molecules by the high-pressure CO_2 flow. As was demonstrated by Hemmen et al. (2012) for the synthetic Na-smectite, the rate of CO_2 intercalation can be very slow (several orders of magnitude slower at ambient pressure and temperature) compared to the interlayer mobility of water species (Hemmen et al., 2012) that is facilitated by swelling of the clay matrix (van Olphen, 1977). Giesting et al. (2012a, b) observed that the swelling kinetics differ significantly depending on the nature of interlayer cation, with Ca-exchanged montmorillonite swelling more slowly.

While these experiments shed some extra light on mechanisms of clay swelling, reproducibility issues, particularly for intermediate swelling between the basal spacing marks corresponding to 1 W and 2 W hydration states, suggest more experimental and modeling studies are needed to fathom this phenomenon.

References

Anandarajah, R., & Lu, N. (1991). Numerical study of the electrical double layer repulsion between non-parallel clay particles of finite length. *International Journal for Numerical and Analytical Methods in Geomechanics, 15*(10), 683–702.

Barbour, S. L., Fredlund, D. G., & Pufahl, D. E. (1992). The Osmotic Role in the behavior of swelling clay soils. In T. K. Karalis (ed.), *Mechanics of swelling: From clays to living cells and tissues. NATO ASI subseries H: Cell biology* (Vol. 64, pp. 97–139). Berlin: Springer-Verlag.

Barrer, R. M., & MacLeod, D. M. (1954). Intercalation and sorption by montmorillonite. *Transactions of the Faraday Society, 50,* 980–989.

Bassett, W. A. (1960). Role of hydroxyl orientation in mica alteration. *Geological Society of America Bulletin, 71*(4), 449–456.

Bolt, G. (1956). Physico-chemical analysis of the compressibility of pure clays. *Géotechnique, 6* (2), 86–93.

Brunauer, S., Emmett, P. H., & Teller, E. (1938). Adsorption of gases in multimolecular layers. *Journal of the American Chemical Society, 60*(2), 309–319.

Busch, A., et al. (2008). Carbon dioxide storage potential of shales. *International Journal of Greenhouse Gas Control, 2*(3), 297–308.

Clementz, D. M., & Mortland, M. (1974). Properties of Reduced Charge Montmorillonite: Tetra-Alkylammonium Ion Exchange Forms. *Clays and Clay Minerals, 22*(3), 223–229.

Debye, P., & Hückel, E. (1923). Zur Theorie der Elektrolyte. I. Gefrierpunktserniedrigung und verwandte Erscheinungen. *Physikalische Zeitschrift*, 24(9), pp. 185–206.

Dreher, P., & Niederbudde, E.-A. (1994). Potassium release from micas and characterization of the alteration products. *Clay Minerals, 29*(1), 77–85.

Eberl, D. (1980). Alkali cation selectivity and fixation by cvlay minerals. *Clays and Clay Minerals, 28*(3), 161–172.

Eisenman, G., & Horn, R. (1983). Ionic selectivity revisited: the role of kinetic and equlibrium processes in ion permeation through channels. *The Journal of Membrane Biology, 76*(3), 197–225.

Fahmy, T. M., Paulaitis, M. E., Johnson, D. M., & McNally, M. E. P. (1993). Modifier effects in the supercritical fluid extraction of solutes from clay, soil, and plant materials. *Analytical Chemistry, 65*(10), 1462–1469.

Fenter, P., & Lee, S. S. (2014). Hydration layer structure at solid–water interfaces. *MRS Bulletin, 39*(12), 1056–1061.

Fripiat, J. J., Cruz, M. I., Bohor, B. F., & Thomas, J., Jr. (1974). Interlamellar adsorption of carbon dioxide by smectites. *Clays and Clay Minerals, 22*(1), 23–30.

Giese, R. F., Jr. (1977). The influence of hydroxyl orientation, stacking sequence, and ionic substitutions on the interlayer bonding of micas. *Clays and Clay Minerals, 25*(2), 102–104.

Giese, R. F. (1978). The electrostatic interlayer forces of layer structure minerals. *Clays and Clay Minerals, 26*(1), 51–57.

Giesting, P., Guggenheim, S., Koster van Groos, A. F., & Busch, A. (2012a). X-ray diffraction study of K- and Ca-exchanged montmorillonites in CO_2 atmospheres. *Environmental Science and Technology, 46*(10), 5623–5630.

Giesting, P., Guggenheim, S., Koster van Groos, A. F., & Busch, A. (2012b). Interaction of carbon dioxide with Na-exchanged montmorillonite at pressures to 640 bar: Implications for CO_2 sequestration. *International Journal of Greenhouse Gas Control, 8,* 73–81.

Hansen, E. L., et al. (2012). Swelling transition of a clay induced by heating. *Scientific Reports, 2* (618), 1–4.

Harward, M. E., Carstea, D. D., & Sayegh, A. H. (1969). Properties of vermiculites and smectites: expansion and collapse. *Clays and Clay Minerals, 16*(6), 437–447.

Hemmen, H., et al. (2012). X-ray studies of carbon dioxide intercalation in sodium fluorohectorite clay at near-ambient conditions. *Langmuir, 28*(3), 1678–1682.

Hillier, S. (2003). Clay Mineralogy. In G. Middleton et al. (Eds.), *Encyclopaedia of sediments and sedimentary rocks* (pp. 139–142). Dordrecht: Kluwer Academic Publishers.

Hoffmann, U., Endell, K., & Wilm, D. (1933). Krystall strukturund Quellung vo montmorillonit (Das Tonmineral der Bentonittone). *Zeitschrift für Kristallographie, 86*(1–6), 340–348.

Katti, D. R., & Shanmugasundaram, V. (2001). Effect of controlled swelling on the microstructure of saturated expansive soil. *Canadian Geotechnical Journal, 38*(1), 175–182.

Katti, D. R., Schmidt, S. R., Ghosh, P., & Katti, K. S. (2005). Modeling the response of pyrophyllite interlayer to applied stress using molecular dynamics. *Clays and Clay Minerals, 53*(2), 171–178.

Kittrick, J. A. (1969). Quantitative evaluation of the strong-force model for expansion and contraction of vermiculite. *Soil Science Society of America Proceedings, 33*(2), 222–225.

Komadel, P., Madejová, J., & Stucki, J. W. (1995). Reduction and reoxidation of nontronite: Questions of reversibility. *Clays and Clay Minerals, 43*(1), 105–110.

Laffer, B. G., Posner, A. M., & Quirk, J. P. (1966). Hysteresis in the crystalline swelling of montmorillonite. *Clay Minerals, 6*(4), 311–321.

Laird, D. A. (1987). Layer charge and crystalline swelling of expanding 2:1 phyllosilicates. In *Retrospective Theses and Dissertations* (Paper 8554). Ames: Digital Repository @ Iowa State University.

Laird, D. A. (1996). Model for crystalline swelling of 2:1 phyllosilicate. *Clays and Clay Minerals, 44*(4), 553–559.

Laird, D. A. (2006). Influence of layer charge on swelling of smectites. *Applied Clay Science, 34* (1–4), 74–87.

Laird, D. A., Shang, C., & Thompson, M. L. (1995). Hysteresis in crystalline swelling of smectites. *Journal of Colloid and Interface Science, 171*(1), 240–245.

Lee, S. S., et al. (2010). Hydrated cation speciation at the muscovite (001)−water interface. *Langmuir, 26*(22), 16647–16651.

Loring, J. S., et al. (2012). In situ molecular spectroscopic evidence for CO_2 intercalation into montmorillonite in supercritical carbon dioxide. *Langmuir, 28*(18), 7125–7128.

Loring, J. S., et al. (2014). In Situ study of CO_2 and H_2O partitioning between Na-montmorillonite and variably wet supercritical carbon dioxide. *Langmuir, 30*(21), 6120–6128.

Low, P. F. (1982). Water in clay-water systems. *Agronomie, 2*(10), 909–914.

Mitchell, J. K., & Soga, K. (2005). *Fundamentals of soil behaviour* (3rd ed.). Hoboken: John Wiley & Sons Inc.

Moore, D. E., & Lockner, D. A. (2007). Friction of the smectite clay montmorillonite: A review and interpretation of data. In T. Dixon & C. Moore (Eds.), *The Seismogenic Zone of Subduction Thrust Faults* (pp. 317–345). New York: Columbia University Press.

Moore, D. M., & Reynolds, R. C., Jr. (1997). *X-Ray diffraction and the identification and analysis of clay minerals* (2nd ed.). New York: Oxford University Press.

Myshakin, E. M., et al. (2014). Molecular dynamics simulations of turbostratic dry and hydrated montmorillonite with intercalated carbon dioxide. *The Journal of Physical Chemistry A, 118* (35), 7454–7468.

Norrish, K. (1954). The swelling of montmorillonite. *Discussions of the Faraday Society, 18,* 120–134.

Norrish, K. (1973a). *Factors in the weathering of mica to vermiculite* (pp. 417–432). Madrid: Division de Ciencias C.S.I.A.

Norrish, K. (1973b). *Forces between clay particles* (pp. 375–383). Madrid: Division de Ciencias C.S.I.A.

Norrish, K., & Quirk, J. P. (1954a). Crystalline swelling of montmorillonite: Use of electrolytes to control swelling. *Nature, 173*(4397), 255–256.

Norrish, K., & Quirk, J. P. (1954b). Crystalline swelling of montmorillonite: Manner of swelling of montmorillonite. *Nature, 173*(4397), 256–257.

Romanov, V. N. (2013). Evidence of irreversible CO_2 intercalation in montmorillonite. *International Journal of Greenhouse Gas Control, 14,* 220–226.

Romanov, V. N., Ackman, T. E., Soong, Y., & Kleinman, R. L. (2009a). CO_2 storage in shallow underground and surface coal mines: Challenges and opportunities. *Environmental Science and Technology, 43*(3), 561–564.

Romanov, V. N., et al. (2009b). *CO_2 trapping in clayey materials*. Paper presented at the 46th Annual Meeting of the Clay Minerals Society, Billings, MT.

Romanov, V. N., et al. (2010a). *Mechanisms of CO_2 interaction with expansive clay*. Poster presented at the SEA-CSSJ-CMS Trilateral Meeting on Clays, Seville, Spain.

Romanov, V. N., et al. (2010b). *CO_2 interaction with geomaterials*. Paper presented at the AGU Fall Meeting (p. H11 J-01*, Invited*), San Francisco, CA.

Rother, G., et al. (2013). CO_2 sorption to subsingle hydration layer montmorillonite clay studied by excess sorption and neutron diffraction measurements. *Environmental Science and Technology, 47*(1), 205–211.

Schaef, H. T., et al. (2012). In situ XRD study of Ca^{2+} saturated montmorillonite (STX-1) exposed to anhydrous and wet supercritical carbon dioxide. *International Journal of Greenhouse Gas Control, 6,* 220–229.

Schaef, H. T., et al. (2014). Surface Condensation of CO_2 onto Kaolinite. *Environmental Science & Technology Letters, 1*(2), 142–145.

Schaef, H. T., et al. (2015). Competitive sorption of CO_2 and H_2O in 2:1 layer phyllosilicates. *Geochimica et Cosmochimica Acta, 161,* 248–257.

Schmidt, S., Katti, D., Ghosh, P., & Katti, K. (2005). Evolution of mechanical response of sodium montmorillonite interlayer with increasing hydration by molecular dynamics. *Langmuir, 21* (17), 8069–8076.

Stucki, J. W., & Roth, C. B. (1977). Oxidation-reduction mechanism for structural iron in nontronite. *Soil Science Society of America Journal, 41*(4), 808–814.

Suquet, H., Iiyama, J. T., Kodama, H., & Pezerat, H. (1977). Synthesis and swelling properties of saponites with increasing layer charge. *Clays and Clay Minerals, 25*(3), 231–242.

Tambach, T. J. (2005). *Swelling of clay minerals: A molecular simulation study (Thesis).* Wrappers (paperback) ed. Amsterdam: Wageningen, Ponsen & Looijen.

Tambach, T. J., Bolhuis, P. G., M Hensen, E. J., & Smit, B. (2006). Hysteresis in clay swelling induced by hydrogen bonding: Accurate prediction of swelling states. *Langmuir, 22*(3), 1223–1234.

Thomas, J., Jr., & Bohor, B. F. (1968). Surface area of montmorillonite from the dynamic sorption of nitrogen and carbon dioxide. *Clays and Clay Minerals, 16*(1), 83–91.

van Olphen, H. (1965). Thermodynamics of interlayer adsorption of water in clays. I.—Sodium vermiculite. *Journal of Colloid Science, 20*(8), 822–837.

van Olphen, H. (1977). *An introduction to clay colloid chemistry* (2nd ed.). New York, London, Sydney, Toronto: John Wiley & Sons.

Zarzycki, P., & Gilbert, B. (2016). Long-range interactions restrict water transport in pyrophyllite interlayers. *Scientific Reports, 6*(25278), 1–5.

Chapter 8
Monte Carlo and Molecular Dynamics Simulations of Clay Mineral Systems

Evgeniy M. Myshakin and Randall T. Cygan

Abstract This chapter is focused on reviewing molecular dynamics and Monte Carlo simulations of greenhouse gases' interactions with swelling clay minerals. This chapter unfolds with the results of simulations on stepwise expansion of interlayer in hydrated montmorillonite. Next, an overview of the simulation data on carbon dioxide intercalation in clays is given with respect to structural changes, transport properties, thermodynamics, spectroscopic characteristics, sorption behavior at the basal clay surfaces, and surface wettability changes in CO_2-brine-mineral systems. Effects of the chemical nature of interlayer ions, as well as charge density and its distribution within clay layers on carbon dioxide/water intercalation and interaction with clay surfaces, are discussed. Then, results of methane interaction with hydrated swelling clays are presented. The discussion is centered around the formation of gas hydrate phase in the interlayer under suitable pressure and temperature conditions. Dynamic nature of hydrate cages encapsulating methane molecules is considered together with a mechanism of their formation in interlayer. A shift of the equilibrium pressure and temperature conditions in comparison with bulk phase is attributed to distortion of hydrate lattice in clay and to finite pore space. Finally, intercalation of the carbon dioxide/methane molecules in interlayer is reviewed through competitive adsorption of the binary mixture on clay surfaces.

Before considering intercalation of greenhouse gases into the interlayer of swelling clay minerals, it is important to realize that such processes can only occur in hydrated systems (refer to Chap. 7). The experimental (Chaps. 6 and 7) and theoretical (Cygan, Guggenheim, & Koster van Groos, 2004a; Botan et al., 2010; Makaremi, Jordan, Guthrie, & Myshakin, 2015; Rao & Leng, 2016a, b) studies indicate that water must be present in the interlayer for CO_2 and methane to be intercalated. It was already mentioned in Chap. 7 that the expansion of clay is

E. M. Myshakin (✉)
U.S. Department of Energy, NETL–AECOM, Pittsburgh, USA
e-mail: Evgeniy.Myshakin@netl.doe.gov

R. T. Cygan
U.S. Department of Energy, Sandia National Laboratories (SNL), Albuquerque, USA

© Springer International Publishing AG 2018

V. Romanov (ed.), *Greenhouse Gases and Clay Minerals*, Green Energy and Technology, https://doi.org/10.1007/978-3-319-12661-6_8

governed by formation of the extended hydrogen-bonding network of water molecules among themselves, with clay surface and interlayer ions. Formation of the first fully developed hydration shell—enthalpies of hydration for sodium and calcium ions are −405 and −1592 kJ/mol, respectively (Burgess, 1999)—around interlayer ions is a leading factor promoting the expansion (Young & Smith, 2000). Carbon dioxide and methane are ineffective solvents of the counter-balancing ions to make the swelling be thermodynamically favorable; so, it requires at least residual amount of water to prop open the interlayer space.

CO_2 and CH_4 retaining in the interlayer space are in equilibrium with surrounding bulk mobile phase in pore and interstitial (between clay particles) regions, and their interlayer concentrations are larger compared with saturated concentrations in water-rich bulk phase at prevailing pressure and temperature conditions. At typical conditions of deep saline aquifers—340–350 K and 10–13 MPa, 800–1000 m below the surface (Benson & Cole, 2008)—a molar fraction of methane and carbon dioxide in liquid phase would be of the order of 10^{-4} and 10^{-2}–10^{-3}, respectively, according to the Peng-Robinson EoS (Huber, 2007). The predicted molar fraction of CO_2 in binary mixture with water in the interlayer at 1 W state of Na-exchanged montmorillonite and 100% relative humidity (RH) is around 0.06–0.12 (348.15 K/12.5 MPa) (Botan et al., 2010; Makaremi et al., 2015) and goes further up to 0.16 at 30% of RH (348 K/13 MPa) (Rao & Leng, 2016b). Injection of supercritical CO_2 into a geological reservoir would result in exposure of smectites (*i.e.,* swelling clay minerals) to CO_2-rich bulk phase, however that phase is unstable in the interlayer space of swelling clays and H_2O-rich one is realized (Schaef et al., 2015; Loring et al., 2014; Rother et al., 2013; Botan et al., 2010; Makaremi et al., 2015; Rao & Leng, 2016a, b). Schaef et al. (2015) and Loring et al. (2014) using a combination of *in situ* X-ray diffraction, infrared (IR) spectroscopic titrations, and quartz crystal microbalance measurements, estimated CO_2 adsorption at internal surface of montmorillonite (MMT). They found that at initial sub-1 W hydrate state of Ca-exchanged MMT exposed to supercritical CO_2 with undersaturated (10%) water concentration, CO_2 concentration in the interlayer can reach 0.8 mmol/g dry clay ($\sim$0.27 molar fraction in the interlayer; 50 °C and 9 MPa). As soon as water concentration in the interlayer increases producing a stepwise hydration profile, CO_2 concentration drops significantly.

Ji et al. (2012) performed a series of CH_4 adsorption experiments on clay-rich rocks conducted at 35–65 °C and at pressure up to 15 MPa under nearly dry conditions. They estimated the Langmuir volume of CH_4 normalized to clay minerals mass: MMT (0.48 mmol/g) > illite/smectite interstratified clay (0.41 mmol/g) > kaolinite (0.12 mmol/g) > chlorite (0.10 mmol/g) > illite (0.08 mmol/g). Assuming that part of adsorbed methane is entered the interlayer space of MMT and taking non-swelling kaolinite/chlorite/illite as a baseline, the internal adsorption of methane might be on an order of 0.4 mmol/g at sub-1 W initial d_{001}-spacings. Those data indicate that CO_2/CH_4 concentrations can reach appreciable values in interlayer space, so the intercalation mechanism provides a way to retain CO_2 and CH_4 in clay-rich geological formations under conditions of underground geologic aquifers or shale reservoirs. At pressure and temperature conditions of permafrost and deep marine

sediments, methane can be trapped in interlayer in a form of gas hydrate clathrate that can be thought as "double trapping" within confining environment of internal basal clay surfaces and additional immobilization is achieved within cages of hydrate lattice, that causes a sharp increase of trapped methane concentration that will be discussed later in this chapter.

The basal d_{001}-spacing of natural clays such as Na-MMT increases in a stepwise fashion with increasing RH that leads to change of an integral number of water layers (up to three, 1 W-3 W) in the interlayer space between adjacent clay layers. A comparison of d_{001}-spacing values from simulation with the corresponding experimental values (X-ray diffraction data) values serves as an excellent probe to validate the applicability of a particular force field to explore processes involving intercalation, dynamics, and transport properties of species in swelling clay minerals. Figure 8.1 reports the expansion of the d_{001}-spacing of Na-MMT upon water intercalation computed using molecular dynamics (MD) simulations with the Clayff force field (Cygan, Liang, & Kalinichev, 2004b). Comparison with experimental data (Fu, Zhang, & Low, 1990) shows that the MD results closely reproduce the experimental trend in the d_{001}-spacing, displaying plateaus corresponding to formation of monolayer and bilayer water arrangements in the interlayer. The spacing

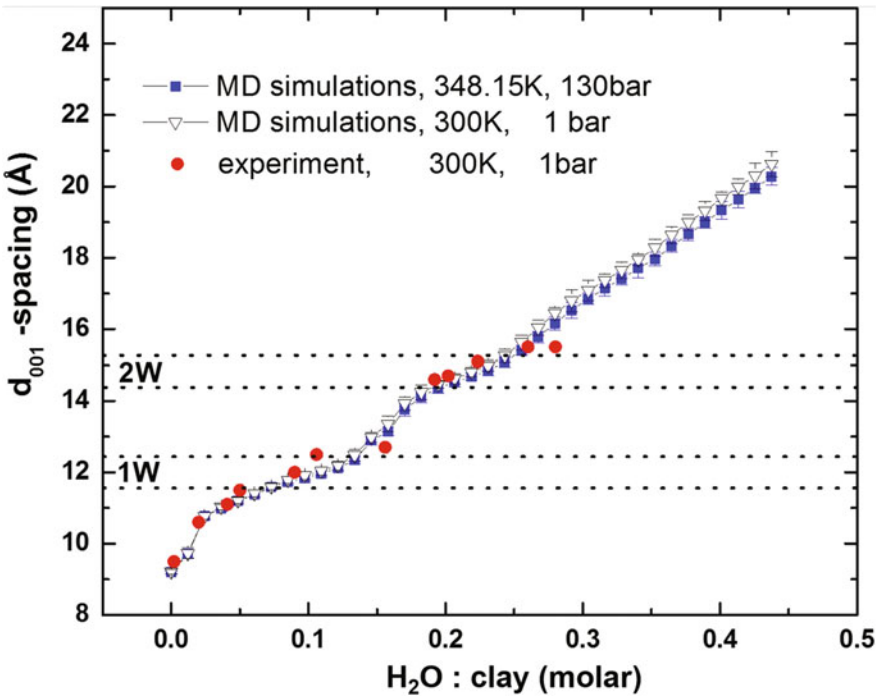

Fig. 8.1 Swelling behavior of Na-MMT upon hydration: *dotted lines* indicate the *d*-spacing ranges corresponding to stable hydration states—reprinted with permission from (Myshakin et al., 2013) Copyright (2013) American Chemical Society

curve calculated for the elevated pressure and temperature corresponding to underground conditions deviates only slightly from that calculated at 1 bar (10^5 Pa or 0.1 MPa) and 300 K. This finding is consistent with XRD measurements of d_{001}-spacing showing that hydration states are weekly dependent on pressure (Giesting, Guggenheim, Koster van Groos, & Busch, 2012b; Ilton et al., 2012) and brings confidence that MD simulations are capable to properly describe the processes of clay mineral expansion and intercalation.

8.1 Carbon Dioxide and Swelling Clay Minerals

Host rock matrix of the geological storage reservoirs used in the CO_2 sequestration (examined in the Chaps. 2 and 3) often includes swelling clay minerals able to intercalate carbon dioxide as a secondary trap, and which fueled a great deal of theoretical work aiming at understanding the molecular mechanisms of intercalation, thermodynamics, structural phenomena, and transport properties of intercalated species (Yang & Zaoui, 2016; Rao & Leng, 2016a, b; Kadoura, Nair, & Sun, 2016; Makaremi et al., 2015; Sena, Morrow, Kirkpatrick, & Krishnan, 2015; Myshakin et al., 2014; Lee, McGrail, & Glezakou, 2014; Myshakin et al., 2013; Cygan, Romanov, & Myshakin, 2012; Yang & Yang, 2011; Botan et al., 2010). Given the abundance of MMT in nature, it was often chosen as a typical swelling clay system and, particularly, Na- or Ca-MMT, which represent natural or Na-exchanged SWy MMT samples from Wyoming, and natural or Ca-exchanged STx MMT samples from Texas, respectively. The differences in chemical nature of interlayer counter-balancing ions and in distributions of isomorphic substitutions in clay layers can significantly affect the intercalation mechanism and will be considered below.

Figure 8.2 presents a schematic representation of tetrahedra (yellow)—octahedra (magenta/green)—tetrahedra (TOT) layer sequences of MMT with intercalated sodium ions, water and carbon dioxide molecules. The color alternation in the octahedral sheet represents the Al/Mg substitutions producing negative charge compensated by the interlayer ions.

Figure 8.3 displays *XY* and *XZ* planes of the internal basal surfaces (yellow tetrahedra in Fig. 8.2) in MMT exposed to the interlayer species. The silicon tetrahedra linked by shared basal oxygens form a periodic system of the hexagonal rings (the *XY* plane). Figure 8.2 depicts two types of interlayer ions; the first type represents surface-bound sodium ions adsorbed at the centers of the hexagonal rings (tetrahedral holes, Fig. 8.3) and coordinated to basal oxygens and oxygens of water molecules (inner-sphere complexes); and the second type is designated as ions fully coordinated to water molecules (outer-sphere complexes). The amount of water in the interlayer, layer charge distributions, and the chemical natures of the ions control the ratio of inner-to-outer sphere complexes (Rao & Leng, 2016a; Makaremi et al., 2015; Myshakin et al., 2013; Young & Smith, 2000). Intercalation of carbon dioxide disrupts the water network (Billemont, Coasne, & De Weireld,

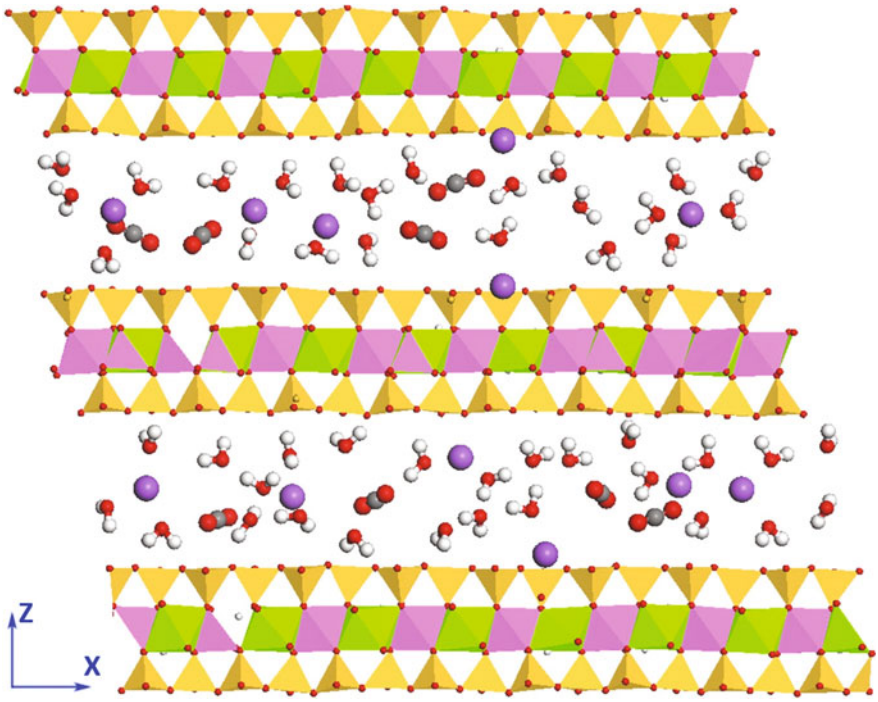

Fig. 8.2 Schematic representation of clay-water-CO_2 system; *Filled violet circle* = sodium ion, *Filled grey circle* = carbon, *Filled red circle* = oxygen, *Open circle* = hydrogen—reprinted with permission from (Myshakin et al., 2013) Copyright (2013) American Chemical Society

2010) and causes the Na^+ ions to be displaced toward the clay surfaces that, in turn, changes their relative wettability (Myshakin et al., 2013).

Classical molecular simulations of clay minerals rely on analytical expressions of potential energy to accurately describe the forces and energies associated with a statistical ensemble of atoms that comprise the clay-water or clay-CO_2 system. Accurate and flexible force fields for clay minerals (Teppen et al., 1997; Cygan et al., 2004b; Heinz, Lin, Mishra, & Emami, 2013) are available and can be implemented with specific H_2O models (SPC, TIP3P, etc.). Although involving nonflexible molecules or other constraints, several energy potentials for CO_2 are suitable for modeling gas, liquid, and supercritical states (Zhang & Duan, 2005; Aimoli, Maginn, & Abreu, 2014). Flexible CO_2 potentials that incorporate bond stretch and bond bend modes are particularly valuable in the analysis of interfaces such as the intercalation and adsorption of CO_2 in clay mineral systems (Harris & Yung, 1995; Zhu, Zhang, Liu, & Zhang, 2009; Cygan et al., 2012). Accurate and reliable force fields are critical in providing realistic molecular dynamics and Monte Carlo simulations, especially when the clay-fluid systems are comprised of many thousands to millions of atoms when quantum chemical methods would be computationally expensive.

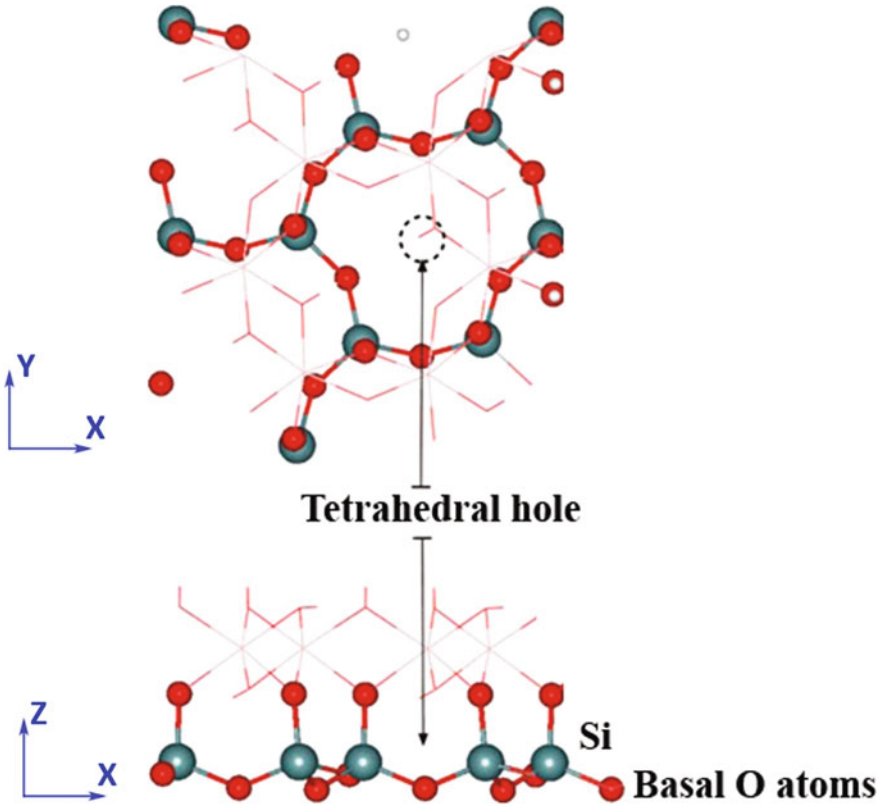

Fig. 8.3 Chemical structure of internal basal surface in smectite clay minerals. The upper *XY* projection shows the centers of hexagonal rings—reprinted with permission from (Michalkova & Tunega, 2007) Copyright (2007) American Chemical Society

In the molecular simulations, TOT layers are assumed to be perfectly oriented, although rotational disorder (in which layers may have different rotations with respect to the normal axis to the clay layer) inherently present in natural samples and manifests itself through turbostratically stacked clay layers (Viani, Gualtieri, & Artioli, 2002; Lutterotti et al., 2010). As a result, instead of having a coherent alignment of hexagonal rings on either side of the interlayer region, rotational disorder results in a Moiré pattern with a periodic variation in alignment of hexagonal rings across the interlayer. At sub-1 W hydration state, the formation of disordered clay layers is energetically favorable driven by electrostatic avoidance of cations adsorbed at the opposite internal surfaces (at the centers of the hexagonal rings). With increase of the interlayer space caused by water and carbon dioxide intercalation, disordering becomes an energetically demanding process (Myshakin et al., 2014).

Figure 8.4 demonstrates the d_{001}-spacing calculated as a function of the number of water molecules for selected numbers of intercalated carbon dioxide molecules per unit cell. The bottom curve, which displays expansion in the absence of carbon

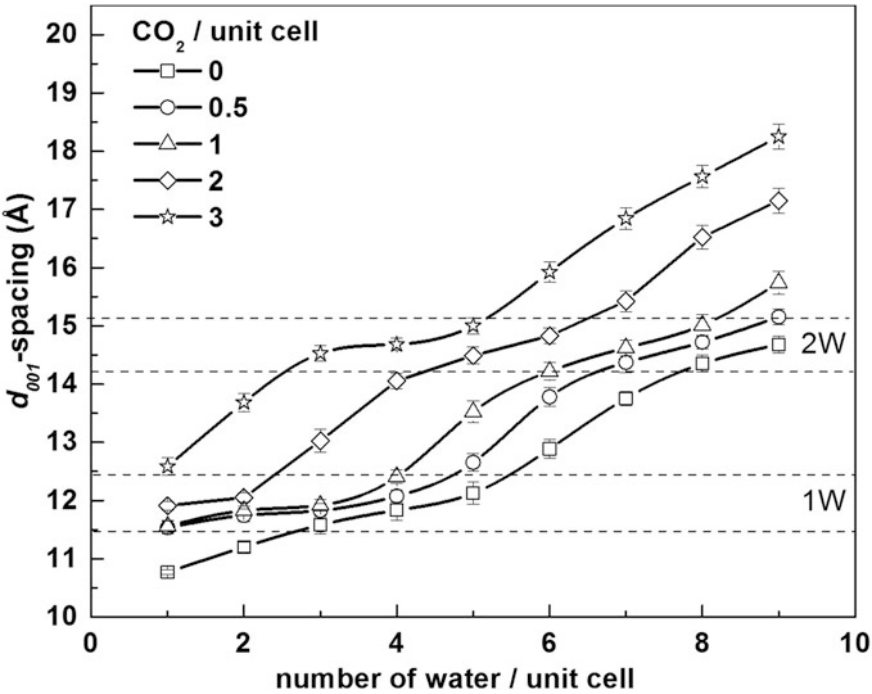

Fig. 8.4 d_{001}-spacing as a function of the number of water molecules at fixed numbers of CO_2 molecules per unit cell: *dashed lines* indicate ranges of basal d_{001}-spacing corresponding to 1W and 2 W hydration states—reprinted with permission from (Myshakin et al., 2013) Copyright (2013) American Chemical Society

dioxide molecules, serves as the reference. The most important observation deduced from these simulations is that introduction of CO_2 into interlayer does not change the characteristic stepwise swelling. Carbon dioxide mainly affects the transition from 1 W to 2 W by shifting it to smaller water amount with an increase of carbon dioxide concentration. It is also interesting to note that water-CO_2 compositions like 8–0.5, 7–1, and 6–2 all demonstrate similar d_{001}-spacings. As a result, the process of CO_2 intercalation can be accompanied by displacement of water molecules while keeping d_{001}-spacing nearly constant rather than further expanding the interlayer spacing. The analysis of atomistic distributions reported by different groups reveal that in CO_2/H_2O monolayer and bilayer, carbon dioxide molecules tend to orient parallel to the clay basal surface (Rao & Leng, 2016b; Kadoura et al., 2016; Makaremi et al., 2015; Sena et al., 2015; Myshakin et al., 2013; Botan et al., 2010). Moreover, with concentration increase, CO_2 (due to its hydrophobic nature) forms clusters/agglomerations in the interlayer facilitating lateral diffusion through percolation pathways (Rao & Leng, 2016b; Sena et al., 2015; Myshakin et al., 2014).

Examination of these clusters has showed that most of the pairs of near-neighbor CO_2 molecules adopt a slipped parallel coordination geometry with respect to each

other while a small fraction displays a tilted T-shaped geometry (Rao & Leng, 2016b; Sena et al., 2015) in line with orientation configuration of CO_2 dimers in supercritical state (Cipriani, Nardone, Ricci, & Ricci, 2001; Saharay & Balasubramanian, 2004a, b; Saharay & Balasubramanian, 2006). Water molecules preferentially form first hydration shells around interlayer ions although the corresponding coordination numbers are lower because of steric hindrance—imposed by the confining environment of the clay layers (for outer-sphere complexes at 1 W state) and ion adsorption at the surfaces with basal oxygens participating in solvation (for inner-sphere complexes)—to add up to the coordination number corresponding to bulk water (Rao & Leng, 2016b; Makaremi et al., 2015). Water molecules that are not part of a hydration shell around interlayer ions also interact with intercalated CO_2 molecules. Infrared spectroscopic measurements have shown that trapping of carbon dioxide in Na- and Ca-MMT leads to a red shift in the asymmetric fundamental stretch frequency of the CO_2 molecule (Romanov, 2013; Hur et al., 2013). DFT-based MD simulations carried out to explain the origin of this red shift identify the electric field of water dipoles mainly responsible for induced elongation of the CO bonds of CO_2 and the observed frequency shift (Myshakin et al., 2013). In other words, the extent of the shift depends on the amount of intercalated water and could serve as a preliminary probe to a hydration state to supplement XRD measurements of d_{001}-spacings.

Transport properties of interlayer species were examined by many researchers focusing on estimation of self-diffusion coefficients of carbon dioxide, water, and ions in the direction parallel to the internal basal surfaces (Yang & Zaoui, 2016; Rao & Leng, 2016b; Kadoura et al., 2016; Makaremi et al., 2015; Sena et al., 2015; Lee et al., 2014; Myshakin et al., 2013; Cygan et al., 2012; Yang & Yang, 2011; Botan et al., 2010). As a general consensus, the presence of CO_2 retards the diffusion of water and counter-balancing ions. The diffusion of H_2O and Na^+ in the presence of CO_2 for the monolayer (1 W) is about 2.5 times smaller than in the absence of CO_2 and 1.5 times for the bilayer (2 W) (Botan et al., 2010). The tendency of CO_2 molecules to form clusters and lack of participation in solvation of interlayer ions result in higher diffusion coefficients than those of water molecules and interlayer ions (Rao & Leng, 2016b). The most retarded motion is estimated for the interlayer ions experiencing strong electrostatic interactions with charged clay layers. As a result, total diffusion of the counter-balancing cations should be separated into contributions from surface-bound cations and those forming outer-sphere complexes (Myshakin et al., 2013).

To estimate the amount of intercalated carbon dioxide in the interlayer, Monte Carlo (MC) simulations are a convenient tool that also provides access to thermodynamics of the swelling process (Rao & Leng, 2016a, b; Makaremi et al., 2015; Botan et al., 2010). Figure 8.5 displays computed free energy of clay swelling due to intercalation of H_2O/CO_2 mixture in Na-MMT and Na-beidellite as a function of d_{001}-spacing. The MMT clay model bears charge in the central octahedral sheets, which is screened from direct exposure to interlayer species by the tetrahedral sheets. In contrast, the beidellite model carries charge in the tetrahedral sheets that allow the study of the effect of negative charge locations on the swelling behavior.

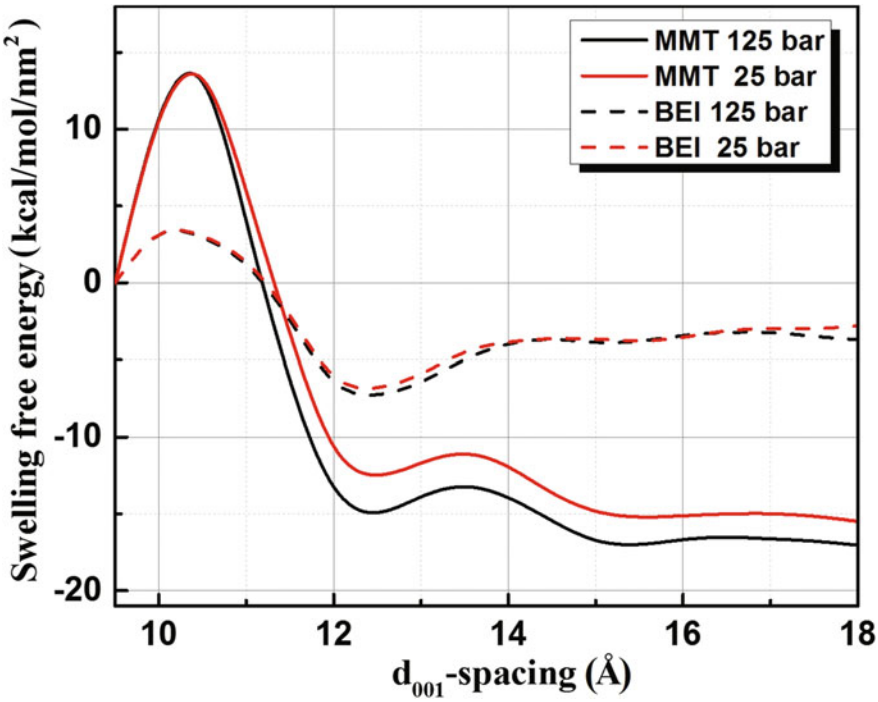

Fig. 8.5 Calculated swelling free energy of Na-MMT and Na-beidellite as a function of *d*-spacing for intercalation of H_2O-CO_2 mixture at $P = 25$ and 125 bar, $T = 348.15$ K—reprinted with permission from (Makaremi et al., 2015) Copyright (2015) American Chemical Society

Both clay systems have same charge ($-0.75e$) per unit cell compensated by sodium ions. The energy curves show that intercalation (starting from the dry clay) required to overcome the energy barriers followed by energy minima corresponding to 1 W (monolayer) and 2 W (bilayer) hydration states. An increase of pressure provides more defined free-energy minima and stabilization of the interlayer configurations. Figure 8.6 presents the CO_2 molar fraction in the intercalated H_2O/CO_2 mixture in equilibrium with bulk phase and corresponding to the swelling energies estimated at the d_{001}-spacing in Fig. 8.5. In both systems, there is a pronounced peak in the CO_2 mole fraction at a d_{001}-spacing corresponding to the 1 W state and a second weaker peak (or shoulder) at a distance corresponding to 2 W, in agreement with experiment showing that the maximum expansion of the interlayer due to CO_2 exposure occurs at the initial sub-1 W hydration state with residual amount of intercalated water (Giesting, Guggenheim, Koster van Groos, & Busch, 2012a, b; Loring et al., 2014; Schaef et al., 2015). The concentration of CO_2 in the interlayer region for both clay mineral systems substantially exceeds that in the bulk water-rich phase. Pressure increase causes an elevation of the intercalated CO_2 concentration. For Na-MMT, the calculated mole fractions of CO_2 in the interlayer region is in good

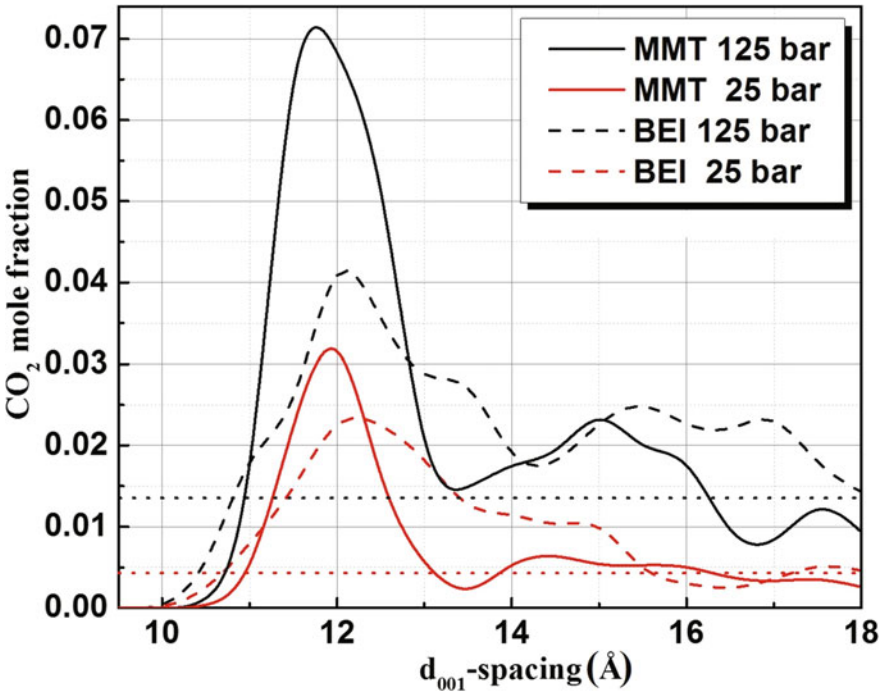

Fig. 8.6 CO_2 mole fraction in interlayer as a function of *d*-spacing for Na-MMT and Na-beidellite at P = 25 and 125 bar, T = 348.15 K. Horizontal *dotted lines* represent CO_2 mole fractions in bulk H_2O-rich phase at P = 25 and 125 bar, T = 348.15 K—reprinted with permission from (Makaremi et al., 2015) Copyright (2015) American Chemical Society

agreement with those reported by Botan et al. (2010) who used a different theoretical approach.

The charge localized at the tetrahedral sheets in beidellite decreases the ability of the interlayer to retain carbon dioxide relative to MMT that has negative charge localized in the octahedral sheets. Swelling free energy also demonstrates that the monolayer of the H_2O/CO_2 mixture is more stable in the interlayer of beidellite compared to MMT, which shows the greater stability of the bilayer (Fig. 8.5). The differences in stability of 1 W and 2 W states for hydrated MMT and beidellite (without CO_2) are documented in the literature and are attributed to specifics of ion solvation (Smith et al., 2004). Figure 8.7 depicts density profile distributions of the interlayer species for Na-MMT-H_2O-CO_2 and Na-beidellite-H_2O-CO_2 systems that provide insight into the relative stability of monolayer and bilayer mixture configurations. The density profiles confirm that carbon dioxide molecules form a mixture with water at monolayer (Fig. 8.7a) and bilayer (Fig. 8.7b) configurations. As a monolayer, the Na^+ distribution demonstrates two peaks for both MMT and beidellite. Due to stronger electrostatic interactions, the positions of the peaks are shifted more closely to the surfaces for beidellite. However, in the bilayer, the

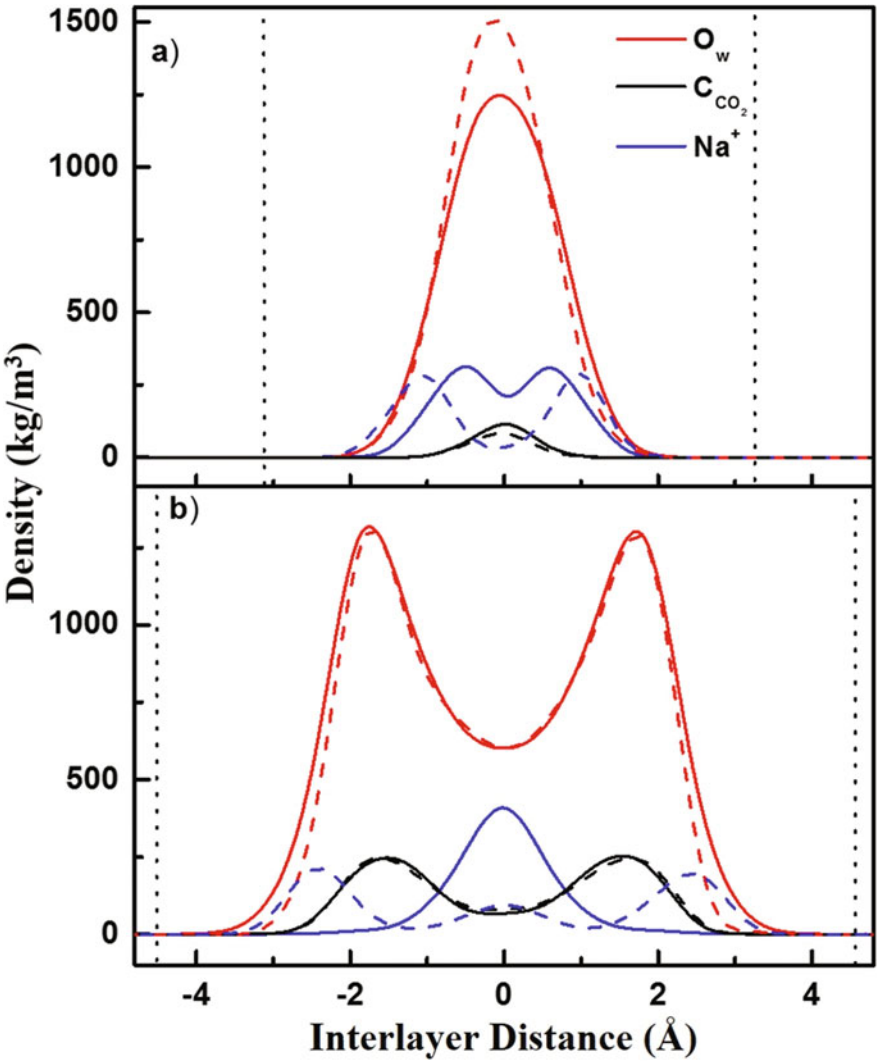

Fig. 8.7 Density profiles of O_w, C_{co_2}, and Na^+ along the interlayer distance perpendicular to internal surfaces of MMT (*solid*) and beidellite (*dashed lines*) reported for *d*-spacing. **a** 12.5 Å and **b** 15.5 Å. For **b** C_{co_2} is magnified by a factor of 10. Vertical *dotted lines* indicate the planes of basal oxygen atoms—reprinted with permission from (Makaremi et al., 2015) Copyright (2015) American Chemical Society

sodium ions in MMT develop a well-defined single peak at the interlayer center indicating the formation of outer-sphere complexes of fully hydrated ions. In beidellite, the ions are predominantly adsorbed at the surfaces forming inner-sphere complexes. Suter et al. (2012) explored the thermodynamics of Li^+, Na^+, and K^+-MMT and beidellite using *ab initio* MD. These authors found that smectites with

the free energy minimum in the middle of the interlayer for bilayer swell to the 2 W hydration state with the ions forming a full hydration sphere. In beidellite, the position of the lowest energy region remains unchanged from a monolayer to bilayer indicating that swelling would tend to stop at monolayer. That is confirmed by the swelling energy curve depicted in Fig. 8.5. Thus, the interplay between the hydration of counter-balancing ions and the attraction to the basal surface determines the swelling behavior of smectites. Localization of charge in the octahedral sheets supports swelling to 2 W (and higher) while isomorphic substitutions in the tetrahedral sheets favor 1 W (Figs. 8.5 and 8.7).

Rao and Leng (2016a, b) reported the effect of layer charge, including the influence of charge amount and charge location, on the intercalation of the carbon dioxide–water mixture in Na-MMT clay interlayers under typical CO_2 geologic sequestration conditions (T = 323 K, P = 90 bar). For the two clay models used in the study, one possessed layer charge of −1.0 *e*/unit cell ("high-charge") in the octahedral sheets only, and the other one had −0.75 *e*/unit cell split between the octahedral (2/3) and the tetrahedral sheets (1/3) ("low-charge"). Using MC and MD simulations they explored the effect of layer charge under variable RH following the recent experimental studies that demonstrated exposure of dry supercritical CO_2 to MMT samples in the 2 W and higher hydration states can induce a collapse of the d_{001}-spacing to that of the 1 W state (Ilton et al., 2012; Schaef et al., 2012). On the other hand, the interaction of those samples with wet $scCO_2$ promotes swelling of smectites to either 1 W or 2 W hydration states (Rother et al., 2013; Ilton et al., 2012; Schaef et al., 2012).

Figure 8.8 demonstrates the changes of the d_{001}-spacing and intercalated amount of carbon dioxide in the interlayer as functions of RH for "high-charge" and "low-charge" models. The simulated data are compared against experimental results reported by Loring et al. (2014) at the same pressure and temperature conditions. The

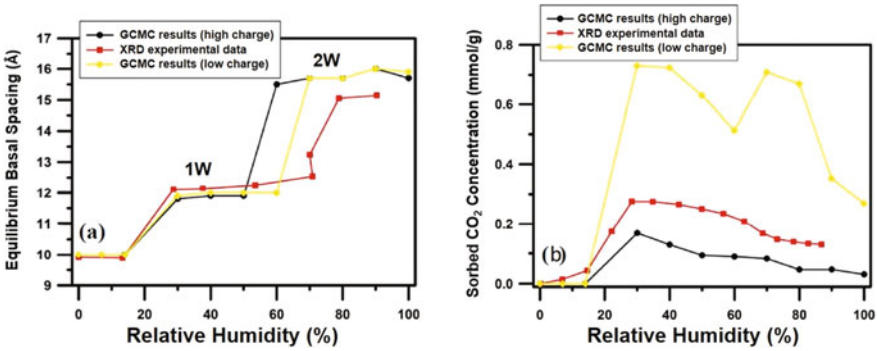

Fig. 8.8 Variations of **a** equilibrium basal spacing and **b** adsorbed CO_2 concentration as a function of RH for the high- and low-charge Na-MMT at T/P = 323 K/90 bar. XRD and IR experimental data obtained by Loring et al. (2014) are shown for comparisons—reprinted with permission from (Rao & Leng, 2016a) Copyright (2016) American Chemical Society

1 W-to-2 W transition occurs at a lower RH in the "high-charge" clay than in the "low charge" one. This 1 W-to-2 W swelling of the high-charge clay is consistent with experimental results (Sato et al., 1992; Michot et al., 2005) and is associated with greater ability of the "high-charge" clay to accommodate water uptake.

Subsequently, "high-charge" clay minerals contain more water and less CO_2 as the RH increases because of the increased number of interlayer cations and the strong hydration energy of sodium ions with polar water molecules. This enhanced hydration process reduces the chances of intercalation of nonpolar CO_2 molecules. The measured adsorbed CO_2 falls in between the "high-charge" and "low-charge" clay-model predictions confirming the importance of the amount of charge and its localization on the intercalation process at variable RH.

The chemical nature of the counter-balancing ions affects the CO_2 intercalation indirectly because CO_2 is not largely participating in the first hydration shell of those ions (Rao & Leng, 2016b; Kadoura et al., 2016; Makaremi et al., 2015; Sena et al., 2015; Botan et al., 2010) due to cation-H_2O interactions are on average ~30% stronger than cation–CO_2 interactions (Criscenti & Cygan, 2013). Differently charged ions, particularly mono- and divalent cations (like Li^+, Na^+, K^+, and Ca^{2+}, Mg^{2+}, respectively) provide different hydration mechanisms with strong implications to the interlayer structure and the ability of swelling clays to retain CO_2. Generally, smectite clay minerals containing divalent interlayer cations require less H_2O saturation to achieve the same d_{001}-spacing values compared to those containing monovalent cations (Ferrage, Lanson, Sakharov, & Drits, 2005; Loganathan et al., 2016). Loring et al. (2014) and Schaef et al. (2015) used a combination of experimental tools to explore CO_2 intercalation into hydrated Na-, Ca-, and Mg-exchanged MMT. They found that Ca-MMT with residual water content (0 W or sub-1 W hydration states) adsorbs almost three times more (1.26 vs. 0.45 mmol/g clay) CO_2 than Na-MMT. The numbers account for non-interlayer adsorption and, assuming similar external surfaces for both clay samples, the difference is primarily due to CO_2 intercalation. The greater ability of smectites with divalent cations to accommodate CO_2 can be associated with a fewer number of those cations per unit cell and their stronger interaction with water molecules comparing to monovalent counterparts. That means less steric hindrance for CO_2 to enter the interlayer, which is facilitated by the larger ionic radii of the divalent cations. This results in propping open the interlayer at near 0 W hydrate states and larger basal d_{100}-spacings (Giesting et al., 2012a; Schaef et al., 2015).

Recently, Michels et al., (2015) studied intercalation of CO_2 in synthetic dried fluorohectorites (representing a "homogeneous" model of natural smectites) with Li^+, Na^+, and exotic Ni^{2+} as counter-ions using X-ray diffraction measurements at −20 °C and 20 bar. Upon exposure to CO_2 the Ni-fluorohectorite develops two distinct diffraction peaks corresponding to d_{001}-spacing at 1.219 and 1.311 nm in contrast to Li- and Na- fluorohectorites demonstrating a well-defined peak at 1.196 and 1.240 nm, respectively. For Ni-fluorohectorite, the peak at 1.311 nm falls between the interlayer distances corresponding to 1 W and 2 W hydration states

(Ferrage et al., 2005, 2011). The author speculated that the unusual (001) diffraction can be attributed to the formation of a CO_2-Ni^{2+} complex in the interlayer and possible interference of a brucite-like structure ($Ni[OH]_2$) (Michels et al., 2014). A theoretical study inspired by these results could be a valuable tool to interpret such observed phenomena.

8.2 Carbon Dioxide and Wettability of Clay Mineral Surfaces

As noted above, the interaction of CO_2 with clay mineral surfaces is expected to be a key process for evaluating the suitability of carbon sequestration to reduce atmospheric carbon emissions and mitigate global climate change. Although the interlayer of swelling clay minerals can potentially provide secondary storage for CO_2 in isolating the greenhouse gas from the environment, the primary interactions during injection and subsequent flow of supercritical CO_2 fluid into the subsurface are the CO_2 fluid interactions with aqueous brine and with external mineral surfaces associated with the reservoir rock and overlying shale caprock. The relative wetting of pore surfaces in the rock matrix by CO_2 and brine will determine the capillary pressure of the fluids, their subsequent transport in the rock matrix, and the ultimate distribution of CO_2 in the reservoir. The integrity of the shale caprock will depend in part on the wettability of CO_2 on the external surfaces of the predominant clay minerals. The relative wetting of pore surfaces is characterized macroscopically by contact angles and interfacial tensions among the three phases (CO_2, brine, and mineral) and which ultimately control the capillary flow and trapping of CO_2 in the rock matrix. This residual trapping mechanism for CO_2 dominates during fluid injection and CO_2 migration stages of carbon sequestration (up to approximately 100 years) and is accompanied by solubility trapping (dissolution of CO_2 into brine) and later (10–10,000 years) by enhanced mineral trapping involving the precipitation of carbonate minerals (Benson et al., 2005).

A molecular basis for the analysis of CO_2-brine-mineral contact angles can be useful in evaluating multiphase flow and the role of residual trapping mechanisms in carbon sequestration. Large-scale molecular dynamics simulations can provide significant insight into competitive wetting of fluids on clay mineral surfaces, especially in view of the large variability of experimental measurements of contact angles which is typically attributed to sample preparation, surface contamination, surface roughness, hysteresis, and other practical issues (Iglauer, Pentland, & Busch, 2015). Simulations of contact angle models involve the equilibration of a large droplet, comprised of many tens to hundreds of thousand fluid molecules (CO_2 or H_2O, or brine) in the coexisting fluid, onto a mineral surface under the appropriate *P*/*T* conditions. Competition between fluids in wetting of the mineral surface ultimately leads to redistribution of fluid molecules and solutes at the

three-phase interface. Also, unique in the contact angle simulations involving CO_2 and H_2O fluids for carbon sequestration applications is the relative significance of polar molecules and the degree to which the molecules interact with various clay mineral surfaces (Tenney & Cygan, 2014; Chen et al., 2016). Other molecular simulation studies that have examined contact angle involving mineral substrates include epoxy on SiO_2 (Hölck et al., 2012), CO_2 and brine on quartz (Iglauer, Mathew, & Bresme, 2012), and water on kaolinite (Šolc, Gerzabek, Lischka, & Tunega, 2011). Often the second "fluid" in many such studies is simply a vacuum. Molecular models to determine interfacial tensions for CO_2-H_2O systems have been developed by Nielsen, Bourg, & Sposito, (2012) and Li et al., (2013).

Figure 8.9 includes a snapshot of an equilibrated supercritical CO_2 droplet in water on the hydroxylated basal surface of kaolinite, obtained after more than 10 ns of molecular dynamics simulation, and which involves more than a half million atoms (Tenney & Cygan, 2014). Corresponding atomic density maps for water derived from equilibrated simulation of pure water, and from similar simulations for CO_2 droplets in NaCl and $CaCl_2$ brine solutions, are also presented. The equilibrium contact angle of 169 ± 63 ° is observed for the case of CO_2 droplet in water and represents the strong interaction with water and the formation of hydrogen bonds with the aluminol groups (-AlOH) of the basal surface; that is, the water phase prefers contact with the clay surface while the CO_2 droplet behaves as a nonwetting fluid. The corresponding water density map shows the uniform ordering of the first surface water layer and a somewhat less-ordered second water layer. The latter exhibits some disruption immediately below the CO_2 droplet; simulations involving such hydrophilic surfaces typically exhibit two to three water layers intermediate between the mineral and the CO_2 droplet. The researchers observed contact angles $31 \pm 6°$ for the case of CO_2 droplet in water on the basal siloxane surface of kaolinite. The siloxane surface of kaolinite is hydrophobic due to limited localized charge associated with the silicate framework and absence of surface hydroxyl groups.

Atomic density maps for the brine components derived from the equilibrated contact angle simulations exhibit compositional distributions consistent with non-wetting CO_2 droplets (i.e., contact angles of 180°). No significant distinction in droplet configuration is observed between NaCl and $CaCl_2$ brines although there is a difference in the distribution of the two cations at the CO_2-brine and brine-kaolinite interfaces. In particular, monovalent Na^+ forms primarily inner-sphere adsorption complexes on the hydroxylated kaolinite surface while divalent Ca^{2+} occurs mostly as an outer-sphere complex. Distributions of both cations directly below the CO_2 droplets are less uniform in the thin film of intermediate water than in the bulk water. Calcium concentration appears slightly enhanced in the brine at the margins of the CO_2 droplet. Chloride exhibits primarily inner-sphere adsorption behavior in both brines at the kaolinite surface. Although the molecular underpinning of wettability is not fully understood for complex natural samples, the use of molecular simulation provides some helpful insights into the fundamental interactions that control the competition of fluids in wetting idealized clay mineral surfaces.

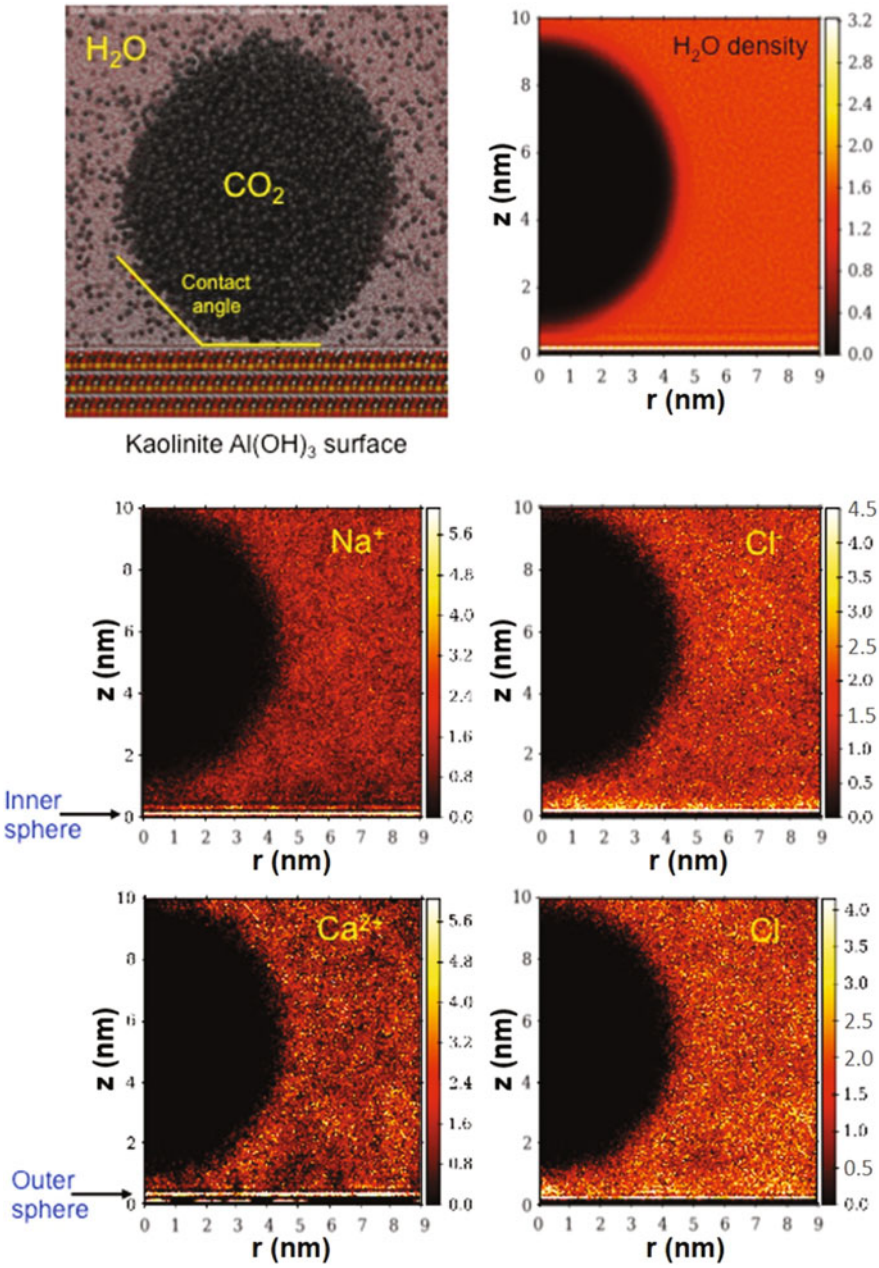

Fig. 8.9 Snapshot of an equilibrated supercritical CO_2 droplet in water at 330 K and 20 MPa on the hydroxylated basal surface of kaolinite, obtained by MD simulation; corresponding atomic density maps for water derived from equilibrated simulation of pure water (*upper right*) and for brine components from equivalent simulations for CO_2 droplets in NaCl and $CaCl_2$ brine solutions (*below*). Reprinted with permission from (Tenney & Cygan, 2014) Copyright (2014) American Chemical Society

8.3 Methane and Swelling Clay Minerals

The interaction of methane with swelling clay has mainly focused on the intercalation of gas hydrates into the interlayer of 2:1 phyllosilicate minerals (Martos-Villa et al., 2014). The high pressure (>20 bar) and relatively low temperature (273–290 K) (Sloan & Koh, 2008; Davie, Zatsepina, & Buffett, 2004; Sun & Duan, 2007) required to form methane hydrate imply that hydrate formation within the interlayer could occur in permafrost areas and the sub-sea surface sediments near continental margins (Milkov, 2000; Kvenvolden, 1998). A unit cell of the stable structure I methane hydrate consists of 46 water molecules per eight gas molecules, which are encapsulated by two small dodecahedral 5^{12} (20 water molecules) and six large tetrakaidecahedral $5^{12}6^{2}$ (24 water molecules) cages formed by a three-dimensional water molecule network (Sloan & Koh, 2008). The molar fraction of methane (0.148) in such ice-like hydrate phases is significant compared to its solubility in liquid water (2.82×10^{-5}, at 273.15 K and 10 MPa, Peng-Robinson EoS). Worldwide the total gas-in-place (GIP) in a form of hydrate is an enormous amount. Researchers have reported global GIP estimates of 1–1.75 $\times$ 10^{17} ft^3 (3–5 $\times$ 10^{15} m^3; 1.5–2.6 $\times$ 10^3 GtC) (Milkov, 2000); 7 $\times$ 10^{17} ft^3 (2.0 $\times$ 10^{16} m^3; 1 $\times$ 10^4 GtC) (Kvenvolden, 1998); 4.2 x10^{18} ft^3 (1.2 $\times$ 10^{17} m^3; 6.4 $\times$ 10^4 GtC) (Klauda & Sandler, 2002) with most hydrate bound in unconsolidated mud generally dominated by clay minerals. Smectites are commonly present on the ocean floor, at continental margins and oceanic ridges (Chamley, 1997) and, therefore, they can host intercalated hydrates. Although gas trapping within expandable clay structures might contribute to the total resource potential, clay-bound hydrates are outside of technically recoverable resources because of the low sediment permeability resulting in low gas flow rates from dissociating hydrates (Boswell & Collett, 2011).

Generally, the presence of clay-based sediments reduces induction time and alters the mechanism of gas hydrate nucleation and growth relative to that in bulk water phase. This suggests prompt hydrate formation under condition of active gas transport into the interlayer region and to the interface between the liquid phase and a growing hydrate phase (Sloan & Koh, 2008; Myshakin, Jiang, Warzinski, & Jordan, 2009; Thompson et al., 2006). Methane hydrate formation experiments in sediments containing quartz grains mixed with kaolinite (non-swelling clay) confirmed highly uniform character of hydrate saturation throughout the samples. In contrast, control tests without clay present resulted in patchy non-uniform hydrate distribution (Ryan, 2012). A series of laboratory scale experiments in test sediment beds of silica sand has shown that particle size distribution plays an important role in hydrate formation, and available void spaces not filled with water increase the hydrate formation kinetics (Linga et al., 2009; Zhou, Castaldi, & Yegulalp, 2009; Bagherzadeh, Moudrakovski, Ripmeester, & Englezos, 2011). On the other hand, based on experiments performed in stirred tank reactors, it was found that the presence of bentonite clay (1 and 5 wt%) in silica sand with different water saturation levels can inhibit hydrate growth rate (Kumar, Sakpal, Roy, & Kumar, 2015). Reduction in hydrate conversion rate was attributed to either poor mass transfer of

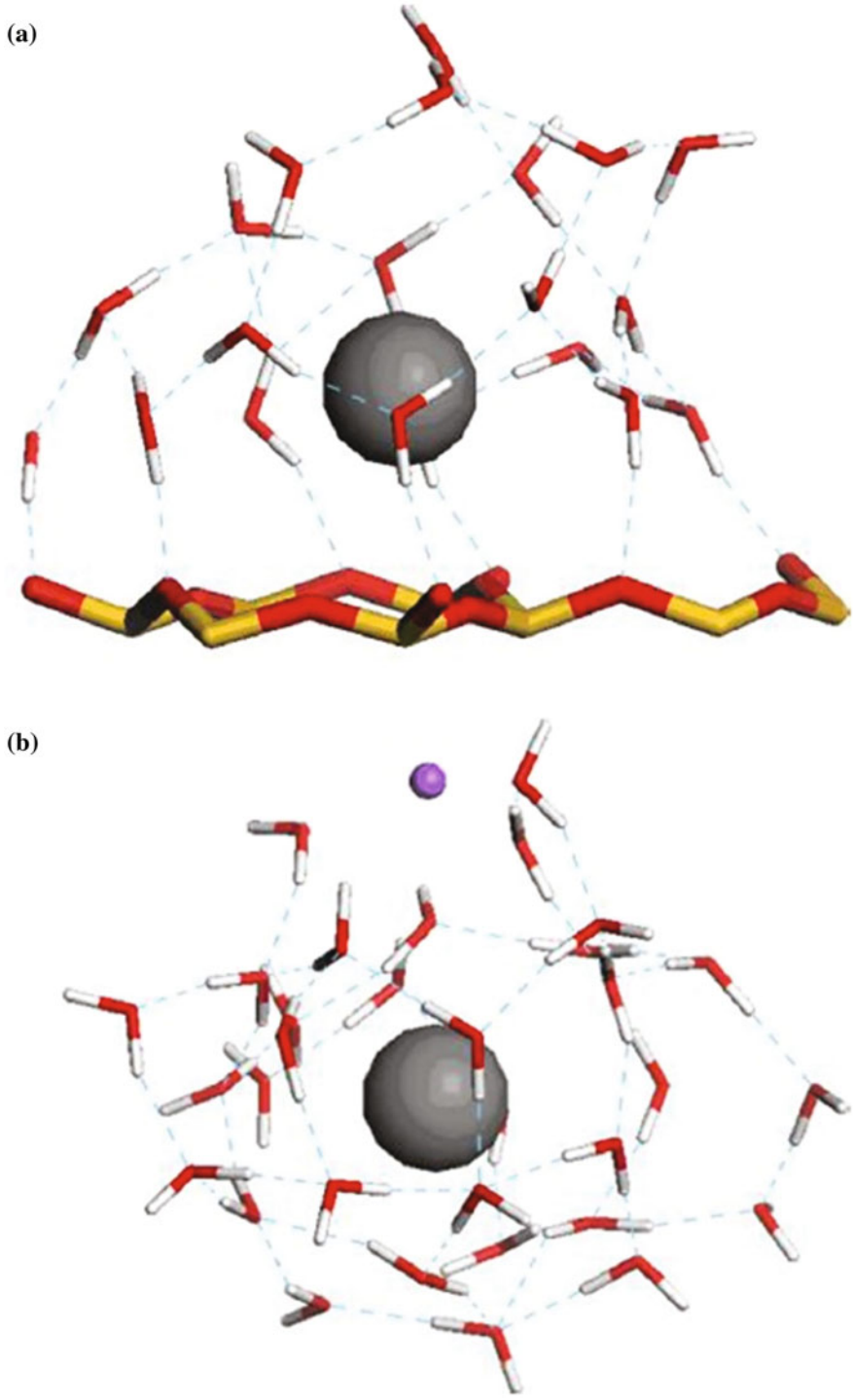
(a)
(b)

◂**Fig. 8.10** Distorted hydrate cage formed around a methane molecule with participation of **a** interlayer water molecules and basal clay surface, and **b** interlayer water only. *Large spheres* indicate CH_4 molecules; *dashed lines* represent hydrogen bonds; *small sphere* indicates Na^+ ion; *white* and *red* (color version) sticks indicate H and O atoms; yellow sticks indicate Si atoms of MMT (Yan et al., 2014) with permission of Springer

hydrate-forming gases due to the clay swelling (resulting in lower pore sizes) or due to unavailability of free water in silica sand pores.

Experimentally, Guggenheim and Koster van Groos (2003) and Koster van Groos and Guggenheim (2009) reported methane hydrate complexes intercalated between the 2:1 layers of Na-exchanged MMT. The intercalated phase is characterized by a strong $\sim$22 Å peak and a weak second-order $\sim$11 Å diffraction. Given the lattice parameter of structure I methane hydrate is about $\sim$12 Å (Sloan & Koh, 2008) the d_{001}-spacing of 22 Å suggests just enough space to intercalate a hydrate cell unit. Cygan et al. (2004a) performed MD simulations to confirm that a structure similar to methane hydrate is stable in the interlayer of MMT with d_{001}-spacing consistent with experiment as observed by Guggenheim and Koster van Groos (2003). Later, Martos-Villa et al. (2014) revisited the Na-MMT model with intercalated methane hydrate using a larger supercell and adding Na-beidellite to explore the effect of charge localization on likelihood of hydrate formation. The results revealed that predominant isomorphic substitutions in the tetrahedral layers of beidellite weaken the stability of hydrate complex compared to MMT. Based on experimental and simulation data the authors concluded that the intercalated hydrate formation depended on the swelling properties of smectites. Divalent cations like Mg^{2+}, Ca^{2+} or monovalent K^+ (in interstratified illite/smectite) inhibit hydrate formation in the interlayer but rather promote it in the interstitial space of clay particles and on the external clay surfaces.

Hydrogen bond network evolution to encapsulate methane molecules in the interlayer were investigated by many authors (Yan et al., 2014; Martos-Villa et al., 2014; Cygan et al., 2004a; Park & Sposito, 2003). The MC and MD simulations performed to study the stable interlayer CH_4 hydrate structures in Na-MMT demonstrated that methane molecules are stabilized above the hexagonal rings of basal clay surfaces and are surrounded by cage-like water network (Park & Sposito, 2003). Yan et al. (2014) studied methane hydrate formation in MMT with one to eight water layers using Clayff (Cygan et al., 2004b), SPC (Berendsen, Postma, Gunsteren, & Hermans, 1981), and OPLS (Jorgensen, Maxwell, & Tirado-Rives, 1996) force fields to examine the clay phase, water, and methane molecules, accordingly under hydrate forming conditions (260 K and 50 MPa). The simulations demonstrate that hexagonal Si-O ring structure of the clay basal surface can participate in formation of distorted cages around CH_4 together with interlayer water molecules by substituting for some of the cage vertices (Fig. 8.10). The interlayer Na^+ ions can occupy the sites of the network to further distort the hydrate cages making them more irregular compared to the ideal bulk hydrate structure. Consequently, the hydrate formation is facilitated in pores sizes equal to integer or half-integer numbers of hydrate unit cells.

The thermodynamic phase diagram of hydrates in pores impacted by either clay surfaces or other surface materials could be significantly different from that of bulk hydrates. Thermodynamics of the confined hydrates with respect to pore size, geometry, and surface chemistry were studied for the case of a silica gel matrix (Handa & Stupin, 1992; Uchida, Ebinuma, & Ishizaki, 1999; Seo, Lee, & Uchida, 2002). These studies show that confined hydrates dissociate at pressures 20–100% higher than that measured in the bulk phase at the same temperature. This suggests that confined hydrates were much less stable due to nonideal cage structures in the hydrate lattice. Chakraborty and Gelb, (2012) utilized MC simulations to predict dissociation temperatures of methane hydrate crystals inside carbon-like slit-shaped pores. Utilizing the TIP4P (Jorgensen et al., 1983) and TIP4P/2005 (Abascal & Vega, 2005) potentials for water molecules they found that dissociation temperatures are depressed proportionally to the inverse of the pore width following the Gibbs−Thomson equation. Importantly, this behavior is observed for pores small enough that only half-cages of the hydrate structure can fit.

The structure and dynamics of the water-methane binary mixture in the interlayer space of MMT were performed by Rao, Xiang, and Leng, (2013) and Rao and Leng (2014) using grand canonical MC simulations at pressure and temperature conditions beyond the hydrate stability zone. The researchers found that at elevated T and P (T = 460 K and P = 900 bar) mimicking the deep underground geologic conditions at 6 km, methane can enter clay interlayer starting from a single hydration layer (Rao et al., 2013). Methane content in clay increases in a stepwise fashion as the basal spacing increases following the formation of multiple hydration layers. The mole fraction of methane remains low and only slightly increases from 0.03 to 0.05 as the basal spacing increases from 16 to 24 Å. The results show that water density in the interlayer decreases with the increase of temperature and pressure consistent with previous reports (de Pablo, Chavez, & de Pablo, 2005; Cygan et al., 2004a). For example, at basal spacing equal to 16 Å, the number of water molecules in the 8-unit cell MMT system drops from 84.1 at T = 298 K and P = 1 bar (Cygan et al., 2004a) to 66.9 at T = 460 K and P = 900 bar (Rao et al., 2013). The presence of methane insignificantly reduces that number to 63.9. On the other hand, charge localization and extent of substitutions in clay structure remarkably affect the behavior of methane hydration and hydration number (Zhang & Choi, 2006; Zhou et al., 2011). In a subsequent study, Rao and Leng (2014) studied methane intercalation into MMT at 300 K and 20–50 bar corresponding to near-surface geologic conditions (Rao et al., 2013). The results show that methane is incapable of entering the interlayer under the saturated water pressure compared to the previous results obtained at 460 K and 900 bar (Rao et al., 2013). RH within the range of 5–30% are reported to be suitable conditions for methane intercalation. The simulations demonstrated that sodium ions are fully hydrated under the range of RH considered while methane is under hydrated having 40–80% of the total hydration number in bulk phase. Analysis of the radial distribution functions indicates that low RH and the hydrophobic nature of methane leads to condensation of methane into dimers in the interlayer space of the swelling clay minerals. The self-diffusion coefficients of methane characterizing the motion parallel to clay

surface are around 10^{-8}–10^{-9} m^2/s with a tendency to decrease with the increase of RH and pressure (at the same temperature). These numbers are in general agreement with methane diffusion in Na-MMT estimated by Titiloye and Skipper (2001) who used MD simulations under similar pressure and temperature conditions. Later, the same authors studied transport properties of methane in hydrated K-MMT and found the diffusion coefficients and dynamics of methane molecules are comparable with the corresponding Na-MMT system (Titiloye & Skipper, 2005).

8.4 Mixture of Carbon Dioxide and Methane in Swelling Clay Minerals

In practical applications like enhanced gas recovery and CO_2 storage in depleted natural gas reservoirs, there is a complex interaction between H_2O, CO_2 and CH_4 molecules (Chaps. 3 and 6). A shale reservoir is typically characterized with natural fracture and pore networks in a rock matrix. The behavior of fluids in those networks and their interactions with minerals control gas storage and release in a shale matrix, influence transport in the fracture network, and ultimately determine production from unconventional reservoirs. Beside intercalation in swelling clays, CO_2 may preferentially adsorb in nanopores, particularly in (organic) kerogen and on (inorganic) external clay surfaces, and displace CH_4 in shale (Nuttall, Ebble, Drahovzal, & Bustin, 2005). Moreover, free and bound (immobile) water can substantially change the behavior of CH_4 and CO_2 trapped in a shale matrix (Godec, Koperna, Petrusak, & Oudinot, 2013).

Grand canonical (μVT) MC simulations of methane and carbon dioxides intercalation in clay minerals and the effect of water on adsorption behavior of CH_4 and CO_2 in pore space of pyrophyllite and Na-MMT have been investigated (Jin & Firoozabadi, 2013, 2014). The adsorption behavior of the CO_2/CH_4 mixture in Na-MMT was studied using GCMC simulations for ranges of pressures, bulk compositions, and pore sizes (Yang, Liu, & Yang, 2015). The authors have calculated the strength of clay surface interaction with CO_2 (as the isosteric heat of adsorption at nearly zero adsorption loading of a single component) to be 55.4 kJ/mol and 40.5 kJ/mol at 14.0 Å and 20.6 Å of basal *d*-spacings, respectively. For methane, the corresponding values are 18.9 kJ/mol and 12.5 kJ/mol at 14.0 Å and 20.6 Å, respectively, in agreement with the experimental value (16.0 kJ/mol) for CH_4 adsorption in the pillared clays (Pereira, Pires, & de Carvalho, 2001). Figure 8.11 displays the adsorption isotherms for the binary CO_2/CH_4 mixtures intercalated in Na-MMT as a function of molar fraction of CO_2 in bulk phase composition at the pressures of 0.1 MPa and 1.0 MPa.

The figure shows that as the bulk phase CO_2 molar fraction approaches 0.5 the intercalated methane level converges nearly to zero. The selectivity parameter expressed as $(x_{CO_2}/x_{CH_4})/(y_{CO_2}/y_{CH_4})$ where x and y are mole fractions of two species in adsorbed and bulk phases, respectively, and calculated at 14.0 Å *d*-spacing can be above 90, while at 20.6 Å the value changes from 25 to 70

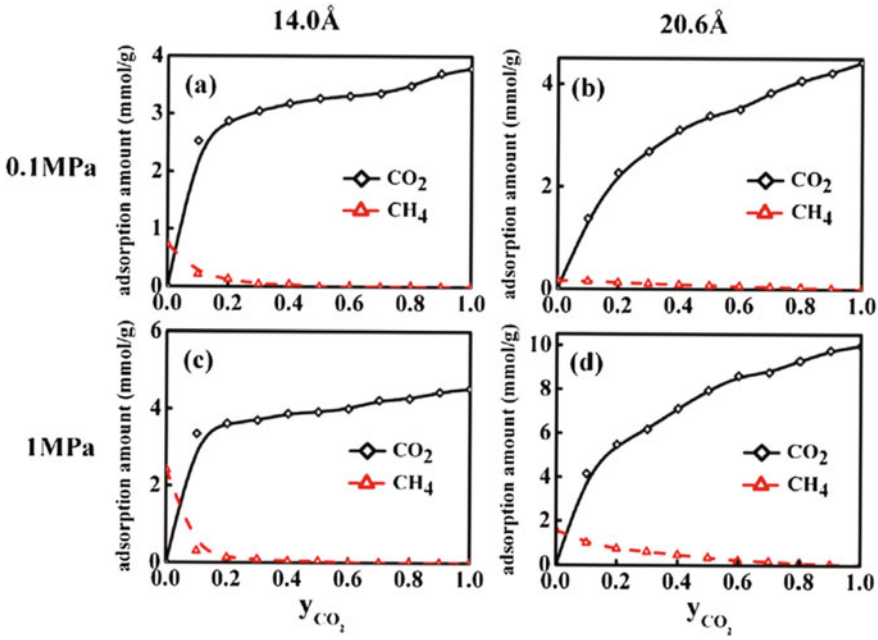

Fig. 8.11 Adsorption isotherms of CO_2/CH_4 mixtures plotted versus mole fraction of CO_2 in bulk phase, for the following examples of gas pressure and basal spacing of Na-MMT: **a** 14.0 Å and **b** 20.6 Å—at 0.1 MPa; **c** 14.0 Å and **d** 20.6 Å—at 1.0 MPa—reprinted from (Yang et al., 2015) with permission from Elsevier

depending on pressure and bulk composition. The greater selectively at the smaller interlayer spacing is attributed to stronger CO_2 interaction with clay surfaces in a more confined environment compared to methane molecules as inferred from the strengths of clay surface interactions given above. The swelling clay demonstrates a substantially higher CO_2 selectivity over methane adsorption indicating that CO_2 molecules competitively replace CH_4 molecules within the interlayer space. This suggests that geological storage of CO_2 in shales (Kulga, Dilmore, Wyatt, & Ertekin, 2014) where clay minerals constitute a significant portion of inorganic matter can induce production of an additional methane volume. Recently, CH_4 adsorption isotherms were measured in clay-dominated rocks to show that the clay mineral composition and the micropore structure significantly affect gas adsorption (Zhang et al., 2012). MMT-rich samples, exhibiting internal surfaces for adsorption, display the highest CH_4 adsorption capacity (Zhang et al., 2012). The additional volume of methane for enhanced gas production also depends on total organic content and the adsorption of CO_2/CH_4 on external surfaces of pores in rock matrix and natural fracture walls. Those results suggest that competitive adsorption/desorption processes should be accounted for in mixed-gas isotherms (Mohammad, Arumugam, Robinson, & Gasem, 2012; Sudibandriyo, Mohammad, Robinson, & Gasem, 2011). Use of mixed-gas isotherms allow more realistic predictions of gas

mixture behavior in shales, which is extremely complex in nature. Another important consideration is the ability of CO_2 molecules exhibit multilayer adsorption. In that case, instead of a Langmuir isotherm implying a monolayer coverage a BET isotherm should be used. For example, Vermylen (2011) studied CO_2 adsorption on crashed and dried Barnett shale samples and found that experimental data are best described by BET isotherms.

References

Abascal, J. L. F., & Vega, C. (2005). A general purpose model for the condensed phases of water: TIP4P/2005. *Journal of Chemical Physics, 123*(234505), 1–12.

Aimoli, C. G., Maginn, E. J., & Abreu, C. R. A. (2014). Transport properties of carbon dioxide and methane from molecular dynamics simulations. *Journal of Chemical Physics, 141*(13), 134101.

Bagherzadeh, S. A., Moudrakovski, I. L., Ripmeester, J. A., & Englezos, P. (2011). Magnetic resonance imaging of gas hydrate formation in a bed of silica sand particles. *Energy & Fuels, 25*(7), 3083–3092.

Benson, S. M., & Cole, D. R. (2008). CO_2 sequestration in deep sedimentary formations. *Elements, 4*(5), 325–331.

Benson, S. M., et al. (2005). Underground geological storage. In B. Metz et al. (Eds.), *IPCC special report on carbon dioxide capture and storage* (Chap. 5, pp. 195–276). Cambridge and New York: Cambridge University Press.

Berendsen, H. J. C., Postma, J. P. M., Gunsteren, W. F., & Hermans, J. (1981). Interaction models for water in relation to protein hydration. In B. Pullman (Ed.), *Intermolecular forces. The Jerusalem symposia on quantum chemistry and biochemistry* (B 14, pp. 331–342). Dordrecht: Springer.

Billemont, P., Coasne, B., & De Weireld, G. (2010). An experimental and molecular simulation study of the adsorption of carbon dioxide and methane in nanoporous carbons in the presence of water. *Langmuir, 27*(3), 1015–1024.

Boswell, R., & Collett, T. S. (2011). Current perspectives on gas hydrate resources. *Energy and Environmental Science, 4,* 1206–1215.

Botan, A., et al. (2010). Carbon dioxide in montmorillonite clay hydrates: Thermodynamics, structure, and transport from molecular simulation. *Journal of Physical Chemistry C, 114*(35), 14962–14969.

Burgess, J. (1999). *Ions in solution: Basic principles of chemical interactions* (1st ed.). Cambridge: Woodhead Publishing.

Chakraborty, S. N., & Gelb, L. D. (2012). A monte carlo simulation study of methane clathrate hydrates confined in slit-shaped pores. *Journal of Physical Chemistry B, 116*(7), 2183–2197.

Chamley, H. (1997). Clay mineral sedimentation in the ocean. *Soils and sediments* (pp. 269–302). Berlin: Springer.

Chen, C., et al. (2016). Pressure and temperature dependence of contact angle for CO_2/water/silica systems predicted by molecular dynamics simulations. *Energy & Fuels, 30*(6), 5027–5034.

Cipriani, P., Nardone, M., Ricci, F. P., & Ricci, M. A. (2001). Orientational correlations in liquid and supercritical CO_2: Neutron diffraction experiments and molecular dynamics simulations. *Molecular Physics, 99*(4), 301–308.

Criscenti, L. J., & Cygan, R. T. (2013). Molecular simulations of carbon dioxide and water: Cation solvation. *Environmental Science and Technology, 47*(1), 87–94.

Cygan, R. T., Guggenheim, S., & Koster van Groos, F. (2004a). Molecular models for the intercalation of methane hydrate complexes in montmorillonite clay. *Journal of Physical Chemistry B, 108*(39), 15141–15149.

Cygan, R. T., Liang, J.-J., & Kalinichev, A. G. (2004b). Molecular models of hydroxide, oxyhydroxide, and clay phases and the development of a general force field. *Journal of Physical Chemistry B, 108*(4), 1255–1266.

Cygan, R. T., Romanov, V. N., & Myshakin, E. M. (2012). Molecular simulation of carbon dioxide capture by montmorillonite using an accurate and flexible force field. *Journal of Physical Chemistry C, 116*(24), 13079–13091.

Davie, M. K., Zatsepina, O. Y., & Buffett, B. A. (2004). Methane solubility in marine hydrate environments. *Marine Geology, 203*(1–2), 177–184.

de Pablo, L., Chavez, M. L., & de Pablo, J. J. (2005). Stability of Na-, K-, and Ca-montmorillonite at high temperatures and pressures: A Monte Carlo simulation. *Langmuir, 21*(23), 10874–10884.

Ferrage, E., Lanson, B., Sakharov, B. A., & Drits, V. A. (2005). Investigation of smectite hydration properties by modeling experimental X-ray diffraction patterns: Part I. *Montmorillonite hydration properties. American Mineralogist, 90*(8–9), 1358–1374.

Ferrage, E., et al. (2011). Hydration properties and interlayer organization of water and ions in synthetic Na-smectite with tetrahedral layer charge. Part 2. Toward a precise coupling between molecular simulations and diffraction data. *Journal of Physical Chemistry C, 115*(5), 1867–1881.

Fu, M. H., Zhang, Z. Z., & Low, P. F. (1990). Changes in the properties of a montmorillonite-water system during the adsorption and desoprtion of water: Hysteresis. *Clays and Clay Minerals, 38*(5), 485–492.

Giesting, P., Guggenheim, S., Koster van Groos, A. F., & Busch, A. (2012a). X-ray diffraction study of K- and Ca-exchanged montmorillonites in CO_2 atmospheres. *Environmental Science and Technology, 46*(10), 5623–5630.

Giesting, P., Guggenheim, S., Koster van Groos, A. F., & Busch, A. (2012b). Interaction of carbon dioxide with Na-exchanged montmorillonite at pressures to 640 bar: Implications for CO_2 sequestration. *International Journal of Greenhouse Gas Control, 8,* 73–81.

Godec, M., Koperna, G., Petrusak, R., & Oudinot, A. (2013). Potential for enhanced gas recovery and CO_2 storage in the Marcellus Shale in Eastern United States. *International Journal of Coal Geology, 118,* 95–104.

Guggenheim, S., & Koster van Groos, A. (2003). Experimental investigation of methane gas production from methane hydrate. *Geology, 31*(7), 653–655.

Handa, Y. P., & Stupin, D. (1992). Thermodynamic properties and dissociation characteristics of methane and propane hydrates in 70 Å radius silica gel pores. *Journal of Physical Chemistry, 96*(21), 8599.

Harris, J. G., & Yung, K. H. (1995). Carbon dioxide's liquid-vapor coexistence curve and critical properties as predicted by a simple molecular model. *Journal of Physical Chemistry, 99*(31), 12021–12024.

Heinz, H., Lin, T.-J., Mishra, R. K., & Emami, F. S. (2013). Thermodynamically consistent force fields for the assembly of inorganic, organic, and biological nanostructures: The INTERFACE force field. *Langmuir, 29*(6), 1754–1765.

Hölck, O., et al. (2012). Comparative characterization of chip to epoxy interfaces by molecular modeling and contact angle determination. *Microelectronics Reliability, 52*(7), 1285–1290.

Huber, M. L., 2007. *NIST Thermophysical Properties of Hydrocarbon Mixtures Database (SUPERTRAPP).* Available online at: https://www.nist.gov/sites/default/files/documents/srd/Supertrapp.pdf. Accessed 8 May 2017.

Hur, T.-B., et al. (2013). Carbonate formation in Wyoming montmorillonite under high pressure carbon dioxide. *International Journal of Greenhouse Gas Control, 13,* 149–155.

Iglauer, S., Mathew, M. S., & Bresme, F. (2012). Molecular dynamics computations of brine-CO_2 interfacial tensions and brine-CO_2-quartz contact angles and their effects on structural and residual trapping mechanisms in carbon geo-sequestration. *Journal of Colloid and Interface Science, 386*(1), 405–414.

Iglauer, S., Pentland, C. H., & Busch, A. (2015). CO_2 wettability of seal and reservoir rocks and the implications for carbon geo-sequestration. *Water Resources Research, 51*(1), 729–774.

Ilton, E. S., et al. (2012). In Situ X-Ray diffraction study of Na^+ saturated montmorillonite exposed to variably wet super critical CO_2. *Environmental Science and Technology, 46*(7), 4241–4248.

Ji, L., et al. (2012). Experimental investigation of main controls to methane adsorption in clay-rich rocks. *Appled Geochemistry, 27*(12), 2533–2545.

Jin, Z., & Firoozabadi, A. (2013). Methane and carbon dioxide adsorption in clay-like slit pores by Monte Carlo simulations. *Fluid Phase Equilibria, 360,* 456–465.

Jin, Z., & Firoozabadi, A. (2014). Effect of water on methane and carbon dioxide sorption in clay minerals by Monte Carlo simulations. *Fluid Phase Equilibria, 382,* 10–20.

Jorgensen, W. L., et al. (1983). Comparison of simple potential functions for simulating liquid water. *Journal of Chemical Physics, 79*(2), 926.

Jorgensen, W. L., Maxwell, D. S., & Tirado-Rives, J. (1996). Development and testing of the OPLS all-atom force field on conformational energetics and properties of organic liquids. *Journal of American Chemical Society, 118*(45), 11225–11236.

Kadoura, A., Nair, A. K. N., & Sun, S. (2016). Molecular dynamics simulations of carbon dioxide, methane, and their mixture in montmorillonite clay hydrates. *Journal of Physical Chemistry C, 120*(23), 12517–12529.

Klauda, J. B., & Sandler, S. I. (2002). Ab initio intermolecular potentials for gas hydrates and their predictions. *Journal of Physical Chemistry B, 106*(22), 5722–5732.

Koster van Groos, A. F., & Guggenheim, S. (2009). The stability of methane hydrate intercalates of montmorillonite and nontronite: Implications for carbon storage in ocean-floor environments. *American Mineralogist, 94*(2–3), 372–379.

Kulga, B., Dilmore, R., Wyatt, C., & Ertekin, T. (2014). *Investigation of CO_2 storage and enhanced gas recovery in depleted shale gas formations using a dual-porosity/dual-permeability, multiphase reservoir simulator*. Morgantown, WV: U.S. Department of Energy.

Kumar, A., Sakpal, T., Roy, S., & Kumar, R. (2015). Methane hydrate formation in a test sediment of sand and clay at various levels of water saturation. *Canadian Journal of Chemistry, 93*(8), 874–881.

Kvenvolden, K. A. (1998). A primer on the geological occurrence of gas hydrate. *The Geological Society, London, Special Publications, 137,* 9–30.

Lee, M. S., McGrail, B. P., & Glezakou, V. A. (2014). Microstructural response of variably hydrated Ca-rich montmorillonite to supercritical CO_2. *Environmental Science and Technology, 48*(15), 8612–8619.

Linga, P., et al. (2009). Gas hydrate formation in a variable volume bed of silica sand particles. *Energy & Fuels, 23*(1), 5496–5507.

Li, X., et al. (2013). Molecular dynamics simulations of CO_2 and brine interfacial tension at high temperatures and pressures. *Journal of Physical Chemistry B, 117*(18), 5647–5652.

Loganathan, N., et al. (2016). Cation and water structure, dynamics, and energetics in smectite clays: A molecular dynamics study of Ca-hectorite. *Journal of Physical Chemistry C, 120*(23), 12429–12439.

Loring, J. S., et al. (2014). In Situ study of CO_2 and H_2O partitioning between Na-montmorillonite and variably wet supercritical carbon dioxide. *Langmuir, 30*(21), 6120–6128.

Lutterotti, L., et al. (2010). Texture analysis of a turbostratically disordered Ca-montmorillonite. *American Mineralogist, 95*(1), 98–103.

Makaremi, M., Jordan, K. D., Guthrie, G. D., & Myshakin, E. M. (2015). Multiphase Monte Carlo and molecular dynamics simulations of water and CO_2 intercalation in montmorillonite and beidellite. *Journal of Physical Chemistry C, 119*(27), 15112–15124.

Martos-Villa, R., et al. (2014). Interaction of methane hydrate complexes with smectites: Experimental results compared to molecular models. *American Mineralogist, 99*(2–3), 401–414.

Michalkova, A., & Tunega, D. (2007). Kaolinite: Dimethylsulfoxide intercalate—A theoretical study. *Journal of Physical Chemistry C, 111*(30), 11259–11266.

Michels, L., et al. (2014). EXAFS and XRD studies in synthetic Ni-fluorohectorite. *Applied Clay Science, 96,* 60–66.

Michels, L., et al. (2015). Intercalation and retention of carbon dioxide in a smectite clay promoted by interlayer cations. *Scientific Reports, 5*(8775), 1–9.

Michot, L. J., et al. (2005). Hydration and swelling of synthetic Na-Saponites: Influence of layer charge. *American Mineralogist, 90*(1), 166–172.

Milkov, A. V. (2000). Worldwide distribution of submarine mud volcanoes and associated gas hydrates. *Marine Geology, 167*(1–2), 29–42.

Mohammad, S. A., Arumugam, A., Robinson, R. L. J., & Gasem, K. A. M. (2012). High-pressure adsorption of pure gases on coals and activated carbon: Measurements and modeling. *Energy & Fuels, 26*(1), 536–548.

Myshakin, E. M., Jiang, H., Warzinski, R. P., & Jordan, K. D. (2009). Molecular dynamics simulations of methane hydrate decomposition. *Journal of Physical Chemistry A, 113*(10), 1913–1921.

Myshakin, E. M., et al. (2013). Molecular dynamics simulations of carbon dioxide intercalation in hydrated Na-montmorillonite. *Journal of Physical Chemistry C, 117*(21), 11028–11039.

Myshakin, E. M., et al. (2014). Molecular dynamics simulations of turbostratic dry and hydrated montmorillonite with intercalated carbon dioxide. *The Journal of Physical Chemistry A, 118* (35), 7454–7468.

Nielsen, L. C., Bourg, I. C., & Sposito, G. (2012). Predicting CO_2-water interfacial tension under pressure and temperature conditions of geologic CO_2 storage. *Geochimica et Cosmochimica Acta, 81,* 28–38.

Nuttall, B., Ebble, C., Drahovzal, J. A., & Bustin, R. M. (2005). *Analysis of Devonian black shales in Kentucky for potential carbon dioxide sequestration and enhanced natural gas production*. Lexington, KY: University of Kentucky.

Park, S.-H., & Sposito, G. (2003). Do montmorillonite surfaces promote methane hydrate formation? Monte Carlo and molecular dynamics simulations. *Journal of Physical Chemistry B, 107*(10), 2281–2290.

Pereira, P. R., Pires, J., & de Carvalho, M. B. (2001). Adsorption of methane and ethane in zirconium oxide pillared clays. *Separation and Purification Technology, 21*(3), 237–246.

Rao, Q., & Leng, Y. (2014). Methane aqueous fluids in montmorillonite clay interlayer under near-surface geological conditions: A grand canonical Monte Carlo and molecular dynamics simulation study. *Journal of Physical Chemistry B, 118*(37), 10956–10965.

Rao, Q., & Leng, Y. (2016a). Effect of layer charge on CO_2 and H_2O intercalations in swelling clays. *Langmuir, 32*(44), 11366–11374.

Rao, Q., & Leng, Y. (2016b). Molecular understanding of CO_2 and H_2O in a montmorillonite clay interlayer under CO_2 geological sequestration conditions. *Journal of Physical Chemistry C, 120*(5), 2642–2654.

Rao, Q., Xiang, Y., & Leng, Y. S. (2013). Molecular simulations on the structure and dynamics of water-methane fluids between Na-Montmorillonite clay surfaces at elevated temperature and pressure. *Journal of Physical Chemistry C, 117*(27), 14061–14069.

Romanov, V. N. (2013). Evidence of irreversible CO_2 intercalation in montmorillonite. *International Journal of Greenhouse Gas Control, 14,* 220–226.

Rother, G., et al. (2013). CO_2 sorption to subsingle hydration layer montmorillonite clay studied by excess sorption and neutron diffraction measurements. *Environmental Science and Technology, 47*(1), 205–211.

Ryan, T. (2012). *Effect of sediment composition on the uniformity of experimentally-formed methane hydrate [MS Thesis]*. Morgantown, WV: West Virginia University, Department of Chemical Engineering.

Saharay, M., & Balasubramanian, S. (2004a). Ab Initio molecular-dynamics study of supercritical carbon dioxide. *Journal of Chemical Physics, 120*(20), 9694–9702.

Saharay, M., & Balasubramanian, S. (2004b). Enhanced molecular multipole moments and solvent structure in supercritical carbon dioxide. *ChemPhysChem, 5*(9), 1442–1445.

Saharay, M., & Dr. Balasubramanian, S. (2006). Errata: Enhanced molecular multipole moments and solvent structure in supercritical carbon dioxide. *ChemPhysChem, 7*(6), 1167.

Sato, T., Watanabe, T., & Otsuka, R. (1992). Effects of layer charge, charge location, and energy change on expansion properties of dioctahedral smectites. *Clays and Clay Minerals, 40*(1), 103–113.

Schaef, H. T., et al. (2012). In situ XRD study of Ca^{2+} saturated montmorillonite (STX-1) exposed to anhydrous and wet supercritical carbon dioxide. *International Journal of Greenhouse Gas Control, 6,* 220–229.

Schaef, H. T., et al. (2015). Competitive sorption of CO_2 and H_2O in 2:1 layer phyllosilicates. *Geochimica et Cosmochimica Acta, 161,* 248–257.

Sena, M. M., Morrow, C. P., Kirkpatrick, R. J., & Krishnan, M. (2015). Supercritical carbon dioxide at smectite mineral–water interfaces: Molecular dynamics and adaptive biasing force investigation of CO_2/H_2O mixtures nanoconfined in Na-montmorillonite. *Chemistry of Materials, 27*(20), 6946–6959.

Seo, Y., Lee, H., & Uchida, T. (2002). Methane and carbon dioxide hydrate phase behavior in small porous silica gels: Three-phase equilibrium determination and thermodynamic modeling. *Langmuir, 18*(24), 9164–9170.

Sloan, E. D., & Koh, C. A. (2008). *Clathrate hydrates of natural gas* (3rd ed.). Boca Raton, FL.: CRC Press.

Smith, D. E., Wang, Y., & Whitley, H. D. (2004). Molecular simulations of hydration and swelling in clay minerals. *Fluid Phase Equilibrium, 222,* 189–194.

Šolc, R., Gerzabek, M. H., Lischka, H., & Tunega, D. (2011). Wettability of kaolinite (001) surfaces—Molecular dynamic study. *Geoderma, 169,* 47–54.

Sudibandriyo, M., Mohammad, S. A., Robinson, R. L. J., & Gasem, K. A. M. (2011). Ono-Kondo model for high-pressure mixed-gas adsorption on activated carbons and coals. *Energy & Fuels, 25*(7), 3355–3367.

Sun, R., & Duan, Z. (2007). An accurate model to predict the thermodynamic stability of methane hydrate and methane solubility in marine environments. *Chemical Geology, 244*(1–2), 248–262.

Suter, J. L., Sprik, M., & Boek, E. S. (2012). Free energies of absorption of alkali ions onto beidellite and montmorillonite surfaces from constrained molecular dynamics simulations. *Geochimica et Cosmochimica Acta, 91,* 109–119.

Tenney, C. M., & Cygan, R. T. (2014). Molecular simulation of carbon dioxide, brine, and clay mineral interactions and determination of contact angles. *Environmental Science and Technology, 48*(3), 2035–2042.

Teppen, B. J., et al. (1997). Molecular dynamics modeling of clay minerals. 1. Gibbsite, kaolinite, pyrophyllite, and beidellite. *Journal of Physical Chemistry B, 101*(9), 1579–1587.

Thompson, H., et al. (2006). Methane hydrate formation and decomposition: Structural studies via neutron diffraction and empirical potential structure refinement. *Journal of Chemical Physics, 124*(16), 164508.

Titiloye, J. O., & Skipper, N. T. (2001). Molecular dynamics simulation of methane in sodium montmorillonite clay hydrates at elevated pressures and temperatures. *Molecular Physics, 99* (10), 899–906.

Titiloye, J. O., & Skipper, N. T. (2005). Monte Carlo and molecular dynamics simulations of methane in potassium montmorillonite clay hydrates at elevated pressures and temperatures. *Journal of Colloid and Interface Science, 282*(2), 422–427.

Uchida, T., Ebinuma, T., & Ishizaki, T. (1999). Dissociation condition measurements of methane hydrate in confined small pores of porous glass. *Journal of Physical Chemistry B, 103*(18), 3659–3662.

Vermylen, J. P. (2011). *Geomechanical Studies of the Barnett Shale, Texas, USA [Ph.D. dissertation].* Stanford, CA: Stanford University, SRB (Vol. 125).

Viani, A., Gualtieri, A. F., & Artioli, G. (2002). The nature of disorder in montmorillonite by simulation of X-ray power patterns. *American Mineralogist, 87*(7), 966–975.

Yang, N., & Yang, X. (2011). Molecular simulation of swelling and structure for Na-Wyoming montmorillonite in supercritical CO_2. *Molecular Simulations, 37*(13), 1063–1070.

Yang, W., & Zaoui, A. (2016). Capture and sequestration of CO_2 in the interlayer space of hydrated calcium montmorillonite clay under various geological burial depth. *Physica A: Statistical Mechanics and its Applications, 449,* 416–425.

Yang, N., Liu, S., & Yang, X. (2015). Molecular simulation of preferential adsorption of CO_2 over CH_4 in Na-montmorillonite clay material. *Applied Surface Science, 356,* 1262–1271.

Yan, K.-F., et al. (2014). Molecular dynamics simulation of the intercalation behaviors of methane hydrate in montmorillonite. *Journal of Molecular Modeling, 20*(6), 2311.

Young, D. A., & Smith, D. E. (2000). Simulations of clay mineral swelling and hydration: Dependence upon interlayer ion size and charge. *Journal of Physical Chemistry B, 104*(39), 9163–9170.

Zhang, J. F., & Choi, S. K. (2006). Molecular dynamics simulation of methane in potassium montmorillonite clay hydrates. *Journal of Physics B: Atomic, Molecular and Optical Physics, 39*(18), 3839–3848.

Zhang, Z., & Duan, Z. (2005). An optimized molecular potential for carbon dioxide. *Journal of Chemical Physics, 122*(21), 214507.

Zhang, T., et al. (2012). Effect of organic-matter type and thermal maturity on methane adsorption in shale-gas systems. *Organic Geochemistry, 47,* 120–131.

Zhou, Y., Castaldi, M. J., & Yegulalp, T. M. (2009). Experimental investigation of methane gas production from methane hydrate. *Industrial and Engineering Chemistry Research, 48*(6), 3142–3149.

Zhou, Q., et al. (2011). Hydration of methane intercalated in Na-smectites with distinct layer charge: Insights from molecular simulations. *Journal of Colloid and Interface Science, 355*(1), 237–242.

Zhu, A. M., Zhang, X. B., Liu, Q. L., & Zhang, Q. G. (2009). A fully flexible potential model for carbon dioxide. *Chinese Journal of Chemical Engineering, 17*(2), 268–272.

Chapter 9
Advances in Molecular Simulation Studies of Clay Minerals

Randall T. Cygan and Evgeniy M. Myshakin

Abstract The unique structure and behavior of swelling clay minerals, as observed in the laboratory and in the environment, present a challenge in understanding of the molecular details associated with these minerals. The chapter introduces the essence of classical methods involving empirically derived potential energy expressions that allow simulation of periodic cells representing bulk and interfacial clay mineral systems. The classical models provide the simulation and analysis of many thousands to more than a million atoms for evaluating structures, adsorption, diffusion, intercalation, physical, and other properties. Quantum chemical calculations, including molecular orbital methods and density functional theory, optimize the configuration of electrons about atoms from first principles, but require significant computational cost to examine many of the important topics in clay mineralogy. Molecular simulation methods such as energy minimization, molecular dynamics, Monte Carlo techniques, vibrational analysis, thermodynamics calculations, transition state analysis, and a variety of related computational methods are utilized to improve our understanding of clay minerals, and to better interpret traditional characterization and spectroscopic methods. An example showing the use of molecular simulation for clay minerals is presented for the process of montmorillonite's swelling as a function of interlayer water.

Application of computational chemistry and molecular simulation methods in clay mineralogy has increased steadily over recent years. The unique structure and behavior of clay minerals as observed in the laboratory and in the environment, present a challenge to improve our understanding of the molecular details associated with these common minerals. Classical-based methods involving empirically derived potential energy expressions allow simulation of periodic cells representing bulk and interfacial clay mineral systems. The classical models allow the simulation

R. T. Cygan
U.S. Department of Energy, Sandia National Laboratories (SNL), Albuquerque, USA

E. M. Myshakin (✉)
U.S. Department of Energy, NETL-AECOM, Pittsburgh, USA
e-mail: Evgeniy.Myshakin@netl.doe.gov

© Springer International Publishing AG 2018

V. Romanov (ed.), *Greenhouse Gases and Clay Minerals*, Green Energy and Technology, https://doi.org/10.1007/978-3-319-12661-6_9

and analysis of many thousands to more than a million atoms for evaluating structures, adsorption, diffusion, intercalation, physical, and other properties. Quantum calculations, including molecular orbital methods and density functional theory, optimize the configuration of electrons about atoms from first principles, but require significant computational cost to examine many of the important topics in clay mineralogy. Molecular simulation methods such as energy minimization, molecular dynamics (MD), Monte Carlo techniques, vibrational analysis, thermodynamics calculations, transition state analysis, and a variety of related computational methods can be used to improve our understanding of clay minerals, and to better interpret traditional characterization and spectroscopic methods.

9.1 Basics of Molecular Simulation

Evaluation of the potential energy of a chemical system is the basic task of any molecular simulation whether one is using classical molecular mechanics or a quantum approach such as density functional theory (DFT). Fundamental to either method is the evaluation of the various contributing components of the total potential energy. For example, in classical-based molecular simulations, it is possible to evaluate each component of the potential energy by summing the nonbond and bond terms separately:

$$E_{\text{total}} = E_{\text{Coul}} + E_{\text{VDW}} + E_{\text{bond stretch}} + E_{\text{angle bend}} + \cdots \tag{9.1}$$

Electrostatics, as represented by the Coulombic energy E_{Coul} and van der Waals energy E_{VDW} comprise the bulk of the potential energy for most clay mineral systems. These two energy contributions correspond to the nonbond interactions associated with a molecular, crystal, or any particular arrangement of atoms. The nonbonded potential energy of interaction for atoms i and j is defined as:

$$E_{ij} = \frac{q_i q_j e^2}{4\pi\varepsilon_0 r_{ij}} + 4\varepsilon_{ij}\left[\left(\frac{\sigma_{ij}}{r_{ij}}\right)^{12} - \left(\frac{\sigma_{ij}}{r_{ij}}\right)^{6}\right] \tag{9.2}$$

where the Coulombic term includes q_i which is the partial charge of the atom (or full charge of an ion), e is the charge of the electron, ϵ_0 is the dielectric permittivity of vacuum, and r_{ij} is the distance between atoms i and j. The van der Waals term represents the dispersive interaction of electrons between atoms and is significant only at relatively short distances. Empirical parameters ε_{ij} and σ_{ij} are typically determined from experimental and spectroscopic measurements or from high-level quantum calculations. The total nonbond energy of a chemical system requires summation of Eq. (9.2) for all atom pairs regardless of atomic positions. Calculations are typically performed for a simulation cell having periodic boundary conditions to represent a three-dimensional infinite-sized representation of a bulk

clay mineral or one incorporating a two-dimensional interface to represent a clay mineral surface exposed to external water or aqueous solution.

The bond terms of Eq. (9.1) represent the covalent interactions of a chemical system and are typically represented in classical-based models by harmonic analytical expressions for bond energy about an equilibrium bond distance

$$E_{\text{bond stretch}} = k(x - x_0)^2 \tag{9.3}$$

or equilibrium three-body bend angle

$$E_{\text{angle bend}} = k(\theta - \theta_0)^2 \tag{9.4}$$

where x and θ are bond distance and bend angle, respectively, and x_0 and θ_0 are the corresponding equilibrium values, with k representing the associated force constants. Additional bond terms can exist for four-body interactions, such as for dihedral torsions and out-of-plane atomic motions, and for coupling among the various stretch and bend modes. Bond terms for clay mineral systems often include all nearest-neighbor metal-oxygen bonds in coordination polyhedra or for just water molecules and hydroxyl bonds.

The convenience of simple analytical expressions in classical models to describe the potential energy for an assembly of atoms makes it relatively easy to use computers to repetitively evaluate the potential energy functions and obtain the lowest total energy configuration (i.e., energy minimization). This is especially the case in deterministic MD simulations where Newton's equations of motion are evaluated over many iterations often involving many millions of time steps, or in simulations relying on stochastic methods such as Monte Carlo methods where hundreds of thousands to millions of configurations are evaluated to determine the most energetically favored geometries. The practical success of any set of potential energy functions—referred to collectively as a force field—ultimately relies on the quality and accuracy of the energy expression in reproducing experimental chemical structures, physical properties, and spectroscopic observations. There are several successful force fields designed specifically for modeling clay minerals and environmental processes (Teppen et al., 1997; Kawamura et al., 1998; Sainz-Díaz, Hernández-Laguna, & Dove, 2001; Cygan, Liang, Kalinichev, 2004; Heinz et al., 2013). Such force fields are typically implemented with specific H_2O models (SPC, TIP3P, etc.) to accurately model hydrated clay interlayers and interactions with aqueous solutions (van der Spoel, van Maaren, & Berendsen, 1998).

Force fields developed for application to clay mineral systems typically rely on fitting of force constants and other parameters for the interatomic potentials to structural, physical properties, and spectroscopic data, or, in some cases, to results of quantum mechanical calculations. The Kawamura et al. (1998) force field involves nonbonded interactions as given in Eq. (9.2) but with additional two-body parameters to explicitly account for the Pauli exclusion of electrons. Covalent, or bonded, terms based on an exponential dependence of atom-atom distances are incorporated to describe the potential energy of metal-oxygen polyhedra and

hydroxyl groups of the clay and for O-H interactions in water molecules. A complex three-body term is also needed to reproduce the structural and physical properties of water, ice, and related structures. Teppen et al. (1997) developed a conventional bonded force field using bond stretch, angle bend, and torsional terms parameterized for the common tetrahedral and octahedral linkages of metal-oxygen polyhedra associated with clay minerals. Additionally, this particular force field includes bonded potentials to describe the difference in energy of Al occurring in either tetrahedral or octahedral coordination. Partial charges were assigned to clay atoms by a combination of deformation electron densities from X-ray diffraction measurements and from electrostatic potentials fitted to high-level ab initio calculations.

A different approach, involving predominantly nonbonded interactions, was taken by Sainz-Díaz et al. (2001) using exponential-based potentials for two-body interactions and a harmonic core-shell potential to account for electronic polarization associated with O ions. Three-body terms are incorporated to improve polyhedral geometries, and formal charges of ions are used for evaluating electrostatics. Cygan et al. (2004) expanded such an approach with the development of Clayff, a primarily nonbonded force field (Eq. 9.2) that includes optimized charge distributions for metals and coordinating oxygens in either tetrahedral or octahedral coordination based on quantum calculations and stoichiometric constraints. Harmonic and Morse potentials describe covalent bonds of hydroxyl groups and water molecules. Clayff was developed to accurately model a variety of oxide, hydroxide, oxyhydroxide, and clay mineral systems and their interactions with aqueous solutions, and has been used to successfully model molecular interactions associated with numerous environmental applications. Recently, Heinz et al. (2013) optimized parameters for two-, three-, and four-body harmonic potentials to accurately reproduce a large set of crystal structures, thermodynamics, and physical properties of mineral and oxide phases. The INTERFACE force field enables molecular simulations of clay minerals and of organic and biochemical molecules interacting with clay interlayers and external surfaces.

Although each may use a different set of analytical functions to describe the potential energy, these validated force fields are useful in providing accurate classical-based descriptions of clay mineral structures and molecular behavior. Use of bonded force fields require constrained metal-O polyhedra while nonbonded force fields allow metal-O bond breaking and bond forming—and therefore support formation of new coordination polyhedra—under extreme or nonequilibrium conditions. Nonbonded force fields are typically used for modeling amorphous and glassy materials where it is not uncommon to have atoms change coordination dynamically throughout the simulation. Accurate nonbonded force fields, usually with limited number of analytical expressions for the potential energy, are also attractive by reducing the computational cost of large-scale molecular simulations when many millions of atoms and time steps (or atomic configurations) require repetitive evaluations. Of course, due to the variety of clay mineral structures and compositions, it is beneficial to utilize a general force field that is accurate and suitable for a wide range of clay mineral applications.

A recent challenge in modeling clay systems is the refinement of force fields to accurately model the edge sites of clay minerals where acid-base reactions can change the protonation state and charge of the clay mineral and therefore impact adsorption phenomena. Depending on the pH of the aqueous solution and the surface properties of the clay mineral, negatively-charged O, neutral hydroxyl groups, or positively-charged groups with doubly-protonated O would be exposed to the solution. Recent efforts by Zeitler et al. (2014), Newton and Sposito (2015) using modified versions of Clayff have developed new approaches to improve modeling these edge sites.

Several interatomic potentials for CO_2 are available for modeling gas, liquid, and supercritical states (Zhang & Duan, 2005; Aimoli, Maginn, & Abreu 2014). Flexible CO_2 potentials incorporate bond stretch and bend modes that assist in the analysis of interfaces involving intercalation processes and adsorption of CO_2 (Harris & Yung, 1995; Zhu, Zhang, Liu, & Zhang, 2009; Cygan, Romanov, Myshakin, 2012). Molecular behavior in carbon sequestration applications, in particular, requires compatible force fields that can collectively model interactions among CO_2, H_2O, and mineral phases, especially clay minerals which can effectively capture CO_2. Accurate and reliable potentials/force fields are important in providing realistic MD and Monte Carlo simulations especially when the clay-H_2O-CO_2 systems are comprised of many tens of thousands to millions of atoms.

9.2 DFT Methods for Clay Systems

First-principles methods offer more precise estimations of thermodynamic, spectroscopic, mechanical, and other parameters of clay systems compared to empirical force field-based molecular simulations. However, even with the use of modern supercomputers, first-principles Density Functional Theory (DFT) methods would be computationally expensive to model complex clay systems due to the size of the simulation cell that must be employed. As a result, first-principles MD calculations on clays systems were limited to perfect bulk systems, and the dynamics were limited to pico-second scale. In those simulations, potential energy of the interacting particles and forces are computed using DFT methods; and evolution of the system is governed by Newtonian dynamics similar to classical molecular dynamics simulations. That means that at each time step, the first-principles method is involved to compute a potential energy of a system. Given that a typical time step is 1 *femto*-second (or even smaller, if a power spectrum for high-frequency modes is of interest) a simulation of 10 *pico*-seconds would require 10,000 single-point calculations of potential energy.

The clays minerals as layered systems provide space for interlayer species like counter-balancing ions and molecules. For example, energy gain resulting from hydration of the interlayer ions serves as a driving force for clay swelling. The interactions between the interlayer molecules themselves, interlayer molecules and

clay layers, and between the neighboring clay layer units are non-bonding in nature. For such interactions, the van der Waals dispersion correction to a total energy is important. In classical molecular dynamics, that correction is accounted for through the Lenard-Jones part of the interatomic potential describing van der Waals forces. In standard DFT calculations, an explicit correction must be added to the DFT energies as the local and semi-local exchange correlation functionals are short ranged and cannot describe the nonlocal interactions. Several approaches have been proposed for correcting DFT for dispersion, including the DFT-D2 (Grimme Antony, Schwabe, & Mück-Lichtenfeld, 2007), DFT-D3 (Grimme, Antony, Ehrlich, & Krieg, 2010), and vdW-TS (Tkatchenko & Scheffler, 2009) methods at an atom-atom level, the DCACP (dispersion-corrected atom-centered pseudopotential) method (Tavernelli, Lin, & Rothlisberger, 2009) at atom-electron level, and explicit consideration of non-local interactions as in the vdW-DF method (Lee et al., 2010).

Dispersion corrections to the DFT energies are important in characterizing clay surfaces (Voora, Al-Saidi, & Jordan, 2011, 2012). This was demonstrated by Voora et al. (2011) who investigated lattice constants, bond lengths, and bulk moduli of pyrophyllite and montmorillonite with alkali and alkali earth metal ions, using density functional theory with and without dispersion corrections. Both the DFT-D2 and vdW-TS methods were used to adjust representations of the layered structures of montmorillonite and pyrophyllite. For pyrophyllite, it was found that inclusion of the dispersion correction significantly improves agreement between the calculated and experimental values of the lattice parameters and bulk modulus. For montmorillonite, the calculations predict that the interlayer spacing varies approximately linearly with the cation radius. Inclusion of the dispersion correction leads to a sizable shift to lower values of the interlayer spacing.

Subtle features in interatomic interactions may be responsible for experimentally observed changes in IR and Raman spectra of intercalated species in clay systems. DFT-based molecular dynamics simulations with DFT-D2 dispersion correction were used to interpret the origin of the observed shift in asymmetric stretch vibration of CO_2 trapped in montmorillonite (Myshakin et al., 2013). The atomic velocities were collected from production runs and used to calculate the velocity autocorrelation functions (VACF) which, in turn, were used to calculate the power spectra. The spectra computed for selected CO_2/H_2O compositions were compared with the experimental FT-IR spectra including the asymmetric stretch fundamental for CO_2 intercalated in sodium-exchanged montmorillonite. The results provide strong evidence that the observed red shift is due to geometry distortions of the CO_2 molecules induced by the water molecules. The data explain why classical MD simulations were unable to predict a red shift for the intercalated carbon dioxide. The force field employed in classical MD only uses a harmonic C–O stretch term, whereas it is necessary to include an anharmonic C–O stretch term to account for the frequency shift accompanying the stretching of CO bonds upon hydration. The results also suggest a way of how to rectify that deficiency by adopting a Morse-type potential to describe the C–O stretch bond.

9.3 Hydration of Montmorillonite

An instructive example in the use of molecular simulation for clay minerals is provided by the swelling of montmorillonite using energy minimization and MD approaches and a classical force field (Cygan et al. 2004) to describe the potential energy of the clay system as a function of interlayer water. In a simple analysis of this system one can evaluate the electrostatic energy for a relatively small periodic simulation cell comprised of a single Na-montmorillonite interlayer in which the layer charge is associated with a Mg^{2+} site in the dioctahedral sheet resulting in a layer charge of −0.5 per $O_{10}(OH)_2$. Figure 9.1 presents a summary of the energy-minimized smectite model without interlayer water and for two different interlayer water contents. The optimized anhydrous model exhibits a collapsed smectite layer in which the interlayer Na^+ exists adsorbs to at a hexagonal hole of the siloxane sheet near the octahedral substitution. The strong Coulombic interactions between charged layers and the interlayer Na^+ control the long-range structure of the collapsed smectite model. However, the clay layers can be expanded with the introduction of nominal number of water molecules into the interlayer to form a monolayer hydrate. The resulting clay structure is stabilized by the partial hydration of the interlayer Na^+ by the water molecules and by the formation of hydrogen bonds among the water molecules and with the clay surfaces of the interlayer. The energy benefit amounts to about 70–80 kJ/mol for each water molecule that is introduced into the clay interlayer. The electrostatic stabilization in the monolayer

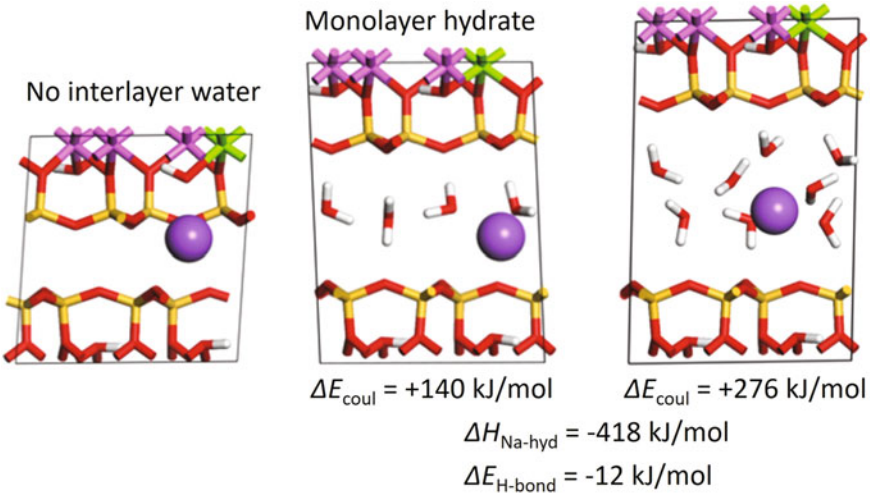

Fig. 9.1 Optimized periodic molecular models of an idealized Na-montmorillonite exhibiting expansion as a function of interlayer water content, and the corresponding changes in the electrostatic energy relative to the anhydrous model. Hydration enthalpy for Na^+ and energy associated with hydrogen bonds are indicated

hydrate is reduced by 140 kJ/mol in this example, but this amount is easily offset by the energy gained through hydrating the Na^+ and the development of a hydrogen bond network.

Further expansion of the smectite interlayer to a bilayer hydrate leads to further reduction in the Coulombic contribution (+276 kJ/mol) and is accompanied by increased hydration of the Na^+; a fully hydrated Na^+ can lead to an energy gain (enthalpy of hydration) of about −418 kJ/mol (Burgess 1999). Such outer-sphere complexes are preferred in Na-montmorillonite rather than the direct adsorption of Na^+ to the clay surface (inner-sphere complex) that would be more likely for a beidellite where the layer charge is localized at the interlayer in the tetrahedral sheet (Teich-McGoldrick, Greathouse, Jové Colón, & Cygan, 2015).

These simple examples demonstrate how important the energy balance for the various atomic and molecular interactions is to the stability of a hydrated clay mineral system. Such simulations allow the modeler to extract very detailed snapshots of the atomic structure and of the thermodynamics to better assess molecular behavior, especially for complicated structures as associated with clay minerals. The significance of water and the development of hydrogen bonds among water molecules and mineral surfaces are crucial to the unique adsorption and swelling properties of clay minerals. The enthalpy of a hydrogen bond—approximately −12 kJ/mol based on an average of 3.5 bonds per tetrahedral coordination of water molecules—can contribute significantly to the stability of clay interlayers and interfaces.

References

Aimoli, C. G., Maginn, E. J., & Abreu, C. R. A. (2014). Transport properties of carbon dioxide and methane from molecular dynamics simulations. *Journal of Chemical Physics, 141*(13), 134101.

Burgess, J. (1999). *Ions in solution: Basic principles of chemical interactions (Horwood Series in Chemical Science).* Reprint (Revised ed.). Chichester: Elsevier.

Cygan, R. T., Liang, J.-J., & Kalinichev, A. G. (2004). Molecular models of hydroxide, oxyhydroxide, and clay phases and the development of a general force field. *Journal of Physical Chemistry B, 108*(4), 1255–1266.

Cygan, R. T., Romanov, V. N., & Myshakin, E. M. (2012). Molecular simulation of carbon dioxide capture by montmorillonite using an accurate and flexible force field. *Journal of Physical Chemistry C, 116*(24), 13079–13091.

Grimme, S., Antony, J., Ehrlich, S., & Krieg, H. (2010). A consistent and accurate ab initio parametrization of density functional dispersion correction (DFT-D) for the 94 elements H-Pu. *Journal of Chemical Physics, 132*(15), 154104.

Grimme, S., Antony, J., Schwabe, T., & Mück-Lichtenfeld, C. (2007). Density functional theory with dispersion corrections for supramolecular structures, aggregates, and complexes of (bio) organic molecules. *Organic & Biomolecular Chemistry, 5*, 741–758.

Harris, J. G., & Yung, K. H. (1995). Carbon dioxide's liquid-vapor coexistence curve and critical properties as predicted by a simple molecular model. *Journal of Physical Chemistry, 99*(31), 12021–12024.

Heinz, H., Lin, T.-J., Mishra, R. K., & Emami, F. S. (2013). Thermodynamically consistent force fields for the assembly of inorganic, organic, and biological nanostructures: The INTERFACE force field. *Langmuir, 29*(6), 1754–1765.

Kawamura, K., et al. (1998). New approach for predicting the long-term behavior of bentonite: The unified method of molecular simulation and homogenization analysis. In I. G. McKinley & C. McCombie (Eds.), *Scientific basis for nuclear waste management XXI, 506* (pp. 359–366). Warrendale: Materials Research Society.

Lee, K., et al. (2010). Higher-accuracy van der Waals density functional. *Physical Review B, 82,* 081101(R).

Myshakin, E. M., et al. (2013). Molecular dynamics simulations of carbon dioxide intercalation in hydrated Na-montmorillonite. *Journal of Physical Chemistry C, 117*(21), 11028–11039.

Newton, A. G., & Sposito, G. (2015). Molecular dynamics simulations of pyrophyllite edge surfaces: Structure, surface energies, and solvent accessibility. *Clays and Clay Minerals, 63*(4), 277–289.

Sainz-Díaz, C. I., Hernández-Laguna, A., & Dove, M. T. (2001). Modeling of dioctahedral 2:1 phyllosilicates by means of transferable empirical potentials. *Physics and Chemistry of Minerals, 28*(2), 130–141.

Tavernelli, I., Lin, I. C., & Rothlisberger, U. (2009). Multicenter-type corrections to standard DFT exchange and correlation functionals. *Physical Review B, 79,* 045106.

Teich-McGoldrick, S. L., Greathouse, J. A., Jové Colón, C. F., & Cygan, R. T. (2015). Swelling properties of montmorillonite and beidellite clay minerals from molecular simulation: Comparison of temperature, interlayer cation, and charge location effects. *Journal of Physical Chemistry C, 119*(36), 20880–20891.

Teppen, B. J., et al. (1997). Molecular dynamics modeling of clay minerals. 1. Gibbsite, kaolinite, pyrophyllite, and beidellite. *Journal of Physical Chemistry B, 101*(9), 1579–1587.

Tkatchenko, A., & Scheffler, M. (2009). Accurate molecular van der Waals interactions from ground-state electron density and free-atom reference data. *Physical Review Letters, 102*(7), 073005.

van der Spoel, D., van Maaren, P. J., & Berendsen, H. J. C. (1998). A systematic study of water models for molecular simulation: Derivation of water models optimized for use with a reaction field. *Journal of Chemical Physics, 108*(24), 10220–10230.

Voora, V. K., Al-Saidi, W. A., & Jordan, K. D. (2011). Density Functional Theory study of Pyrophyllite and M-Montmorillonites (M = Li, Na, K, Mg, and Ca): Role of dispersion interactions. *Journal of Physical Chemistry A, 115*(34), 9695–9703.

Voora, V. K., Al-Saidi, W. A., & Jordan, K. D. (2012). An assessment of the vdW-TS method for extended systems. *Journal of Chemical Theory and Computation, 8*(4), 1503–1513.

Zeitler, T. R., Greathouse, J. A., Gale, J. D., & Cygan, R. T. (2014). Vibrational analysis of brucite surfaces and the development of an improved force field for molecular simulation of interfaces. *Journal of Physical Chemistry C, 118*(15), 7946–7953.

Zhang, Z., & Duan, Z. (2005). An optimized molecular potential for carbon dioxide. *Journal of Chemical Physics, 122*(21), 214507.

Zhu, A. M., Zhang, X. B., Liu, Q. L., & Zhang, Q. G. (2009). A fully flexible potential model for carbon dioxide. *Chinese Journal of Chemical Engineering, 17*(2), 268–272.

Index

A
Ab initio, *141*, *157*, *178*
Acid, *2*, *3*, *11*, *16*, *20*, *21*, *24*, *44*, *79*, *80*, *84*, *85*, *107*, *109*, *110*, *114*, *135*, *179*
  mineral dissolution, *58*, *79–81*, *91*, *92*, *106*, *107*, *114*
Atomic density, *161*, *162*

B
Basalt, *44*, *106*
Bentonite, *36*, *47*, *50*, *58*, *81*, *85*, *108*, *163*

C
Capillary. *See* Wettability
Carbon capture and storage, *12*
Carbon dioxide, *3*, *7*, *9–12*, *15*, *16*, *18–30*, *41–47*, *79*, *80*, *85*, *86*, *96*, *105–120*, *132*, *139–142*, *147*, *148*, *150–156*, *158–162*, *167–169*, *179*, *180*
  water dissolution, *107*
Carbon management, *10–12*
Cation exchange, *60*, *64*, *70*, *71*, *81*, *92*, *97*, *100*, *107*, *108*, *113*, *116*, *127*, *128*, *130*, *138–142*, *148*, *150*, *159*, *165*, *180*
  exchange capacity, *60*, *81*, *107*, *127*
Climate, *9–12*, *16*, *17*, *19*, *21*, *24*, *29*, *30*, *160*
Coal, *10*, *19*, *26*, *37*, *38*, *43*, *44*, *91*, *108*, *141*
Contact angle. *See* Wettability
Crystal, *36*, *56–58*, *62*, *65*, *66*, *72*, *73*, *82*, *83*, *92*, *140*, *148*, *176*, *178*
  crystallization, *34*, *36*, *48*, *49*, *56*, *57*, *65*, *73*, *78*, *80*, *85*, *128*

D
Development of life. *See* Evolution
Diffraction
  Debye-Scherrer, *82*
  electron diffraction, *65*, *83*
  Laue indices, *66*
  neutron diffraction, *89*, *139*
  (Wulff-)Bragg's condition, *66*, *82*
  X-ray diffraction, *55*, *65–68*, *72*, *81–87*, *89*, *107*, *113*, *137*, *139*, *141*, *148–150*, *154*, *158*, *159*, *178*
Drilling, *36*, *38–40*, *50*, *51*, *69*, *126*
  drilling mud, *40*, *50*, *51*, *69*, *126*

E
Economics, *11*, *12*, *27*, *29*, *30*, *38*, *39*, *43*, *45*, *47*, *118*
Ecosystem, *3*, *9–12*, *16*, *21*, *33*
Emissions, *9*, *10*, *19–21*, *24–30*, *84*, *86*, *160*
Evolution, *1*, *2*, *5–7*, *9–11*
Extinction of species. *See* Evolution

F
Fossil, *10–12*, *19*, *26*, *27*, *29*, *30*, *38*, *43*
Free energy, *139*, *154–156*, *158*

G
Geology, *11*, *12*, *29*, *34*, *36–39*, *43*, *44*, *47*, *50*, *56*, *73*, *78*, *81*, *84*, *89*, *96*, *106*, *108*, *119*, *148*, *150*, *158*, *166*, *168*
  caprock, *39*, *106*, *140*, *160*
  Earth's crust, *7*, *10*, *56*, *60*, *78*, *84*
  geothermal, *38*, *43*, *58*
  lava, *10*, *56*, *106*
  magma, *34*, *78*, *80*
  seal, *36*, *38*, *39*, *44*, *50*, *119*
  structural and stratigraphic trapping, *39*, *44*
  volcanic, *17*, *34*, *36*, *58*
Global warming, *16*, *18*, *19*, *21*
  Global Warming Potential (GWP), *18*, *27*
  risk, *11*, *12*, *42*

© Springer International Publishing AG 2018

V. Romanov (ed.), *Greenhouse Gases and Clay Minerals*, Green Energy and Technology, https://doi.org/10.1007/978-3-319-12661-6

Greenhouse, *9*, *10*, *12*, *15*, *16*, *18*, *19*, *26*, *27*, *29*, *30*, *86*, *92*, *96*, *147*, *160*

I

In situ, *86*, *88*, *89*, *105*, *113*, *114*, *132*, *141*, *148*
Isotherm, *85*, *107*, *108*, *117*, *119*, *167–169*

L

Life, *1–12*, *18*, *21*, *24*, *34*, *48*, *78*, *79*
  biochemical, *2*, *3*, *9–11*, *21*, *23*, *24*, *27*, *43*, *50*, *56*, *78*, *178*
  living species, *4*, *9–11*, *48*, *78*, *79*
Lineages. *See* Evolution
Living species. *See* Life

M

Mesopores, *136*
Methane, *3*, *7*, *10*, *11*, *18*, *19*, *21*, *38*, *45*, *79*, *96*, *117–120*, *147–149*, *163*, *165–168*
  methane hydrates, *163*, *165*, *166*
  natural gas, *19*, *29*, *37*, *43–47*, *96*, *119*, *167*
  shale gas, *38*, *39*
  tight gas, 38, 46
Microorganisms, *3*, *79*
  bacteria, *7*, *37*, *79*
Microscopy
  atomic force, *91*, *133*
  electron, *58*, *59*, *65*, *66*, *82–84*, *88*
  laser scanning, *85*
  optical, *85*
Mineral structure, *58*, *90*, *92*, *178*
  basal spacing, *65*, *66*, *68*, *70*, *92*, *110*, *131–133*, *135*, *138*, *139*, *141*, *142*, *158*, *166*, *168*
  coherence, *65*, *82–84*
  d-spacing, *66*, *82*, *102*, *132*, *139*, *140*, *149*, *150*, *152–159*, *165*, *167*
  fundamental particle, *65*, *82–84*
  interlayer spacing, *133*, *153*, *168*, *180*
  interstratification, *62*, *64*, *66*, *70*, *72*, *82*, *131*, *148*, *165*
  lattice, *34*, *65*, *66*, *69*, *82*, *83*, *99*, *102*, *130*, *149*, *165*, *166*, *180*
  Miller indices, *65*
  octahedral, *58–63*, *68–70*, *72*, *92*, *99*, *126–131*, *150*, *154*, *156*, *158*, *178*, *181*
  primary particle, *65*
  tetrahedral, *58–61*, *65*, *68–70*, *72*, *78*, *92*, *99*, *100*, *108*, *126–128*, *130*, *131*, *150*, *154*, *156*, *158*, *165*, *178*, *182*
Mineral trapping, *45*, *106*, *114*, *154*, *160*, *163*
  carbonation, *24*, *43*, *44*, *88*, *107*, *109*, *114–117*, *141*
  Elovich equation, *117*
  nano-confinement, *107*, *109*, *111*, *112*, *138*, *149*, *154*, *166*, *168*
Molecular dynamics, *114*, *132*, *133*, *147*, *149*, *151*, *160*, *161*, *176*, *179*, *180*
  force field, *149*, *151*, *165*, *177–181*
Monte Carlo, *97*, *136*, *141*, *147*, *154*, *176*, *177*, *179*
Mudrock, *34*, *35*, *72*, *126*, *163*

O

Ocean, *3*, *7*, *9–11*, *16*, *20*, *21*, *24*, *25*, *27*, *163*
Oil, *29*, *36*, *38–40*, *44–47*, *50*, *126*
  shale oil, *38*
Organic, *3*, *7*, *9*, *21–25*, *34*, *36–39*, *44*, *45*, *48*, *57*, *66*, *69*, *70*, *78*, *79*, *101*, *102*, *106*, *117*, *120*, *127*, *167*, *168*, *178*
Oxidation, *7*, *23*, *56*, *79*, *80*, *84*, *128*, *129*

P

Permeability, *38*, *39*, *41*, *45–47*, *117*, *136*, *163*
Photosynthesis, *7*, *9*, *21–24*
  Calvin cycle, *22*
Phyllosilicates, *34*, *36*, *47*, *56*, *58*, *59*, *64*, *72*, *73*, *84*, *92*, *126*, *129–131*, *137*, *139*, *163*
  chlorite, *36*, *57–59*, *61*, *64*, *72*, *73*, *117*, *148*
  kaolin, *36*, *57–59*, *61*, *64*, *68*, *69*, *72*, *97*, *106–108*, *113*, *117*, *126–128*, *130*, *140*, *148*, *161–163*
  illite, *36*, *57*, *58*, *61–64*, *66*, *67*, *70*, *72*, *81–83*, *97*, *107*, *108*, *117*, *118*, *127*, *128*, *148*, *165*
  mica, *34*, *36*, *56*, *57*, *62*, *78*, *128—130*, *137*
  montmorillonite, *57–59*, *61*, *64*, *68–70*, *72*, *84*, *97*, *99–101*, *103–105*, *107–110*, *113*, *114*, *117*, *118*, *127*, *130–133*, *135*, *138–142*, *148*, *180–182*
  pillared clay, *70*, *71*, *167*
  pyrophyllite, *64*, *108*, *127*, *130*, *133*, *167*, *180*
  serpentine, *36*, *64*, *68*, *126*
  smectite, *36*, *57–59*, *61–72*, *81–85*, *92*, *97*, *100*, *107*, *110–112*, *117*, *118*, *127–131*, *134*, *135*, *139–142*, *148*, *152*, *157–159*, *163*, *165*, *181*, *182*
  vermiculite, *57*, *61*, *64*, *69*, *72*, *99*, *100*, *107*, *108*, *127–129*, *131*, *133*, *135*
Porosity, *34*, *38*, *43–46*, *51*, *79*, *107*, *108*, *115*, *117*, *135*, *136*, *148*, *160*, *165–168*

Precipitation, *35*, *36*, *58*, *106*, *107*, *114*, *160*
Protonation, *3*, *22*, *81*, *102–104*, *128*, *129*, *179*

R
Radiative balance, *3*, *6*, *10*, *12*, *16–19*, *41*
Radioactive waste, *47*, *58*
Rare earth elements, *71*
Residual trapping, *44*, *45*, *108*, *148*, *155*, *159*, *160*

S
Shale, *34–41*, *44–50*, *72*, *78*, *106*, *107*, *117–120*, *126*, *141*, *148*, *160*, *167–169*
Shrinkage, *69*, *133*, *135*, *141*
Small-angle scattering
  neutron scattering, *89*
  X-ray scattering, *86*
Soil, *23*, *47*, *48*, *72*, *78*, *79*, *81*, *91*, *128*, *135*
Sorption, *85*, *92*, *96*, *106–108*, *117*, *118*, *139–141*
  absorption, *18*, *20*, *24*, *84–90*, *98–100*, *104*, *105*, *110–112*
  adsorption, *43–45*, *71*, *79*, *85*, *96–98*, *101*, *103–108*, *117–120*, *127*, *129–132*, *134*, *138*, *140*, *148*, *150–152*, *154*, *157–159*, *161*, *167–169*, *176*, *179*, *182*
  chemisorption, *84*, *117*
  physical trapping, *109*
  physisorption, *109*, *112*, *117*
Spectroscopy
  atomic absorption, *84*
  flame emission, *84*
  ICP-MS, *84*
  infrared, *15–18*, *21*, *65*, *85–87*, *89–92*, *98*, *100*, *104*, *105*, *107–111*, *113–116*, *140*, *148*, *154*, *158*, *180*
  molecular vibrations, *89*, *91*, *92*, *97–102*, *104*, *105*, *108–110*, *113*, *114*, *116*, *140*, *151*, *154*, *176–180*
  near field, *90*, *91*
  nuclear magnetic resonance (NMR), *87*, *88*, *113*, *140*
  Raman, *85*, *90*, *180*
  ultraviolet, *3*, *7*, *89*
Surface area, *70*, *71*, *107*, *108*, *117*, *118*, *140*
Swelling, *36*, *47*, *50*, *61*, *68*, *69*, *85*, *86*, *117*, *126*, *128*, *130–142*, *147–150*, *153–155*, *158–160*, *163*, *165–168*, *179*, *181*, *182*
  crystalline regime, *131–134*, *136–139*
  osmosis, *79*, *131*, *132*, *135*, *136*
Synchrotron, *86–89*

T
Tomography, *88*

W
Water, *3*, *7*, *9–11*, *16*, *18–20*, *22*, *24*, *34–36*, *38–40*, *44*, *45*, *47–50*, *55*, *56*, *58*, *61*, *64*, *66*, *68–70*, *72*, *73*, *78–81*, *85*, *89*, *90*, *96–108*, *110*, *114*, *116*, *117*, *126*, *127*, *130–142*, *147–156*, *158–163*, *165–167*, *177–182*
  brine, *44*, *106*, *140*, *160–162*
  carbon dissolution, *11*, *20*, *21*, *24*, *44*, *80*, *106*, *160*
  dehydration, *68*, *80*, *85*, *104*, *105*, *108*, *138*, *139*
  gravitational water, *79*
  hydration, *36*, *65*, *67*, *68*, *70*, *79–81*, *86*, *89*, *96*, *107*, *108*, *112*, *113*, *125–127*, *130–134*, *136–139*, *141*, *142*, *147–150*, *152–155*, *158*, *159*, *166*, *179–182*
  hydrothermal, *3*, *34*, *57*, *73*
  oxygen dissolution, *38*
Weathering, *9*, *13*, *24*, *34*, *56–58*, *60*, *72*, *78–80*, *126–129*
Wettability, *151*, *160*, *161*
  capillary, *79*, *160*
  contact angle, *160*, *161*